Titre: Title:	Development and Optimization of a Melt Electrospun Scaffold from a Polymer Ternary Blend for Biomedical Applications
Auteur: Author:	Elham Karimi
Date:	2026
Type:	Mémoire ou thèse / Dissertation or Thesis
Référence: Citation:	Karimi, E. (2026). Development and Optimization of a Melt Electrospun Scaffold from a Polymer Ternary Blend for Biomedical Applications [Thèse de doctorat, Polytechnique Montréal]. PolyPublie. https://publications.polymtl.ca/76872/

POLYTECHNIQUE MONTRÉAL

affiliée à l'Université de Montréal

Development and Optimization of a Melt Electrospun Scaffold from a Polymer Ternary Blend for Biomedical Applications

ELHAM KARIMI

Département de génie chimique

Thèse présentée en vue de l'obtention du diplôme de *Philosophiæ Doctor*

Génie chimique

Avril 2026

POLYTECHNIQUE MONTRÉAL

affiliée à l'Université de Montréal

Cette thèse intitulée :

Development and Optimization of a Melt Electrospun Scaffold from a Polymer Ternary Blend for Biomedical Applications

présentée par **Elham KARIMI**
en vue de l'obtention du diplôme de *Philosophiæ Doctor*
a été dûment acceptée par le jury d'examen constitué de :

Jason Robert TAVARES, président
Abdellah AJJI, membre et directeur de recherche
Marie-Claude HEUZEY, membre et codirectrice de recherche
Frej MIGHRI, membre et codirecteur de recherche
Geraldine MERLE, membre
Shih-Jung LIU, membre externe

DEDICATION

To my husband, Mohsen, my steadfast companion through every step of this journey, and to my mother, whose love and support I have always felt, even from afar.

ACKNOWLEDGEMENTS

Pursuing my PhD has been both a demanding and deeply meaningful journey—one that would not have been possible without the support, guidance, and generosity of many remarkable individuals. Along this path, I had the privilege of learning from inspiring mentors and working alongside dedicated colleagues who shaped not only my scientific development but also my personal growth.

First and foremost, I would like to express my sincere and heartfelt gratitude to my supervisors, Prof. Abdellah Ajji, Prof. Marie-Claude Heuzey, and Prof. Frej Mighri, for their continuous support, encouragement, and invaluable guidance throughout my doctoral studies. Their trust, expertise, and commitment played a fundamental role in completing this work, and I am truly honored to have been under their supervision.

I am profoundly grateful to Prof. Abdellah Ajji and Prof. Marie-Claude Heuzey at Polytechnique Montréal for everything they have taught me—both scientifically and personally. Beyond guiding my research with patience, insight, and rigor, they supported me during some of the most challenging periods of my PhD and my life. Their constant presence, understanding, and encouragement gave me a sense of reassurance and calm during difficult times and showed me that mentorship can extend far beyond academic responsibilities. From them, I learned not only how to be a better researcher but also how to face challenges with resilience, integrity, and humanity. I will always be deeply thankful for their support and the lasting impact they have had on my journey.

I would also like to sincerely thank my supervisor at Université Laval, Prof. Frej Mighri, for his valuable contributions to this work. His insightful comments, constructive suggestions, and thoughtful feedback significantly strengthened the quality of my research and publications. I am grateful for his expertise and support throughout this collaboration.

My deepest gratitude goes to Prof. Derek Rosenzweig and Dr. Mansoureh Mohseni Garakani for their tremendous support in the biological aspects of this research. I am particularly thankful to Prof. Rosenzweig, from whom I learned the foundations of cell biology. His constant guidance, insightful discussions, and energetic, kind nature played a crucial role in advancing my project. The knowledge and experience gained through working with Prof. Rosenzweig and Dr. Mohseni Garakani have profoundly influenced my academic development and will continue to guide me in my future career.

I am sincerely thankful to my colleagues and friends at École Polytechnique de Montréal for their valuable assistance, technical support, and constructive discussions throughout this journey. I am also profoundly grateful to my colleagues and friends in the Department of Surgery, Division of Orthopaedic Surgery, at the Montréal General Hospital, for their practical help and emotional support during my studies.

I would like to thank the members of my thesis committee for the time they devoted to reading and evaluating this thesis, as well as for their valuable and constructive feedback.

I am also grateful to Matthieu Gauthier and Claire Cerclé for their technical assistance.

I want to express my deepest gratitude to my mother, Maryam, and my brothers, Kaveh and Hamid, who have always been a constant source of love, support, and encouragement throughout my life.

Finally, my most special thanks go to the love of my life, my patient and kind husband, Mohsen. Words cannot express how grateful I am for your constant love, strength, and motivation. Thank you for all the weekends and late nights you spent at the university because of my experiments, days that could have been exhausting but that you turned into meaningful, treasured moments. I feel truly blessed to have you by my side.

RÉSUMÉ

La capacité de l'organisme à régénérer les défauts osseux au-delà de ses capacités de réparation naturelles demeure un obstacle majeur en médecine [1]. Malgré des avancées significatives dans les approches thérapeutiques conventionnelles, leurs limites cliniques et leurs effets indésirables soulignent la nécessité de développer des échafaudages alternatifs issus de l'ingénierie tissulaire, plus efficaces et associés à moins d'effets secondaires pour l'organisme [1, 2]. Ces dernières décennies, les matériaux polymères synthétiques, notamment le poly-ε-caprolactone (PCL), ont suscité un vif intérêt en raison de leur biocompatibilité et de leur facilité de mise en œuvre ; toutefois, la forte hydrophobicité et la lenteur de dégradation de ce polymère limitent sa biodisponibilité [3, 4]. Afin de pallier ces limitations, la présente étude a conçu un système ternaire innovant de poly-ε-caprolactone/oxyde de polyéthylène/polyéthylène glycol (PCL/PEO/PEG) renforcé par des nanoparticules d'hydroxyapatite (nHA). Ce système utilise une technique d'électrofilage à l'état fondu sans solvant pour produire des échafaudages fibreux alignés.

Dans une première étape, le comportement rhéologique et l'aptitude à la mise en œuvre du système ternaire ont été étudiés afin de permettre la production de fibres continues présentant un diamètre uniforme et une structure interconnectée. L'ajout de pourcentages contrôlés de PEO et de PEG a permis d'obtenir des fibres régulières, alignées et dotées d'une stabilité structurale adéquate. Les analyses morphologiques ont révélé que le système PCL/PEO/PEG forme, à l'échelle microscopique, un réseau ouvert et poreux, essentiel à la pénétration cellulaire, aux échanges de matière et au dépôt de la matrice extracellulaire.

Ensuite, l'effet du choix de la voie de mélange appropriée pour les nanoparticules d'hydroxyapatite a été évalué. Les résultats obtenus à partir de trois différentes voies de préparation de masterbatch (incorporation des nHA dans le PCL, le PEO ou le PEG) ont montré que la dispersion des nanoparticules dans les phases hydrophiles PEO ou PEG entraîne la formation de zones hétérogènes ainsi que le lessivage des phases hydrophiles lors de l'immersion en milieu aqueux. En revanche, la voie basée sur le PCL assure une stabilité morphologique et le maintien des nanoparticules, même après une exposition prolongée à un environnement aqueux. Par conséquent, la voie nHA@PCL a été retenue comme la stratégie optimale pour le développement des nanocomposites.

Dans un second temps, l'effet de la concentration en nanoparticules sur les performances biologiques et physiques des échafaudages a été étudié. Les premières évaluations ont montré qu'une augmentation de la concentration en nHA jusqu'à 10 % en poids accroissait significativement l'activité métabolique et l'adhésion initiale des ostéoblastes. Cependant, des concentrations plus élevées (20 %) ont entraîné une diminution de la réponse initiale, due à des modifications de l'énergie de surface et au risque d'agglomération des nanoparticules. Lors des tests à long terme (jour 28), la différence du nombre de cellules entre les groupes était limitée. Néanmoins, la composition à 10 % a été retenue comme optimale, car elle offre simultanément une réponse initiale supérieure et une bonne biostabilité.

Une augmentation significative de l'hydrophilie a été observée dans les échafaudages à trois composants, en particulier pour celui contenant 10 % de nanoparticules, comme en témoignent la diminution des angles de contact et la création de surfaces plus actives. Ces modifications peuvent améliorer les interactions entre la surface de l'échafaudage et des protéines favorables, telles que la fibronectine et la vitronectine, réduisant ainsi le risque de réponses inflammatoires précoces dans l'organisme [5]. De plus, la structure de surface altérée des fibres, après la dissolution relative des parties hydrophiles, crée un substrat micro-rugueux qui joue également un rôle déterminant dans l'adhésion et l'activité des cellules endothéliales.

Des évaluations biologiques in vitro ont été réalisées avec deux lignées cellulaires clés : les ostéoblastes et les cellules endothéliales de veine ombilicale humaine (HUVEC). Les résultats ont montré que le système nanocomposite ternaire, et plus particulièrement sa version optimisée, non seulement améliorait l'adhésion initiale des cellules ostéogéniques, mais favorisait également de manière significative l'adhésion et l'activité endothéliales, essentielles à la formation osseuse et à l'angiogenèse simultanées. Le comportement de ces deux lignées cellulaires suggère que la présence de nHA pourrait favoriser la prolifération cellulaire et l'activité métabolique, possiblement en raison de la libération d'ions calcium et des interactions cellulaires associées au Ca^{2+}. De plus, la rugosité contrôlée et l'hydrophilie accrue des surfaces ternaires ont permis d'améliorer significativement les performances des HUVEC.

Enfin, le test de dépôt de calcium a démontré que les échafaudages ternaires contenant des nanoparticules présentent une très forte capacité à induire la minéralisation de la matrice extracellulaire, et que la quantité de calcium déposée est nettement supérieure aux valeurs rapportées dans de nombreux systèmes similaires. Ces résultats confirment que la composition du

mélange ternaire nanocomposite (PCL/PEO/PEG-nHA) et le procédé d'électrofilage à l'état fondu permettent d'obtenir un système favorisant simultanément l'ostéogenèse et l'angiogenèse. Du point de vue des applications, ce système représente une avancée majeure dans le développement de substituts de greffe osseuse de pointe.

En résumé, cette thèse démontre l'efficacité de la stratégie de conception d'échafaudages ternaires à base de PCL/PEO/PEG, développés par électrofilage à l'état fondu et renforcés par des nanoparticules d'hydroxyapatite dans un système multicomposant.

Mots-clés : Électrofilage à l'état fondu, Mélange ternaire, Ingénierie tissulaire osseuse, Biocompatibilité, Hydroxyapatite, Échafaudages nanocomposites, Échafaudages bioactifs

ABSTRACT

The ability of the body to regenerate bone defects beyond its natural repair capacity is still a significant barrier in medicine [1]. Despite significant advances in conventional therapeutic approaches, their clinical limitations and side effects underscore the need to develop efficient, tissue-engineered alternative scaffolds with fewer side effects for the body [1, 2]. In recent decades, synthetic polymeric materials, especially poly-ε-caprolactone (PCL), have attracted attention for their biocompatibility and favorable processability; however, the polymer's strong hydrophobicity and slow degradation rate limit its bioavailability [3, 4]. To overcome these limitations, the present study designed an innovative ternary poly-ε-caprolactone/ polyethylene oxide/ polyethylene glycol (PCL/PEO/PEG) system reinforced with hydroxyapatite (nHA) nanoparticles. It used a solvent-free melt electrospinning approach to produce aligned fibrous scaffolds.

In the first step, the rheological behavior and processability of the ternary system were analyzed to enable the production of continuous fibers with uniform diameter and interconnected structure. The addition of controlled percentages of PEO and PEG enabled the production of regular, aligned fibers with appropriate structural stability. Morphological studies showed that the PCL/PEO/PEG system forms an open, porous network at the microscopic scale, which is crucial for cellular penetration, material exchange, and extracellular matrix deposition.

Next, the effect of selecting the appropriate mixing route for hydroxyapatite nanoparticles was evaluated. The results of three different masterbatch preparation routes (adding nHA to PCL, PEO, or PEG) showed that nanoparticle dispersion in the hydrophilic PEO or PEG phases leads to heterogeneous areas and leaching of the hydrophilic phases upon water immersion. In contrast, the PCL-based route ensures morphological stability, and the retention of nanoparticles even after long-term exposure to aqueous environments. Therefore, the nHA@PCL route was selected as the optimal route for developing nanocomposites.

In the next step, the effect of nanoparticle loading on the biological and physical performance of the scaffolds was investigated. Initial evaluations showed that increasing nHA up to 10 wt% significantly increased the metabolic activity and initial adhesion of osteoblasts. However, higher values (20%) led to a decrease in the initial response due to changes in surface energy and the potential for nanoparticle aggregation. In long-term tests (day 28), the difference in cell number

between groups was limited. However, the 10% composition was chosen as optimal due to its simultaneous provision of a superior initial response and good biostability.

A significant increase in hydrophilicity was observed in the ternary blend scaffolds, especially in the 10% nanoparticle-containing type, as evidenced by decreased contact angles and the creation of more active surfaces. These changes can improve interactions between the scaffold's surface and favorable proteins, such as fibronectin and vitronectin, thereby decreasing the risk of early inflammatory responses in the body [5]. Also, the altered surface structure of the fibers, after the relative dissolution of the hydrophilic parts, creates a micro-rough substrate that also plays a decisive role in the adhesion and activity of endothelial cells.

In vitro biological evaluations were performed with two key cell lines, osteoblasts and human umbilical vein endothelial cells (HUVEC). The results showed that the ternary nanocomposite system, especially the optimized one, not only enhanced the initial adhesion of osteogenic cells but also significantly supported endothelial adhesion and activity, which are essential for simultaneous bone formation and angiogenesis. The behavior of these two cell lines suggests that the presence of nHAs may promote cell proliferation and metabolic activity, possibly due to calcium ion release and Ca^{2+}-related cellular interactions. In addition, the controlled roughness and increased hydrophilicity of the ternary surfaces were highly effective in improving HUVEC performance.

Finally, the calcium deposition test showed that the ternary scaffolds containing nanoparticles have a very high ability to induce extracellular matrix mineralization, and their deposition amount is significantly higher than the values reported in many similar systems. These findings confirm that the nanocomposite ternary blend (PCL/PEO/PEG-nHA) composition and melt electrospinning process can provide a system that simultaneously supports osteogenesis and angiogenesis, and, from an application perspective, it can be considered an effective step in the development of advanced bone graft substitutes.

Overall, this thesis demonstrates that the design strategy of PCL/PEO/PEG-based ternary scaffolds, developed via melt electrospinning and reinforced with hydroxyapatite nanoparticles in a multicomponent system, can provide a completely innovative platform for bone tissue engineering. The complete free-solvent processing of these three polymer components, along with the optimized mixing route and the determination of the appropriate nHA content (10%), yields a melt electrospun scaffold with a stable microstructure, improved surface properties, high

bioactivity, and the ability to induce both osteogenesis and vascularization. Beyond innovation in formulation design, this study provides the first report of the biological application of a ternary nanocomposite scaffold prepared by melt electrospinning. This system could be a practical step in the development of advanced bone graft alternatives. These achievements highlight the importance of the present approach in the repair and regeneration of bone lesions and pave the way for more extensive in vivo or ex vivo studies, evaluation of long-term mechanical durability, and optimization of 3D architecture.

Keywords: Melt electrospinning, Ternary blend, Bone tissue engineering, Biocompatibility, Hydroxyapatite, Nanocomposite scaffolds, Bioactive scaffolds

TABLE OF CONTENTS

DEDICATION iii

ACKNOWLEDGEMENTS iv

RÉSUMÉ vi

ABSTRACT ix

TABLE OF CONTENTS xii

LIST OF TABLES xvi

LIST OF FIGURES xvii

LIST OF SUPPLEMENTARY TABLES xxii

LIST OF SUPPLEMENTARY FIGURS xxiii

LIST OF SYMBOLS AND ABBREVIATIONS xxvi

CHAPTER 1 INTRODUCTION AND THESIS ORGANIZATION 1

1.1 Introduction 1

1.2 Thesis organization 3

CHAPTER 2 LITERATURE REVIEW 5

2.1 Introduction to Bone Tissue Engineering 5

2.1.1 Challenges in Bone Regeneration 5

2.1.2 Limitations of Current Synthetic and Natural Scaffolds 8

2.1.3 Desired Properties of Bone Tissue Engineering Scaffolds 10

2.2 Materials for bone tissue engineering 16

2.2.1 Poly(ε-Caprolactone) (PCL) as a Base Polymer 19

2.2.2 Common Polymers Used for Blending with PCL for bone tissue engineering applications 21

2.3 Polymer Blending for Tailoring Scaffold Properties 25

2.3.1 Fundamentals of Polymer Blending and Morphology Development 27

2.3.2 Composition Design and Processing Strategies of Polymer Blends for Tissue Engineering Scaffolds 30

2.4 Melt Electrospinning Technique 32
2.4.1 Principles and Mechanisms of Electrospinning 32
2.4.2 Solution vs. Melt Electrospinning: Advantages and Drawbacks 35
2.4.3 Process Parameters Affecting Fiber Morphology 37
2.5 Incorporation of Bioactive Nanofillers in Polymeric Scaffolds 38
2.6 Cellular approach in bone tissue engineering 41
2.6.1 In Vitro Cell analysis for Bone Tissue Engineering 43
2.6.2 In vitro vascularization in Bone Tissue Engineering 44
2.6.3 Ex vivo and In vivo Bone Tissue Engineering advances 46
2.7 Summary and Identified Research Gaps 49
CHAPTER 3 OBJECTIVES 51
3.1 Motivation 51
3.2 Objectives 52
3.2.1 Main objective 52
3.2.2 Specific objectives 53
CHAPTER 4 ARTICLE 1: MELT ELECTROSPINNING OF POLY (ε-CAPROLACTONE)/ POLYETHYLENE OXIDE / POLYETHYLENE GLYCOL BLEND: EFFECTS ON STRUCTURE AND CELLULAR COMPATIBILITY 55
4.1 Introduction 56
4.2 Materials and methods 57
4.2.1 Materials 57
4.2.2 Sample preparation 58
4.2.3 Morphological analysis 60
4.2.4 Fourier transform infrared (FTIR) 61
4.2.5 X-ray diffraction (XRD) 61
4.2.6 Thermal properties 61
4.2.7 In Vitro Biological Evaluation 62

4.2.8 Statistical analysis 64
4.3 Results 64
4.3.1 Morphological properties 64
4.3.2 Structural and chemical characteristics 71
4.3.3 Thermal properties 73
4.3.4 Cellular Metabolic Activity and Viability Assessment 77
4.4 Conclusion 79
4.5 Supplementary materials 81
CHAPTER 5 ARTICLE 2: MELT ELECTROSPINNING OF POLY (ε-CAPROLACTONE) /POLYETHYLENE OXIDE /POLYETHYLENE GLYCOL –HYDROXYAPATITE NANOCOMPOSITE FIBERS: MORPHOLOGY, PROPERTIES AND HYDROLYTIC DEGRADATION 84
5.1 Introduction 85
5.2 Material and methods 87
5.2.1 Materials 87
5.2.2 Sample preparation 88
5.2.3 Scaffold characterization 90
5.2.4 Statistical analyses 94
5.3 Results and discussion 94
5.3.1 Morphological and Compositional Characterization 94
5.3.2 Chemical Structure Analysis 97
5.3.3 Differential Scanning Calorimetry (DSC) 100
5.3.4 Thermal stability 103
5.3.5 Mechanical properties 107
5.3.6 Hydrolytic degradation behavior 109
5.4 Conclusion 112
5.5 Supporting Information Description 113
5.6 Supplementary materials 115

CHAPTER 6 ARTICLE 3: BIOACTIVE NANOCOMPOSITE SCAFFOLDS BY MELT ELECTROSPINNING OF POLY-ε-CAPROLACTONE/POLYETHYLENE OXIDE/POLYETHYLENE GLYCOL-HYDROXYAPATITE BLENDS FOR BONE TISSUE ENGINEERING 118
6.1 Introduction 119
6.2 Materials and Methods 121
6.2.1 Materials 121
6.2.2 Scaffolds fabrication 121
6.2.3 Scaffold characterization 124
6.2.4 Scaffolds biocompatibility 125
6.2.5 Statistical analysis 128
6.3 Results and discussions 129
6.3.1 Optimization of Fabrication Strategy and Nanoparticle Loading 129
6.3.2 Evaluation of Optimized Scaffolds 134
6.4 Conclusion 142
6.5 Supporting Information Description 143
6.6 Supplementary materials 144
CHAPTER 7 GENERAL DISCUSSION 151
CHAPTER 8 CONCLUSION, ORIGINAL CONTRIBUTIONS, AND RECOMMENDATIONS 161
8.1 Conclusion 161
8.2 Original contributions 163
8.3 Recommendations 165
REFERENCES 168

LIST OF TABLES

Table 2.1 A comparison of the advantages and disadvantages of various methods for treating bone lesions 9
Table 2.2 Overview of cellular and protein-surface interactions. Adapted from Ref. [76] under the Creative Commons CC BY 4.0 license 13
Table 2.3 Advantages and limitations of natural and synthetic polymers used in bone tissue engineering. Adapted from Ref.[86, 87] under the Creative Commons CC BY 4.0 license 18
Table 2.4 Overview of polymeric systems commonly blended with PCL for bone tissue engineering applications Adapted from Refs. [44, 112] under the Creative Commons CC BY 4.0 license 23
Table 2.5 Examples of research conducted in the field of polymer blends processing for biological applications 26
Table 2.6 Examples of works on polymer blend melt electrospinning 36
Table 2.7 Commonly used nanoparticles in bone tissue engineering 39
Table 4.1 Thermal properties of neat polymers: glass transition (T_g), melting (T_m), and crystallization (T_c) temperatures 58
Table 4.2 Thermal properties of the samples before (BME) and after (AME) the melt electrospinning 74
Table 5.1 Thermal properties of neat polymers: melting, crystallization, and glass transition temperatures 88
Table 5.2 Developed formulations of the composition 89
Table 5.3 Key thermal metrics obtained from the first heating cycle for melt electrospun fibers at a scan rate of 10 ˚C.min^{-1} 101
Table 5.4 Results of thermogravimetric analysis (TGA) and calculated thermal parameters and residual weight of melt electrospun fibers before (BW) and after (AW) immersion in water^{I} 107
Table 5.5 Combining the results of exponential model fitting and experimental data to evaluate the degradation behavior of samples 112
Table 6.1 Formulation composition of the samples used in this study 123
Table 6.2 Demographic characteristics of vertebral tissue donors 126

LIST OF FIGURES

Figure 2.1 Schematic representation of the functions and chemical composition of bones, and four types of cells in bone: bone marrow mesenchymal stem cells (BMSCs) (to differentiate to osteoblast and help bone regeneration), osteoblasts (to form matrix), osteocytes (to orchestrate bone homeostasis), and osteoclasts (to resorb matrix). Reproduced from Ref. [16] with permission from [Elsevier], © [2021]. 6
Figure 2.2 Hierarchical structure of the cortical (compact part) and cancellous (spongy part) bone. The diverse structural parts are illustrated, from the mesostructures (i.e., osteons/lamellar packets) to the sub-nanostructures (i.e., collagen molecule). Reproduced from Ref. [60] under the terms of the Creative Commons CC BY license. 11
Figure 2.3 The schematic diagram of the requirements of bone scaffold on design and properties, and the process of implanting a tissue-engineered bone scaffold in the body. Reproduced from Ref. [62] under the terms of the Creative Commons CC BY license..... 12
Figure 2.4 Schematic representation of the tissue-engineered scaffold's porosity and pore size impact on bone regeneration. Reproduced from Ref.[77] under the terms of the Creative Commons CC BY license. 14
Figure 2.5 Compressive strength, morphology, and porosity of chitosan/carboxymethyl cellulose (CS/CMC) nanocomposite mats containing 0%, 1%, 2.5%, 5%, and 10% carboxylated cellulose nanowhiskers (CCNWs-AgNPs) with silver nanoparticles named as SCA-0, SCA-1, SCA-2.5, SCA-5, and SCA-10, respectively. Reproduced from Ref. [77] under the terms of the Creative Commons CC BY license. 15
Figure 2.6 Potential morphologies in a polymeric ternary blend fabricated from B, as the major phase, and A and C, as dispersed phases, as predicted by the spreading coefficient. (a) A-rich domain is encapsulated by C. (b) A and C are dispersed in B. (c) C-rich domain is encapsulated by A. (d) Partial wetting morphology of A and C. Reproduced from Ref. [123] with permission from [American Chemical Society], © [2014]. 29
Figure 2.7 A schematic showing the key distinctions between melt and solution electrospinning. Reproduced from Ref. [177] under the terms of the Creative Commons CC BY license. 35
Figure 2.8 The evolutions of the microstructure in (a) plain polyethylene/ polyamide 6 (PE/PA6) (75/25 vol%), (d) plain PE/PA6 (25/75 vol%), and the localization of organoclay within the droplet phase and (e-f) within the matrix phase. Reproduced from Ref. [216] with permission from [Elsevier], © [2010]. 41
Figure 2.9 Distribution of bone tissue engineering research based on the types of scaffolds. Reproduced from Ref. [220] under the terms of the Creative Commons CC BY license..... 42

Figure 2.10 An overview of the relationship between the scaffolds' biochemical properties, architectural designs, co-culture factors, and angiogenesis. Reproduced from Ref. [76] under the terms of the Creative Commons CC BY license. 46
Figure 2.11 The role of ex vivo models in the preclinical and clinical development of novel bone tissue engineering therapies. Reproduced from Ref. [235] under the terms of the Creative Commons CC BY license. 47
Figure 4.1 A schematic view of the melt electrospinning apparatus: (1) melt-blended sample loaded stainless steel syringe, (2) stainless steel heater, (3) the temperature-controlled syringe, equipped with an in-line heater, was secured to the syringe pump to ensure a consistent flow of the molten mixture, (4) needle, (5) pump, (6) temperature controller, (7) collector and (8) high voltage supplier. 60
Figure 4.2 Morphology of (A)PCL/PEG (75/25)-BME, (B) PCL/PEO (75/25)-BME and (C) PCL/PEO/PEG (67/16.5/16.5)-BME samples (After mixing in the Brabender) with (D–F) corresponding area-weighted domain-size distributions quantified from the respective micrographs. 66
Figure 4.3 Surface SEM micrographs of melt-electrospun fibers: (A) PCL/PEG (75/25), (C) PCL/PEO (75/25), and (E) PCL/PEO/PEG (67/16.5/16.5). Quantitative pore-size distribution plots extracted from the corresponding images are provided in (B, D, F). The inset in (A) (30 μm scale) 69
Figure 4.4 Cross-sectional SEM morphology of melt-electrospun fibers: (A) PCL/PEG (75/25), (C) PCL/PEO (75/25), and (E) PCL/PEO/PEG (67/16.5/16.5). The corresponding area-weighted pore-size distribution plots are shown in (B, D, F). The inset in (A) (10 μm scale) 70
Figure 4.5 (A) FTIR spectrum for samples before and after melt electrospinning and (B) XRD pattern of neat polymers and their binary and ternary blends. 73
Figure 4.6 (A) Metabolic activity of fibroblasts on different scaffolds over a period of 28 days. Cellular metabolic activity was measured using the Alamar Blue assay on days 1, 3, 7, 14, 21, and 28 after culture. Data is presented as mean ± SD. Two-way ANOVA performed statistical analysis with Tukey's post hoc test. Statistical symbols are displayed as follows: *$p < 0.05$, **$p < 0.01$, ***$p < 0.001$, ***$p < 0.0001$, and ns indicates non-significance. To avoid cluttering the form and maintaining readability, only two key families of comparisons are shown in the graph: (1) ternary combination (PCL/PEO/PEG) versus PCL as the baseline reference, and (2) PCL/PEO versus PCL/PEG. All other comparisons (including all pairs between formulations at each time point) are presented in full in the Supporting Information (Figure S. 4.1). (B) SEM image of fibroblast cells on PCL scaffold at day 28 showing scattered cell distribution. (C) SEM image of PCL/PEO/PEG scaffold on the same day showing formation of a dense network of cells and extracellular matrix. Scale bar: 50 μm. 79

Figure 5.1 A schematic of the electrospinning apparatus: (1) stainless steel syringe, (2) stainless steel heater, (3) to supply the molten mixture at a steady flow, the temperature-controlled syringe (in-line heater) was strapped onto the syringe pump, (4) pump, (5) temperature controller, and (6) drum collector..... 90
Figure 5.2 SEM images and EDX analysis of melt electrospun scaffolds after one week of water immersion. (A-B) depicts the cross-sections of PCL/nHA and ternary blend/nHA samples, respectively; in (B), a magnified view with a 10 μm scale bar is provided for more detail. Surface images of the fibers are shown for (C) PCL/nHA and (D) ternary blend/nHA. All SEM images in (A–D) are recorded with a 50 μm scale bar. The size distribution of hydroxyapatite nanoparticles on the fiber surface is shown in histogram format for (E) PCL/nHA and (F) ternary blend/nHA. EDX maps of Ca (K-series) and P (K-series) elements are presented for (G) PCL/nHA and (H) ternary blend/nHA samples, respectively, confirming the uniform dispersion of inorganic nanoparticles in the fibrous matrix. The scale bar in the EDX images is 100 μm. 96
Figure 5.3 FTIR spectra comparing hydroxyapatite (nHA) loading and processing routes. (A) PCL-based formulations (pristine PCL and PCL/nHA) presented as melt-blended samples (BME) and electrospun fibers (AME). (B) Ternary-based formulations (PCL/PEG/PEO blend and its nHA-loaded counterpart) presented as melt-blended samples (BME) and melt electrospun fibers (AME). Key diagnostic absorptions-including ether linkages (C-O-C, ≈1293/1240/1160 cm^{-1}), carbonyl stretching (C=O, ≈1720 cm^{-1}) and phosphate groups (ν_1 ≈630 cm^{-1}; ν_3 ≈1030–1100 cm^{-1})-are displayed, with nHA powder (green trace) overlaid as reference. (C) Magnified carbonyl region shows no detectable peak shifting (vertical dashed line at 1720 cm^{-1}). (D) Full-range spectra (4000–600 cm^{-1}) for AME samples, confirming overall spectral consistency across formulations..... 99
Figure 5.4 DSC of melt electrospun fibers (A) first heating endotherms. (B) Cooling exotherms. Heat flow is normalized per sample mass ($W.g^{-1}$) and exothermic direction is upward. 101
Figure 5.5 Comparing TGA curves of (A) PCL, (B) PCL/nHA, (C) Ternary blend, (D) Ternary blend/nHA melt electrospun fibers before (BW) and after (AW) immersion in water (E) Derived thermogravimetric (DTG) curves for the melt electrospun ternary blend/nHA fibers before (BW) and after (AW) immersion in water, and (F) the thermogravimetric (TGA) curve and its derivative (DTG) for hydroxyapatite nanoparticles in the powder form..... 105
Figure 5.6 (A) Schematic view of uniaxial tensile testing on melt electrospun fibers after one week of water immersion, to evaluate mechanical properties. (B) Elastic modulus, (C) strain at the yield point, and (D) yield stress for PCL, PCL/nHA, ternary blend, and ternary blend/nHA samples. The results show a significant improvement in mechanical parameters with the addition of nHA as well as in ternary blend systems compared to neat PCL. Data are reported as mean ± standard deviation, and statistical differences were determined based on one-way ANOVA test with Tukey's post-test (*$p < 0.05$, **$p < 0.01$, ****$p < 0.0001$). 108

Figure 5.7 Changes in the percentage of mass loss of PCL, PCL/nHA, ternary blend, and ternary blend/nHA samples during 28 weeks in an aqueous environment. The ternary blend and ternary blend/nHA samples showed significant mass loss, while the PCL and PCL/nHA samples had high stability. 110
Figure 6.1 Schematic representation of three different routes for preparing polymer masterbatches, including: (A) dispersion of nanoparticles in PCL, (B) dispersion in PEO, (C) dispersion in PEG, and (D) base compounds. 122
Figure 6.2 A schematic view of the melt electrospinning apparatus: (1) stainless steel syringe, (2) stainless steel heater, (3) to supply the molten mixture at a steady flow, the temperature-controlled syringe (in-line heater) was strapped onto the syringe pump, (4) needle, (5) pump, (6) temperature controller, (7) drum collector and (8) high voltage supplier. 124
Figure 6.3 SEM images of PCL/PEO/PEG ternary blend fibers with 1% nHA prepared from three masterbatch routes. (A) Ternary-nHA1@PEG, before water immersion; (B) the same sample after one week of immersion. A magnified image is provided to more clearly show the created pores (scale bar: 10 μm). (C) Ternary-nHA1@PEO, before immersion; (D) the same sample after immersion. (E) Ternary-nHA1@PCL, before immersion; (F) the same sample after immersion. The scale bar of all images is 50 μm. 130
Figure 6.4 Assessment of the optimal quantity of nHA in the ternary blend formulated from the chosen PCL/nHA masterbatch. (A) Schematic design of the experiment and decision path. (B) Alamar Blue assay on day 1 for 1, 5, 10, and 20 wt% nHA loadings. (C) DNA-based cell count assay on day 28. (D) Time course of Alamar Blue for 10 wt% (optimal option) compared to 5 wt%. Error bars: SD., n = 3, *p < 0.05, **p < 0.01, ****p < 0.0001. 134
Figure 6.5 Evaluation of water contact angle on the surface of different scaffolds to investigate the wettability and hydrophilicity properties of the surface. Error bars: SD., n = 3, *p < 0.05, **p < 0.01, ****p < 0.0001. 135
Figure 6.6 Results of cellular evaluation on different scaffolds. (A) Osteoblast cell adhesion at day 1; (B) HUVEC cell adhesion at day 1; (C) Metabolic activity of osteoblast cells during the culture period from day 1 to day 28 , the relative metabolic activity with respect to the PCL is reported in the Supporting Information (Figure S. 6.5); (D) Metabolic activity of HUVEC cells during the culture period from day 1 to day 28; (E) DNA quantification for osteoblast cells at day 28; (F) DNA quantification for HUVEC cells at day 28. To avoid cluttering the graphs, only the main comparisons between the Ternary-nHA10@PCL vs. the neat ternary, and the Tternary-nHA10@PCL vs. the neat PCL scaffolds are shown, while other comparisons are provided in the Supporting Information (Tables S. 6.1-4). 139
Figure 6.7 Evaluation of cellular mineralization using the Alizarin Red assay. (A) Quantitative comparison of mineral deposition by osteoblast cells after 28 days of culture. Error bars: SD., n = 3, *p < 0.05, **p <

0.01, ****p < 0.0001. The relative mineralization response with respect to neat PCL is presented in Supporting Information (Figure S. 6.6) (B) Representative images of Alizarin Red-stained samples for the indicated scaffolds, along with cell-free controls (Blank). 142

LIST OF SUPPLEMENTARY TABLES

Table S. 4.1 Statistical comparison between different groups in terms of cellular metabolic activity on days 1, 3, 7, 14, 21, and 28 using one-way ANOVA and Tukey's post hoc test[I] 83
Table S. 5.1 Results of EDX analysis for PCL/nHA and Ternary/nHA melt electrospun fibers after one week of water immersion. The values indicate the percentage of surface area covered with calcium, the weight percentage of calcium and phosphorus elements, and the Ca/P atomic ratio in the samples. 115
Table S. 5.2 DSC test results (first heating cycle) for PCL, PCL/nHA, ternary, and ternary/nHA samples. Data include glass transition temperature (T_g), melting temperature (T_m), melting enthalpy (ΔH_m), crystallization temperature (T_c), and crystallization enthalpy (ΔH_c). BME represents samples before the melt electrospinning process, and AME represents samples after the melt electrospinning process. 116
Table S. 6.1 pairwise comparisons between all groups in the DNA quantification test on day 1, for osteoblasts and HUVEC cells (Figures 6.6A and B in the main manuscript) based on one-way ANOVA statistical analysis[I] 147
Table S. 6.2 The pairwise comparisons between all groups in the osteoblast metabolic activity test (Alamar Blue test) at different time intervals (days 1, 7, 14, 21, and 28) (Figure 6.6C in the main manuscript), based on two-way ANOVA statistical analysis[I] 147
Table S. 6.3 The pairwise comparisons between all groups in the HUVEC metabolic activity test (Alamar Blue test) at different time intervals (days 1, 7, 14, 21, and 28) (Figure 6.6D in the main manuscript), based on two-way ANOVA statistical analysis[I] 148
Table S. 6.4 pairwise comparisons between all groups in the DNA quantification test on day 28, for osteoblasts and HUVEC cells (Figures 6.6E and F in the main manuscript) based on one-way ANOVA statistical analysis[I] 148

LIST OF SUPPLEMENTARY FIGURS

Figure S. 4.1Experimental design generated by JMP software (version 18) illustrating the selected blend compositions used for this study. `Red dots indicate compounds that were not electrospinnable. Black dots indicate compounds that were electrospinnable. 81

Figure S. 4.2 Rheology isotherm plots for different samples in the time sweep test at 150 ˚C when the frequency was adjusted to one. The images on the left (A, C, E) show the results for samples that were tested immediately after reaching the test temperature. In contrast, the images on the right (B, D, F) show the same samples that were preheated at 150 ˚C for one hour before starting the test. The changes in (A, B) the complex viscosity (η*), (C, D) the storage modulus (G′), and (E, F) the loss modulus (G″) are plotted as a function of time. The results show that preheating the samples results in more stable modulus and viscosity values over time, indicating that the system reaches rheological equilibrium. 82

Figure S. 4.3 Changes in relative metabolic activity (Normalized Metabolic Activity) of fibroblast cells on different samples (PCL/PEO, PCL/PEG, and PCL/PEO/PEG) at different time intervals. Data was calculated by dividing the values obtained from the Alamar Blue test by the corresponding values of the PCL sample at each time point. Results were statistically analyzed based on two-way ANOVA and Tukey's post-hoc test. 83

Figure S. 5.1 SEM image of hydroxyapatite nanoparticles in the initial state (A) as received from the supplier and histogram (B) of the size distribution of these nanoparticles. The scale bar in the SEM image is 50 µm. 115

Figure S. 5.2 EDX mapping of the distribution of phosphorus (P) and calcium (Ca) elements on the surface of melt electrospun fibers before immersion in an aqueous medium. (A) PCL/nHA, and (B) ternary/nHA. 115

Figure S. 5.3 DSC curves for investigating the thermal behavior of samples before the melt electrospinning process (BME) in (A) first heating cycle and (B) cooling cycle. Exothermic direction is upward. 116

Figure S. 5.4 Temperature dependence of storage modulus (E′), loss modulus (E″), and damping factor (tan δ) for the Ternary/nHA system obtained by dynamic mechanical analysis (DMA). Measurements were performed in dual cantilever mode at a frequency of 1 Hz, a strain within the linear viscoelastic region (0.16%), and a heating rate of 3 ˚C min^{-1} over the temperature range of -85 to 0 ˚C. 117

Figure S. 5.5 DTG curves of PCL/nHA samples before water immersion (BW) and after water immersion (AW). The results show that the thermal degradation behavior of the fibers was similar in both cases, and immersion in water or non-immersion does not significantly alter the thermal degradation profile. 117

Figure S. 6.1 Energy-dispersive X-ray (EDX) elemental mapping of melt electrospun nanocomposite fibers after water immersion. Representative elemental maps of C, O, Ca, and P are shown for the ternary-

nHA1@PEG and ternary-nHA1@PEO samples. In both systems, the Ca and P signals are weak and sparse after immersion, indicating a very limited detectable presence of hydroxyapatite nanoparticles (nHA) under these conditions. These observations support the reduced persistence of nHA in the PEG- and PEO-based systems following aqueous extraction. 144
Figure S. 6.2 Temperature dependence of (A) damping factor (tan δ), (B) storage modulus (E′), and loss modulus (E″) for the Ternary and Ternary-nHA10@PCL systems obtained by dynamic mechanical analysis (DMA). Measurements were conducted in dual cantilever mode at a frequency of 1 Hz, a strain within the linear viscoelastic region (0.16%), and a heating rate of 3 ˚C min^{-1} over the temperature range of -85 to 0 ˚C. 144
Figure S. 6.3 Scanning electron microscopy (SEM) images and corresponding fiber diameter distributions of electrospun scaffolds with different compositions. (A, B) SEM micrographs of ternary systems containing nHA at 10 wt% (ternary-nHA10@PCL) and 5 wt% (ternary-nHA5@PCL), respectively. (C, D) Fiber diameter histograms with Gaussian fitting obtained from ImageJ analysis for ternary-nHA10@PCL and ternary-nHA5@PCL, respectively. (E, F) SEM micrographs of PCL-based systems containing nHA at 10 wt% (PCL-nHA10) and 5 wt% (PCL-nHA5), respectively. (G, H) Corresponding fiber diameter distributions for PCL-nHA10 and PCL-nHA5. Fiber diameters were quantified from SEM images and reported as mean ± standard deviation. 145
Figure S. 6.4 (A) Schematic illustration of the cyclic tensile (fatigue) test setup under uniaxial cyclic tensile loading along the fiber alignment direction. Rectangular specimens measuring approximately 10 mm × 5 mm and 350 μm thick were used. As shown, each specimen was mounted in a paper frame and gripped using sandpaper-covered tabs to minimize slippage during cyclic loading. Fatigue tests were conducted in strain-controlled tension–tension mode between 0 and 3% strain (strain amplitude of 1.5% and mean strain of 1.5%) at a frequency of 0.5 Hz for a total of 5000 cycles under ambient conditions. At least five specimens per group were tested. (B) Evolution of maximum stress as a function of loading cycle for PCL–nHA and Ternary–nHA10@PCL scaffolds, highlighting the mechanical stability and stress retention behavior over 5000 cycles. (C–D) Representative stress–strain hysteresis loops at selected cycles (1, 100, 1000, 3000, and 5000) for (C) Ternary–nHA10@PCL and (D) PCL–nHA samples, demonstrating cyclic softening, energy dissipation, and structural evolution during fatigue loading. 146
Figure S. 6.5 Relative metabolic activity of osteoblast cells on different scaffolds at different culture time points, obtained by Alamar Blue assay. All values are normalized to the PCL group as the control. Two-way ANOVA performed statistical comparisons; **** indicates highly significant ($p < 0.0001$) and ns indicates no significant difference. 149
Figure S. 6.6 Calcium deposition of osteoblast cells on different scaffolds at day 28, assessed by Alizarin Red assay. All values are normalized to the PCL group as the control. Statistical comparisons are performed

by one-way ANOVA; *** and **** indicate different levels of statistical significance ($p < 0.001$ and $p < 0.0001$, respectively). 150

LIST OF SYMBOLS AND ABBREVIATIONS

3D	Three-Dimensional
AME	After melt electrospinning,
AgNPs	Silver nanoparticles
ALP	Alkaline phosphatase
ANOVA	Analysis of Variance
ASTM	American Society for Testing and Materials
AW	After immersion in water
BME	Before melt electrospinning,
BMSCs	Bone marrow mesenchymal stem cells
Bo_e	Electric Bond number
BW	Before immersion in water
Ca/P	Calcium to Phosphorus ratio
CAB	Cellulose Acetate Butyrate
CaP	Calcium phosphate
CCNWs	Carboxylated cellulose nanowhiskers
CMC	Carboxymethyl cellulose
C_p	Polymeric heat capacity
CPC	Calcium Phosphate Cement
CS	Chitosan
CVA	Cerebrovascular Accident
De	Deborah number

$D_{eq,i}$	The equivalent diameter of component i
DMA	Dynamic mechanical analysis
DMEM	Dulbecco's Modified Eagle Medium
DNA	Deoxyribonucleic Acid
DOE	Design of Experiments
DSC	Differential Scanning Calorimetry
DTG	Derivative thermogravimetric analysis
E	Tensile modulus (Young's modulus)
E_t	Electrostatic force
E′	Storage modulus in tension (elastic component measured by DMA)
E″	Loss modulus in tension (viscous component measured by DMA)
EBM-2	Endothelial Basal Medium-2
ECM	Extracellular matrix
EDX	Energy-Dispersive X-ray spectroscopy
EGM-2	Endothelial Growth Medium-2
FBS	Fetal bovine serum
FDA	USA Food and Drug Administration
Fe_2O_3	Iron oxides nanoparticles
F_T	Viscoelastic tensile force in the jet
FTIR	Fourier transform infrared
G′	Storage modulus in shear (elastic component measured by rheological tests)
G″	Loss modulus in shear (viscous component measured by rheological tests)

GuHCl	Guanidine HydroChloride buffer
h	Convective heat transfer coefficient
hEGF	Human Epidermal Growth Factor
HUVECs	Human Endothelial Cells
iPP	Isotactic Polypropylene
IRB	Institutional Review Board
k	Degradation rate constant
L	Characteristic length scale of the jet
M_0	Initial mass of the sample
Mg-HA	Magnesium-substituted Hydroxyapatite
M_n	Number-average molecular weight
M_t	Sample's mass at time point t
M_v	Viscosity-average molecular weight
nHA	Hydroxyapatite nanoparticles
nHA@PCL	Masterbatch of hydroxyapatite nanoparticles in poly(ε-Caprolactone)
nHA@PEG	Masterbatch of hydroxyapatite nanoparticles in polyethylene glycol
nHA@PEO	Masterbatch of hydroxyapatite nanoparticles in polyethylene oxide
PA6	Polyamide 6
PBS	Phosphate-buffered saline solution
PCL	Poly (ε-caprolactone)
PDLLA	Poly (D, L-lactic acid)
PE	Polyethylene

PEG	Poly (ethylene glycol)
PEG-b-PCL	Poly (ethylene glycol)-block-poly (ε-caprolactone)
PEO	Poly (ethylene oxide)
PFA	Paraformaldehyde
PGS	Poly (glycerol sebacate)
PLA	Poly (lactic acid)
PLCG	Poly (lactide-co-caprolactone)
PLGA	Poly (lactic-co-glycolic acid)
PLLA	Poly (L-lactic acid)
PMMA	Poly (methyl methacrylate)
PP	Polypropylene
PS	Penicillin-streptomycin
P-value	Probability value
PVB	Polyvinyl Butyral
Q	Volumetric heat source
R	Jet radius
R^2	Coefficient of Determination
Re	Reynolds number
Ref.	Reference
RFP	Red Fluorescent Protein
SAN	Styrene-Acrylonitrile
SD	Standard Deviation

SEM	Scanning Electron Microscope
Sr-HA	Strontium-substituted Hydroxyapatite
T	Temperature of the polymer jet
T_s	5% weight loss temperature
T_{so}	50% weight loss temperature
T_∞	External air temperature
tan δ	Damping factor
T_c	Crystallization temperature
T_g	Glass transition temperature
TGA	Thermogravimetric Analysis
T_m	Melting temperature
T_{onset}	Degradation onset temperatures
UCST	Upper Critical Solution Temperature
UV	Ultraviolet
v	Axial velocity
$\dot{V}$	Flow rate
v/v	Volume / Volume
VEGF	Vascular Endothelial Growth Factor
VMT	Vermiculite
w/w	Weight / Weight
W_o	Dry weight
W_d	Weight after degradation

X_C	Crystallinity percentage,
XRD	X-ray diffraction
β-TCP	Beta-Tricalcium Phosphate
ΔHC	Crystallization enthalpy
ΔH_m	Melting enthalpy
ΔH_m^0	Specific melting enthalpy of a fully crystalline polymer
ε_y	Yield strain
η^*	Complex viscosity
γ	Surface tension
σ	Viscoelastic stress
σ_y	Yield stress
λ	Relaxation time of polymer
ω	Mass fraction

CHAPTER 1 INTRODUCTION AND THESIS ORGANIZATION

1.1 Introduction

Recent medical statistics published in The Lancet indicate a consistent increase in bone fractures from the 1990s to 2019, with projections suggesting that the total number of cases will double by 2050 [6]. Many bone defects caused by trauma, degenerative diseases, infection, or surgery exceed the body's natural capacity for repair [2]. Although bone has the natural ability to repair itself, full regeneration is impossible for large or complex lesions due to a lack of an adequate physical foundation, enough biological signals, and efficient angiogenesis [7]. Common bone treatment methods, such as autograft (tissue graft obtained from the same individual) and allograft (tissue graft sourced from another individual of the same species), also have limitations, including the risk of disease transmission, donor-site complications, and immune reactions [8]. It highlights the need for treatments that proactively facilitate and enhance bone repair.

In recent decades, bone tissue engineering has attracted widespread attention as an interdisciplinary field focused on designing temporary structures to replace or support damaged tissue [8, 9]. In this approach, engineered scaffolds serve as a three-dimensional microenvironment that must simultaneously provide the necessary conditions for osteogenic cell adhesion, survival, and activity, while also allowing material exchange, cellular infiltration, and extracellular matrix formation [1]. In this regard, synthetic polymers have been widely used due to their designability and controllable properties [8, 10]. However, using a single polymer often comes with limitations, such as surface hydrophobicity, slow degradation rate, and a lack of biological activity [11]. Hence, the development of multicomponent systems, especially polymer blends, has been proposed as an effective means to simultaneously improve surface and biological properties [11, 12].

Polycaprolactone (PCL) is a common choice in this field due to its biocompatibility and good processability, but its hydrophobicity and slow degradation limit its biological performance [4]. Its combination with hydrophilic polymers, such as polyethylene oxide (PEO) and polyethylene glycol (PEG), can enhance the surface's hydrophilicity and its interactions with biological systems [2, 6]. The addition of hydroxyapatite nanoparticles (nHA) as a bioactive mineral phase also enables the scaffold to be upgraded into a bone-inducing system, provided that its distribution and stability are properly controlled [4, 11].

In addition to the composition of the materials, the fabrication method also plays a decisive role in the scaffold's microstructure and performance [1, 8]. The fabrication of fibers at the micro- and nanoscale has attracted particular attention in tissue engineering owing to their similarity to the natural extracellular matrix [8, 10]. Although solution electrospinning has been widely used for the fabrication of scaffolds, it has challenges such as solvent retention and scalability limitations [2, 3]. In contrast, melt electrospinning, as a solvent-free and stable method, enables the production of uniform, controllable fibers [13]; however, the application of multicomponent systems, especially ternary systems, in this context has not yet been systematically developed [13, 14]. Therefore, an important research gap is how to transfer common strategies for controlling properties in multicomponent systems (common in solution electrospinning) to the melt electrospinning platform without sacrificing the structural integrity, stability, and comparability of the scaffolds [4, 14].

Ultimately, the success of a bone scaffold is not limited to bone tissue formation alone; angiogenesis also plays a crucial role in the nutrition, survival, and integrity of the newly formed tissue [9, 15]. Therefore, the engineering of advanced scaffolds requires a multifactorial approach that addresses both bone regeneration and vascularization [1-4, 6-15]. This perspective further underscores the necessity for multifactorial design approaches. Accordingly, the main objective of this thesis is to develop a "design-build" strategy for solvent-free bioactive scaffolds in bone tissue engineering, in which (1) the role of melt electrospinning and the PCL/PEO/PEG ternary system in shaping the microstructure and creating functional porosity is elucidated, (2) the effect of the presence of nHA on the morphology, physical/mechanical properties, and hydrolytic degradation behavior in a multicomponent system is systematically investigated, and (3) finally, an optimal formulation and manufacturing route is introduced that can simultaneously satisfy structural requirements (stability, integrity, and processability), surface requirements (hydrophilicity and cell interaction), and biological requirements (support of osteogenesis and angiogenesis) as much as possible. This approach aims to bridge the gap between the concepts of multicomponent material design and the practical requirements of biomedical scaffold fabrication. It provides a scientific foundation for developing a new generation of bone tissue engineering scaffolds.

1.2 Thesis organization

This thesis is organized as an article-based document and consists of three interconnected articles. This thesis consists of the following chapters:

✍ **Chapter 1: Introduction and Organization of the Articles**

This chapter serves as a framework that tries to familiarize the reader with the project's main context, the importance of the problematic, and the scientific path taken. It aims to connect the project's overarching objectives, the selected strategy, and the current difficulties. Accordingly, chapter one serves as an analytical bridge, preparing the reader to enter the chapters based on articles.

✍ **Chapter 2: Literature review**

This highly interdisciplinary research project has been carried out through close collaboration with some laboratories across diverse fields. The literature review aims to cover all aspects of the project in the best possible way. Moreover, at the end of the chapter, an attempt has been made to make it crystal clear what the current project aims to bring to the table, which gap in science it seeks to fill, and how it can push the boundaries.

✍ **Chapter 3: Objectives**

In this chapter, the main and specific objectives of this project are introduced.

✍ **Chapters 4-6: The three articles**

In these chapters, the main results addressing the project's specific objectives are discussed. Chapter 4 presents Article 1, which focuses on the structure and initial compatibility of the PCL/PEO/PEG ternary system via melt electrospinning and on the logic of creating porosity by removing hydrophilic phases. Chapter 5 presents Article 2. The second article develops the ternary system into a bioactive nanocomposite with nHA and investigates its effect on morphology, properties, and hydrolytic degradation. Chapter 6 presents Article 3, which focuses on masterbatch strategies and different nHA percentages, performs formulation optimization, shows how the selected composition and manufacturing route can improve hydrophilicity and osteogenic and endothelial cell responses, as well as mineralization, and introduces the optimal option.

These three articles together report the principal findings of this research.

✍ **Chapter 7: General discussion**

In Chapter 7, the results from all three papers are analyzed in an integrated manner. This general discussion provides a coherent framework for understanding the relationship between material design, fabrication process, and biological response. It highlights the position of this multi-component system as an advanced approach for mimicking natural bone function.

✍ **Chapter 8: Conclusions and recommendations**

At the end of the thesis, the project's conclusion and outcome are presented. This project marks the beginning of a journey and opens a new field for the fabrication of bone tissue-engineering scaffolds. There are some recommendations because there are still many things to do that seem very interesting and might complete the project and push it forward toward meeting the project's long-term objectives.

CHAPTER 2 LITERATURE REVIEW

2.1 Introduction to Bone Tissue Engineering

2.1.1 Challenges in Bone Regeneration

Bone is a complex calcified tissue composed mostly of organic matrices, minerals, water, and lipidic compounds, as shown in Figure 2.1 Bone performs several critical roles in the human body. It supports the body, shields the inner organs, generates blood cells, facilitates movement, controls blood pH, and stores and releases minerals and fats [16]. Bone is a dynamic, living tissue that constantly undergoes modeling and remodeling to maintain its structure and function [17]. It not only provides structural strength and supports soft tissues but is also the primary site of hematopoiesis in adults and plays a critical role in regulating mineral homeostasis, particularly calcium and phosphate [17]. This dynamism and inherent regenerative capacity allow bone to repair many minor injuries without the need for external intervention, a process driven by a combination of biological, chemical, and mechanical stimuli [17].

Despite this valuable regenerative capacity, natural bone healing remains limited and is generally effective only in small injuries under stable physiological conditions [18]. In large, complex, or severely damaged defects, the structural integrity and biological cues required to support coordinated tissue regeneration are disrupted, preventing the body's intrinsic repair mechanisms from fully restoring the original structure and function [17, 18]. This limitation is particularly evident in critical-sized bone defects (CSDs), which are classically defined as the smallest osseous defects that will not heal spontaneously during the lifetime of the organism or without therapeutic intervention [19]. In preclinical models, this threshold is commonly associated with defects exceeding 2 to 2.5 times the diameter of the affected bone, whereas in clinical settings, defects larger than 2 cm are generally considered critical, depending on anatomical location, patient age, and biological condition [20-23]. Such defects frequently arise from severe trauma, tumor resection, infection, or degenerative disease, and the absence of a suitable physical framework for cell migration, mineral deposition, and new extracellular matrix formation severely compromises the healing process [4]. Lack of adequate vascularization is another key challenge in bone repair [24]. New tissue growth requires the effective formation of blood vessels to deliver oxygen, nutrients, and biological messengers to the actively regenerating cells [25]. Severe damage to the

vascular network or conditions such as diabetes and chronic inflammation can disrupt angiogenesis and slow or halt the repair process [24].

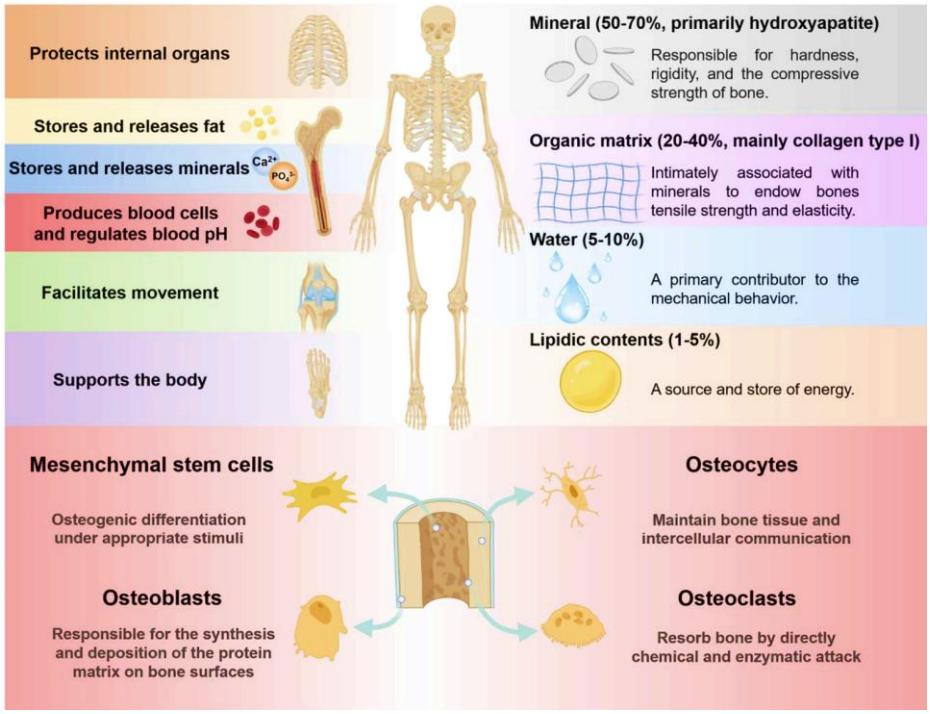

Figure 2.1 Schematic representation of the functions and chemical composition of bones, and four types of cells in bone: bone marrow mesenchymal stem cells (BMSCs) (to differentiate to osteoblast and help bone regeneration), osteoblasts (to form matrix), osteocytes (to orchestrate bone homeostasis), and osteoclasts (to resorb matrix). Reproduced from Ref. [16] with permission from [Elsevier], © [2021].

There are also significant biomechanical challenges [26]. Mechanical instability at the injury site, displacement of bone fragments, or the lack of a structure that can withstand the initial stresses of repair all inhibit the growth of new tissue [27]. Therefore, for successful repair, an alternative structure is essential to provide initial strength in the area and to serve as a suitable substrate for cell adhesion, proliferation, and differentiation [27].

In addition to the biological and mechanical challenges, bone fractures in today's societies have significant economic and social consequences [28-30]. Quebec health records show that hip and other related fractures in the elderly not only increase hospitalization rates and the need for long-term care services, but are also directly associated with reduced quality of life, loss of personal independence, and increased mortality in the first year after injury [31]. In the Montreal region, where the population over the age of 40 exceeds 1 million, the trend in hip fractures over the years

has highlighted the importance of prevention, improved treatment pathways, and the development of new bone repair technologies [32]. Because fractures due to osteoporosis occur primarily in weight-bearing areas such as the hip, these injuries are not only costly but can also lead to permanent disability and reduced social participation [31].

In general, bone tissue engineering has received widespread attention as an emerging field in regenerative medicine, aiming to develop solutions to overcome the limitations of natural bone repair [4]. This field focuses on the design and development of biocompatible structures that provide a suitable environment for cell adhesion, proliferation, differentiation, and new tissue formation [33, 34]. Among them, porous polymer scaffolds have become one of the most widely used systems in bone tissue engineering due to their ability to partially mimic the extracellular matrix, provide physical support for cell organization, and enable tuning of structural and surface properties [35, 36].

In recent years, the use of multicomponent polymer systems has attracted increasing attention because the combination of several polymers enables simultaneous tuning of mechanical properties, degradation behavior, surface wettability, and biological response [4]. In such systems, each component can play a different functional role; For example, one component can provide mechanical strength, another can regulate wettability or degradation rate, and a third can be effective in creating porosity or modifying the microstructure [37]. Furthermore, the combination of these systems with bioactive components, especially inorganic nanoparticles such as hydroxyapatite, has been widely investigated to improve cellular interactions, enhance surface bioactivity, and more closely align the scaffold composition with the natural mineral phase of bone [38, 39]. These multicomponent and multifunctional approaches are particularly important in bone regeneration, as successful regeneration of this tissue requires a simultaneous balance between mechanical support, bioconductivity, and structural reconfiguration [40, 41].

Among the various scaffold fabrication methods, electrospinning has been widely used to produce fibrous structures with high surface-to-volume ratios and morphologies similar to those of the extracellular matrix [42, 43]. The majority of published studies in this field have been based on solution electrospinning, as this method enables the facile production of nano- and microscale fibers from a wide range of polymers [4, 42, 44]. However, the use of organic solvents in this process comes with limitations, including the potential toxicity of residual solvents, the complexity of their complete removal, and the challenges associated with biomedical translation [13].

In contrast, melt electrospinning, an emerging alternative, has attracted increasing attention for its complete elimination of organic solvents, greater compatibility with biomedical applications, and the potential for better control over fiber diameter, structural arrangement, and process stability [45]. This method also offers significant advantages in scalability and compliance with industrial fabrication requirements for biomedical applications [46]. Despite these advantages, the application of melt electrospinning in bone tissue engineering remains limited compared to solution electrospinning [14, 47]. In particular, the use of this method in the design and construction of multicomponent scaffolds, particularly systems consisting of more than two components with distinct functional roles, remains under-investigated and requires further fundamental and structural studies [14, 47, 48].

2.1.2 Limitations of Current Synthetic and Natural Scaffolds

Table 2.1 compares the six main approaches for treating bone lesions, including metallic implants, autografts, allografts, xenografts, and synthetic or tissue-engineered scaffolds [26]. Metallic implants are used to provide mechanical strength and stability and to serve as replacements or structural fixators. Autografts are the patient's own bone grafts, offering the highest immunological compatibility and superior bone-forming potential, attributed to their living cells and natural growth factors [49, 50].

Allografts use human bone harvested from a donor, which is stored in a bone bank after processing, providing a larger volume of tissue. Xenografts are bone grafts harvested from non-human species, particularly bovine or porcine bone, which are prepared as a mineral scaffold after complete removal of cells and antigenic components [3].

Table 2.1 A comparison of the advantages and disadvantages of various methods for treating bone lesions

Treatment method	Advantages	Disadvantages	Ref.
Metal implants	- Very high mechanical strength and stability - Suitable for high-load areas and large lesions - Ability to produce in various shapes and a wide clinical application	- Elastic modulus mismatch with bone (tension shield) - Lack of bioactivity and lack of induction of bone formation - Non-degradable and possible need for secondary surgery - Possibility of corrosion or ion release and inflammation	[51, 52]
Autograft (patient's own bone graft)	- The gold standard of repair - Complete immunocompatibility and no risk of rejection - Contains living cells and natural growth factors - Excellent bone conduction and induction	- Severe limitation in the amount of bone that can be harvested - Donor site morbidity (pain, infection, scarring) - Need for an additional surgery - Inappropriate for large lesions	[49, 50]
Allograft (human bone from a donor)	- No need to remove from the patient's body - Ability to provide high volume - Possibility of long-term storage in the bone bank	- Possibility of immune responses - Reduction in biological activity due to processing and sterilization - Reduction in toughness and mechanical strength after irradiation - Minimal but possible risk of disease transmission	[49, 53]
Xenograft (animal bone, such as bovine or porcine)	- Abundant and affordable resource - Mineral structure similar to human bone - After processing, it can form a suitable scaffold for bone conduction	- Lower bioactivity and bone induction than human sources - Potential to stimulate immune responses, especially in less processed varieties - Typically, just an inactive scaffold, lacking cells or biological factors - Dependent on processing quality for complete removal of antigens	[53-56]
Common synthetic materials Calcium phosphate cement/ poly (methyl methacrylate) (CPC/PMMA)	CPC: Bioactive PMMA: High strength	CPC: Brittle and weak under load PMMA: Non-degradable and bio-inert	[49]
Tissue engineered scaffolds	- 3D design capability with precise control of porosity and structure - Possibility of combining with cells and biological factors - Adjustable degradation rate	- Mostly lacks bioactivity in the pure state - Challenge of coordinating degradation rate with tissue formation - Insufficient strength of some polymers for high-load areas	[57, 58]

Evaluation of these six approaches shows that although each can be effective in certain situations, they also have certain limitations. Metallic implants are mechanically strong but remove the surrounding tissue from normal loading and lack bioactivity [51, 52]. Autografts have the highest clinical success rate, but the restricted quantity of bone that can be harvested and the risk of donor-site complications limit their use in large lesions [49, 50]. Allograft, despite its ease of supply, is prone to immune responses and reduced bioactivity due to processing [49, 53]. Xenografts are more affordable and have a similar mineral structure to bone [54-56]. However, they carry a higher risk of immunogenicity and lower bioactivity than human sources and are usually considered inactive scaffolds [49]. Synthetic and tissue-engineered scaffolds, despite their potential for precise design, still face challenges in balancing sufficient strength, bioactivity, and a controlled degradation rate [49].

Overall, this comparison shows that existing methods only partially meet the needs of bone repair. Therefore, the development of multi-component materials and scaffolds with advanced structural and biological design could enable us to meet clinical requirements better and achieve more efficient, sustainable bone regeneration. Systems based on multicomponent materials and their related fabrication methods are reviewed in Section 2.3 of this thesis, entitled "Polymer Blending for Tailoring Scaffold Properties".

2.1.3 Desired Properties of Bone Tissue Engineering Scaffolds

Designing an efficient scaffold for bone tissue engineering requires meeting biological, mechanical, and structural requirements to effectively serve as a temporary framework for tissue regeneration [59]. Natural bone tissue, as depicted in Figure 2.2, has a complex, hierarchical structure that depends on proper angiogenesis and involves precise cell-matrix interactions [60].

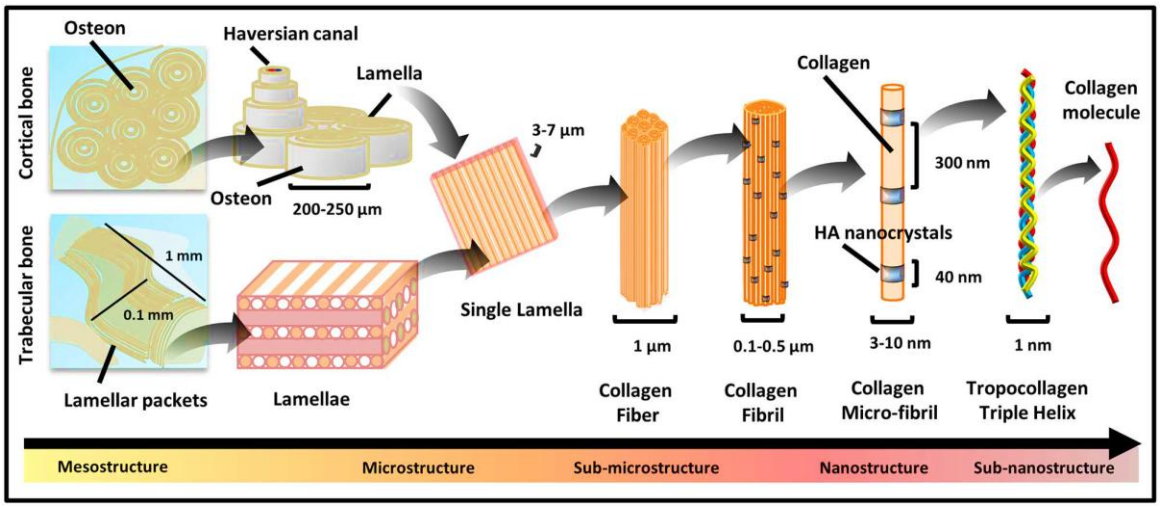

Figure 2.2 Hierarchical structure of the cortical (compact part) and cancellous (spongy part) bone. The diverse structural parts are illustrated, from the mesostructures (i.e., osteons/lamellar packets) to the sub-nanostructures (i.e., collagen molecule). Reproduced from Ref. [60] under the terms of the Creative Commons CC BY license.

The alternative scaffold must offer properties that most closely resemble in vivo conditions while overcoming existing clinical limitations [53, 59, 61]. A detailed selection of the factors influencing the structure and biological properties of a bone tissue-engineered scaffold is required to make it more consistent with natural bone tissue (Figure 2.3) [62].

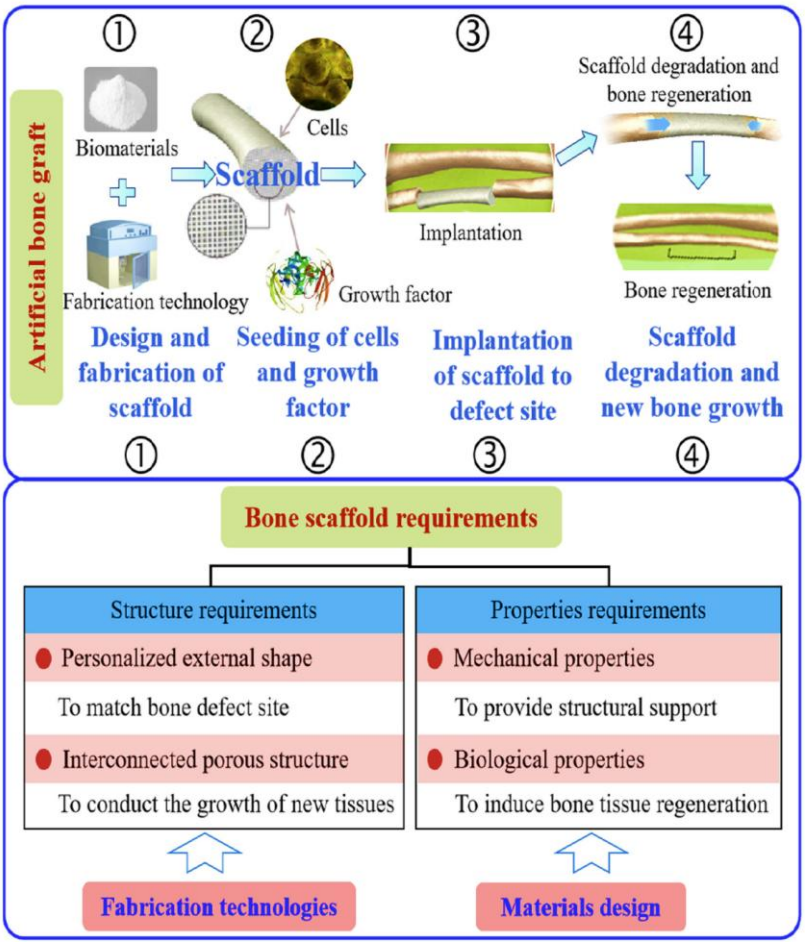

Figure 2.3 The schematic diagram of the requirements of bone scaffold on design and properties, and the process of implanting a tissue-engineered bone scaffold in the body. Reproduced from Ref. [62] under the terms of the Creative Commons CC BY license.

The most important properties required for these scaffolds include biocompatibility, appropriate porosity, adequate mechanical properties, and controlled biodegradability, which are briefly explained below [62].

The first and most fundamental property is biocompatibility [59]. The scaffold must support the adhesion, proliferation, and differentiation of osteogenic cells without inducing inflammatory responses, cytotoxicity, or adverse immune reactions [59]. In addition, the scaffold surface must provide conditions that enable the initial adsorption of proteins and the attachment of extracellular matrix components in a controlled and biologically favorable manner, as the first event following the contact of an implanted material with the biological environment is the rapid adsorption of proteins onto its surface [63, 64]. However, the biological response is not determined solely by the amount of adsorbed protein, but also by the manner of adsorption, molecular orientation, and the

extent to which the native protein conformation is preserved [65-67]. Alterations in protein conformation or denaturation of adsorbed proteins can modify their biological activity and significantly influence subsequent cellular and tissue responses [66, 68, 69]. For example, denaturation of proteins such as fibrinogen following surface adsorption may expose otherwise hidden molecular domains, leading to platelet activation, initiation of the coagulation cascade, and ultimately amplification of the inflammatory response [70-72]. Therefore, protein–surface interactions must be considered not only in terms of adsorption quantity, but also with respect to the preservation of protein structure and biological function, as this stage plays a critical role in directing the initial host response to an implanted surface and ultimately determining the biological success of the scaffold [70, 71, 73-75]. Some factors that affect the cell/protein and surface interactions are summarized in Table 2.2. In addition, the ideal scaffold should have osteogenic properties to provide a suitable pathway for cell migration and new tissue growth [59].

Table 2.2 Overview of cellular and protein-surface interactions. Adapted from Ref. [76] under the Creative Commons CC BY 4.0 license

Property	Cell response	Protein response
Hydrophilicity	Lower cell adhesion on a hydrophobic surface.	Higher hydrophilicity results in a higher-quality protein layer. VEGF on fibronectin is exposed only on the surface with high wettability
Geometry	Grooves improve the cell alignment on the surface. Grooves improve cell adhesion Endothelial cells and Vascular smooth muscle cells favour aligned grooves	Grooves improve the surface area available for protein attachment.
Roughness	A rough surface allows for more binding sites. Increased cell adhesion was observed on organized rough surfaces, as they provide more cell anchoring.	Proteins respond to nanoscale features. Roughened surfaces entrap more proteins and expose more surface area for protein attachment.
Surface modification and composition	Loading surfaces with bioactive agents, such as heparin, can enhance osteogenesis and angiogenesis.	The incorporation of silicon ions into the hydroxyapatite lattice may enhance protein attachment.
Charge	Positive surfaces may attract cells due to their negative cell membranes. However, the overall cell attachment and behaviour appear to be more strongly modulated by the protein response to surface charge.	It improves the orientation and unfolding of proteins

Another important feature is the porosity and pore size. The presence of a network of interconnected pores is a necessary condition for the penetration of nutrients, oxygen, and cells

into the deep regions of the scaffold and is also a prerequisite for angiogenesis [77]. The pore size must be selected to enhance cell-scaffold contact area while avoiding a significant reduction in strength (Figure 2.4) [77]. In general, appropriate porosity design helps to create a balance between mechanical and biological properties [77].

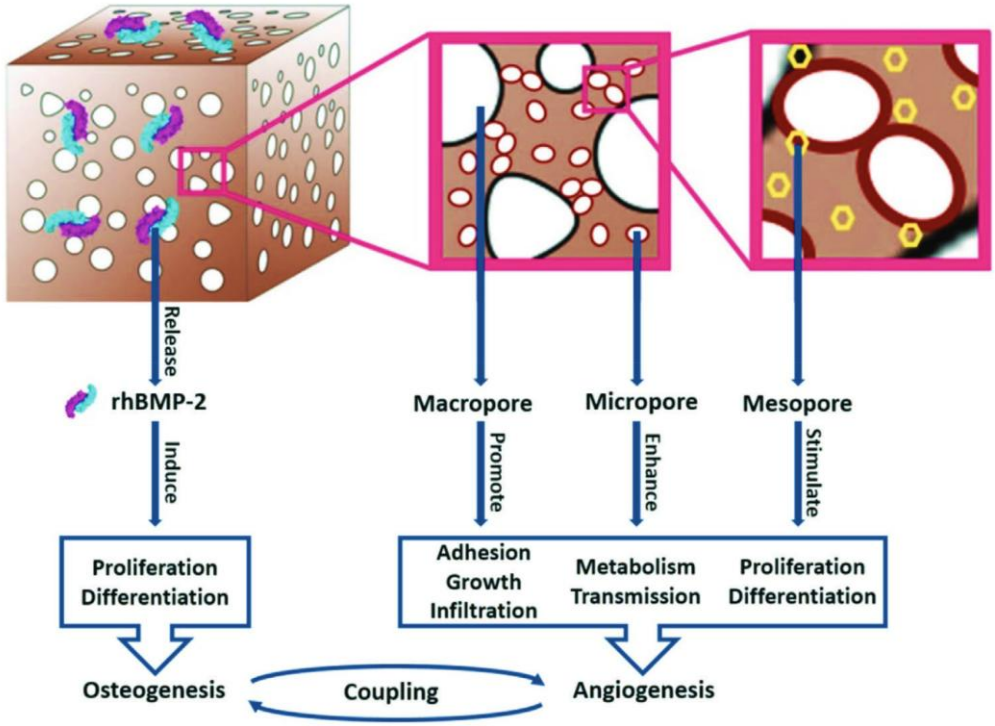

Figure 2.4 Schematic representation of the tissue-engineered scaffold's porosity and pore size impact on bone regeneration. Reproduced from Ref.[77] under the terms of the Creative Commons CC BY license.

Next, the mechanical properties of the scaffold play a decisive role in the success of the repair process [59]. The scaffold must be capable of withstanding the physiological loads imposed on the defect site, particularly during the early stages following implantation, while maintaining its structural integrity [59]. Among these properties, elastic modulus is one of the most critical design parameters, as it should be as close as possible to that of the target bone tissue in order to minimize the risk of stress shielding. In natural bone, the elastic modulus varies depending on tissue type and anatomical location [78], with reported values typically ranging from approximately 0.05 to 2 GPa for trabecular bone and from approximately 7 to 30 GPa for cortical bone [79]. This variation reflects the hierarchical and heterogeneous nature of bone and highlights the importance of tailoring scaffold mechanical properties to the specific target tissue [80]. A scaffold with a modulus

significantly higher than that of the host tissue may divert mechanical load away from the surrounding bone and lead to stress-shielding-induced bone resorption, whereas a scaffold with insufficient stiffness or strength may fail to provide the mechanical stability required to support tissue regeneration [81, 82]. Therefore, precise tuning of mechanical properties, particularly elastic modulus, is essential to achieve an appropriate balance between mechanical support and biological compatibility in the design of bone tissue engineering scaffolds [81, 82]. The three-dimensional structure, material composition, crystallinity degree, and fiber orientation all affect the strength and flexibility of scaffolds [59]. The inverse relationship between compressive strength and porosity for bone tissue scaffolds is shown in Figure 2.5. In this regard, advances in techniques such as melt electrospinning have enabled the production of structures with finely tuned mechanical and geometric properties.

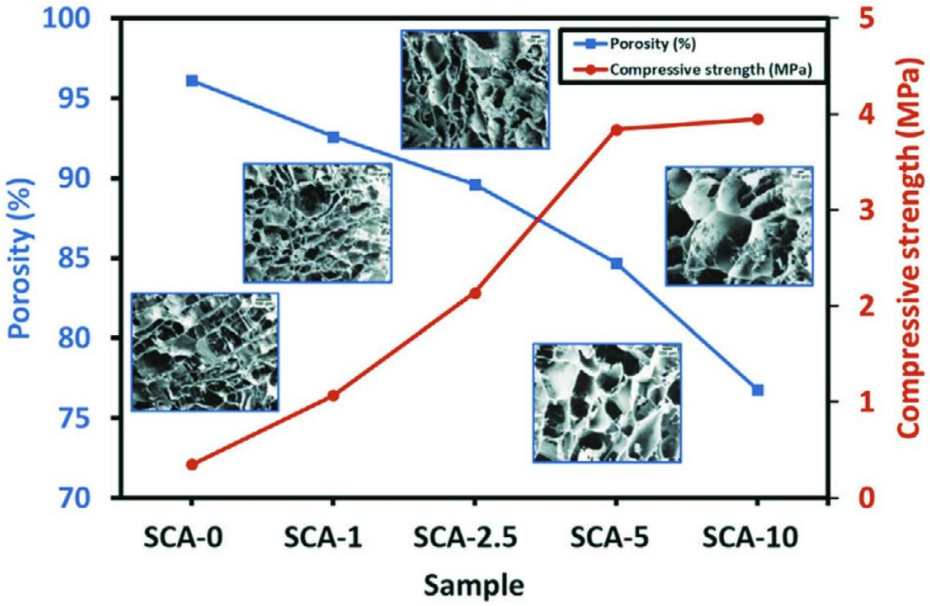

Figure 2.5 Compressive strength, morphology, and porosity of chitosan/carboxymethyl cellulose (CS/CMC) nanocomposite mats containing 0%, 1%, 2.5%, 5%, and 10% carboxylated cellulose nanowhiskers (CCNWs-AgNPs) with silver nanoparticles named as SCA-0, SCA-1, SCA-2.5, SCA-5, and SCA-10, respectively. Reproduced from Ref. [77] under the terms of the Creative Commons CC BY license.

Controlled biodegradability is another key characteristic of bone tissue engineering scaffolds [59, 83]. The scaffold should be designed to degrade gradually in parallel with new tissue formation, while its degradation by-products must remain non-toxic to the host [61, 64]. The degradation rate is governed by factors such as polymer molecular structure, degree of crystallinity, molecular

weight, chemical bond composition, and scaffold permeability [83]. Quantitatively, the degradation rate should be matched to the time required for bone regeneration, which is typically reported to range from approximately 8 to 24 weeks for initial tissue formation and several months up to about one year for more complete bone remodeling and maturation [36]. Within this framework, rapid degradation generally refers to systems that lose a substantial portion of their structural integrity or undergo significant mass loss (e.g., more than 30–50%) within less than 4 to 6 weeks, thereby risking insufficient mechanical support before adequate tissue formation occurs [84]. In contrast, slow degradation refers to systems that retain a substantial portion of their mass or structure beyond 12 to 18 months, which may hinder tissue regeneration by prolonged space occupation, restricted cell infiltration, and delayed replacement by newly formed tissue [85]. Therefore, an ideal scaffold for bone regeneration should maintain sufficient mechanical stability during the first 6 to 12 weeks following implantation and then progressively degrade over a period of approximately 3 to 12 months, in accordance with the rate of new tissue formation and maturation [85].

Overall, achieving an ideal scaffold requires a balance between biological, structural, and mechanical requirements. The scaffold must have the appropriate architecture, sufficient mechanical properties, support cellular interactions, and degrade at a controlled rate. This combination of properties enables the scaffold to serve not only as a supporting structure but also as an active platform providing effective bone regeneration.

2.2 Materials for bone tissue engineering

A comparative study of the polymers listed in Table 2.3 shows that natural polymers, although highly bioactive due to their intrinsic similarity to the extracellular matrix, often face limitations such as low mechanical strength, limited stability under physiological conditions, and limited control over degradation [86, 87]. This high bioactivity is primarily attributed to their structural and chemical characteristics, as many natural polymers, such as collagen, gelatin, chitosan, and alginate, possess bioactive functional groups, cell-recognizable chemical motifs, and molecular architectures that resemble the native extracellular matrix [41, 88]. For example, the presence of polar functional groups such as amine, carboxyl, and hydroxyl groups in these polymers can facilitate protein adsorption, interaction with growth factors, and cell adhesion [41, 89]. In addition, some of these polymers, particularly collagen and gelatin, contain well-known biological

motifs such as RGD (Arg-Gly-Asp) sequences or similar integrin-recognition sites that can directly mediate cell adhesion, migration, and organization [90, 91]. These features enable natural polymers to provide a more biologically familiar microenvironment for cells and, consequently, to promote more favorable cellular responses [91]. In contrast, synthetic polymers offer greater structural tunability, adjustable mechanical properties, and more predictable degradation behavior, allowing the development of more stable scaffolds [82]. However, they generally exhibit lower intrinsic bioactivity and often require surface modification or the incorporation of bioactive components to improve biological interactions [82].

Among synthetic polymers, poly(ε-caprolactone) (PCL) is recognized as one of the most prominent candidates for bone tissue engineering due to its favorable biocompatibility, high chemical stability, slow degradation rate, and suitable processability [92]. However, PCL is not the only polymer investigated in this field, and several other synthetic polymers have also been widely used as base matrices in bone scaffold systems [93]. For example, polylactic acid (PLA) and poly(lactic-co-glycolic acid) (PLGA) are among the most commonly used biodegradable polymers in tissue engineering because of their good biocompatibility, tunable mechanical properties, and extensive history in biomedical applications [86, 93, 94]. Nevertheless, these polymers generally degrade faster than PCL, and in some cases, early loss of mechanical properties or the generation of acidic degradation by-products may compromise environmental stability and long-term scaffold performance [95, 96]. In addition, polymers such as poly(L-lactic acid) (PLLA), polyhydroxyalkanoates (PHA), and biodegradable polyurethanes have also been explored as potential candidates for bone-related applications; however, each presents certain limitations, including increased brittleness, greater processing complexity, or lower reproducibility during fabrication [34]. Among these options, PCL exhibits particular compatibility with melt electrospinning due to its lower melting temperature, suitable thermal stability, and favorable rheological behavior [13, 47, 92]. Compared with many alternative polymers, it offers improved process control and greater structural stability during fabrication [86, 94, 97]. Therefore, although several other polymers have been considered as base matrices for composite and multicomponent scaffold systems, PCL was selected as the base polymer in this study due to its balanced combination of processability, stability, and long-term functional performance.

Table 2.3 Advantages and limitations of natural and synthetic polymers used in bone tissue engineering. Adapted from Ref.[86, 87] under the Creative Commons CC BY 4.0 license

Scaffold	Advantage	Disadvantage
Natural polymers	Biomimetic surface Bioactivity	Microbial contamination Poor mechanical properties Poor processability Uncontrollable degradation rate Immunogenic response
Gelatin	Biodegradability Cytocompatibility Osteoconductivity Porosity tunability	weak mechanical properties Lack of stability in physiological conditions
Chitosan	Cytocompatibility Simple properties adjustment Biodegradability Strong cell-binding, migration, and differentiation properties Good antibacterial properties Mucoadhesivity	Poor mechanical strength Accelerated in vivo degradation rate
Collagen	Similarity to extracellular matrix FDA-approved Cytocompatibility Enzymatic biodegradability Adaptability in processing various physical forms Cytocompatibility and cell-binding properties Possible injectability	Poor mechanical properties Difficult handling Challenging disinfection
Synthetic Aliphatic polymers	Tailored structure FDA-approved Predictable and reproducibility properties Water solubility Tuneable crystallinity Tuneable mechanical and physical properties	Weak bioactivity Lack of cell recognition sites Low osteoconductivity Risk of adverse tissue reaction for acid degradation product Poor cellular adhesion
Poly (lactic-co-glycolic acid) (PLGA)	Broad range of degradation rate Tunability	Inadequate mechanical properties Poor osteoconductivity
Poly (ε-caprolactone) (PCL)	Biodegradability Cytocompatibility Slow degradation rate	Hydrophobicity Insufficient bioactivity
Poly (lactic acid) (PLA)	Cytocompatibility Adjustable properties Thermal stability	Insufficient flexibility

2.2.1 Poly(ε-Caprolactone) (PCL) as a Base Polymer

2.2.1.1 Physicochemical and Mechanical Properties of PCL

Poly(ε-caprolactone) (PCL) is one of the most important biocompatible polymers used in tissue engineering and scaffold fabrication [98]. This semicrystalline, flexible, and biodegradable polymer is a highly desirable choice for melt electrospinning due to its low melting point (about 60 ˚C) and a very low glass transition temperature, which facilitates its melt processability [99]. The flexibility of the polymer chains and the appropriate crystallinity result in scaffolds with sufficient mechanical strength and modulus for tissue applications. PCL is FDA-approved and has been used in various medical applications for many years [99]. Its favorable physicochemical properties, high biocompatibility, and easy structural modification make it an efficient base polymer for the development of multicomponent scaffolds [99].

Its favorable rheological behavior, which depends on molecular weight, in particular, the relatively low melt viscosity, enables jet stability and the production of small-diameter fibers in the melt electrospinning process. Its chemical structure also allows its surface and functional properties to be easily improved by adding hydrophilic polymers or bioactive nanoparticles [8].

2.2.1.2 Biocompatibility and Degradation Behavior

PCL is a biocompatible and biodegradable polymer [100] whose degradation occurs primarily through hydrolytic cleavage of its ester bonds, producing low-molecular-weight oligomers and ultimately 6-hydroxycaproic acid as the principal degradation product [92, 101-103]. These degradation products are generally considered biocompatible and non-cytotoxic, as they can be further metabolized through normal physiological pathways and do not typically induce the pronounced local acidification associated with faster-degrading aliphatic polyesters [100, 102].

The slow degradation rate of this polymer, which may take months to years, could be considered as an advantage for the regeneration of hard tissues, including bone, because the scaffold maintains mechanical support until new extracellular matrix is formed.

In vitro studies have shown that scaffolds produced from PCL, especially by melt electrospinning, provide a compatible environment for the growth of a variety of tissue cells and specifically for bone cells [104, 105]. For example, Brown et al. [106] reported that tubular scaffolds obtained by melt electrospinning of PCL were nontoxic and supported the growth of three cell types, including mouse primary osteoblasts, human mesothelial cells, and human osteoblasts. Coating these fibers

with calcium phosphate (CaP) mimicked the bone microenvironment, and after 4 weeks, mineral matrix formation and more than 90% human cell viability were reported [106]. However, the mechanical results showed that the degree of fusion and bonding between fibers at the intersection points was limited. Besides, the structure's behavior was more similar to a network of relatively independent fibers than to a fully integrated structure. In addition, with increasing fiber twist angle, a significant decrease in tensile stiffness and compressive performance was observed, such that at higher angles, relative rearrangement and disintegration of the fibers, and the occurrence of buckling under compressive load, can affect the mechanical performance of the structure.

In another study by Zaiss et al. [107], CaP-coated PCL scaffolds supported the effective proliferation of ovine osteoblasts, with more than 90% cell viability reported at 20 and 40 days. These findings confirm PCL's suitability as a bone cell growth environment [107].

In vivo studies have also reported that PCL performs remarkably well [108]. Highly porous PCL scaffolds loaded with mesenchymal stem cells and periodontal ligament cells showed significant improvement in periodontal tissue regeneration after 5 to 10 weeks of implantation in a sheep model [108]. Also, in another study, a PCL/β-TCP composite scaffold coated with CaP resulted in a structure similar to native periodontal tissue and improved integration between bone and ligament [109]. These results prove the key role of PCL in the regeneration of hard and soft tissues in the body [8].

2.2.1.3 Limitations of Neat PCL for Biomedical Applications

Despite its many advantages, PCL has limitations that make its use in its neat form challenging in some tissue engineering applications. The most important of these limitations are [8]:

- PCL is a hydrophobic polymer, which reduces cell adhesion and surface wettability.
- It has a very slow degradation rate, which is not suitable for applications requiring faster replacement;
- PCL's limited surface activity for the attachment of biological or pharmaceutical molecules;
- PCL's limitations in creating very fine microstructures under certain process conditions.

To address these issues, modifying PCL by blending with hydrophilic polymers such as PEG and PEO [14] was proposed. The addition of Poly(ethylene glycol) (PEG) to PCL, a low-molecular-weight component, may reduce melt viscosity, raise jet tension, decrease fiber diameter, and improve cell adhesion of the system [14]. Additionally, the presence of polyethylene oxide (PEO) in the scaffold could improve the adsorption and retention of proteins in cell culture media, thereby

providing more suitable conditions for cell adhesion and activity. Also, combining PCL with hydrophilic phases could enable controlled release of bioactive compounds and enhance the biological conditions at the scaffold surface [14]. In addition to the benefits of adding hydrophilic components to hydrophobic systems such as PCL, these components can also confer other structural and biological functions [110]. Specifically, hydrophilic components can act as sacrificial phases and, upon removal, form a controllable porous structure in the scaffold [111]. In addition to increasing surface roughness and improving hydrophilicity, this porosity enhances scaffold permeability, enabling the effective transfer of oxygen and nutrients to cells and the removal of metabolic products such as carbon dioxide [111]. As a result, such a structure can provide more suitable conditions for cell adhesion, proliferation, and survival [111].

In addition to polymer blending, the incorporation of hydroxyapatite (nHA) nanoparticles could enhance mechanical strength, promote bioactivity, and promote osteoblast differentiation [98]. The combination of PCL with nHA has very favorable performance, especially in bone applications [98].

2.2.2 Common Polymers Used for Blending with PCL for bone tissue engineering applications

Although PCL is one of the most widely used polymers for the fabrication of tissue-engineering scaffolds (especially bone) due to its biocompatibility and good processability, its hydrophobicity and slow degradation rate limit the biofunctionality and permeability of the scaffold [44]. To address these shortcomings, various strategies have been used in the literature, such as alloying/elongating PCL with other biodegradable polymers (e.g., PLA, PLGA, biodegradable polyurethanes, PGS) or combining it with bioactive biopolymers (e.g., gelatin, chitosan, and collagen)[44]. Each of these options has a “dominant advantage”; for example, PLA and PLGA mainly modify the mechanical/kinetic properties of degradation, while biopolymers such as gelatin and chitosan can improve the biological response by adding cell-binding sites, but are usually more challenging in terms of stability in an aqueous environment and sensitivity to processing/sterilization [44, 112]. Table 2.4 presents an overview of common polymers that are used to blend with PCL to enhance the properties of PCL-based scaffolds for bone tissue engineering applications. Among them, PEG and PEO are considered effective options for modifying PCL due to their hydrophilicity, tunability by molecular weight and percentage, and the

possibility of creating effective changes in wettability/permeability (and even creating porosity through washing/leaching in some designs), and have been reported in various studies to improve wettability, mineralization, and cellular response [113]. At the same time, these polymers can be considered compatible with melt electrospinning (section 2.4), solution electrospinning, and melt electrowriting manufacturing routes because their physicochemical properties fall within processable ranges for these techniques [112-114]. In particular, their relatively low melting temperatures, thermoplastic behavior, and adequate thermal stability enable melt-based processing, while their solubility in common polar solvents and ability to form entangled polymer networks support solution electrospinning [115, 116]. In addition, their molecular weight–dependent rheological behavior allows adjustment of melt viscosity, chain entanglement density, and jet stability, which are key parameters governing continuous fiber formation, diameter control, and deposition fidelity in electrohydrodynamic manufacturing processes [13, 115, 117]. These characteristics make PEG- and PEO-based systems adaptable to multiple fiber fabrication platforms, provided that molecular weight, blend composition, and processing conditions are appropriately tuned [115].

Table 2.4 Overview of polymeric systems commonly blended with PCL for bone tissue engineering applications Adapted from Refs. [44, 112] under the Creative Commons CC BY 4.0 license

Polymer	Structure	Advantages	Disadvantages
Alginate 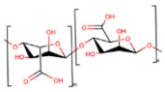	Mainly made up of carboxyl groups Made up of mannuronate and gluronate monomers	Promotes hydrophilicity Bioabsorbable Biodegradability Thickening/gel-forming agent	Difficult to sterilize Low cell adhesion Poor mechanical properties
Silk fibroin 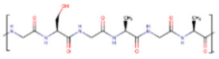	Fibrinogen Dimer consisting of three of pairs of polypeptides	Promotes affinity for biological surfaces and molecules Non-immunogenicity Supports cell adhesion	Weakening the mechanical properties Risk of fast degradation
Poly (ethylene glycol) (PEG) 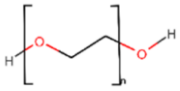	Synthesized using ring-opening polymerization of ethylene oxide	Biocompatible Acts like plasticizer, improves PCL's processability Decrease risk of inflammation Non-immunogenic Mucoadhesive Bio adhesive	Very short-term degradation
Polylactic acid (PLA) 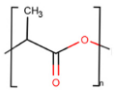	Highly crystalline	Provides biocompatible Cytocompatibility Improves thermal stability Nontoxic degradation products Good degradation rat	Brittleness Poor thermal stability Hydrophobicity
Poly (ethylene oxide) (PEO) 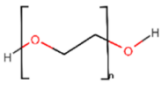	Semi-crystalline polymer	Enhances cell adhesion, proliferation, and osteogenic response when blended with PCL Acts as a porogen or sacrificial phase, enabling controlled porosity and permeability after leaching.	Water solubility leads to rapid leaching, which may reduce long-term structural stability. Excessive content can negatively affect mechanical integrity of PCL-based scaffolds.

2.2.2.1 Polyethylene Oxide (PEO) and Polyethylene Glycol (PEG) as Hydrophilic Modifiers

Polyethylene oxide (PEO) and polyethylene glycol (PEG) are two hydrophilic polymers with the same chemical structure H−(O−CH_2−CH_2)n−OH, and their main difference lies in the chain length and molecular weight; so that those with a molecular weight of less than about 20,000 g/mol are usually called PEG and those with a higher molecular weight are called PEO [118]. The ether groups in the structure of these polymers allow for extensive hydrogen bonding with water molecules and some proteins. In addition, both polymers are soluble in water, which has led to

their potential for multiple functional roles in systems based on hydrophobic polymers such as polycaprolactone [119].

In some studies, the addition of specific amounts of PEG or PEO to PCL has been reported to act as a surface modifier, decreasing the water contact angle, increasing wettability, and hence improving surface hydrophilicity and biocompatibility [120]. In contrast, in another set of studies, these hydrophilic polymers have been used as a sacrificial phase; upon contact with an aqueous environment and dissolution, they form a porous structure and increase surface roughness, thereby indirectly increasing hydrophilicity and improving cellular response [121, 122]. Therefore, the role of PEG and PEO in PCL systems can be explained through both surface chemistry modification and microstructural engineering, including the creation of controlled porosity.

Both PEO and PEG with a melting temperature of about 65˚C, exhibit semicrystalline structures, with their degree of crystallinity influenced by factors such as molecular weight, thermal history, and cooling rate [118]. PEG with a lower molecular weight shows higher mobility in the molten state and a significant tendency to migrate to the surface [123]. This property makes PEG an efficient modifier for improving surface properties, such as reducing contact angle and increasing adhesion of adhesive proteins [123, 124]. Additionally, PEG usually acts as a plasticizer; this means that, by reducing melt viscosity, it improves processability in melt electrospinning, increases jet tension, and reduces fiber diameter [14]. This behavior has been reported in numerous studies, especially for PLA/PEG and PCL/PEG systems [14].

In contrast, PEO with a high molecular weight mostly remains within the matrix and often forms big PEO-rich domains due to its high melt viscosity, which plays an important role in spreading behavior and rheology and, later, in the formation of associated porosity within the scaffold [125]. These differences indicate that selecting the appropriate molecular weight is crucial for achieving the desired rheology and the final morphology in PCL/PEG and PCL/PEO systems [14].

PEO and PEG play a key role in improving the hydrophilicity and biocompatibility of polymer scaffolds [126]. These two polymers, by increasing surface energy and reducing contact angle, facilitate the adsorption of adhesive proteins such as laminin, fibronectin, and vitronectin and enhance initial cell adhesion [127]. In addition to increasing hydrophilicity, PEG acts as a drug carrier in solid dispersion systems and directs the release pathway mainly towards diffusional release [14]. It has also been reported that PEG can increase gene expression and the activity of proteins involved in bone regeneration [14]. On the other hand, PEO creates a very suitable

environment for the growth and proliferation of bone cells and has shown a more favorable performance in supporting cell adhesion compared to many other hydrophilic polymers [126, 127]. These features are one of the main reasons for choosing the ternary PCL/PEG/PEO system in the current research.

Employing hydrophilic components like PEO and PEG within the body of a hydrophobic component and dissolving the hydrophilic polymers in aqueous environments as sacrificial components to create the desired morphology is a promising strategy in tissue engineering, particularly for bone tissue engineering, which requires a spongy structure to mimic natural bone [128, 129]. These polymers gradually dissolve in an aqueous environment and leave the matrix, thereby creating a network of interconnected channels and diffusion pathways [128]. The formation of these pores is very effective in improving permeability, facilitating material exchange, promoting endothelial cell migration, and initiating the angiogenesis process [128, 129]. Overall, the combination of hydrophilic chemical properties, semicrystalline structure, distinct behavior due to molecular weight, and solubility capacity in aqueous media has made PEO and PEG very valuable modifiers for PCL-based systems [8]. The presence of these two polymers can simultaneously improve processability, enhance surface properties, create suitable pore architecture, and facilitate cell adhesion and growth; a set of capabilities that play a decisive role in the success of polymer scaffolds used in bone tissue engineering.

2.3 Polymer Blending for Tailoring Scaffold Properties

Polymer blending is one of the most effective approaches for structural engineering and performance improvement of biomedical scaffolds [130]. By enabling the combination of polymers with different behaviors without the need to synthesize new materials, this method enhances mechanical properties, modifies surface behavior, controls degradation rates, and increases biocompatibility [124]. Most polymers are naturally incompatible or only partially compatible; hence, understanding the morphological principles, thermal behavior, and biological effects of blending is essential for designing efficient and predictable scaffolds. In other words, blending facilitates precise tuning of microstructures, the development of controlled phases, and enhanced distribution of active components within the scaffold. It means blending allows tissue engineers to customize the scaffold's required properties and fabricate a suitable substrate for

cellular growth and proliferation [131]. Table 2.5 provides an overview of some of the work done in this field.

Table 2.5 Examples of research conducted in the field of polymer blends processing for biological applications

Blend	Fabrication method	Biomedical application	Advantages of blending	Ref.
Chitosan/ PEO/silica	Solution electrospinning	Bone tissue engineering	To promote apatite crystal coverage To improve the cell adhesion and proliferation	[132]
Poly (lactic acid)/ Poly (ε-caprolactone)/ Poly (methyl methacrylate) (PLA/PCL/PMMA)	3D printing	Bone tissue engineering	To enhance toughness without compromising stiffness and strength	[133]
Poly (ε-caprolactone)/ Poly (ethylene glycol)/ Poly (lactide-co-caprolactone) (PCL/PEG /PLCG)	Solution electrospinning	Bone tissue engineering	To enhance the hydrophilicity To increase the biodegradation	[134]
PMMA/ PCL /Gelatin	Solution electrospinning	Drug delivery	Compared to the separate components, the mechanical properties of the blend exhibited notable enhancements.	[135]
Poly (ε-caprolactone)/ Gelatin / Poly (glycerol sebacate) PCL/Gelatin /PGS	Solution electrospinning	Nerve tissue engineering	Significant improvement in cell attachment and proliferation	[136]
PCL/PLA	3D printer	Bone tissue engineering	PCL coating promoted cell migration compared to PLA	[137]
Poly (lactic acid)/ Poly (ε-caprolactone)/ Cellulose Acetate Butyrate) PLA/PCL/CAB	Solution electrospinning	Skin tissue engineering	Stimulation of cell growth	[138]
Poly (vinyle alcohol)/ Chitosan/ Poly (lactic acid) PVA/ CS /PLA	Freeze-drying and extrusion	Wound healing	To introduce a practical method for processing Cs in high-temperature proces	[139]

2.3.1 Fundamentals of Polymer Blending and Morphology Development

In this thesis, the system under study is designed based on a ternary blend consisting of PCL/PEO/PEG; therefore, investigating the principles governing the formation of morphology in ternary blends is of particular importance. The morphology of polymeric blends results from the interactions among the polymers' intrinsic properties, the thermodynamics of mixing, and the process conditions [130].

Figure 2.6 summarizes the classical equilibrium morphologies that may arise in immiscible ternary polymer blends as a function of interfacial interactions between the three phases. These morphologies are commonly interpreted using spreading coefficients (λ), which are derived from the interfacial tensions between phases A, B, and C and provide a thermodynamic criterion for predicting the preferred spatial arrangement of the dispersed phases within the matrix [140, 141]. Depending on the sign and magnitude of these coefficients, four general morphological classes may be obtained [142, 143]: (a) partial engulfment, in which one dispersed phase partially wets and partially encapsulates the second phase; (b) separated dispersed domains, where phases A and C remain as independent droplets within the continuous phase B; (c) complete engulfment (core–shell morphology), in which one dispersed phase fully encapsulates the second [140]; and (d) partial wetting with interfacial contact, in which the two dispersed phases remain distinct but maintain direct interfacial contact within the matrix [143]. These thermodynamically driven configurations represent the simplest morphological states expected in ternary immiscible systems and provide the basis for understanding phase arrangement in multicomponent blends [142, 144]. While Figure 2.6 illustrates the general classes of phase organization, the actual microstructures developed in polymer blends are often significantly more complex than these idealized equilibrium morphologies [145, 146]. In practice, the final morphology is not governed solely by interfacial thermodynamics, but also by kinetic and rheological factors such as viscosity ratio, elasticity contrast, shear history, cooling rate, composition, and phase relaxation dynamics during processing [146]. As a result, each of the generalized morphologies shown in Figure 2.6 may evolve into a broader range of structural motifs, including spherical droplets, elongated fibrillar domains, lamellar structures, co-continuous networks, and core–shell inclusions with irregular interfaces [146, 147]. For example, dispersed spherical domains are typically favored when interfacial tension dominates and droplet breakup is limited, whereas elongated or fibrillar morphologies may emerge under strong extensional flow or high shear when one phase is stretched prior to

solidification [140, 148]. Likewise, lamellar and co-continuous structures can form when the volume fractions of the phases are comparable and interfacial rearrangement is kinetically restricted [140]. These non-equilibrium morphologies are particularly important because they directly determine the effective interfacial area, stress transfer efficiency, surface roughness, and accessibility of functional domains, and therefore strongly influence the mechanical performance, degradation behavior, and biological response of the resulting scaffold [140, 144, 149].

In the context of polymer scaffolds, the distinction between these morphological states is especially important because phase morphology governs not only bulk mechanical behavior but also surface functionality and biological performance [149]. Spherical dispersed domains generally provide limited interfacial connectivity and may behave primarily as isolated inclusions, whereas fibrillar or lamellar morphologies can increase interfacial contact area, promote stress transfer between phases, and alter crack propagation behavior [140, 149]. Co-continuous morphologies are of particular interest because they can generate interconnected pathways that enhance mass transport, phase accessibility, and selective extraction of sacrificial components [148, 150, 151]. Similarly, core–shell and partially engulfed structures may influence the degree of surface exposure of each phase, thereby affecting wettability, protein adsorption, and subsequent cell–material interactions [149]. Consequently, understanding not only the thermodynamic categories shown in Figure 2.6, but also the kinetic evolution of these morphologies into real structural motifs, is essential for rationally designing multicomponent polymer blends with tunable mechanical, physicochemical, and biological properties.

Factors such as chemical structure, molecular weight, polarity, and glass transition temperature affect the degree of miscibility or phase separation between polymers [130]. When the free energy of mixing is negative, a single-phase system forms; however, in most cases, polymers tend to form separate phases [130]. The way these phases form and are distributed in the final microstructure plays a decisive role in the material's mechanical, thermal, and surface properties. Thermal behavior and crystallinity are also important parts of the microstructural evolution [130]. Changes in crystallinity, crystallization rate, or crystal organization can affect the strength, flexibility, thermal stability, and degradation rate of the polymer [124]. In multicomponent systems, differences in chain mobility or component polarity may facilitate or restrict crystallization and produce distinct structural patterns; these patterns collectively result in a more complex and diverse microstructure [131].

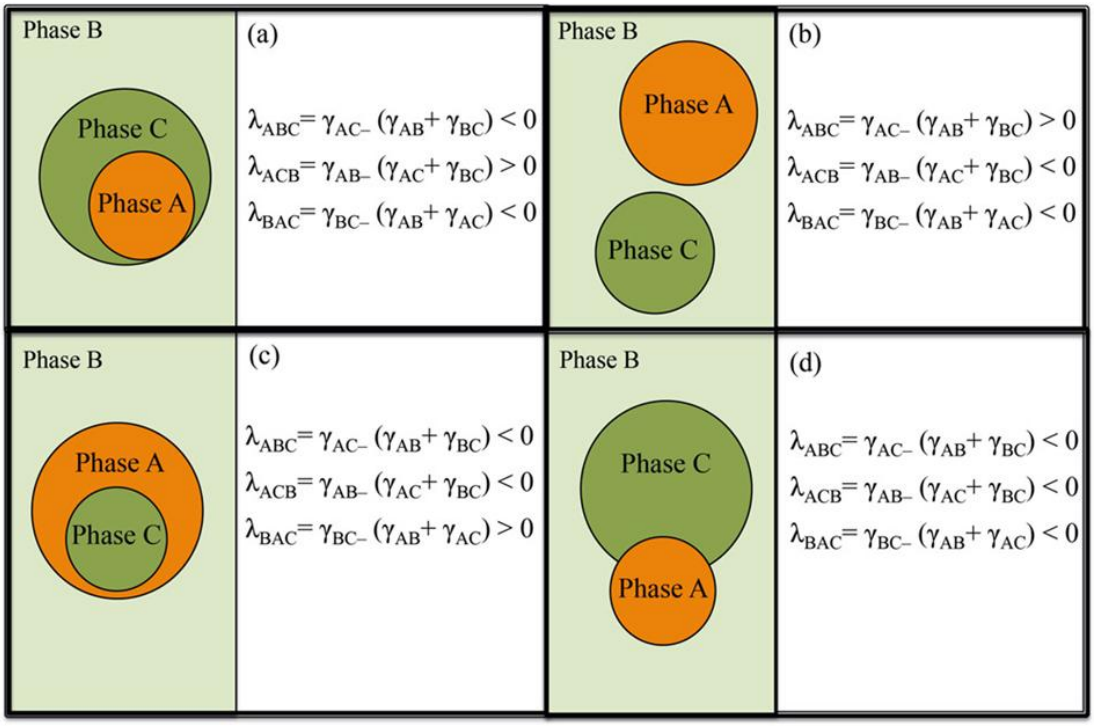

Figure 2.6 Potential morphologies in a polymeric ternary blend fabricated from B, as the major phase, and A and C, as dispersed phases, as predicted by the spreading coefficient. (a) A-rich domain is encapsulated by C. (b) A and C are dispersed in B. (c) C-rich domain is encapsulated by A. (d) Partial wetting morphology of A and C. Reproduced from Ref. [123] with permission from [American Chemical Society], © [2014].

The final morphology also plays a direct role in the biological response of polymeric materials. Properties such as the percentage of the amorphous phase, porosity, phase distribution, surface free energy, and roughness can affect biological responses, including cell adhesion, proliferation, cellular activity, and scaffold permeability, which can determine cell access to nutrients. In other words, a suitable microstructure offers a promising environment for cell-material interaction and may facilitate tissue regeneration [152].

Overall, understanding the link between the principles of mixing and morphological evolution, and their mechanical and biological consequences, is fundamental to the design of high-performance polymeric scaffolds [152]. Choosing the right composition, controlling process conditions, and accurately analyzing the microstructure are key to achieving materials that meet the stringent requirements of tissue engineering [76].

2.3.2 Composition Design and Processing Strategies of Polymer Blends for Tissue Engineering Scaffolds

In the design of scaffolds from polymer blends for tissue engineering applications, selecting appropriate composition ranges for each component is crucial for controlling scaffold morphology, mechanical properties, and biological behavior [92, 153, 154]. In general, in multicomponent systems, the presence of a polymer as a continuous phase is usually established at levels above about 50 wt% [146]. In contrast, secondary component at lower levels can act as dispersed phase, surface modifier, or porosity-inducing agent [146]. At low percentages, the added component mainly affects the surface properties and wettability [146]. At the same time, as its weight fraction increases, the likelihood of forming co-continuous networks (co-continuous morphology) or phase inversion increases, leading to significant changes in mechanical and biological properties [146]. Also, in ternary blend systems, the mixing ratios must be selected so that, while maintaining thermal and rheological stability during the melting process, uncontrolled phase separation and strength loss are prevented [155]. Therefore, the determination of optimal mixing ranges is based not only on thermodynamic considerations but also on process requirements and the scaffold's final performance.

Polymer mixing is a fundamental approach in the design of multicomponent scaffolds for tissue engineering [130]. It is usually carried out through three main routes: solution mixing, melt mixing, and hybrid methods. In solution mixing, polymers are dissolved in a common solvent and subsequently blended at the molecular level prior to solvent evaporation [130]. This approach can provide relatively homogeneous structures, particularly when the selected components exhibit compatible solubility behavior and similar solution thermodynamics [130]. In this context, the selection of a common solvent is not solely empirical and can be rationally guided using predictive tools such as Hansen solubility parameters and related miscibility criteria, which estimate polymer–solvent affinity based on dispersive, polar, and hydrogen-bonding interactions [152, 156]. These approaches can facilitate solvent selection for multicomponent systems; however, identifying a single solvent capable of dissolving multiple polymers while preserving solution stability, adequate viscosity, and processing compatibility remains challenging, especially for chemically dissimilar polymers [157]. In addition, solvent choice in biomedical processing must be evaluated not only in terms of solubilization efficiency, but also with respect to toxicity, volatility, and residual solvent limits [89]. Importantly, not all solvents present the same

toxicological risk [89]. For example, solvents such as chloroform and dichloromethane are generally regarded as more hazardous due to their higher toxicity and stricter residual limits, whereas solvents such as ethanol or acetic acid are comparatively less hazardous and more acceptable in biomedical processing when used under controlled conditions [158]. From a regulatory perspective, acceptable residual solvent levels are typically defined according to ICH Q3C guidelines and depend on solvent class; for instance, class 2 solvents such as chloroform are generally limited to residual concentrations on the order of tens of ppm (e.g., ~60 ppm), whereas class 3 solvents with lower toxic potential may be tolerated up to several thousand ppm (typically ≤5000 ppm) [158, 159]. Therefore, while solution mixing remains a useful and widely employed strategy for polymer blending, its suitability for biomedical scaffold fabrication depends on careful solvent selection, effective solvent removal, and quantitative control of residual solvent content [152]. In this regard, the need for solvent recovery, drying control, and residual solvent verification introduces additional environmental, processing, and scale-up constraints compared with solvent-free melt-based approaches [47, 124].

In contrast, melt mixing, as an efficient and biocompatible method, is carried out without the need for solvents and relies solely on controlled heat and shear, and therefore offers significant advantages over the solution method [130]. The complete elimination of the solvent makes this method very desirable from the perspective of biocompatibility and concerns about toxic residues [124]. However, the success of this method depends on precise adjustment of process parameters, such as temperature, mixing time, and shear rate, especially given the sensitivity of many biomedical polymers to thermal degradation [124]. Also, the proximity of the melting temperatures and rheological behavior of the polymers to be mixed is of great importance, since significant differences in viscosity or thermal behavior can lead to the formation of separated phases, inefficient mixing, or undesirable changes in the scaffold morphology. For this reason, evaluating rheological properties, conducting thermal analyses (DSC/TGA), and investigating degradation indices are essential to ensure the stability and quality of the final product [130]. Understanding the degree of thermodynamic compatibility of polymers also plays an important role in predicting the final microstructure and performance of the scaffold [130].

In cases where neither the solution nor the melt methods alone can achieve the desired dispersion, control morphology, or stabilize multicomponent structures, hybrid methods are used [130]. In this approach, part of the process is carried out in the solution phase and the rest in the melt phase,

exploiting the advantages of both methods [130]. Typically, the solution phase is used to predisperse incompatible polymers or nanoparticles that tend to aggregate, while the melt phase helps stabilize the final structure. Despite these advantages, the hybrid method has limitations, such as being time-consuming, increasing the risk of degradation due to performing two separate steps, and the risk of solvent remaining in the event of incomplete drying, all of which can affect the final properties of the scaffold and its biological function [130].

2.4 Melt Electrospinning Technique

2.4.1 Principles and Mechanisms of Electrospinning

In the electrospinning process, the application of a high potential difference between a metallic nozzle and a collector generates the electric field required to stretch the polymer jet and form fibers [13]. In this configuration, the nozzle connected to the syringe acts as the active electrode, and the polymer droplet formed at the needle tip accumulates surface charge under the applied electric field [47]. As the charge density increases, the balance between surface tension and electrostatic force is progressively disrupted until the droplet deforms from a hemispherical shape into the characteristic Taylor cone [13, 47]. Once the electrical stress exceeds the capillary stress, a polymer jet is ejected from the apex of the cone and undergoes elongation and thinning under electrohydrodynamic forces [47]. This transition can be classically described by comparing electrostatic stress ($\sim \varepsilon E^2$) and capillary stress ($\sim \gamma/R$), where ε is the dielectric permittivity of the medium, E is the electric field strength, γ is the surface tension, and R is the characteristic droplet radius. Jet initiation occurs when the electrical stress overcomes the restoring force imposed by surface tension, which defines the onset of Taylor cone formation and electrospinning [160-163]. Jet behavior in electrospinning is governed by the coupled interaction of electrical, viscous, capillary, and elastic forces, and its stability can be described using several key dimensionless groups. One of the most important is the Electric Bond number ($Bo_e = \varepsilon E^2 R/\gamma$), which represents the ratio of electrostatic to capillary forces; Stable jet formation occurs when electric forces overcome surface tension forces [160-163]. The Capillary number ($Ca = \eta U/\gamma$), where U is the characteristic jet velocity and η is the dynamic viscosity of the polymer melt or solution describes the ratio of viscous to capillary forces and determines whether the jet remains stable under viscous stretching or tends toward droplet breakup [164]. The Deborah number ($De = \lambda U/L$), where λ is the characteristic relaxation time of the polymer system and L is the characteristic length scale of

the jet (typically taken as the jet diameter or the characteristic stretching length) characterizes the role of viscoelasticity in jet stability and reflects whether polymer chains have sufficient time to relax during deformation; values of De> 1 are generally favorable for continuous fiber formation, as they indicate sufficient elastic resistance to maintain jet continuity [165]. In addition, the Reynolds number (Re= ρUL/η), where ρ is the density of the polymer fluid in electrospinning is typically very small (Re << 1), indicating that jet flow remains in the laminar regime and is dominated by viscous forces, while inertial effects are negligible [166]. This is one of the main reasons why electrospinning is strongly dependent on solution properties such as viscosity and viscoelasticity, as sufficient chain entanglement is required to maintain a stable jet. electrospinning is highly sensitive to viscosity and rheological structure of the melt or solution [167].

In practice, uniform and stable fiber formation is achieved only when this electrohydrodynamic balance is coupled with an appropriate processing window. In conventional electrospinning systems, the electric field strength is typically maintained in the range of approximately 0.5 to 2 kV cm^{-1}; lower values are often insufficient to overcome surface tension, whereas higher values may induce jet instability, fiber breakup, or electrical discharge [168-170]. Similarly, viscosity must be sufficiently high to provide adequate chain entanglement for jet continuity, but not so high as to prevent stable extrusion of the melt or solution. The effect of viscosity on the droplet size can be determined using the dimensionless number π_n (Equation 2.1) [171]:

$$\pi_n = \frac{\left(\gamma^2 \rho \left(\frac{\varepsilon \varepsilon_0}{K}\right)\right)^{\frac{1}{3}}}{\eta} \tag{2.1}$$

When π_n <<1, an increase in polymer fluid would increase droplet size. When π_n >>1, the effect of viscosity on droplet size is considered negligible [171].

In general, successful fiber formation in electrospinning results from a delicate balance among electric field strength, surface tension, viscosity, chain relaxation time, and flow rate, all of which directly govern fiber diameter, jet stability, and final structural fidelity [168-170, 172, 173]. In melt electrospinning, unlike solution electrospinning, the absence of a solvent means that the behavior of the polymer jet is controlled not only by electrostatic forces but also by heat transfer, temperature-dependent viscosity changes, and the viscoelastic behavior of the melt, which play decisive roles in the stability and thinning of the jet [174-176]. For this reason, modeling of this process is usually based on the simultaneous solution of the conservation equations for mass

(Equation 2.2), momentum (Equation 2.3), electric charge (Equation 2.4), and energy (Equation 2.5). In one-dimensional models based on the thin filament approximation, the conservation of mass is expressed as Equation 2.2 [175, 176]:

$$Mass: \pi R^2 v = \dot{V} \tag{2.2}$$

Which describes the relationship between the jet radius, R, axial velocity, v, and flow rate, $\dot{V}$ [175]. The momentum equation, Equation 2.3, describes the balance among F_T, the viscoelastic tensile force in the jet, surface tension, γ, viscoelastic stresses, σ, and electrostatic forces, E_t, acting along the jet [175, 176]:

$$Momentum: \rho v v' = \rho g + \frac{F_T{}'}{\pi R^2} + \frac{\gamma R'}{R^2} + \frac{\sigma \sigma'}{\varepsilon_0} + (\varepsilon - \varepsilon_0) E_t E_t{}' + \frac{2\sigma E_t}{R} \tag{2.3}$$

In this equation, the role of the electric field, in stretching the jet and overcoming capillary forces becomes evident, while the viscoelastic stresses of the melt provide the resistance required to suppress jet breakup [175]. In addition, charge transport along the jet is governed by the charge conservation equation (Equation 2.4) [175, 176]:

$$Charge: \pi R^2 K E_t + 2\pi R V \sigma = I \tag{2.4}$$

Which accounts for the combined contributions of electrical conduction within the melt and convective transport of surface charges by the moving jet [175]. Since solidification in melt electrospinning occurs through cooling of the melt rather than solvent evaporation, the energy equation (Equation 2.5) also plays a critical role [175, 176]:

$$Energy: \rho C_P v T' = \frac{v' F_T}{\pi R^2} - \frac{2h(T - T_\infty)}{R} + Q \tag{2.5}$$

Where Q is the volumetric heat source, Cp is the polymeric heat capacity, T is temperature of the polymer jet, T_∞ is the external air temperature, and h is the convective heat transfer coefficient [175]. Equation 2.5 describes the influence of heat loss to the surroundings, viscous heating, and temperature evolution of the jet on the rheological behavior of the melt [175]. Overall, these non-isothermal electrohydrodynamic equations demonstrate that the final fiber diameter and

morphology in melt electrospinning are governed by the complex interplay among the electric field, melt viscoelasticity, surface tension, charge transport, and heat transfer [174, 176].

2.4.2 Solution vs. Melt Electrospinning: Advantages and Drawbacks

Figure 2.7 illustrates the fundamental distinctions between melt and solution electrospinning.

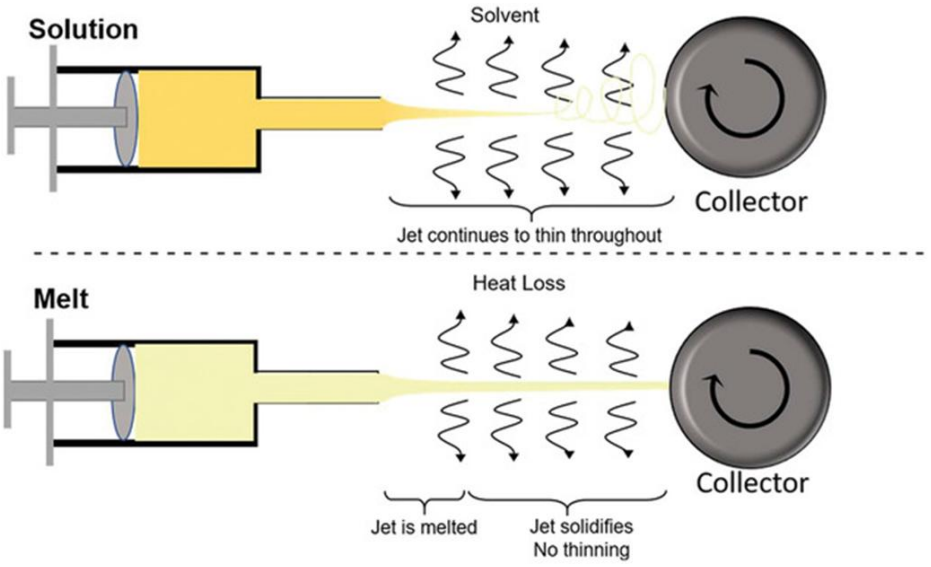

Figure 2.7 A schematic showing the key distinctions between melt and solution electrospinning. Reproduced from Ref. [177] under the terms of the Creative Commons CC BY license.

In solution electrospinning, the polymer is dissolved in an appropriate solvent, and the dynamics of jet formation are predominantly governed by mass-transfer phenomenon and the progressive evaporation of the solvent [14]. The continuous reduction of the effective mass of the jet and the increase of the surface charge density allow for continuous stretching and the achievement of nanometer diameters [178]. Despite this advantage, the possibility of solvent traces remaining in the final structure can be challenging for biomedical applications [14]. In melt electrospinning, the polymer is processed in a molten state and the evolution of the jet is mainly controlled by heat transfer, temperature history, and the melt's viscoelastic behavior. High viscosity and long relaxation times limit the jet's stretching range and usually confine the fiber diameter in the micron range; however, applying secondary mechanical stresses, such as high-speed collector rotation, can enhance chain orientation and reduce fiber diameter [14]. The complete elimination of solvent, chemical stability, scalability, and ability to create ordered and porous 3D architectures make this

method a very attractive option for tissue engineering and drug delivery systems [124]. However, melt electrospinning of multicomponent systems, specifically those consisting of more than two components, remains relatively untouched. Table 2.6 presents a compilation of studies conducted on the melt electrospinning of polymer blends. Considering the literature review and Table 2.6, melt electrospinning of ternary blend systems, especially in the field of tissue engineering, still has significant potential for systematic research and the development of innovative approaches in the design of multicomponent scaffolds.

Table 2.6 Examples of works on polymer blend melt electrospinning

Blend	Effects of using blend	Ref.
PLA/PEG	Improving biodegradability, cell affinity, as well as mechanical and physical properties	[125, 179, 180]
Isotactic Polypropylene/ Styrene-Acrylonitrile (iPP/ SAN)	More uniform fibers	[181]
PLA /PCL	The blending of PCL and PLA significantly improved cell viability, making the PCL/PLA scaffold suitable for heart tissue engineering.	[182]
Polyvinyl Butyral/ Isotactic Polypropylene (PVB/ iPP)	PVB enhanced PP's crystallinity and thermal characteristics. Due to decreased viscosity and increased surface adhesion and polarity, the addition of PVB led to the formation of finer fibers at a faster rate.	[183]
Poly (ε-caprolactone)/ Poly (ethylene glycol)-block-poly (ε-caprolactone) (PCL/PEG-b-PCL)	The presence of PEG-b-PCL as an amphiphilic substance encourages the release of hydrophilic compounds from the scaffold. Fabrication of thinner fibers compared to neat PCL Blending caused a decrease in the uniformity of the fabricated fibers compared to the melt electrospinning of neat PCL	[48, 178]

Despite numerous merits associated with melt electrospinning, including the elimination of organic solvents, promising control over fiber deposition, and greater compatibility with biomedical applications, it has some limitations [14]. One of the most important challenges is the limitation on reducing fiber diameter compared to solution electrospinning; owing to the high melt viscosity and the lack of a thinning mechanism from solvent evaporation, it is much more challenging to produce fibers at the nanometer scale [106]. In addition, the requirement for high temperatures to melt the polymer can lead to thermal degradation of sensitive materials and limit the range of usable polymers, reducing the possibility of direct loading of bioactive molecules such

as proteins and growth factors [14]. The choice of polymer is also limited to thermoplastics with thermal stability and suitable rheological behavior [14]. From the perspective of adjusting processing parameters, accurate control of temperature, shear rate, and cooling conditions is essential, as minor deviations can alter the degree of fiber fusion at junctions, thereby affecting the scaffold's morphology and mechanical properties [106, 184]. Furthermore, industrial scalability and increased production rates compared to conventional melt spinning methods still face challenges [184, 185]. Overall, although melt electrospinning is a promising approach for designing scaffolds for tissue engineering, understanding and managing these limitations is essential to optimize the system's ultimate performance.

2.4.3 Process Parameters Affecting Fiber Morphology

The efficiency of melt electrospinning depends on precisely adjusting a set of process parameters and material properties that determine the quality, uniformity, and final morphology of the melt electrospun fibers [178]. The distance from the needle to the collector must be selected in proportion to the cooling rate and the time required for the jet to solidify, as too short a distance results in deposition of the semi-molten jet and the formation of unwanted connections in the scaffold structure. Excessive distances lead to process discontinuities due to fiber breakage [178]. The processing temperature affects the melt viscosity and jet elasticity. The temperature is usually set at 10 to 30 ˚C above the polymer's melting point [14]. However, very high temperatures increase the risk of thermal degradation of the polymer chains [178]. In such processes, adding a component that could reduce melt viscosity seems a practical solution to address the issue [178]. Besides, to create a stable Taylor cone and avoid jet splashing or whipping, the applied voltage must be carefully selected; properties such as the melt's viscosity and conductivity are crucial in determining the ideal voltage range [47]. Injection flow rate is another factor that directly affects fiber diameter; increasing flow rate reduces the opportunity for jet stretching and increases fiber diameter, which is why melt electrospinning typically uses very low flow rates to allow the jet sufficient time to stretch and solidify [14].

On the other hand, nozzle diameter imposes an inherent limitation on the fabrication of very thin fibers, as it is difficult for a highly viscous polymer melt to pass through small orifices [14]. Finally, melt rheology, including viscosity, viscoelastic behavior, conductivity, and dielectric constant, plays a critical role in jet stability; very high viscosities prevent stable jet formation, while very

low viscosities cause jet instability, whipping, or splashing [14, 186, 187]. Therefore, precise adjustment of rheological properties via temperature variation, polymer composition modification, or nanoparticle addition is essential to achieve uniform, defect-free fibers [14].

2.5 Incorporation of Bioactive Nanofillers in Polymeric Scaffolds

Natural bone consists of three main phases: the mineral phase, which includes calcium and phosphate compounds in the form of biological nanoapatites, the organic phase, which is mainly composed of type I collagen, and the aqueous phase, which plays an important role in regulating the mechanical behavior and material transport in the tissue [188]. For this reason, in many studies, the use of bioactive nanoparticles along with natural or synthetic polymers has been considered as a practical approach to create nanocomposites with behavior similar to bone tissue [189]. Table 2.7 presents examples of widely used nanoparticles for bone regeneration and their roles in improving scaffold properties.

Among these nanoparticles, nanohydroxyapatite holds a special place because of its ceramic properties and crystalline structure, which increase hardness, improve mechanical stability, and enhance cell interactions [189]. The presence of this nanoparticle in electrospun fibers provides conditions for more efficient absorption of biomolecules, cell attachment, proliferation, and mineralization. Therefore, the combination of polymers with nanohydroxyapatite has been introduced as a logical approach to achieve scaffolds with optimal biological and mechanical properties [188]. The synergistic behavior resulting from the combination of biocompatible polymers with inorganic nanoparticles can also accelerate osteogenic differentiation and new tissue formation [189].

However, achieving proper dispersion of nanoparticles in the polymer matrix, especially during electrospinning, requires careful attention to their nanoscale behavior and the process conditions. One of the important challenges in the production of polymer nanocomposites is the tendency of the inorganic nanophase to aggregate, forming beaded, discontinuous structures in the fibers, which can reduce the mechanical properties and the final quality of the scaffolds [14]. Therefore, several studies have focused on controlling nanoparticle size, improving dispersion, and preventing nanoparticle aggregation. The results show that an excessive increase in the nanohydroxyapatite weight percentage in the polymer mixture increases the likelihood of particle

aggregation and decreases fiber strength; therefore, the nanofiller amount should be carefully optimized [14].

Nanocomposites allow the surface, physical, and chemical properties of the scaffold to be tuned to biological needs [189]. Among other things, it has been shown that surface topography, chemical composition, and microstructural organization can play an important role in guiding stem cell behavior and determining their differentiation pathways [152]. Numerous studies have shown that direct cell contact with the nanocomposite matrix is an essential step for initiating [188, 189]. It has also been reported that increasing the amount of nanohydroxyapatite in scaffolds can affect biomolecule release without detrimental effects on cell viability [188].

Table 2.7 Commonly used nanoparticles in bone tissue engineering

Nanoparticle	Polymeric matrix	Effect	Ref.
Nano-hydroxyapatite (nHA)	PCL PLA PLGA Chitosan Gelatin	To promote the proliferation of osteoblast cells To encourage the cellular activities of bone cells To promote mineralization To increase the scaffold's mechanical properties	[98]
Carbon nanotubes	PLA poly (lactic-co-glycolic acid)	To improve osteoblast attachment and proliferation To manipulate cells' preferential orientation and alignment on the nanofibers To increase the thermal stability, tensile strength, and Young's modulus	[190, 191]
Iron oxides nanoparticles (Fe_2O_3)	PCL PLA	To improve protein adsorption To enhance apatite-forming To accelerate differentiation and proliferation of mesenchymal stem cells To increase hydrophilicity, and mechanical strength To modify degradation rate	[192-197]
Bioglass®	PLA PLLA PDLLA	To enhance the in vitro and in vivo biocompatibility To boost cell adhesion To control the degradation rate	[198-201]
Nanodiamond	PCL Gelatin poly(lactide-co-glycolide)	To promote the mechanical properties, and cell growth for various cell types, exclusively bone-associated cells	[202-206]
Sinapic acid-loaded Chitosan	PCL	To enhance the bone cell attachments	[207]
Cellulose nanocrystal	Gelatin PLA	To enhance the biodegradability of nanofibers	[208, 2

Another important point is the behavior of nanoparticles in multicomponent mixtures [152]. The presence of nanoparticles in polymer systems can lead to microstructures that differ from those of pure polymers. The location of the nanoparticles, whether in the matrix, in the dispersed phase, or in the interfacial region, plays a decisive role in the final properties of the nanocomposite [14]. Both thermodynamic and kinetic factors govern the final morphology of a nanocomposite, and the ultimate localization of nanoparticles is not determined solely by their thermodynamic affinity for a given phase, but also by the processing pathway and mixing history [210]. From a thermodynamic perspective, nanoparticles tend to localize in the phase with which they exhibit the lowest interfacial energy or the most favorable chemical interactions [211]. However, reaching this equilibrium state is not always guaranteed, as nanoparticle migration between phases is also constrained by kinetic limitations. In this context, the order of component addition plays a decisive role because the initial location of the nanoparticles determines their subsequent migration pathway, the extent of their contact with each phase, and their opportunity for redistribution during mixing [14, 212-214]. For example, if nanoparticles are first premixed with a thermodynamically less favorable phase, they may later migrate toward the more favorable phase upon introduction of the second component; however, if the viscosity of the initial phase is high or the mixing time and shear stress are insufficient, the particles may remain kinetically trapped in the original phase [211, 215-217]. In contrast, introducing nanoparticles first into the phase with more favorable interfacial interactions can promote preferential localization from the outset and lead to a more homogeneous final distribution [212, 214]. In addition, processing conditions such as temperature, mixing time, shear intensity, and cooling rate directly affect nanoparticle mobility, their ability to cross interfacial boundaries, and the time available for redistribution [215, 218]. Higher temperatures or stronger shear generally facilitate interphase migration by reducing viscosity and increasing particle mobility, whereas rapid cooling or early viscosity buildup may freeze the morphology before thermodynamic equilibrium is reached [215, 218]. Therefore, the final nanocomposite morphology results from direct competition between thermodynamic driving forces and kinetic constraints, with component addition sequence and processing conditions acting as key parameters governing this balance. Figure 2.8 illustrates the potential morphology of a binary blend that incorporates organoclay.

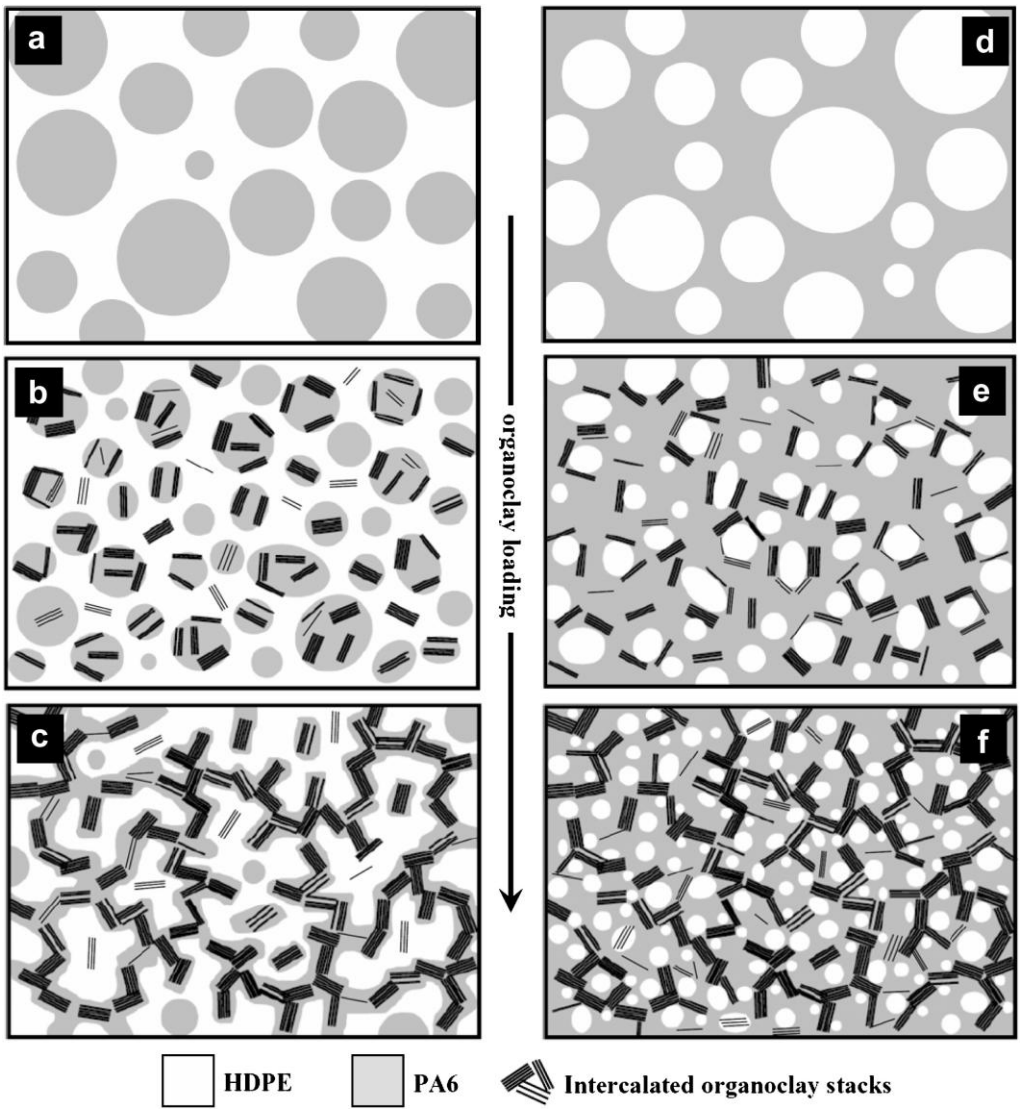

Figure 2.8 The evolutions of the microstructure in (a) plain polyethylene/ polyamide 6 (PE/PA6) (75/25 vol%), (d) plain PE/PA6 (25/75 vol%), and the localization of organoclay within the droplet phase and (e-f) within the matrix phase. Reproduced from Ref. [216] with permission from [Elsevier], © [2010].

2.6 Cellular approach in bone tissue engineering

Bone tissue engineering is based on three fundamental components: cells, scaffolds, and biochemical stimuli, which synergistically drive tissue repair and regeneration [188, 219]. Among them, cells play a key role in initiating, developing, and completing bone formation, and their behavior is the main criterion for evaluating biocompatibility, differentiation induction, and regenerative capacity [188]. Cell-based evaluations in vitro and in vivo provide a platform to accurately assess the efficacy of designed scaffolds in stimulating cellular processes,

mineralization, angiogenesis, and new bone tissue formation [219]. Considering the type of scaffold, in the field of bone tissue engineering, in vitro studies were more focused on polymeric scaffolds, whereas most in vivo experiments used ceramic scaffolds (Figure 2.9) [220].

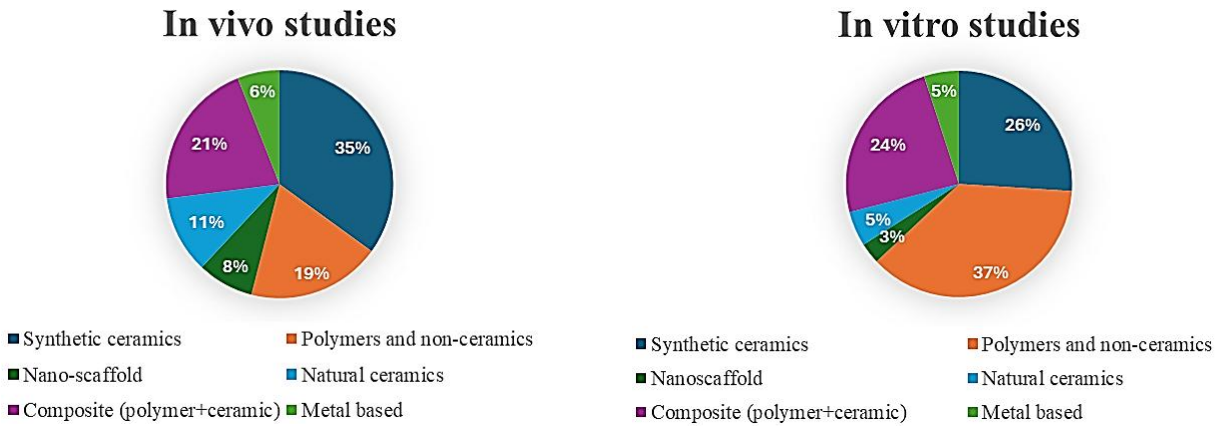

Figure 2.9 Distribution of bone tissue engineering research based on the types of scaffolds. Reproduced from Ref. [220] under the terms of the Creative Commons CC BY license.

The main goal of tissue engineering studies is to commercialize a suitable scaffold that has passed all the pre-clinical in vitro and in vivo investigations, clinical trial approval, and patient expectations. The successful clinical translation of an engineered scaffold requires consideration of multiple scientific, technical, clinical, and regulatory factors beyond its initial laboratory design [219]. The development pathway of a clinically relevant scaffold starts from biomaterial design and fabrication, followed by physicochemical and biological characterization, preclinical validation, clinical evaluation, scalable manufacturing, and regulatory approval [219]. This process involves multiple actors, including biomaterial scientists responsible for material design and scaffold fabrication, researchers conducting in vitro and preclinical studies, clinicians and surgeons evaluating implantation performance in clinical settings, industrial partners responsible for large-scale, reproducible manufacturing, and regulatory agencies overseeing safety, quality, and clinical compliance. In addition, patient-specific needs and clinical expectations remain central throughout this translational pathway. Therefore, the development of an effective scaffold for clinical use requires not only appropriate biological and structural performance, but also reproducibility, manufacturability, regulatory acceptability, and clinical relevance [221].

2.6.1 In Vitro Cell analysis for Bone Tissue Engineering

In vitro tests are the first step in evaluating the efficacy of a scaffold in bone tissue engineering. This step allows the behavior of relevant cell types, including fibroblasts, osteoblasts, and human endothelial cells (HUVECs), to be investigated in contact with the scaffold structure and its bioactive components [222].

2.6.1.1 Fibroblast Behavior and Initial Biocompatibility Assessment

Fibroblasts serve as the starting point for evaluating scaffold biocompatibility [222]. The degree of cell adhesion, cell proliferation, and cytoskeletal organization are important indicators of whether the scaffold provides a stable, nontoxic environment for cells [223-226]. In the evaluation of early biocompatibility, adequate cell adhesion is generally considered satisfactory when a significant proportion of seeded cells (generally more than 60–70% within the first 4 to 24 hours) remain attached to the scaffold surface and show a spread, adherent morphology [224, 227]. For cell proliferation, viability above 70% relative to the control, in accordance with ISO 10993- 5, is generally accepted as the minimum threshold for non-cytotoxicity [224, 226, 228]. In contrast, progressive increases in metabolic activity or cell number over 3 to 7 days are commonly considered promising indicators of scaffold support for cell growth. In terms of cytoskeletal organization, the building of a well-defined actin network, appropriate cell spreading, and the presence of distinct focal adhesions are generally considered indicative of stable attachment and favorable cell–surface interactions [229, 230]. Overall, a scaffold is typically considered appropriate for early cellular responses when it simultaneously supports effective initial adhesion, cell viability above the standard cytotoxicity threshold, and appropriate cytoskeletal organization [231]. Numerous studies have shown that scaffolds containing hydroxyapatite and biodegradable polymers, such as PCL, PLGA, and collagen-based materials, generally meet these criteria and support favorable fibroblast adhesion, spreading, and proliferation [220, 232].

2.6.1.2 Osteoblast Behavior and Bone Differentiation

Osteoblasts are the main cells involved in bone formation and play a crucial role in evaluating the performance of tissue-engineered scaffolds [220]. A suitable scaffold must ensure osteoblast viability at the outset while promoting osteogenic differentiation and the formation of the mineral matrix. The primary indicator of scaffold effectiveness is the metabolic activity of cultured cells,

commonly assessed using tests such as MTT or Alamar Blue assay [188]. A high level of metabolic activity suggests that the scaffold is a robust environment for osteoblast activity. Several studies have reported that the presence of mineral nanoparticles, such as Mg-HA, Sr-HA, and especially nHA, that gradually release bioactive ions, boosts this activity and enhances the potential for cell growth [222].

Next, the rate of cell proliferation is usually assessed by measuring DNA content [188]. Research results show that scaffolds with a nanostructure similar to natural bone tissue or bioactive compounds exhibit a significant increase in DNA content and, as a result, increased osteoblast proliferation during the early and middle days of culture, especially between days 7 and 14 [188]. Following initial growth, the cells enter the differentiation phase, a key indicator of which is an increase in the activity of the enzyme alkaline phosphatase (ALP) [53]. This enzyme plays an important role in the hydrolysis of phosphorus compounds and prepares the substrate for the initiation of mineralization, and is usually significantly increased in the early stages of differentiation [188].

In advanced stages, the scaffold's capacity to promote complete bone differentiation is evaluated by measuring mineral deposition. Tests such as Alizarin Red S and von Kossa assess the scaffold's capacity to promote mineralization and osteoblast maturation. The presence of HA usually triggers mineralization on the scaffold [232].

2.6.2 In vitro vascularization in Bone Tissue Engineering

Efficient angiogenesis is a fundamental building block for the success of bone tissue engineering, as the formation of an orderly vascular network allows the delivery of oxygen, nutrients, and biological factors to the healing tissue and prevents necrosis or arrest of new tissue growth [76]. In in vitro studies, endothelial cells, especially human umbilical vein endothelial cells (HUVECs), are used as a standard model to examine scaffolds' ability to induce angiogenesis [76]. The behavior of these cells indicates the scaffold's performance in providing a suitable environment for triggering angiogenesis. Increased migration capacity of HUVECs and the formation of tubular structures, which reflect the initial formation of blood vessels, are considered the most important indicators of a scaffold's performance for vascularization [188]. Several researches have shown that scaffolds containing hydroxyapatite, mineral nanoparticles, or bioactive ions such as lithium, magnesium, and strontium can significantly enhance endothelial cell migration and formation of

stable tubular networks by activating intracellular signaling pathways, including the PTEN/AKT pathway, and increasing the expression of angiogenic genes such as VEGF and ANG-1 [76, 188]. These findings established that even subtle changes in the chemical composition or microstructure of the scaffold can have broad biological consequences on the angiogenesis process [188].

In addition to single-cell studies, co-culture systems are an advanced, practical approach for assessing angiogenesis. Co-culture of mesenchymal stem cells (MSCs) with endothelial cells creates an environment similar to in vivo tissue and enables investigation of complex interactions between these cell lines [233, 234]. MSCs stimulate HUVECs to migrate, organize, and form vascular-like structures by secreting angiogenic factors, while endothelial cells promote MSC osteogenic differentiation by providing a suitable biostratigraphy [234]. This bidirectional communication plays a fundamental role in the simultaneous processes of osteogenesis and angiogenesis. Furthermore, the use of mesenchymal stem cell-derived exosomes attached to the scaffold surface or loaded into its structure has been shown to significantly enhance the tubular growth pattern of HUVECs, the expression of angiogenesis-related genes, and the integrity of the established vascular network [76]. This phenomenon underscores the key role of cell signaling in the formation of new vessels and the necessity of a multidimensional approach in the design of tissue-engineering scaffolds [26].

Finally, in vitro angiogenesis assessment is a crucial indicator for predicting scaffold behavior in animal models. Scaffolds that promote endothelial behavior, stimulate cell migration, and form stable tubular structures are generally more successful in vivo and can provide adequate blood flow, proper nutrition, and favorable microbiota conditions for bone repair [76]. Therefore, designing and engineering scaffolds that, in addition to structural and mechanical compatibility, possess effective angiogenic properties is a fundamental step in achieving clinical success in repairing bone defects. Figure 2.10 shows the main parameters affecting the angiogenesis process.

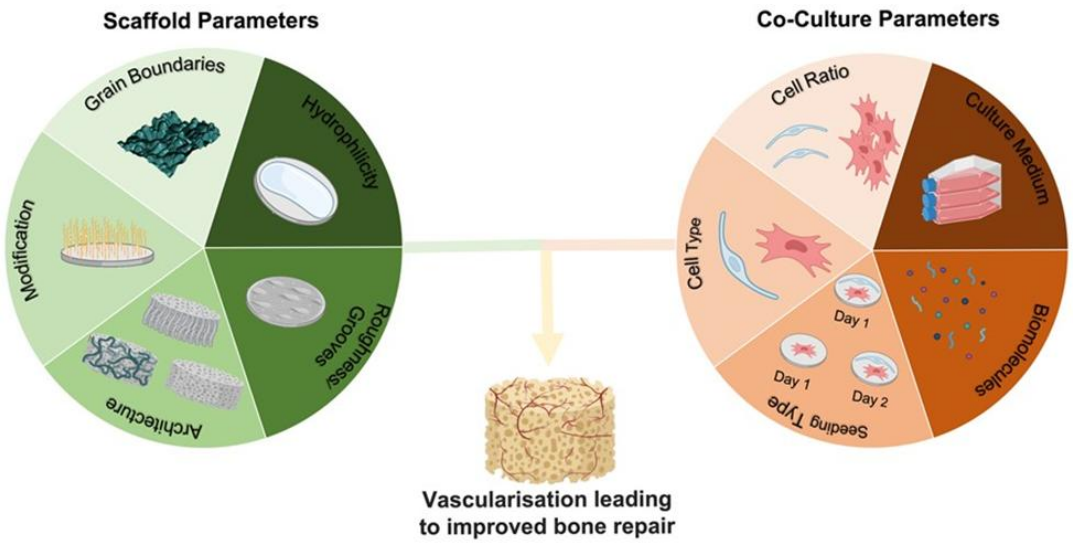

Figure 2.10 An overview of the relationship between the scaffolds' biochemical properties, architectural designs, co-culture factors, and angiogenesis. Reproduced from Ref. [76] under the terms of the Creative Commons CC BY license.

2.6.3 Ex vivo and In vivo Bone Tissue Engineering advances

Ex vivo studies play an important role in evaluating the performance of bone tissue engineering scaffolds as an intermediate and complementary step between in vitro and in vivo tests (Figure 2.11) [235]. In this approach, tissues or organs extracted from a living organism are maintained under regulated laboratory conditions, allowing the scaffold to interact with the native tissue microenvironment to perform the experiments without the systemic challenges of clinical treatments [236]. Ex vivo studies have the advantage of simultaneously maintaining key components, such as the natural extracellular matrix, immune cells, blood vessels, and local mechanical signals, while allowing laboratory variables to be controlled more precisely than in animal models [236, 237]. In bone tissue engineering, ex vivo models have been widely used to study cell adhesion and infiltration, mineralization initiation, the local inflammatory response, and scaffold-host tissue interactions [235]. A comprehensive literature review suggests that the results of these studies can provide a more accurate prediction of scaffold in vivo performance and help identify inappropriate designs before entering the in vivo phase, thereby reducing the number of animal experiments and associated costs [236-240]. For this reason, the ex vivo approach has attracted increased interest as a valuable tool for enriching preclinical evaluations and optimizing the design of bone scaffolds [235, 241, 242].

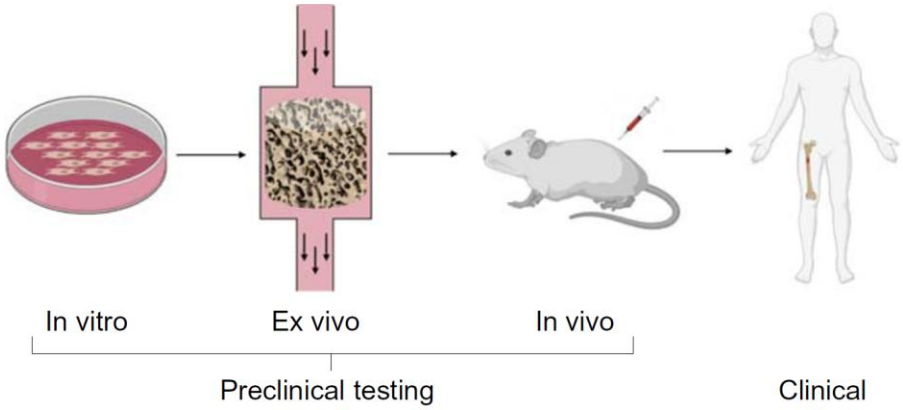

Figure 2.11 The role of ex vivo models in the preclinical and clinical development of novel bone tissue engineering therapies. Reproduced from Ref. [235] under the terms of the Creative Commons CC BY license.

The in vivo study is the final and most important step in assessing the efficacy of bone tissue engineering scaffolds, as it allows measurement of the scaffold's performance in a real biological environment that includes microbial factors, mechanical forces, immune cells, and natural tissue repair processes [219]. In animal studies, various models, such as calvarial defects in mice and rats, segmental defects in femurs and tibias, significant bone defects in rabbits, and simulated osteomyelitis or bone tumor models, are used to investigate the behavior of scaffolds under different conditions [220, 233]. The findings show that scaffolds that have demonstrated favorable biocompatibility, osteoblastic differentiation, and significant angiogenic potential in vitro usually perform well in vivo and guide repair, leading to the restoration of bone structure and function [220].

A large number of hydroxyapatite-based scaffolds and their nanoparticles have been shown to enhance new bone formation and establish a good connection between the newly formed tissue and the host bone in animal models [26, 219]. Imaging studies, particularly micro-CT, have shown that these scaffolds accelerate bone formation by increasing mineral density and thickness [26, 232]. In many cases, a significant portion of the scaffold has been replaced by new bone tissue within 8 to 12 weeks [26]. At the same time, the presence of such scaffolds is often accompanied by a minimal inflammatory response, and their gradual, controlled resorption has enabled stable tissue regeneration [26]. One reason for the success of these scaffolds is their ability to support simultaneous angiogenesis [234]. This process is essential for the survival of osteogenic cells and the stabilization of the mineral matrix [234].

The addition of bioactive ions to the scaffold structure, such as lithium, magnesium, strontium, and zinc, has attracted much attention in recent years [219]. These ions have been shown to increase bone formation rates and improve the quality of new tissue by gradually releasing and activating signaling pathways involved in osteogenesis [232]. Scaffolds such as Mg-HA or Zn-containing compounds have effectively repaired critical bone defects in animal models and, in addition to enhancing osteogenesis, have also provided better angiogenesis and biointegration [232]. These findings highlight the importance of bioactive agents in simultaneously promoting mechanical strength, cell adhesion, and improved repair potential [188]. On the other hand, advances in 3D scaffold fabrication technology, especially 3D printing technology, have enabled the production of structures with precise control of porosity, pore size, and channel architecture; properties that are critical for cell infiltration, blood flow, and provision of a suitable substrate for bone regeneration [222]. Several studies have reported that 3D-printed scaffolds with engineered nanostructures can increase cellular permeability and vascular infiltration, resulting in more stable and extensive bone formation at the defect site [26, 222]. Due to precise control of fabrication parameters, these scaffolds exhibit greater ability to mimic the structure of natural bone, and their biological performance has been more favorable than that of conventional scaffolds [26].

Overall, evidence from in vivo models clearly shows that a scaffold's success in repairing critical bone defects depends on its ability to simultaneously stimulate bone formation and angiogenesis [26]. The presence of bioactive minerals such as HA and the use of gradual-release growth factor systems are among the most important features that promote biointegration, effective regeneration, and long-term performance of the scaffold [188, 232]. These results highlight the importance of multi-level, intelligent scaffold engineering to achieve complete and stable bone tissue regeneration. Cellular approaches in bone tissue engineering provide powerful tools for evaluating scaffold efficacy [233]. In vitro results indicate that three key components, including initial biocompatibility, osteoblastic differentiation, and angiogenesis, must be simultaneously improved for a scaffold to have real potential for clinical applications [233]. In vivo results also confirm these findings and highlight the importance of designing scaffolds with a three-dimensional structure, the presence of bioactive ions, and the ability to stimulate angiogenesis and osteogenesis processes [233].

2.7 Summary and Identified Research Gaps

The melt electrospinning of multicomponent systems, particularly ternary blend systems, has remained underexplored despite its significant potential to enhance scaffold quality and performance. The importance of this area is highlighted when the inherent advantages of the melt electrospinning method, including the complete elimination of organic solvents and the potential for high production scale, are considered. These features pave the way for the development of polymeric scaffolds that can provide the properties required for a specific type of tissue in a targeted, tunable manner by adding different components to the matrix.

This aspect is of particular importance in bone tissue engineering, as bone is a complex, heterogeneous, and multiphasic tissue that must simultaneously fulfill several structural, mechanical, and biological requirements [78]. Structurally, native bone exhibits a hierarchical organization spanning from the nanoscale to the macroscale and consists of an organic phase, a mineral phase, and a porous interconnected network that supports mass transport and cellular organization [78, 243]. At the macroscopic level, particularly in cancellous bone, interconnected porosity is essential for cell infiltration, nutrient transport, gas exchange, and waste removal [244, 245]. At the same time, this porosity must not compromise mechanical integrity, as the scaffold must maintain sufficient structural stability during the early stages of implantation and withstand stresses imposed by the surrounding environment [82, 246]. In addition, the scaffold must possess adequate flexibility to allow a degree of mechanical compliance with the surrounding tissue without undergoing brittle failure. Achieving such a combination of properties—including effective porosity, mechanical stability, flexibility, and appropriate biological response—is generally not feasible using a single polymer alone, as each polymer typically satisfies only part of these requirements [41]. Therefore, the use of multicomponent systems, in which each constituent serves a distinct functional role in tuning the final scaffold properties, emerges as a rational and necessary strategy [37].

Previous studies have shown that the incorporation of bioactive components, particularly hydroxyapatite nanoparticles, can improve scaffold–cell interactions and enhance osteogenic response due to their close chemical and mineral resemblance to the native inorganic phase of bone [39, 247]. The presence of hydroxyapatite can improve surface roughness, bioactivity, protein adsorption, and ultimately cell adhesion and proliferation, thereby promoting osteogenic guidance [38, 248]. However, although the biological benefits of these nanoparticles have been widely

reported in polymeric systems, their systematic integration into multicomponent matrices and the simultaneous evaluation of their processing behavior and final performance under melt electrospinning remain very limited [248]. In such systems, the incorporation of bioactive nanoparticles is not merely a simple compositional modification, but a factor that directly influences melt rheology, flow stability, phase distribution uniformity, and the final quality of the electrospun fibers [14, 47]. Challenges such as achieving homogeneous nanoparticle dispersion within the matrix, preventing particle agglomeration, maintaining stable melt flow during processing, and simultaneously controlling fiber morphology and biological performance have not yet been comprehensively and systematically evaluated [13].

Given the increasing need for advanced scaffolds for bone repair applications and the key role of hydroxyapatite in enhancing biological response, it is clear that further research is needed on the incorporation of multicomponent polymer systems with bioactive nanoparticles and on their performance during melt electrospinning. The study of the integration of multicomponent polymer systems with nanohydroxyapatite in the melt electrospinning platform is important because each selected component can play a specific role in improving the properties and final performance of the scaffold. Designing a multicomponent blend allows simultaneous adjustment of mechanical properties, wettability, porosity, and structural stability. At the same time, the presence of nanohydroxyapatite can enhance osteoconductivity and biological response by creating greater chemical and mineral similarity to natural bone. In addition, the choice of the melt electrospinning process, which eliminates organic solvents and reduces the risk of residual toxic residues, provides a safer, more reliable platform for the development of bone tissue engineering scaffolds. This research gap indicates that there is still a long way to go before developing more efficient and biocompatible systems for bone tissue engineering.

CHAPTER 3 OBJECTIVES

3.1 Motivation

Bone disorders, especially in relation to diseases such as osteoporosis and osteoarthritis, have become one of the most important clinical challenges in the world [233]. International statistics show the widespread prevalence of these diseases and the increasing trend of fractures caused by them in aging societies; a trend that imposes high medical and economic costs, making the need for the development of new and efficient solutions for bone regeneration more evident than ever [30, 59, 76]. Despite hundreds of thousands of bone grafts being performed annually and the significant growth of the orthopedic products market, the limitations of conventional methods such as autograft and allograft—including limited donor tissue source, pain at the site of harvest, risk of infection, and incomplete regeneration—as well as the limited efficacy of commercial alternatives, highlight the need for alternative strategies [233, 249].

In the meantime, tissue engineering, as an interdisciplinary approach, has offered a promising prospect for bone regeneration [86]. The goal of this approach is to design temporary 3D scaffolds that mimic the natural tissue microenvironment, providing a suitable substrate for cell penetration, adhesion, migration, and proliferation [62, 107, 232]. Such scaffolds should have high porosity and an interconnected structure for nutrient and gas exchange, mechanical properties tailored to loading conditions, and the ability to be degraded in a controlled manner without generating toxic byproducts [250].

Among scaffold fabrication methods, electrospinning has attracted widespread attention due to its ability to produce micro- and nanoscale fibers with high specific surface area and structural similarity to the extracellular matrix [251-254]. However, the dependence of solution electrospinning on organic solvents poses challenges, including residual solvent toxicity, limited polymer selection, and difficulty with industrial scalability [107]. In response to these limitations, melt electrospinning has been developed as an alternative approach that provides greater biosafety by eliminating solvents and allows better control of fiber geometry and scaffold structural stability [107].

Since each polymer has its own inherent advantages and disadvantages—some are biocompatible but lack sufficient mechanical strength, while others are robust but are poorly cell-compatible [12, 153]. The use of polymer blends and multicomponent systems is a logical approach to

simultaneously achieve the desired balance between rheological, mechanical, biological, and structural properties [12, 255, 256]. Despite extensive studies on multicomponent systems in solution electrospinning [255-258], the fabrication of multicomponent polymer composites, especially ternary systems, via melt electrospinning has remained underexplored [14, 47, 107]. Most existing research has focused on single- or at most two-component polymers, and the targeted use of three-component polymer scaffolds to simultaneously tune process behavior, mechanical properties, and biological response, especially in bone tissue engineering applications, has not been comprehensively studied [10, 14, 48]. Therefore, the design and investigation of targeted multicomponent systems for melt electrospinning are essential steps towards the development of high-performance scaffolds for bone regeneration. [11, 12, 14, 29, 47-50, 76, 86, 107, 189, 233] [250, 255]. This scientific gap has led to limitations in achieving the optimal balance among processability, structural stability, and biological performance of scaffolds. Accordingly, the present study, focusing on the design and development of engineered ternary polymer systems, seeks to provide a novel solution to simultaneously improve the structural and biological properties of bone scaffolds and fill this gap in the scientific literature.

3.2 Objectives

3.2.1 Main objective

The main objective of this PhD research is:

“To develop a melt electrospun scaffold from a ternary polymer blend with improved morphology and biological performance for bone tissue engineering applications”

Given its extensive scientific background, PCL has been chosen as the main polymer because it performs well in terms of biocompatibility, processability, and electrospinning ability, especially in the melt state. However, its strong hydrophobicity, slow degradation rate, and biological limitations highlight the need to improve its properties. For this purpose, two hydrophilic polymers, PEO and PEG, have been added to the system to improve wettability and cellular interaction, while also allowing control of the microstructure and porosity.

Furthermore, the addition of hydroxyapatite (nHA) nanoparticles as a bioactive mineral phase has two key functions: on the one hand, the presence of nHA opens up new avenues for investigating the melt electrospinning process in ternary nanocomposite systems; and on the other hand, it

significantly enhances the bioefficacy of the scaffold by enhancing osteogenesis induction, cell adhesion, and matrix mineralization.

To the best of our knowledge, this is the first study to produce and evaluate a ternary polymer system with an nHA mineral phase as a complete nanocomposite via melt electrospinning. Accordingly, the ultimate goal of this research is to achieve a PCL/PEO/PEG-nHA scaffold with a stable microstructure, tunable physical and biological properties, promising hydrophilicity, and performance in two fundamental criteria of osteogenesis and angiogenesis for use in bone tissue engineering.

3.2.2 Specific objectives

Considering the main objective the following specific objectives have been pursued:

1- To investigate the structural and physicochemical behavior of the ternary PCL/PEO/PEG system under the melt electrospinning process (Chapter 4)

Study the effect of the melt electrospinning process on the morphology, crystallinity, surface microstructure, and cross-section of fibers obtained from polycaprolactone in combination with polyethylene oxide and polyethylene glycol, comparison of the role of each hydrophilic component in creating porosity and fibrous structure, and preliminary evaluation of the cellular compatibility of ternary scaffolds as a potential substrate for bone applications. In the first paper of this work, the main results of the project's first specific objective are discussed. The paper was submitted to " Materials Today Communications" on March 9, 2026.

2- To develop and characterize PCL/PEO/PEG-hydroxyapatite nanocomposites obtained by melt electrospinning (Chapter 5)

Design and preparation of nanocomposite fibers based on the ternary PCL/PEO/PEG system containing hydroxyapatite nanoparticles, investigation of the distribution and persistence of nanoparticles within the fibers, analysis of thermal, morphological, and mechanical properties before and after immersion in an aqueous environment, and study of hydrolytic degradation behavior to achieve a suitable balance between structural stability and degradation rate. In the second paper of this work, the main results of the second specific objective of this project are discussed. This paper is submitted "Polymer Engineering & Science" on 30 December 2025.

3-To evaluate the physical, chemical, and biological properties of PCL/PEO/PEG-hydroxyapatite nanocomposite scaffolds for bone tissue engineering (Chapter 6)

Optimization of the masterbatch preparation route and percentage of hydroxyapatite nanoparticles in melt-electrospun ternary scaffolds, investigation of hydrophilicity, microstructure, and study of cellular response, including adhesion, metabolic activity, proliferation, and matrix mineralization by bone cells and endothelial cells, to introduce an optimal formulation with simultaneous potential to enhance osteogenesis and angiogenesis. The main results of the third specific objective of this project are discussed in the third paper of this work. This paper is submitted to "ACS Applied Bio Materials" on 15 January 2026.

CHAPTER 4 ARTICLE 1: MELT ELECTROSPINNING OF POLY (ε-CAPROLACTONE)/ POLYETHYLENE OXIDE / POLYETHYLENE GLYCOL BLEND: EFFECTS ON STRUCTURE AND CELLULAR COMPATIBILITY

Elham Karimi[a], Mansoureh Mohseni Garakani[b], Marie-Claude Heuzey[a], Frej Mighri[c], Derek H. Rosenzweig[b,d], Abdellah Ajji[a,*]

[a] Department of Chemical Engineering, Polytechnique Montréal, Montreal, Québec, H3T 1J4, Canada

[b] Department of Surgery, Division of Orthopaedic Surgery, McGill University, Montreal, Québec, H3G 1A4, Canada

[c] Department of Chemical Engineering, Laval University, Québec, Québec, G1V 0A6, Canada

[d] Department of Orthopedic Surgery, University of Connecticut School of Medicine, Farmington, Connecticut, 06032, USA

*Corresponding Author: abdellah.ajji@polymtl.ca

Submitted to Materials Today Communications, March 9, 2026

Authorship contribution statement of Elham Karimi: Conceptualization; Data curation; Formal analysis; Investigation; Methodology; Validation; Visualization; Writing – original draft; Writing – review and editing.

Abstract

This work aims to investigate the effects of the melt electrospinning process on the properties of ternary blend poly(ε-caprolactone)/ polyethylene oxide/polyethylene glycol (PCL/PEO/PEG) fibers. The utterly different morphology of the specimens before and after melt electrospinning acknowledges the significant effect of melt electrospinning on the sample's properties. However, it does not chemically alter the samples. The Scanning Electron Microscope (SEM) images showed that PEO and PEG behave differently in the PCL matrix, producing distinctly different morphologies in the respective binary blend fibers. Differences in morphology also lead to differences in the crystallization behavior of the specimen. Wide-angle X-ray diffraction (XRD) and differential scanning calorimetry (DSC) also reveal that although PEO and PEG are fundamentally the same polymer with different molecular weights, their behaviors in the PCL matrix are entirely different; PEG mostly remains in the amorphous state, while PEO can form its crystalline structure. Hence, the final morphology of the ternary melt electrospun fiber is a combination of the morphology of PCL/PEO and PCL/PEG binary blends. Preliminary biological

tests showed that the porosity created by the removal of the PEO and PEG hydrophilic phases improved fibroblast metabolic activity, highlighting the potential of this system for further investigation in bone tissue engineering applications.

Keywords: Melt electrospinning, Ternary blend, Biocompatibility, Molecular weight, PCL-based blend, Melt mixing

4.1 Introduction

Bone defects beyond the capacity of natural repair remain a major challenge in regenerative medicine [2]. Although conventional methods such as autograft and allograft are widely used, limitations such as resource scarcity, donor site complications, and risk of immune response highlight the need to develop alternative solutions [8]. In this regard, tissue-engineered scaffolds have emerged as one of the most promising approaches, especially when they can simultaneously mimic the hierarchical structure, appropriate porosity, and biological properties of bone tissue [8, 9].

Among synthetic polymers, poly(ε-caprolactone) (PCL) has been widely studied in biomedical applications due to its high biocompatibility, favorable processability, and good mechanical stability [4]. However, the hydrophobic nature, limited bioactivity, and especially the very slow degradation rate of this polymer limit its widespread application in tissue engineering, particularly in bone regeneration, which requires matching the scaffold's degradation rate to the tissue regeneration process[4, 44]. Therefore, the design of multicomponent systems and structural engineering through composition and process modification has been proposed as an effective solution to improve PCL performance [44].

One efficient approach in this field is the use of polymer blending with hydrophilic polymers, such as polyethylene oxide (PEO) and polyethylene glycol (PEG) [2, 44]. Despite their chemical similarity, these polymers could exhibit kinetic behaviors due to differences in molecular weight, leading to the formation of complex, controllable morphologies in multiphase systems [146, 259, 260]. In addition, these hydrophilic components can act as sacrificial phases and, upon removal, form porous intrafibrous structures that play a key role in improving cellular penetration, nutrient transport, and biological response of the scaffold [111].

In addition to the composition design, the process method also plays a decisive role in the scaffold's final structure. While solution electrospinning has been used in numerous investigations on polymer blends [261-263], melt electrospinning of blends has received much less attention. Melt electrospinning presents several key advantages over solution electrospinning, most notably its solvent-free nature, which eliminates the risk of residual toxicity and enriches the biocompatibility of the fabricated fibers [14]. This technique aligns with environmentally sustainable manufacturing approaches, avoids the need for post-processing phases such as solvent evaporation or drying, and significantly improves process safety. Due to these features, melt electrospinning is a scalable and appealing method for industrial and biological applications [14]. It is fundamental to study the properties of polymer blends during melt electrospinning, as there is limited information on this process, which limits morphology control.

In this study, for the first time, the behavior of a ternary PCL/PEO/PEG system in the melt electrospinning process has been systematically investigated; an approach that, beyond conventional studies based on single polymers or binary systems, allows for the design of multiphase structures with precise control. The main focus of this research is to elucidate the role of the molecular weight difference between PEO and PEG in the formation of morphology, crystal organization, and, ultimately, the biological response of the scaffolds. Also, the relationship between the resulting structural features and the initial biological performance, especially in improving cellular metabolic activity, has been evaluated. The results of this research pave the way for the design of engineered scaffolds with optimal performance in bone tissue engineering applications.

4.2 Materials and methods

4.2.1 Materials

The poly(ε-caprolactone) (PCL) Capa™ 6500 was obtained from Perstrop (Canada) with a mean molecular weight of 50000 g/mol in granular form. Polyethylene glycol (PEG) and Polyethylene oxide, with M_n 20000 and M_v 600000 g/mol in flakes and powder, respectively, were purchased from Sigma Aldrich, USA. Table 4.1 summarizes the glass transition (T_g), melting (T_m), and crystallization (T_c) temperatures of the neat polymers. Values are obtained from differential scanning calorimetry (DSC) under a nitrogen purge; T_g and T_m are extracted from the first-heating scan and T_c from the subsequent cooling scan (see Section 4.2.6 for conditions).

Table 4.1 Thermal properties of neat polymers: glass transition (T_g), melting (T_m), and crystallization (T_c) temperatures

Polymer	T_g [˚c]	T_m [˚c]	T_c [˚c]
PCL	-51.4 ± 0.7	63.9 ± 1.0	27.5 ± 0.3
PEO	-51.9 ± 1.7	69.3 ± 0.0	42.5 ± 1.6
PEG	-55.1 ± 2.0	69.1 ± 0.1	43.9 ± 1.9

4.2.2 Sample preparation

4.2.2.1 Melt blending

In this study, ternary blends consisting of PCL, PEO, and PEG were prepared with three different compositions to explore the effect of blend ratio on the final structure and properties. Specifically, blends with PCL/PEO/PEG with weight ratios of 90/5/5, 67/16.5/16.5, and 50/25/25 were initially prepared and evaluated. To better understand the individual contribution of each secondary polymer (PEO or PEG), corresponding binary blends of PCL/PEO and PCL/PEG were also studied, with ratios of 90/10, 75/25, and 50/50 (w/w). The tested compositions were determined using JMP Statistical Discovery software (version 18) and based on the Design of Experiments (DOE) approach to cover a wide range of component ratios and to investigate the effect of each component on the behavior of the system (details are provided in Figure S. 4.1 of Supporting Information). In this paper, the ternary blend with a composition of 67/16.5/16.5 (PCL/PEO/PEG) and the binary blends with compositions of 75/25 (PCL/PEO and PCL/PEG) were selected for detailed analysis. The selected compositions were chosen due to their balanced characteristics, representing a middle ground among the compositions studied. They avoid the issues observed in both lower and higher amounts of dispersed components, such as unclear morphology or excessively large cavities after dissolution. Furthermore, the X-ray diffraction (XRD), Fourier transform infrared (FTIR), and DSC results for these compositions exhibit appropriate peak intensities, making them the most suitable candidate for discussing the physicochemical properties of the ternary and respective binary blends and the subsequent melt electrospun samples.

To prepare the samples PCL, PEO, and PEG were dried at 40 ˚C in a vacuum oven overnight to avoid hydrolytic scission during melt processing [264]. Subsequently, 15.41 g of PCL was poured

into the Brabender-30 mL batch mixer (Plasticorder DDRV501, Brabender). The compounding was conducted at 70 ˚C using a screw speed of 50 rpm and beneath a nitrogen blanket. Next, the molten PCL was gradually mixed with 3.79 g PEO and 3.79 g PEG for 15 minutes under the same conditions to prepare the ternary blend. In preparing binary blends, 17.25 g of PCL was mixed with 5.75 g of PEO or PEG. Additionally, the neat polymers went into melt mixing before electrospinning for comparison purposes. The estimated average shear rate under the employed processing conditions is 25 s^{-1} [265]. After cooling the samples, they were cut into small pieces to prepare for the melt electrospinning process.

4.2.2.2 Melt electrospinning

The prepared specimens were used immediately after melt mixing for melt electrospinning to minimize any risk of morphology change. The blend was loaded into an 8-mL stainless steel syringe surrounded by a heating jacket. A cylindrical collector was linked to the positive electrode of the high-voltage power source, while the nozzle was secured to the ground wire. A schematic representation of the melt electrospinning apparatus utilized in the present study, highlighting its principal parts, is shown in Figure 4.1. The operation was started following one hour of heating and equilibrating at 150 ˚C. The results of time-sweep oscillatory tests showed that this heating step did not cause any signs of thermal degradation or reduced structural stability in the samples (Figure S. 4.2 of Supporting Information). The applied voltage was adjusted to 7.5 kV for the flow rate of 500 µL/h. The fibers were collected on a rotating cylinder collector at 20 rpm, 3 cm away from the 20G needle. The suffix BME in this paper stands for “before melt electrospinning”. AME refers to the samples “after melt electrospinning” or to the melt electrospun fibers. PEO seems to be too viscous in the molten state to be melt electrospun alone. Although PEG is melt electrospinnable, the final fibers are too fragile to be detached from the collector without breaking. On the other hand, PCL is readily electrospinnable, and the final fibers are flexible.

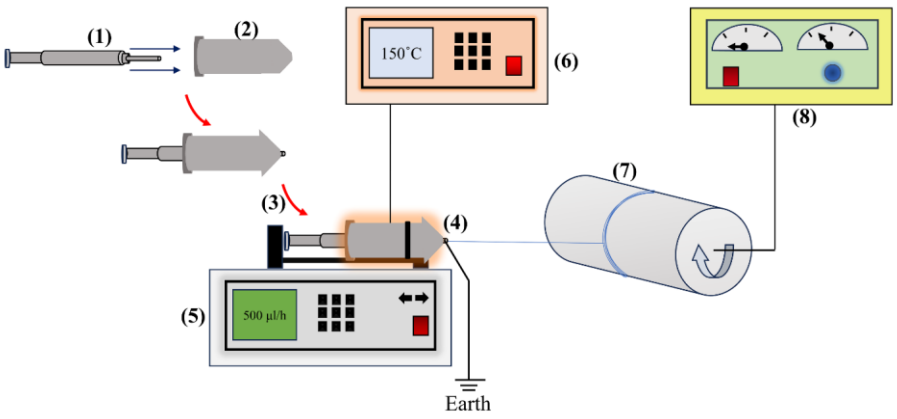

Figure 4.1 A schematic view of the melt electrospinning apparatus: (1) melt-blended sample loaded stainless steel syringe, (2) stainless steel heater, (3) the temperature-controlled syringe, equipped with an in-line heater, was secured to the syringe pump to ensure a consistent flow of the molten mixture, (4) needle, (5) pump, (6) temperature controller, (7) collector and (8) high voltage supplier.

4.2.3 Morphological analysis

To examine the morphology of the blends in the cross-section and surface of the samples before and after melt electrospinning, a Scanning Electron Microscope (SEM) (TM3030Plus, HITACHI) was used at a voltage of 15 kV. In order to prepare the samples, the melt electrospun fibers were immobilized into epoxy. Later, samples were microtomed using a Leica RM2165 fitted with a glass knife in a liquid nitrogen cryo-chamber. They were then immersed in water as an effective solvent for extracting PEO and/or PEG from the blends. PEO and PEG exhibit very similar solubility parameters ($\delta \approx 19–21$ $MPa^{1/2}$) due to their identical chemical backbone, which prevents selective dissolution of one component over the other in aqueous media [266-268]. Beyond a week of immersion, specimens were put under vacuum for two days to be thoroughly free of water. Finally, to better scan the PEO or/and PEG empty regions, the cross-section of the samples was coated with chromium of about 20 nm in thickness. To compare the morphology of the blends before and after melt electrospinning, blends were microtomed and soaked into water following the exact procedure employed for the fibers before the SEM test. The ImageJ software was then used to evaluate the pore size and mean fiber diameter.

The equivalent diameter of the footprints of the dispersion components after immersion in water, $D_{eq,i}$, is estimated through Equation 4.1 [269]:

$$D_{eq,i} = \sqrt{\frac{4 \times A_i}{\pi}} \tag{4.1}$$

where A_i is the measured domain area.

4.2.4 Fourier transform infrared (FTIR)

A PerkinElmer spectrometer (Waltham, MA, USA) was used to run a Fourier transform infrared (FTIR) test in Attenuated Total Reflection (ATR) mode at room temperature, with a wavenumber ranging from 600 to 4000 cm^{-1}, using 16 scans, with a nominal resolution of 4 cm^{-1}. In order to mitigate experimental errors, the test was conducted thrice, and the mean values were recorded.

4.2.5 X-ray diffraction (XRD)

The crystalline structure of the specimens was assessed employing an Empyrean diffractometer (Malvern Panalytical) with Cu Ka radiation generated at 45 kV and 40 mA, a 2θ spectrum of 3˚-60˚ with a 0.0131˚ step size. This test was performed to identify crystalline and amorphous phases and evaluate the structural order of the samples, thereby providing an accurate examination of the crystallinity characteristics and phase structure of polymer systems in the binary and ternary samples.

4.2.6 Thermal properties

The thermal and crystallization behavior of neat polymers, binary, and ternary blends was probed by DSC (Q1000, TA Instruments, New Castle, DE, USA). An aluminum pan and lid were used to encapsulate five to ten milligrams of the samples. The samples were subjected to the following procedure under a nitrogen atmosphere (50 mL/min):

- Starting point= -90 ˚C
- Heating rate=10 ˚C/min
- End point= 150 ˚C
- Equilibrium
- Cooling to -90 ˚C with the same ramp
- Heating to 150 ˚C with the same ramp

The crystallinity percentage, X_C, of the specimens was determined using Equation 4.2 [270]:

$$X_c = \frac{\Delta H_m}{\omega \times \Delta H_m^0} \times 100 \quad (4.2)$$

Where ω represents the mass fraction of the polymer, the experimental melting enthalpy of a fraction, ΔH_m, is determined as the area under the melting peak. ΔH_m^0 is the specific melting enthalpy of a fully crystalline polymer, which is 139.5 $J.g^{-1}$ [271], 205 $J.g^{-1}$ [272], and 197.7 $J.g^{-1}$ [125], for PCL, PEO, and PEG, respectively.

4.2.7 In Vitro Biological Evaluation

4.2.7.1 Cell Culture and Scaffold Seeding

Passage 3 of IMR-90 mCherry fibroblasts expressing red fluorescent protein (RFP) were cultured in high-glucose Dulbecco's Modified Eagle Medium (DMEM) supplemented with 10% fetal bovine serum (FBS) and 1% penicillin-streptomycin (PS) (all sourced from Gibco, Thermo Fisher) as previously described [273]. The cells were cultured in T75 culture flasks (Sarstedt, TC Flask T75, Stand, Vent. Cap, Germany) and maintained at 37 ˚C in a humidified atmosphere containing 5% CO_2, following previously established protocols [273].

When the cells reached 90% confluence, they were first washed with 3 mL sterile phosphate-buffered saline solution (PBS) (Gibco, Thermo Fisher, USA), then detached with 0.25% trypsin (Gibco, Thermo Fisher, USA). Fresh DMEM medium containing 10% FBS and 1% PS was immediately added, and the suspended cells were centrifuged for 5 minutes at 1500 rpm. The obtained fibroblast cell pellet was resuspended in 3 mL of fresh complete medium (DMEM supplemented with 10% FBS and 1% PS), counted using a hemocytometer, and adjusted to a cell concentration of 2.5×10^5 cells/mL to seed on the scaffolds.

The scaffolds prepared by melt electrospinning were precisely punched into 9 mm diameter disks. Next, the scaffolds, which had previously been placed in deionized water for a week, were sterilized under ultraviolet radiation for 15 minutes. Afterwards, scaffolds were sterilized in DMEM containing 1% antibiotics (PS) to remove any contamination and then placed in each well of a 48-well non-adherent cell culture plate (SARSTEDT AG & Co.). Subsequently, 200 µL of fibroblast cell suspension (containing 50,000 cells per scaffold) was added to each well and incubated for 24 h under humidified conditions and 5% CO_2 atmosphere.

To ensure that only cells attached to the melt electrospun scaffolds were examined, the scaffolds were transferred to new plates with fresh media one day after cell seeding. Then, the scaffolds were maintained under standard culture conditions for 1, 3, 7, 14, 21, and 28 days, and the medium was changed every 3 days.

4.2.7.2 Metabolic Activity Measurement (Alamar Blue Assay)

Alamar Blue assay (Invitrogen, USA) was performed to determine the cellular metabolic activity. At designated intervals, the growth medium was substituted with the fresh DMEM high-glucose medium containing 10% (v/v) Alamar Blue reagent [273]. 200 µL of assay solution was added to each scaffold in 48-well plates, and the scaffolds were incubated for two hours at 37 ˚C in a humidified atmosphere containing 5% CO_2.

After the incubation period, 100 µL of the liquid from each well was transferred to 96-well black half-area plates (Corning). Fluorescence intensity was quantified using a Tecan Infinite M200 Pro microplate reader (Tecan Trading, AG) with excitation and emission wavelengths set to 540 nm and 585 nm, respectively.

To eliminate background fluorescence, two types of controls (blank) were considered: (i) scaffolds without cells and (ii) test solution (DMEM containing 10% Alamar Blue) without contact with cells or scaffolds. Data obtained from the controls were subtracted from the sample signals. All experiments were performed in at least three independent replicates ($n \geq 3$) for each condition and time, and the results are reported as mean ± standard deviation (Mean ± SD).

4.2.7.3 Preparation of Cell-Seeded Scaffolds for SEM Observation

On day 28, the fibroblast-cultured melt electrospun scaffolds were gently washed with PBS (pH 7.4) to remove non-adherent fibroblast and residual culture medium. The samples were then fixed with a freshly prepared 4% paraformaldehyde (PFA, methanol-free, Thermo scientific, USA) solution for 20 minutes at ambient conditions. After removal of the fixative solution, they were washed three times with PBS to obliterate residual fixative and then dehydrated through a graded ethanol series (30%, 50%, 70%, 90%, and 100%), each for 5 min [274]. The dehydrated samples were subsequently air-dried in a desiccator before observation under a scanning electron microscope (Hitachi TM3030Plus, Japan) at an accelerating voltage of 15 kV.

4.2.8 Statistical analysis

Statistical analysis of data was performed using GraphPad Prism software version 10. A two-way ANOVA was used to examine group differences, and post hoc comparisons were performed with Tukey's test. Results were reported as mean ± standard deviation (Mean ± SD). The class of statistical significance in all analyses was determined as $p < 0.05$; $p < 0.01$ and $p < 0.001$, indicating low, moderate, and very high levels of statistical significance, respectively, and thus increasing the level of confidence in the observed differences. All experiments were performed with at least three independent replicates to ensure reproducibility and reliability of the results.

4.3 Results

4.3.1 Morphological properties

The SEM micrographs of binary and ternary blends (PCL/PEG, PCL/PEO, and PCL/PEO/PEG) are presented in Figure *4.2* (before melt electrospinning, BME), Figure 4.3 (after melt electrospinning, AME; fiber surfaces), and Figure 4.4 (AME; fiber cross-sections). Note that the scanned morphology is representative of the particular processing technique used in this investigation (i.e., Brabender). While the current results provide a consistent picture under these conditions, the impact of alternative processing methods on the final morphology is currently being explored. It will be the subject of our future studies.

The morphologies of the blends before melt electrospinning are shown in Figures 4.2A-C, while the corresponding microfibers produced by melt electrospinning are depicted in Figures 4.3 A, C, and E. Distributions of dispersed-domain diameters (expressed as pore area fraction) are provided in Figures 4.2D-F for the samples before the melt electrospinning and in the Figures 4.3B, D, and F for the melt electrospun samples. Note that Figure 4.3B does not include diameter data for the dispersed domains. In the PCL/PEG (75/25)-AME sample, the PEG, as the dispersed component, does not form spherical domains. In the PCL/PEG-AME sample, the dispersed PEG phase forms fibrils aligned along the longitudinal axis of the melt electrospun fibers. The binary and ternary blends and their fibers do not show pores on the surface or cross-section before soaking the samples in water. However, the immersion of binary and ternary blend samples into water led to the appearance of pores in the specimens (Figures 4.2A-C, Figures 4.3A, C, and E, and Figures 4.4A, C, and E).

In PCL/PEG-BME and PCL/PEO-BME blends, PEG and PEO form a Drop-in-Matrix structure in the samples (Figure 4.2A, B). Considering the pore-size distribution plots (Figures 4.2D-E), the domains of PEO (~4.2 ± 1.6 μm) compared to PEG (~2.8 ± 0.8 μm) are slightly larger, which may reflect differences in molecular weight and crystallization kinetics. PEO is expected to exhibit a high melt viscosity and elasticity, which intrinsically restricts its chain mobility because of its very high molecular weight (~600,000 g/mol). Hence, it tends to remain poorly dispersed in the PCL, creating large, well-defined domains.

The ternary blend-BME sample consists of two different sizes of dispersed phases (Figure 4.2C). The large pores, with a mean diameter of 60 ± 0.1 μm, could be attributed to the PEO-rich domains, and the tiny pores, with a mean diameter of 0.3 ± 0.0 μm, could be the footprints of PEG-rich domains. The reason for the distinct domain sizes in the ternary blend compared to the binary blends is probably the assumption that the different molecular weights of PEO and PEG influence the complex interplay of phase separation and crystallization processes. The impact of molecular weight on the liquid-liquid phase separation and miscibility of different polymers was reported before [275, 276]. PEO and PEG, as the polymer's high and low molecular weights, introduce a complex interaction to the system. The high molecular weight PEO tends to form larger domains due to its slower diffusion. Simultaneously, the low molecular weight PEG, being more mobile, might be squeezed into smaller regions, resulting in smaller domains.

PCL/PEG (75/25)	PCL/PEO (75/25)	PCL/PEG/PEO (67/16.5/16.5)

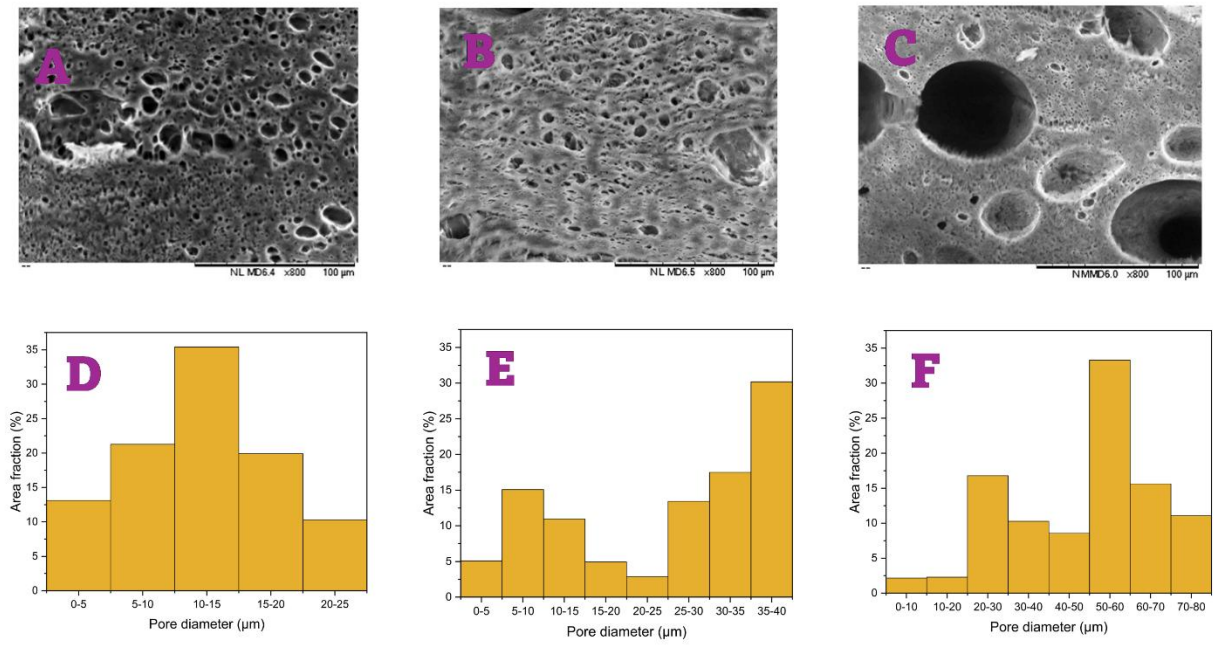

Figure 4.2 Morphology of (A)PCL/PEG (75/25)-BME, (B) PCL/PEO (75/25)-BME and (C) PCL/PEO/PEG (67/16.5/16.5)-BME samples (After mixing in the Brabender) with (D–F) corresponding area-weighted domain-size distributions quantified from the respective micrographs.

The average fiber diameter of PCL fibers decreases from 43.6 ± 0.5μm to 39.4 ± 1 μm when PEG is added to the sample (Figure 4.3A). This could be because adding PEG decreases the melt viscosity due to its low molecular weight, which acts like a plasticizer in the system. On the other hand, the addition of PEO to the system increases markedly the average fiber diameter to 116.4 ± 24.8 μm (Figure 4.3C). This observation emphasizes the importance of molecular weight and its impact on the sample's viscosity, which can significantly change the fiber diameter. The same statement for different systems was reported before [277]. Because of its low molecular weight, PEG can be stretched easily during electrospinning and form a fibril shape, all aligned in the direction of the applied stretching force caused by the electrical charge difference applied between the needle and the collector. In order to illustrate the traces of PEG "fibrils" after dissolving in water, a high-magnification inset is used in the left corner of Figure 4.3A (scale bars: main 100 μm; inset 30 μm). It illustrates the homogeneous creation of fibrils of the PEG in the PCL matrix. The imposed stretching triggers the PEG-rich domains to be thinner. The tiny pores on the cross-

section of the fibers (Figure 4.4A) show the cross-section of PEG fibrils trapped in the PCL matrix. The lack of pore on the fiber's surface confirms the alignment of the PEG fibrils in the direction of imposed tension (Figure 4.3A).

Unlike PCL/PEG-AME, in the PCL/PEO-AME, PEO domains in the PCL (Figures 4.3C and 4.4C) create a sea-island phase morphology [278]. The sea-island morphology is analogous to the droplet-matrix morphology, though there is a critical difference in the scale and distribution. The "islands" describe the dispersed PEO phase embedded within the "sea," PCL, the continuous matrix phase. The islands are usually more extensive and less uniformly shaped compared to the droplets in droplet-matrix morphology [279]. This is why large pores are observed in PEO-containing binary (Figures 4.3C and 4.4C) and ternary mixtures (Figures 4.3E and 4.4E). The formation of sea-island morphology for the PCL/PEO system was reported before where the sea-island morphology was defined as when the PEO spherulite exclusively develops near the PCL phase borders during the cooling step, like water streaming around pebbles and engulfing them inside [279]. There are signs of the simultaneous presence of PEO and PEG on the ternary blend melt electrospun samples (Figures 4.3E and 4.4E). In the fiber structure of the ternary blend, fibrils are observed that are slightly shorter than those formed in the PCL/PEG-AME sample and are scattered on the surface and interior of the fibers. The authors believe that this feature reflects the role of PEG in the system. In addition, the presence of large, connected, and open pores on the surface and cross-section of the fibers, according to the authors, indicates the effect of PEO in creating structural porosity in this blend. These observations were also confirmed by hot-stage microscopic analysis (Supplementary Information). The results showed that PEG is distributed as dispersed droplets within the PCL matrix, while PEO undergoes coarsening at the processing temperature and forms distinct morphologies. Also, the examination of the PEO/PEG binary sample clearly showed that under the applied mixing conditions, these two polymers form distinct phases. This behavior is also repeated in the ternary system, indicating the simultaneous presence of both types of morphologies, such that PEO is observed as island structures and PEG as dispersed droplets within the PCL matrix. The creation of two separate domains of PEO and PEG in a blend was previously reported by Soo et al. [280]. They explained that this phase separation is due to the significant differences in molecular weight between PEO and PEG, which disrupt uniform crystallization and result in distinct crystallite domains, even though the two polymers share similar chemical structures. However, it is important to note that the miscibility of PEO and PEG

strongly depends on factors such as their initial concentrations, the ratio of PEO to PEG in the system, the difference between their molecular weights, and the employed blending method [260, 275, 281].

One limitation of the current work is that the morphology is characterized for specimens fabricated through Brabender. Given that polymer blend morphology can be sensitive to processing parameters, further studies are planned to investigate whether and how various blending approaches might affect phase distribution and domain formation.

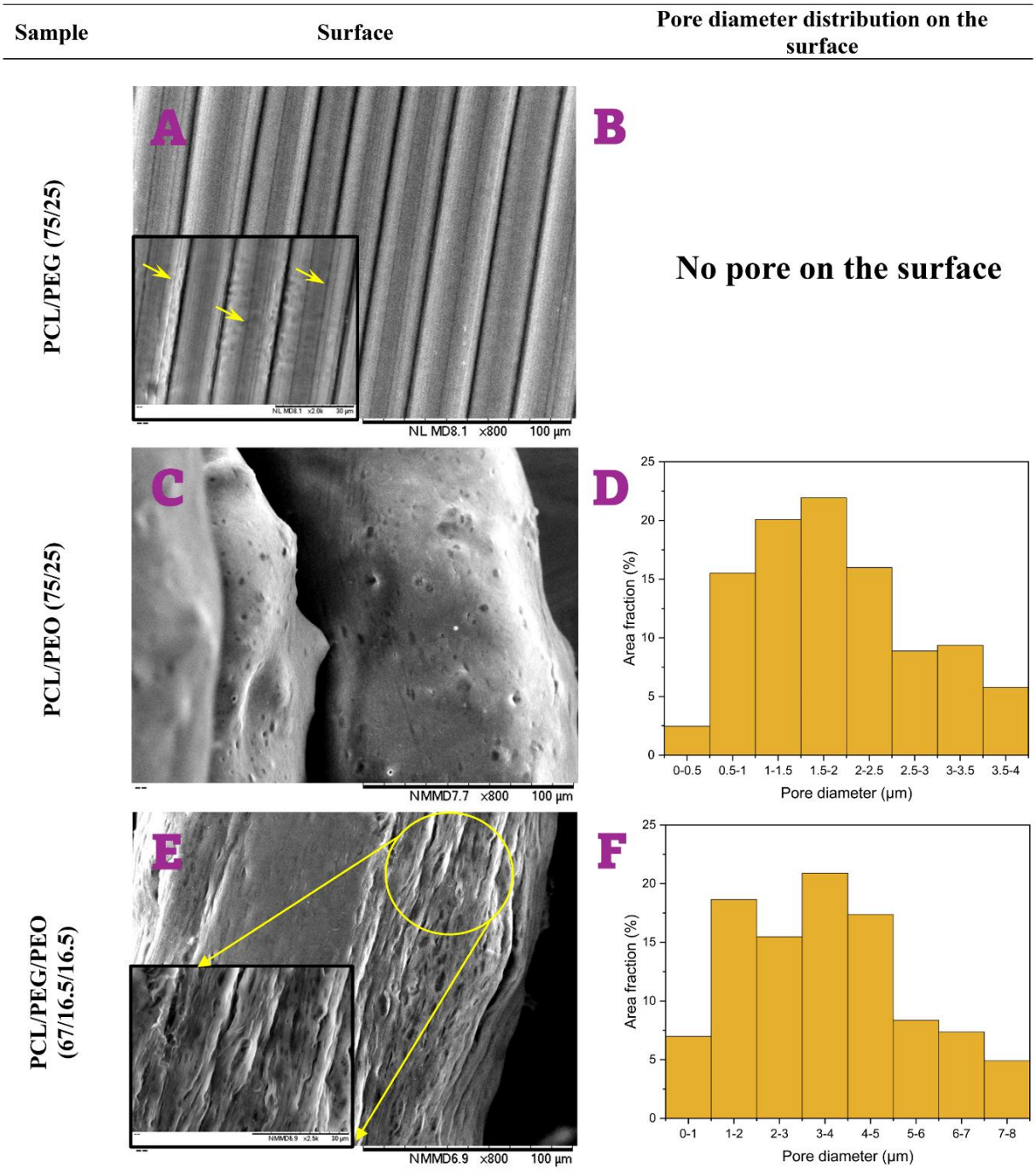

Figure 4.3 Surface SEM micrographs of melt-electrospun fibers: (A) PCL/PEG (75/25), (C) PCL/PEO (75/25), and (E) PCL/PEO/PEG (67/16.5/16.5). Quantitative pore-size distribution plots extracted from the corresponding images are provided in (B, D, F). The inset in (A) (30 µm scale)

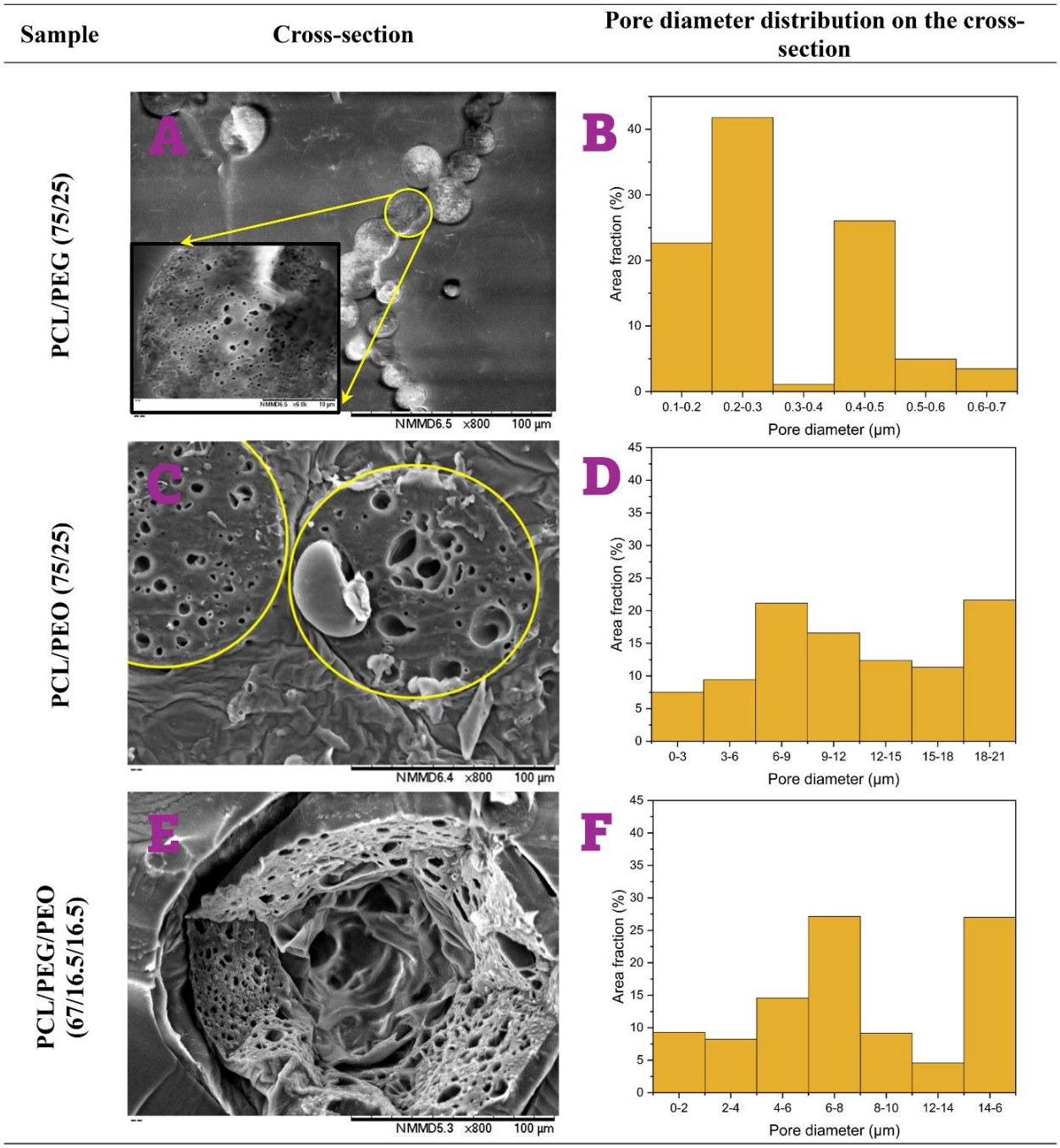

Figure 4.4 Cross-sectional SEM morphology of melt-electrospun fibers: (A) PCL/PEG (75/25), (C) PCL/PEO (75/25), and (E) PCL/PEO/PEG (67/16.5/16.5). The corresponding area-weighted pore-size distribution plots are shown in (B, D, F). The inset in (A) (10 µm scale)

4.3.2 Structural and chemical characteristics

Figure 4.5A presents the FTIR spectra of all the samples before and after melt electrospinning. Measurements were conducted at ambient conditions with no additional thermal treatment, allowing a direct comparison of chemical fingerprints between the pre-electrospinning blends and the as-spun fibers. The samples before melt electrospinning show higher intensities than the melt electrospun fibers. This is owing to the higher thickness of samples before melt electrospinning than the fine and distinct melt electrospun fibers. Besides, it is worth mentioning that the characteristic peaks that emerged for specimens before and after melt electrospinning are entirely duplicates. Peaks of neat polymers can be distinguished in the blend samples, with no evidence of additional peaks or shifts, confirming no presence of intermolecular interactions. This result confirmed also that there is no chemical interaction between PCL and PEO or PEG nor degradation. The study by Nguyen Tri et al. [278] in the PCL/PEG (50/50) system also reported no chemical interactions between the blend components. Yet, minor physical interactions between the phases in that system were suggested. Nevertheless, in the current study, no such changes were observed, which could be attributed to differences in process conditions or the sensitivity of the test methods [278, 282]. The FTIR spectra of PEO and PEG are identical as they are the same polymers with different molecular weights.

Figure 4.5B depicts the XRD patterns recorded under ambient conditions for neat PCL-AME, PEO-BME, PEG-BME, and their binary-AME and ternary-AME blends. Considering the fact that PEO and PEG are identical polymers with different molecular weights, their characteristic peaks are the same and determined at 2θ of 18.9˚ and 23.3˚ [283, 284]. Signals correlated with PCL orthorhombic crystal construction, peaks (110) and (200) emerged at 21.2 ˚ and 23.3 ˚, respectively, and the latter overlaid with the PEO or PEG [283-285]).

The comparison of XRD patterns between melt electrospun fibers of PCL and PCL/PEG reveals the disappearance of PEG's characteristic peaks in the binary blend, suggesting that PEG either remained in an amorphous phase or formed crystalline domains too small or disordered to be detected by XRD.

In the PCL/PEO sample (Figure 4.5B), it is indicative of the ability of PEO domains to crystallize and form independent crystal structures. Due to the high molecular weight of PEO, the melt viscosity increases, limiting the ability to stretch and flow the chains during melt electrospinning; as a result, under the same process conditions, fibers with larger diameters are formed (Figures

4.3A and 4.4A). This increase in fiber diameter reduces the cooling rate, providing sufficient time for PEO chains to organize and form crystals. As a result, the presence of PEO crystal peaks in the XRD pattern of the PCL/PEO binary sample is expected and justified. Also, the difference in crystallization behavior between PEO and PEG has been confirmed by hot-stage microscopic observations (Supplementary Information).

The characteristic peak of PEO ($2\theta = 18.9^{\circ}$) is observed in the ternary melt electrospun fibers. The shorter peak of PEO in the ternary blend fibers, PCL/PEO/PEG-AME, compared with the neat PEO-BME, can be attributed to less PEO in the ternary blend fiber. The total amount of PEO and PEG in the ternary blend, 33wt% (16.5wt% PEO and 16.5wt% PEG) is higher than the amount of PEO, 25wt%, in PCL/PEO (75/25)-AME and the amount of PEG, 25wt%, in PCL/PEG(75/25)-AME; if the PEO and PEG were miscible with the same peaks, they would have shown a sharper peak in PCL/PEO/PEG (67/16.5/16.5) fibers. In line with the SEM results, in the PCL/PEO/PEG-AME sample (Figures 4.3E and 4.4E), the simultaneous presence of features attributed to PEG and PEO is clearly discernible. PEG, by creating surface grooves and fine pores in the fiber cross-section, and PEO, by forming large, interconnected pores, a sea-island morphology in the cross-section, and surface porosity, all play a role in the formation of the final structure. This distinct behavior is attributed to the formation of distinct domains for PEO and PEG, and to differences in their behavior during cooling, as confirmed by hot-stage microscopic observations (Supplementary Information). Based on hot-stage microscopy, the crystallization sequence in the ternary PCL/PEO/PEG-AME system is PEO first, then PCL with a slight delay, while PEG is in the final stage and remains mainly in the amorphous state. This behavior is intensified under the rapid-cooling conditions of the melt electrospinning process, leading to the dominance of the amorphous phase within the PEG domains.

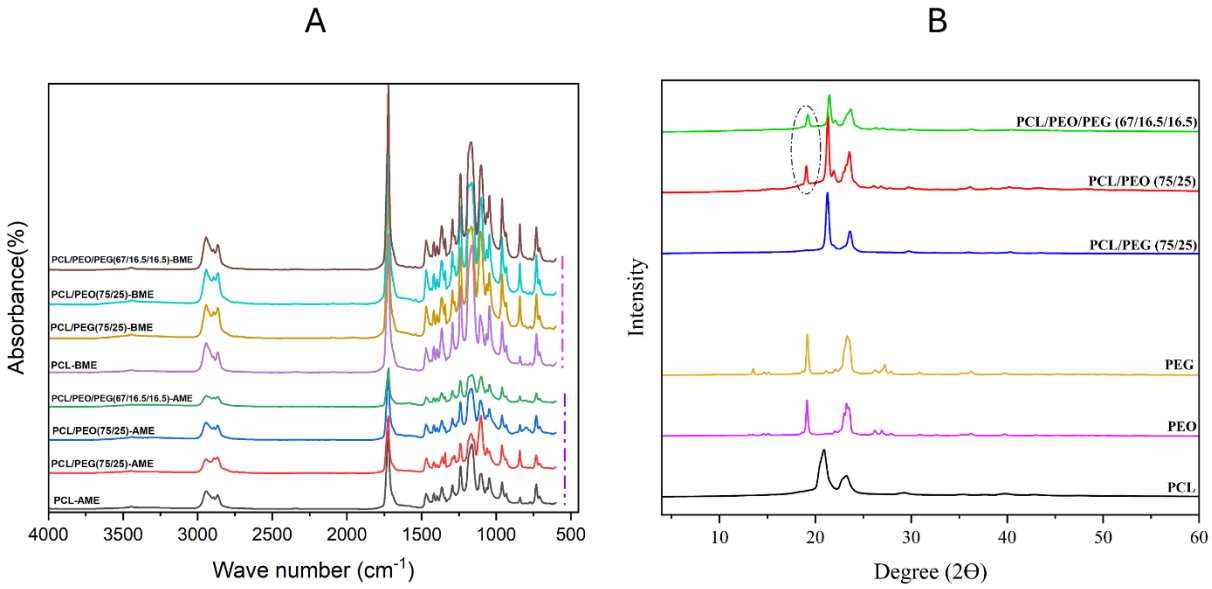

Figure 4.5 (A) FTIR spectrum for samples before and after melt electrospinning and (B) XRD pattern of neat polymers and their binary and ternary blends.

4.3.3 Thermal properties

Table 4.2 summarizes the thermal indices obtained from DSC results of the first heating cycle and cooling run of the samples before (BME) and after (AME) the melt-electrospinning process. In Table 4.2, the changes in crystallization enthalpy (ΔH_C), melting temperature (T_m), crystallization temperature (T_c), and crystallinity percentage (X_C) are reported for each polymer component, allowing for the evaluation of the effect of composition and electrospinning process on the thermal behavior. All the samples show one T_g (Table 4.2). On the condition that a sample shows one single glass transition, the components are miscible in the molten state. However, in this study, it could be because of the closeness of the components' glass transition temperatures (Table 4.1). So, distinguishing their T_g would be impossible using DSC.

Table 4.2 Thermal properties of the samples before (BME) and after (AME) the melt electrospinning

Property	Component	PCL/PEO-BME	PCL/PEG-BME	PCL/PEO/PEG-BME	PCL/PEO-AME	PCL/PEG-AME	PCL/PEO/PEG-AME
T_C [I] [˚c]	PCL	31.3 ± 0.7	29.4 ± 0.4	32.3 ± 1.5	35.8 ± 1.8	30.5 ± 0.9	29.9 ± 0.4
	PEO	45.8 ± 0.8	-	44.8 ± 1.4	42.4 ± 1.8	-	44.8 ± 0.6
	PEG	-	0.9 ± 0.1, 44.4 ± 1.5	-0.7 ± 0.2	-	-1.3 ± 0.1	1.3 ± 0.1
ΔH_C [I] [J/g]	PCL	33.0 ± 0.9	53.4 ± 0.5	34.1 ± 0.9	32.7 ± 0.5	32.9 ± 0.7	29.5 ± 1.1
	PEO	20.7 ± 1.4	-	20.8 ± 0.8	6.0 ± 0.0	-	25.3 ± 1.0
	PEG	-	9.5 ± 0.0, 8.8 ± 0.1	1.0 ± 0.0		19.9 ± 0.2	3.0 ± 0.0
T_m [II] [˚c]	PCL	60.9 ± 0.1	61.6 ± 1.1	62.1 ± 1.3	59.9 ± 0.2	60 ± 0.8	58.3 ± 0.4
	PEO	66.1 ± 0.0	-	66.9 ± 1.8	63.3 ± 0.0	-	64.3 ± 1.0
	PEG	-	65.4 ± 1.3	-	-	63.1 ± 0.1	-
X_C [II, III] [%]	PCL	33.3 ± 1.3	50.1 ± 0.5	54.1 ± 1.0	63.8 ± 0.9	70.7 ± 0.6	50.1 ± 1.2
	PEO	35.3 ± 0.8	-	48.0 ± 1.0	44.1 ± 1.1	-	40.0 ± 2.0
	PEG	-	31.5 ± 0.6	-	-	-	-
T_g [II] [˚c]	Blend	-50.2 ± 1.3	-49.3 ± 1.5	-50.9 ± 1.5	-50.2 ± 3.4	-51.7 ± 1.9	-52.9 ± 1.6

[I] Data is obtained from the cooling cycle.
[II] Data is obtained from the first heating cycle.
[III] Crystallinity percentage, X_C, is calculated using Equation 4.2.

DSC shows one melting point (Table 4.2) for PCL/PEG-AME, PCL's melting point for PCL/PEG fiber. This observation could be because of the remaining PEG in the amorphous phase due to rapid solidification during the melt electrospinning. However, it is worth noting that a subtle deviation from the main melting peak of PCL is detected in the first heating cycle (Supporting information), such that a slight shoulder arises on the typical melting peak of PCL. Although this feature is not well-defined as an independent melting peak, it may suggest the existence of a slight portion of PEG chains trapped within the PCL matrix, which could have experienced limited crystallization during the cooling step. This hypothesis is further supported by the distinct crystallization signal observed at approximately 1 ˚C during the cooling scan (Table 4.2). This phenomenon has also been reported in several studies [286-288]. For instance, Luo et al. [287] reported a similar low-temperature crystallization peak in PCL/PEG systems, which they attributed to the construction of microcrystalline domains by PEG chains that remained confined within the

PCL matrix. Their analysis confirmed that these crystals are remarkedly small, consistent with limited phase separation of PEG during solidification while the larger portion of PEG, phase separated from PCL. These findings further support the hypothesis that the minor crystallization peak detected at ~1 ˚C (Table 4.2) may originate from trapped PEG chains within the PCL phase. Furthermore, it implies that the larger portion of PEG forming fibrils in the system remains in the amorphous phase, as indicated by the comparison between the original amount of PEG in the system and the minor enthalpy of this peak. This interpretation is further supported by the absence of any characteristic PEG diffraction peaks in the XRD pattern (Figure 4.5B) in addition to the lack of a distinct melting point for the PEG in the first heating cycle of DSC (Table 4.2).

On the other hand, the same sample exhibits two melting points before being processed through melt electrospinning (Table 4.2). It suggests that some PEG chains in the PCL/PEG-BME sample may remain trapped within the PCL matrix, as evidenced by the emergence of a crystallization peak near 1 ˚C (Table 4.2). The other part of PEG is speculated to be repelled out of the PCL, forming independent PEG domains, as evidenced by the appearance of a broad crystallization peak at 37 ˚C and ending at 51 ˚C.

The DSC curve of the ternary blend exhibits two melting points for both samples before and after melt electrospinning (Table 4.2). To elucidate the behavior of the ternary blend, it is helpful to understand the crystallization characteristics of the samples by studying the cooling cycle of DSC analysis. The neat polymers indicate well-defined and distinct crystallization patterns (Table 4.1), mirroring their inherent thermal properties. For instance, PEO and PEG crystallize at the same temperature (Table 4.1); nonetheless, with its lower molecular weight, PEG demonstrates a much sharper crystallinity peak. This is explained by the shorter PEG polymer chains, which facilitate quicker and more effective crystallization. In contrast, with its higher molecular weight, PEO has longer, more entangled chains, resulting in slower crystallization and a broader peak (Table 4.2).

The cooling curve for the PCL/PEO-AME blend (Table 4.2) suggests that melt electrospinning does not disrupt the construction of crystalline networks for PEO and PCL. This could be attributed to the high molecular weight of PEO, which may lead to the melt exhibiting significantly high viscosity, thereby restricting the chain mobility during processing. As a result, PEO lacks sufficient stretchability under the applied shear conditions, resulting in the formation of discrete, island-like domains within the system (Figure 4.3C, and Figure 4.4C). Given the relatively large size and

PEO-rich nature of these islands, they readily crystallize upon cooling, as evidenced by the distinct crystallization behavior observed in the DSC cooling curve.

In the PCL/PEO/PEG-BME blend, a small portion of PEG remains in the PCL and form microcrystalline structure. This claim can be proved by the relatively insignificant peak around -1 ˚C (Table 4.2). The crystallization peak at 44 ˚C in PCL/PEO/PEG-BME likely conveys crystallization of the PEO-rich domain. Although the miscibility of PEO and PEG is possible, considering the XRD (Figure 4.5B) and DSC (Table 4.2) data obtained after melt electrospinning it is less probable. The cooling curve of PCL/PEO/PEG-AME (Table 4.2) shows that a portion of PEG remains within the PCL matrix, which conflicts with the hypothesis of PEO and PEG forming one uniform phase under these conditions. Considering that in the PCL/PEO-BME and PCL/PEO-AME, there is no sign of trapping PEO chains in the PCL, the attribution of the crystallization peak at around 1 ˚C to the PEO phase does not seem correct. The PCL/PEO/PEG-AME system exhibits a crystallization peak at around 1 ˚C in addition to the PCL and PEO crystallization peaks, which are seen at about 30 ˚C and 45 ˚C, respectively. This peak may be attributed to the crystallization of the small fraction of the PEG chains that are partially trapped within the PCL matrix.

The PCL/PEO/PEG-BME is the feed for the melt electrospinning for PCL/PEO/PEG-AME fabrication. On the condition that PEG was miscible with PEO in PCL/PEO/PEG-BME, the cooling curve of PCL/PEO/PEG-AME would not display a separate crystallization peak around 1 ˚C, suggesting that PEG chains are trapped within the PCL. This statement underlines that, despite the chemical resemblance between PEO and PEG, their notable difference in molecular weight leads to distinctive behaviors in the blend, forming separate domains and crystalline configurations. Regarding the first heating cycle of PCL/PEO/PEG-BME, there are two melting points for the ternary blend, which means PEG mostly remains in the amorphous phase. In the PCL/PEO/PEG-BME specimen, the relatively slow cooling rate allows PEG chains to phase-separate from the PCL matrix and construct larger PEG-rich domains. However, despite this longer timeframe, PEG stays in the amorphous phase, as no distinct melting peak arises for PEG. This suggests that instead of crystallizing, the PEG chains use the available time to segregate and enlarge their domains. Furthermore, the existence of PEO-rich domains may potentially hinder the crystallization of PEG since PEG chains could become entangled with PEO, thereby limiting their capacity to reorganize into a crystalline form. In addition, as both PCL and PEO are most likely to

start crystallizing earlier than PEG, they may suppress the heterogeneous nucleation of PEG. It is also plausible that PEO occupies interfacial boundaries and, together with the earlier crystallization of PCL, reduces the spatial and dynamic chances required for PEG crystallization.

However, in PCL/PEO/PEG-AME, due to the fast solidification, most parts of PEG chains remain in the PCL phase. This can be explained by considering the more pronounced crystallinity peak of the PEG chains trapped in the PCL phase, the emerged peak at approximately 1 ˚C [287] in PCL/PEO/PEG-AME rather than PCL/PEO/PEG-BME. Those chains that had the chance to go out of PCL form tiny PEG domains, which, because of the fast solidification, never have sufficient time to complete their crystalline structure.

4.3.4 Cellular Metabolic Activity and Viability Assessment

To evaluate the initial cellular compatibility of melt electrospun scaffolds, the Alamar Blue assay was performed to quantify the metabolic activity of cultured fibroblasts on different samples (Figure 4.6A). The SEM of cell-seeded PCL and ternary blend fibers after 28 days of culturing is shown in Figures. 4.6 B and C. The Alamar Blue assay indicates the initial response to the samples' surface and morphology. The results show that, across all groups, fibroblast cell metabolic activity increases in a time-dependent manner, indicating overall compatibility with the scaffold and the absence of toxic effects. However, the signal intensity in the scaffolds coming from binary and ternary blends is significantly higher than that of the neat PCL sample (Figure 4.6A). This increase cannot be attributed solely to increased cell numbers; rather, it most likely reflects improvements in physiological status, spatial penetration, and the dynamic interactions of cells with the open scaffold network. The results of relative metabolic activity, obtained by dividing the Alamar Blue test data by the corresponding PCL values at each time interval, are presented in Figure S. 4.3 of Supporting Information.

Since the scaffolds were placed in water for a week before cell seeding, the PEO and PEG phases are mostly dissolved (Figures 4.3 and 4.4), yielding a structure with interconnected intrafibrous porosity. SEM observations (Figures 4.3 and 4.4) clearly show that after this stage, the fiber surface transitioned from a dense to a porous state. Such a morphological transformation, similar to that reported for multiphase electrospun scaffolds, increases the effective contact area, facilitates nutrient and oxygen exchange, and forms three-dimensional microenvironments for cell adhesion and survival [289-291].

This finding aligns with the report by Giacaman et al. [291] on PCL-b-PEG/PCL mats, which identified enhanced porosity and permeability as critical factors for fibroblast migration and metabolic stability. Also, Xia et al.,[289] in their study of PCL/nHA/PEG hybrid scaffolds, provided a multiscale porous environment that led to a significant increase in cell density and activation of growth-related metabolic pathways. These results are consistent with the present observation of a gradual increase in Alamar Blue signal in ternary blend samples (Figure 4.6A).

From the perspective of cell physiology, in such substrates, cells not only grow on the scaffold surface but also penetrate the voids created by the removal of soluble phases, gradually forming a three-dimensional network (Figure 4.6C) [128]. The increase in metabolic signaling in this situation could be because of enhanced intercellular communication, activation of mitochondrial respiratory pathways, and improved gas exchange, rather than merely an increase in cell number. A similar observation has been reported for studies of electrospun blends with connected porosity, in which the increase in metabolic capacity was attributed to upregulation of ECM-related genes and integrins [292].

In contrast, the neat PCL scaffold, due to its smooth surface, likely limited cell penetration into the network and cell accumulation on its surface (Figure 4.6B). Under such conditions, nutrient exchange in the lower layers might be reduced, and it could be the reason why the metabolic signal intensity remained lower than in the open-pore groups.

Overall, the results of metabolic activity (Figure 4.6A), along with imaging evidence (Figures 4.6B, and C), demonstrate that transforming the PEO and PEG phases into porous intrafibrous structures after a pre-immersion step in water creates a microenvironment with enhanced permeability, three-dimensional accessibility, and a cellular metabolic response. This feature, coupled with the morphological stability provided by the PCL matrix, suggests a beneficial equilibrium between structural integrity and biological activity, a concept previously proposed as a key indicator for scaffold design in bone tissue engineering [290]. However, since this evaluation is only a preliminary fibroblast-based test, larger in vitro studies with primary osteoblast cells are necessary to investigate the biological behavior of the scaffolds for bone tissue engineering application, which is the subject of our future work.

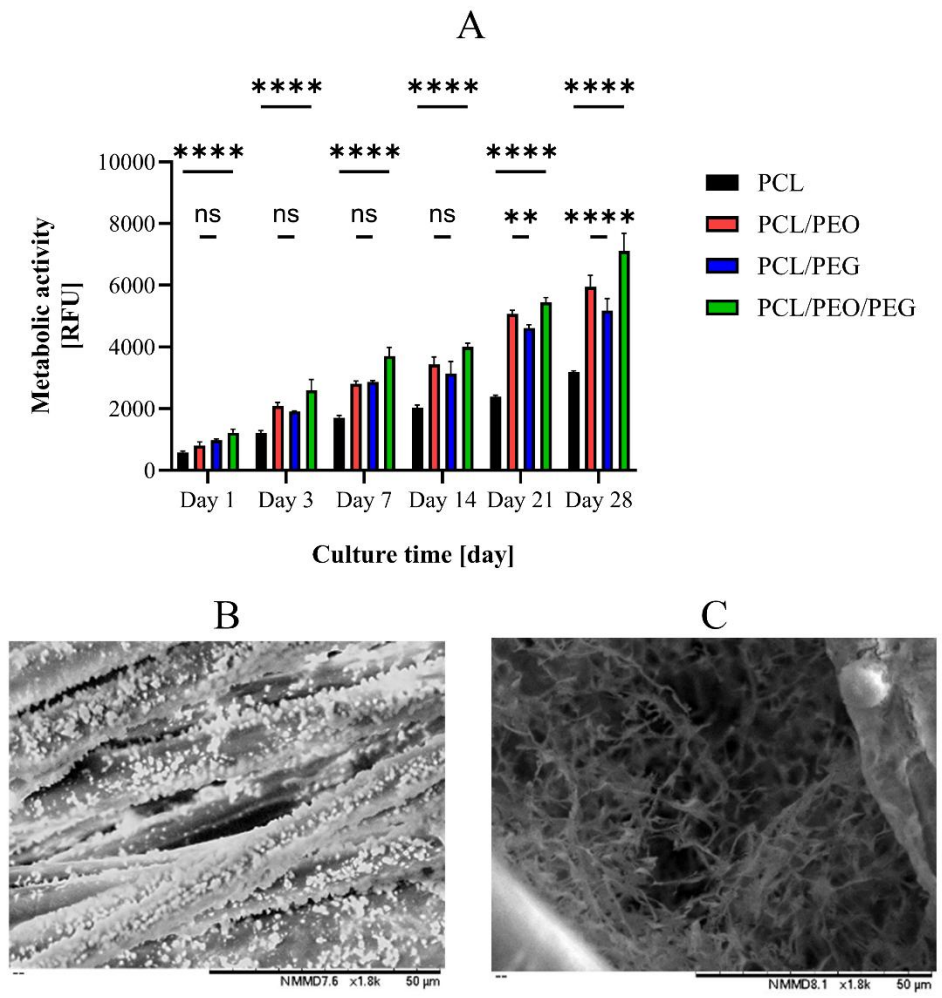

Figure 4.6 (A) Metabolic activity of fibroblasts on different scaffolds over a period of 28 days. Cellular metabolic activity was measured using the Alamar Blue assay on days 1, 3, 7, 14, 21, and 28 after culture. Data is presented as mean ± SD. Two-way ANOVA performed statistical analysis with Tukey's post hoc test. Statistical symbols are displayed as follows: *$p < 0.05$, **$p < 0.01$, ***$p < 0.001$, ***$p < 0.0001$, and ns indicates non-significance. To avoid cluttering the form and maintaining readability, only two key families of comparisons are shown in the graph: (1) ternary combination (PCL/PEO/PEG) versus PCL as the baseline reference, and (2) PCL/PEO versus PCL/PEG. All other comparisons (including all pairs between formulations at each time point) are presented in full in the Supporting Information (Figure S. 4.1). (B) SEM image of fibroblast cells on PCL scaffold at day 28 showing scattered cell distribution. (C) SEM image of PCL/PEO/PEG scaffold on the same day showing formation of a dense network of cells and extracellular matrix. Scale bar: 50 µm.

4.4 Conclusion

In this work, the behavior of a ternary blend of PCL/PEO/PEG under the melt electrospinning process was studied. The SEM images reveal the different morphology of the samples before and

after melt electrospinning because of the effects of the high temperature of the process, heating time, which acts like annealing, fast solidification, and stretching that is due to the imposed electrical field to the system. A comparison between the behavior of PEG and PEO mixing with PCL was also made. The FTIR spectra of melt electrospun fibers indicate no reaction or chemical interaction between PCL, PEO, and PEG. It also alludes to no difference between the FTIR spectra of samples before and after melt electrospinning. PEO can form large, PEO-rich domains during the solidification of melt electrospun fibers made from PCL/PEO/PEG-BME. These larger domains develop a crystalline structure as they solidify. In contrast, the XRD spectra of samples vividly indicate that the bulk of PEG remains in the amorphous phase in the ternary blend fibers, which DSC confirms. However, the minor fraction of PEG trapped in the PCL could form the microcrystalline structure. Metabolic activity results indicate that the use of PEO and PEG as sacrificial components is a practical approach to improve the biological properties of scaffolds. However, further studies with osteoblast cells are required to evaluate the actual potential of these scaffolds for bone tissue engineering. Besides, the results explained here are specific to the selected processing technique (i.e, Brabender). To assess the possible effects of different compounding techniques on the blend's microstructure, more research is underway.

Supporting Information (Supporting_Information.docx): Design of experiments (JMP), rheological isotherm/time-sweep plots, normalized fibroblast metabolic activity data, and statistical comparisons (ANOVA with Tukey post hoc analysis).

Acknowledgments

The authors sincerely thank Mohsen Hasani Zadeh and Mojtaba Mohammadi for their valuable scientific contributions. Special thanks are extended to Matthieu Gauthier and Claire Cerclé for their technical assistance. This work was supported by the Natural Sciences and Engineering Research Council of Canada (NSERC); and the Fonds de recherche du Québec – Nature et Technologies (FRQNT). The authors sincerely thank them for their financial support.

4.5 Supplementary materials

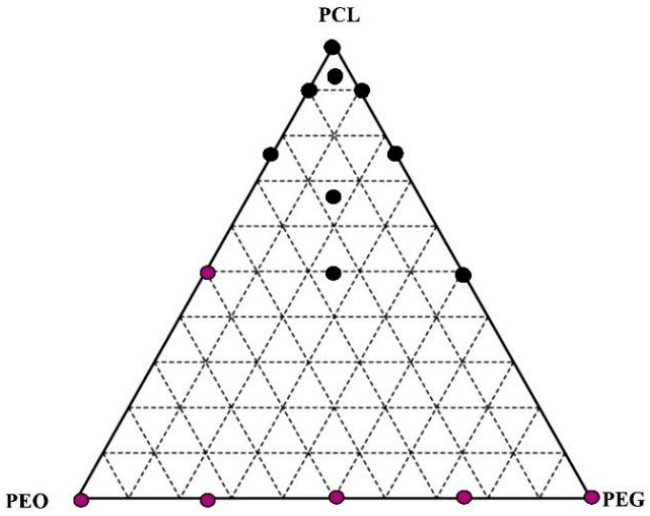

Figure S. 4.1Experimental design generated by JMP software (version 18) illustrating the selected blend compositions used for this study. `Red dots indicate compounds that were not electrospinnable. Black dots indicate compounds that were electrospinnable.

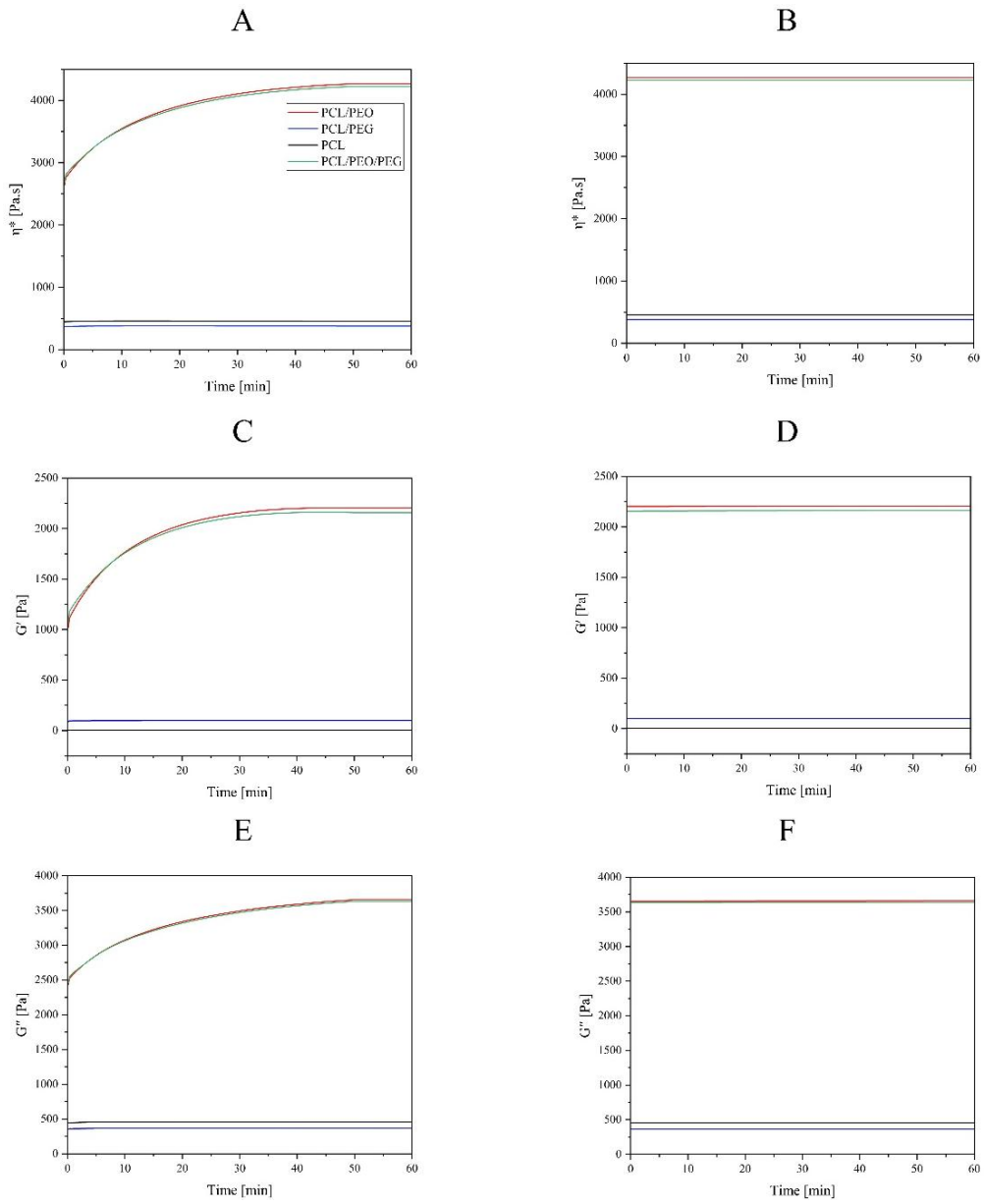

Figure S. 4.2 Rheology isotherm plots for different samples in the time sweep test at 150 ˚C when the frequency was adjusted to one. The images on the left (A, C, E) show the results for samples that were tested immediately after reaching the test temperature. In contrast, the images on the right (B, D, F) show the same samples that were preheated at 150 ˚C for one hour before starting the test. The changes in (A, B) the complex viscosity (η*), (C, D) the storage modulus (G′), and (E, F) the loss modulus (G″) are plotted as a function of time. The results show that preheating the samples results in more stable modulus and viscosity values over time, indicating that the system reaches rheological equilibrium.

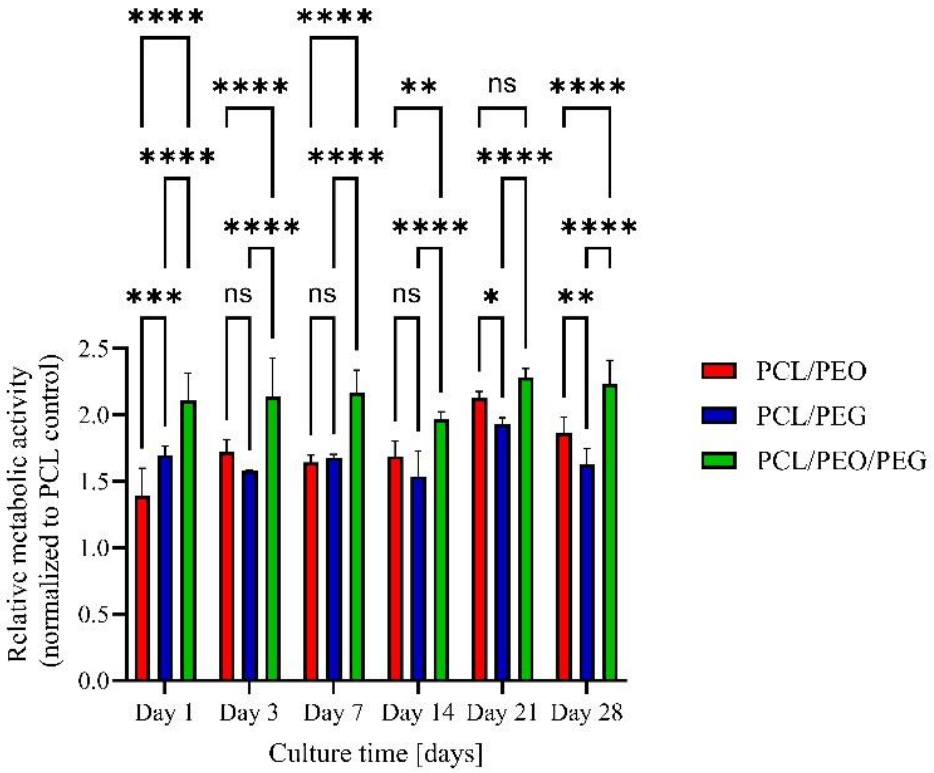

Figure S. 4.3 Changes in relative metabolic activity (Normalized Metabolic Activity) of fibroblast cells on different samples (PCL/PEO, PCL/PEG, and PCL/PEO/PEG) at different time intervals. Data was calculated by dividing the values obtained from the Alamar Blue test by the corresponding values of the PCL sample at each time point. Results were statistically analyzed based on two-way ANOVA and Tukey's post-hoc test.

Table S. 4.1 Statistical comparison between different groups in terms of cellular metabolic activity on days 1, 3, 7, 14, 21, and 28 using one-way ANOVA and Tukey's post hoc test[I]

Contrast	Day 1	Day 3	Day 7	Day 14	Day 21	Day 28
PCL vs. PCL/PEO	ns	****↑	****↑	****↑	****↑	****↑
PCL vs. PCL/PEG	*↑	****↑	****↑	****↑	****↑	****↑
PCL vs. PCL/PEO/PEG	****↑	****↑	****↑	****↑	****↑	****↑
PCL/PEO vs. PCL/PEG	ns	ns	ns	ns	**↓	****↓
PCL/PEO vs. PCL/PEO/PEG	**↑	**↑	****↑	****↑	*↑	****↑
PCL/PEG vs. PCL/PEO/PEG	ns	****↑	****↑	****↑	****↑	****↑

[I]*Asterisks describe statistical significance ($p < 0.05$: , $p < 0.01$: **, $p < 0.001$: ***, $p < 0.0001$: ****) and arrow symbols indicate the direction of change; an upward arrow (↑) indicates an increase in the value in the second group compared to the first group and a downward arrow (↓) shows a decrease in the value in the second group. The term ns means no significant difference between groups.*

CHAPTER 5 ARTICLE 2: MELT ELECTROSPINNING OF POLY (ε-CAPROLACTONE) /POLYETHYLENE OXIDE /POLYETHYLENE GLYCOL –HYDROXYAPATITE NANOCOMPOSITE FIBERS: MORPHOLOGY, PROPERTIES AND HYDROLYTIC DEGRADATION

Elham Karimi[a], Frej Mighri[b], Marie-Claude Heuzey[a], Abdellah Ajji[a,*]

[a] Center for High Performance Polymer and Composite Systems (CREPEC), Department of Chemical Engineering, Polytechnique Montréal, Montreal, Québec, H3T 1J4, Canada

[b] Center for High Performance Polymer and Composite Systems (CREPEC), Department of Chemical Engineering, Université Laval, Quebec, Québec, G1A 0A6, Canada

[*] Author to whom correspondence should be addressed, Email: abdellah.ajji@polymtl.ca

Submitted to Polymer Engineering & Science, December 30, 2025

Authorship contribution statement of Elham Karimi: Conceptualization; Data curation; Formal analysis; Investigation; Methodology; Validation; Visualization; Writing – original draft; Writing – review and editing.

Abstract

In this study, a ternary blend consisting of poly (ε-caprolactone) (PCL), polyethylene oxide (PEO), and polyethylene glycol (PEG), reinforced with hydroxyapatite nanoparticles (nHA), was designed and prepared via melt electrospinning. The distinctive feature of this research is the use of a ternary blend (PCL/PEO/PEG) in melt electrospinning, which has been rarely investigated so far. Scanning electron microscopy (SEM) revealed that the addition of hydrophilic polymers to PCL results in a more uniform distribution of nHA within the fibers. Fourier transform infrared (FTIR) analyses confirmed the absence of chemical changes and the preservation of the nanoparticles' structure. Differential Scanning Calorimetry (DSC) analysis showed that the presence of nHA in PCL increases crystallinity. In contrast, in the ternary blend, physical interactions between nanoparticles and PEO and PEG chains decrease crystallinity. Thermal stability tests showed that the nHA remained stable in the polymer matrix, and their migration in aqueous environments was negligible. Mechanical tests showed increases in stress and yield strain. Also, the hydrolytic

degradation results indicated a higher degradation rate for the ternary blend than for neat PCL. Overall, these results indicate the high efficiency of the prepared fibers for potential applications in bone tissue engineering.

Keywords: *Melt electrospinning, Polymer nanocomposites, PCL-based blends, Hydroxyapatite nanoparticles, Biodegradable scaffolds*

Highlights

- PCL/PEO/PEG-nHA fibers were successfully fabricated by melt electrospinning.
- The addition of PEO and PEG to PCL improved the distribution of nHA.
- nHA in the ternary blend fibers was not leached upon immersion in water.
- The addition of nHA increased the yield stress and strain.
- The ternary blend showed faster hydrolytic degradation than the PCL.

5.1 Introduction

In recent years, bone tissue engineering has emerged as a strategic approach in regenerative medicine, providing a suitable microenvironment for cellular function by designing three-dimensional (3D) scaffolds inspired by the natural extracellular matrix (ECM) [4, 293, 294]. Despite therapeutic advances such as autografts and allografts, limitations such as resource scarcity, clinical complications, and the risk of immune responses have highlighted the necessity of developing engineered systems with controllable structure and function [295]. Therefore, designing scaffolds with engineered architecture, tunable mechanical properties, and controlled degradation behavior has become a fundamental challenge in this field [295].

Synthetic biodegradable polyesters such as Polylactic-co-glycolic acid (PLGA), polylactic acid (PLA), and poly(ε-caprolactone) (PCL) have been widely used in the manufacture of bone scaffolds due to their good processability, favorable thermal stability, and ability to tune the modulus and degradation rate [4, 296]. Several fabrication methods, including gas foaming, freeze drying, solvent casting, and particulate leaching, have been developed to produce scaffolds [297]. However, these methods generally lack a fibrous structure similar to natural ECM [298]. Among other techniques, electrospinning has attracted attention due to its ability to produce ECM-like fibrous networks [298]. However, most studies have focused on solution electrospinning, which

poses challenges such as residual toxic solvents, environmental considerations, and limitations to industrial scalability [14, 47].

In response to these limitations, melt electrospinning has been proposed as a sustainable, solvent-free technology that enables transfer to the industrial scale [14]. However, most research in this area has focused on neat polymers or simple nanocomposites, and the investigation of complex multicomponent systems, especially systems with more than two components, remains underdeveloped [14, 47, 107]. On the other hand, simultaneously achieving appropriate mechanical strength, controllable degradability, and desirable surface properties is rarely achieved with a single polymer and requires the design of advanced multicomponent systems [44, 299]. For example, PCL is suitable in terms of processability and thermal stability, but is inherently hydrophobic and has a low degradation rate [44, 300]. In contrast, hydrophilic polymers such as poly (ethylene oxide) (PEO) and poly (ethylene glycol) PEG can modify surface hydrophilicity, degradation behavior, and crystalline microstructure, but do not have sufficient mechanical strength on their own [258, 299]. Blending PCL with PEO or PEG has also been reported to be an effective strategy for enhancing cell adhesion and proliferation [301]. Therefore, polymer blending has been proposed as an effective strategy to create synergy between different properties [296, 302].

Previous studies on PCL/PEG and PCL/PEO binary systems, primarily in the context of solution electrospinning, have shown that PEG can reduce viscosity and, consequently, decrease fiber diameter [299, 301, 303]. For the PCL/PEO system, it has been reported that, despite the thermodynamic immiscibility of these two polymers in the bulk, electrospinning can result in interwoven structures and nanoscale mixing within each nanofiber [304]. Thermal results confirm this nanoscale mixing, and, mechanically, increasing the PCL proportion increases the modulus, while increasing the PEO proportion decreases ductility [304]. To more closely mimic the mineral phase of bone, several studies have reported adding bioactive ceramics, especially hydroxyapatite (HA), to the PCL matrix, and these nanocomposites have been shown to improve mechanical properties, enhance biocompatibility, and osteoconductivity [293, 298].

Therefore, a systematic analysis of the effects of polymer blending and the presence of the inorganic phase on the morphology and chemical and physical properties of fibers fabricated by melt electrospinning can fill the current knowledge gap and provide a structure–process–property framework for the design of advanced multicomponent systems.

In this study, a ternary blend of PCL/PEO/PEG containing hydroxyapatite nanoparticles was used to fabricate fibers via melt electrospinning. The processing parameters were adjusted to fabricate PCL/PEO/PEG-nHA fibers with a uniform microstructure and a suitable distribution of nanoparticles, thereby preventing particle agglomeration throughout the fibers and mitigating potential effects on the mechanical and surface performance of the system. This system not only allows us to investigate the synergistic role of hydrophilic polymers (PEO and PEG) with PCL, but also to examine how the presence of bioactive mineral nanoparticles affects the mechanical and surface properties of the fibers, as well as their hydrolytic degradation. Although the direct application of this system has not been biologically tested in this article, its primary goal is to provide a promising platform for developing scaffolds that can be used in the field of bone tissue engineering.

5.2 Material and methods

5.2.1 Materials

Polycaprolactone (PCL, Capa™ 6500, Mn ≈ 50,000 $g.mol^{-1}$, granular form) was supplied by Perstorp (Canada). Polyethylene oxide (PEO, Mv ≈ 600,000 $g.mol^{-1}$, powder) and Polyethylene glycol (PEG, Mn ≈ 20,000 $g.mol^{-1}$, flakes) were obtained from Sigma Aldrich (USA). Hydroxyapatite nanoparticles (nHA, < 200 nm particle size, ≥ 97% purity) were obtained from Sigma Aldrich (USA) and used as the inorganic phase for composite preparation. Phosphate-Buffered Saline (PBS, pH 7.4 (1X)) was acquired from Gibco, Thermofisher (Canada). All materials were used as received without further purification. Table 5.1 summarizes the melting (T_m), crystallization (T_c), and glass transition (T_g) temperatures of the neat polymers. Values were obtained from differential scanning calorimetry (DSC) under a nitrogen purge; T_m and T_g were extracted from the first-heating scan and T_c from the subsequent cooling scan (see Section 2.3.3 for conditions).

Table 5.1 Thermal properties of neat polymers: melting, crystallization, and glass transition temperatures

Polymer	Melting temperature (T_m) [˚c]	Crystallization temperature (T_c) [˚c]	Glass transition temperature (T_g) [˚c]
PCL	63.9 ± 1.0	27.5 ± 0.3	-51.4 ± 0.7
PEO	69.3 ± 0.0	42.5 ± 1.6	-51.9 ± 1.7
PEG	69.1 ± 0.1	43.9 ± 1.9	-55.1 ± 2.0

5.2.2 Sample preparation

5.2.2.1 Melt blending

All polymeric formulations were prepared using a micro twin-screw compounder (DSM Xplore, Micro 5 cc, Netherlands) with a total batch size of 3 g. All components were subjected to vacuum drying at 30 ˚C to ensure the complete removal of moisture prior to use. A masterbatch of PCL/nHA was produced by compounding polycaprolactone (2.70 g) with hydroxyapatite nanoparticles (0.30 g, 10 wt%) at a temperature of 70 ˚C and a speed of 50 rpm for a duration of 7 minutes. This masterbatch was then combined with PEO (0.15 g, 5 wt%) and subsequently PEG (0.15 g, 5 wt%) under the same conditions for 8 minutes, resulting in a nanocomposite comprising 80 wt% PCL, 10 wt% nHA, 5 wt% PEO, and 5 wt% PEG. The final composition of 80 wt% PCL, 10 wt% nHA, 5 wt% PEO, and 5 wt% PEG was selected based on initial evaluations and considerations related to process and bioperformance, as explained below. Preliminary studies on different compositions containing 1 to 20 wt% hydroxyapatite nanoparticles showed that increasing the nanoparticle concentration above 10 wt% decreased uniformity of distribution, increased aggregation, and consequently decreased mechanical properties and processability. In contrast, values less than 10 wt% had no noticeable effect on the biological behavior of the system. Therefore, 10 wt% was selected as the optimal point between structural stability and bioperformance.

In addition, different ratios of PEO and PEG were also investigated. Increasing these components to more than 5 wt% led to accelerated degradation in aqueous environments. It reduced the stability of the melt electrospun fibers, making it difficult to maintain the integrity of the samples. Accordingly, the present composition was selected for its suitable balance of thermal

processability, physical stability, and desirable biological properties. It was deemed the optimal system for producing bioactive scaffolds.

For comparison, additional control compositions were prepared following the same protocol, including a neat PCL (100 wt%), a PCL/nHA (90/10 wt%) composite, and a ternary blend of PCL/PEO/PEG (90/5/5 wt%) without nHA. Table 5.2 summarizes the complete formulations of all samples. This uniform blending condition facilitated the direct assessment of the impacts of nanoparticle reinforcement and polymeric additives on the material's final properties.

Table 5.2 Developed formulations of the composition

Sample	PCL [wt%/g]	nHA [wt%/g]	PEO [wt%/g]	PEG [wt%/g]	Total mass [wt%/g]
PCL	100/3	-	-	-	100/3
PCL/nHA	90/2.70	10/0.30	-	-	100/3
PCL/PEO/PEG	90/2.7	-	5/0.15	5/0.15	100/3
PCL/PEO/PEG/nHA	80/2.40	10/0.30	5/0.15	5/0.15	100/3

5.2.2.2 Melt electrospinning

Melt-blended samples from the micro-compounder were sliced into small fragments using scissors, loaded into a 9 mL stainless steel syringe, and placed within a cylindrical heating jacket of a custom-designed melt electrospinning apparatus. The heating system kept the syringe at 130 ˚C throughout the process. The syringe was equipped with a stainless-steel needle (20 G) functioning as the spinneret, which was electrically grounded, while the rotating drum collector was maintained at a positive potential. A schematic illustration of the melt electrospinning setup is shown in Figure 5.1.

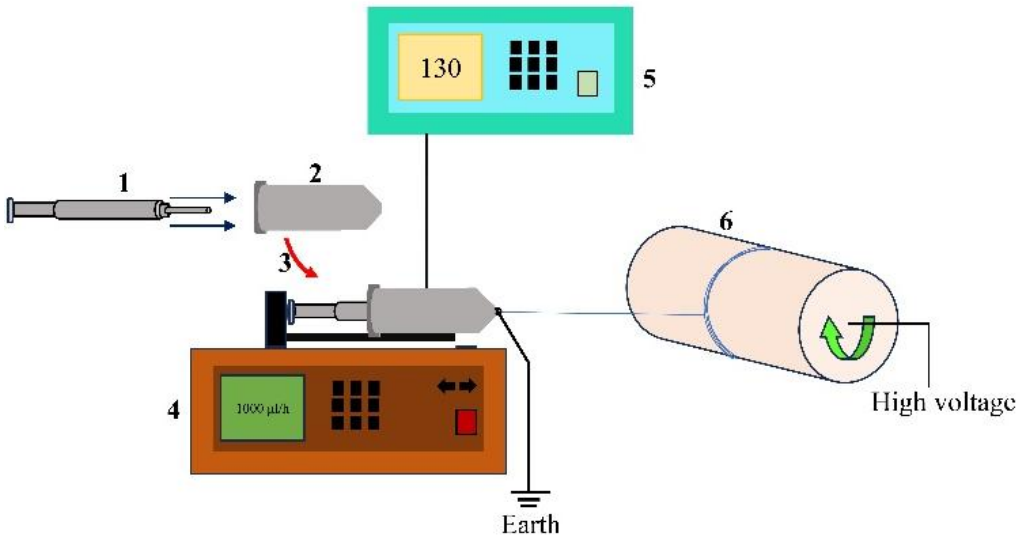

Figure 5.1 A schematic of the electrospinning apparatus: (1) stainless steel syringe, (2) stainless steel heater, (3) to supply the molten mixture at a steady flow, the temperature-controlled syringe (in-line heater) was strapped onto the syringe pump, (4) pump, (5) temperature controller, and (6) drum collector.

In order to guarantee uniform fiber fabrication, the melt electrospinning process was carried out when the collector rotated at 21 rpm and the applied voltage was 7.5 kV, while the feeding rate was adjusted at 1000 $\mu L.h^{-1}$ and the tip-to-collector distance was 7.5 cm. Under these regulated settings, all formulations (PCL/PEO/PEG, PCL/PEO/PEG/nHA, neat PCL, and PCL/nHA) resulted in continuous aligned fibers with uniform morphology, thereby ensuring reproducibility and facilitating direct comparison among formulations. In this paper, the BME suffix indicates samples obtained from melt mixing Before Melt Electrospinning (BME) process, and the AME suffix refers to samples processed through melt electrospinning.

5.2.3 Scaffold characterization

5.2.3.1 Scanning Electron Microscopy (SEM) and Energy-Dispersive X-ray (EDX) Analysis

The morphology of the melt electrospun fibers with and without hydroxyapatite nanoparticles was characterized using a scanning electron microscope (SEM; TM3030Plus, HITACHI, Japan) operated at an accelerating voltage of 15 kV. For cross-sectional analysis, fibers were embedded in epoxy resin and cryo-microtomed (Leica RM2165, Leica Microsystems, Germany) in liquid

nitrogen when the temperature was adjusted 40 ˚C lower than the T_g of the samples (Table 5.3), using a glass knife to obtain ultrathin sections. To reveal the morphology associated with the water-soluble polymeric domains, specimens were immersed in deionized water for one week to remove polyethylene oxide (PEO) and polyethylene glycol (PEG). The samples were subsequently dried under vacuum for 48 h to ensure complete elimination of residual water. In this paper, the suffix AW is assigned to samples that were examined after immersion in water for one week, while the suffix BW refers to samples before immersion in water. Quantitative image analysis of fiber diameter and nanoparticle size distribution was performed using ImageJ software.

Elemental analysis was carried out via Energy-Dispersive X-ray spectroscopy (EDX; OXFORD instruments, X-max^N, UK) on nanocomposite melt electrospun fibers coated with gold to assess the relative content and distribution of hydroxyapatite nanoparticles within the specimens. EDX spectra were acquired before and after aqueous extraction to evaluate potential loss of hydroxyapatite nanoparticles and to confirm nanoparticle dispersion within the polymeric matrix.

5.2.3.2 Fourier transform infrared (FTIR)

A PerkinElmer spectrometer (Waltham, MA, USA) was employed to obtain Fourier Transform Infrared (FTIR) spectra. FTIR was performed to examine the presence or absence of physical interactions and potential chemical reactions among the components of the nanocomposite, as well as to evaluate the potential dehydroxylation of nHAs during the high-temperature melting process. These analyses allowed the evaluation of any possible chemical changes or degradation in the structure of the polymers and nanoparticles. Measurements were performed with 16 scans at a nominal resolution of 4 cm^{-1} in the spectral range of 600-4000 cm^{-1}, in ambient conditions. To ensure reliability and reproducibility of the spectral profiles, each specimen was examined in triplicate, and the averaged spectra were employed for subsequent interpretation.

5.2.3.3 Differential Scanning Calorimetry (DSC) Measurements

Thermal and crystallization behaviors of neat components as well as blends were characterized using a differential scanning calorimeter (DSC, Q1000, TA Instruments, New Castle, DE, USA). Approximately 5-10 mg of each sample was encapsulated in an aluminum pan and lid, and measurements were conducted under a nitrogen environment at a constant flow rate of 50 mL/min. The thermal program consisted of an initial cooling to -90 ˚C, followed by heating to 130 ˚C at a rate of 10 ˚C.min^{-1}. At 130 ˚C, the samples were held at equilibrium before being cooled to -90 ˚C

at the same rate. They were then reheated to 130 ˚C to record the second heating cycle under identical conditions. The crystallinity of the samples was calculated using the Equation 5.1 [270]:

$$X_c = \frac{\Delta H_m}{\omega \times \Delta H_m^0} \tag{5.1}$$

Where ω is the mass fraction of the polymer , excluding nHA, and ΔH_m is the experimental melting enthalpy of a fraction, determined as the area under the melting peak, ΔH_m^0 is the specific melting enthalpy of 100% crystalline polymer, which is 139.5 $J.g^{-1}$ [271], 205 $J.g^{-1}$ [272], and 197.7 $J.g^{-1}$ [125] for PCL, PEO, and PEG, respectively.

5.2.3.4 Thermogravimetric analysis (TGA)

Thermogravimetric analysis (TGA5500, Waters TM, USA) was employed to evaluate the thermal stability of the formulations and to quantify the retention of hydroxyapatite (nHA) within the polymeric matrix before and after aqueous immersion. Approximately 8-10 mg of each specimen was loaded into an aluminum pan and heated from 35 ˚C to 600 ˚C under a nitrogen atmosphere at a constant rate of 10 ˚C·min^{-1}. The heating program was extended to 800 ˚C under air to ensure complete oxidative degradation of the polymeric components.

For each blend, measurements were performed on both as-prepared samples and specimens that had been immersed in deionized water for one week and subsequently vacuum-dried for 48 h. The residual mass at 800 ˚C was attributed to a thermally stable hydroxyapatite fraction. Three parameters were computed in order to evaluate the degree of nanoparticle retention:

(i) The difference in residual content prior to and after immersion (Equation 5.2):

$$\Delta Residue = Residue\ before\ immersion - Residue\ after\ immersion \tag{5.2}$$

(ii) The percentage of leached hydroxyapatite, Equation 5.3 [305]:

$$nHA\ leached\ [\%] = 100 \times \frac{\Delta Residue\ [\%]}{Initial\ percentage\ of\ nHA\ in\ sample\ [\%]} \tag{5.3}$$

(iii) And the percentage of hydroxyapatite retained (*nHA Retention*, Equation 5.4) [305]:

$$nHA\ Retention\ [\%] = 100 - nHA\ leached\ [\%] \quad (5.4)$$

These formulas let us figure out how stable the hydroxyapatite was inside the scaffolds, which gave us direct information about how well the nanocomposite formulations resisted leaching and how long the interfaces lasted.

5.2.3.5 Mechanical properties

Tensile properties were measured under uniaxial loading on rectangular strips (~10 mm × 5 mm, length × width; thickness ~350 μm) that were cut with a precision cutter, pre-conditioned by soaking in deionized water at 37 ˚C for 7 days, and vacuum-dried to constant mass. Each specimen was fixed to a paper frame using double-sided adhesive. Both sides of the frame tabs were covered with sandpaper to avoid slippage. Tests were conducted using a tensile strength tester machine (Instron, E3000, USA) equipped with a 250 N load cell at a crosshead speed of 1 $mm.min^{-1}$ under ambient conditions. Modulus (E) was extracted from the toe-corrected stress–strain response by least-squares fitting to the initial linear region. Yield stress (σ_y) and yield strain (ε_y) were obtained using the 0.2% offset criterion applied to the toe-corrected curve. For each formulation, at least seven specimens were tested ($n \geq 7$); results are reported as mean ± standard deviation (Mean ± SD).

5.2.3.6 Hydrolytic degradation test

Hydrolytic degradation studies were conducted in accordance with ASTM F1635-11. Melt electrospun fibers were fully immersed in PBS, pH 7.4, at 37 ˚C under static conditions. To keep sink conditions throughout the investigation, the amount of PBS was changed so that the PBS-to-fibers (v/v) ratio was about 100:1, in line with ASTM F1635-11. The medium was refreshed every three days to prevent ionic accumulation and pH variations.

At predetermined time points (up to 28 weeks), specimens were rinsed with deionized water and soaked for 24 h with repeated water exchange to remove salts and loosely bound degradation products. To further eliminate salts entrapped within specimens, they were briefly agitated in deionized water prior to final drying. Samples were then vacuum-dried at room temperature for 48 h to constant weight.

The initial dry weight (W_o) and dry weight after degradation (W_d) were measured using a precision analytical balance (± 0.1 mg). The percentage of weight loss was calculated using Equation 5.5 [306]:

$$Weight\ loss = \frac{W_0 - W_d}{W_0} \times 100 \quad (5.5)$$

5.2.4 Statistical analyses

Statistical analyses are performed using GraphPad Prism version 10. A one-way ANOVA with Tukey's post hoc test is used to compare the groups. Results are reported as mean ± standard deviation (Mean ± SD), and a significance level of 0.05 is considered.

5.3 Results and discussion

5.3.1 Morphological and Compositional Characterization

Figure 5.2 shows SEM images and EDX analysis of melt electrospun PCL/nHA and ternary blend/nHA fibers after one week of water immersion. Images (Figures 5.2A–D) include cross-sections and surfaces of the fibers; (Figure 5.2A) and (Figure 5.2C) correspond to the PCL/nHA samples and (Figure 5.2B) and (Figure 5.2D) to the ternary blend/nHA samples. In Figure 5.2B, a magnified view with a scale bar of 10 μm is presented to show more details of the cross-section, while the other SEM images in Figures 5.2A–D have a scale bar of 50 μm. Histograms (Figures 5.2E and F) show the size distribution of hydroxyapatite nanoparticles on the fiber surface for PCL/nHA and ternary blend/nHA, respectively. The SEM image of hydroxyapatite nanoparticles (as received) and the histogram of particle diameter distribution are shown in Figure S. 5.1 (Supporting Information). Furthermore, EDX elemental maps (Figures. 5.2G and H) for calcium (Ca, K-series) and phosphorus (P, K-series) elements confirm the uniform dispersion of mineral nanoparticles in both fiber systems; EDX images are recorded with a scale bar of 100 μm. EDX elemental maps (Figures. 5.2G and H) also imply that the nHA is firmly localized in the matrix so that immersion in water does not wash nHA away. EDX elemental maps for calcium (Ca, K-series) and phosphorus (P, K-series) elements for samples before water immersion are presented in Figure S. 5.2 (Supporting Information). Additional information regarding the weight percentage of calcium and phosphorus, as well as the atomic ratio of Ca/P, is provided in Table S. 5.1 of the Supporting Information. In PCL/nHA samples, significant agglomerates of hydroxyapatite nanoparticles are observed (Figure 5.2A), indicating limited dispersion and localized aggregation of particles in the polymer matrix. In contrast, in ternary blend/nHA fibers, a more uniform distribution and favorable dispersion of nanoparticles on the surface (Figure 5.2D) and cross-

section (Figure 5.2B) of the fibers are observed. This phenomenon may be attributed to increased physical interactions between nanoparticles and the multicomponent matrix, as well as improved phase compatibility of the polymer components. A more uniform dispersion of particles, especially on the surface of ternary blend/nHA fibers, could provide a higher capacity to increase cell contact and improve the biocompatibility of the fibers.

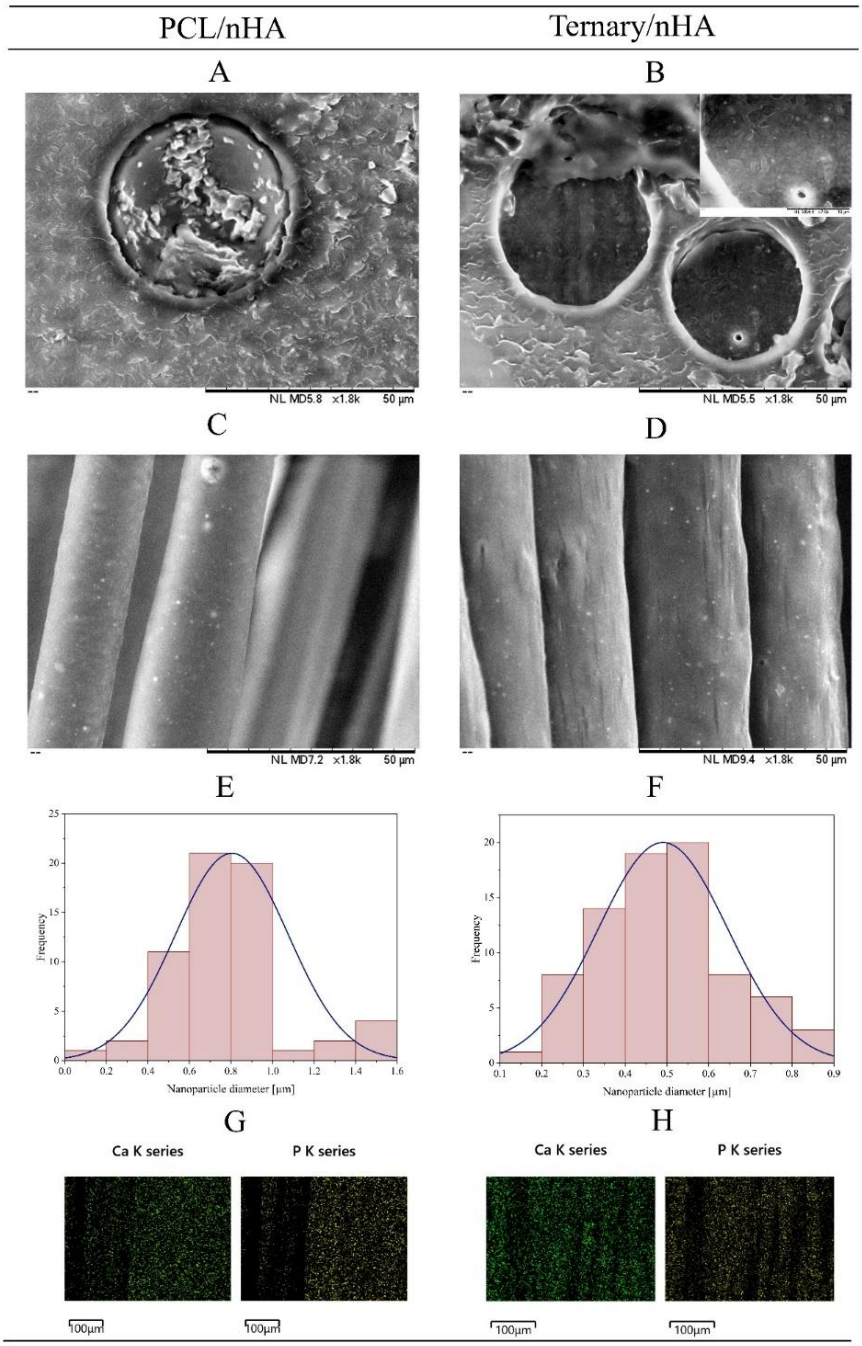

Figure 5.2 SEM images and EDX analysis of melt electrospun scaffolds after one week of water immersion. (A-B) depicts the cross-sections of PCL/nHA and ternary blend/nHA samples, respectively; in (B), a magnified view with a 10 µm scale bar is provided for more detail. Surface images of the fibers are shown for (C) PCL/nHA and (D) ternary blend/nHA. All SEM images in (A–D) are recorded with a 50 µm scale bar. The size distribution of hydroxyapatite nanoparticles on the fiber surface is shown in histogram format for (E) PCL/nHA and (F) ternary blend/nHA. EDX maps of Ca (K-series) and P (K-series) elements are presented for (G) PCL/nHA and (H) ternary blend/nHA samples, respectively, confirming the uniform dispersion of inorganic nanoparticles in the fibrous matrix. The scale bar in the EDX images is 100 µm.

The quantitative results presented in the histograms of Figures 5.2E and F, also confirm these observations. In the PCL/nHA sample, the nanoparticle size distribution is broader and more heterogeneous, and a wider range of particle diameters is observed on the fiber surface (Figure 5.2E). While in the ternary blend/nHA, the particle size distribution is narrower and more concentrated, and the maximum abundance is located in a smaller size range (Figure 5.2E). These results suggest that the homogeneous incorporation of hydrophilic polymers (PEG and PEO) into PCL enhances the hydrophilicity and compatibility between the polymeric matrix and nHA, ultimately leading to a more uniform dispersion of the nanoparticles. Similar observations on the improvement of nHA dispersion in PCL-based systems with the addition of PEG were previously reported by Cacciotti et al. [307].

In addition, short and shallow channel patterns are observed on the surface of the fibers in the ternary blend/nHA fibers. This phenomenon seems to be due to the formation of some PEO/PEG microdomains within the PCL matrix, although the majority of the PEO/PEG chains are distributed in the PCL. In other words, stretching of PEO/PEG microdomains during the melt electrospinning process caused by the applied voltage, as well as the rotating collector, leads to the formation of some short and shallow fibril domains, which form shallow channels after water immersion. This patterned surface, clearly visible in the ternary blend/nHA scaffold, may play a role in increasing surface roughness and thereby promoting cell adhesion and response. Overall, the results show that the use of the ternary blend composite ensures a more suitable dispersion of mineral nanoparticles and the creation of desirable surface patterns. These features can synergistically improve the hydrophilicity and enhance the biological performance of the fibers in bone tissue engineering applications.

5.3.2 Chemical Structure Analysis

Figure 5.3 summarizes the FTIR spectra of the investigated formulations. It should be noted that these spectra were recorded from samples before immersion in aqueous media. Figure 5.3A shows the spectra of PCL-based systems (plain and nHA-loaded) prepared by melt blending (BME) and melt electrospinning (AME). The FTIR spectra of PCL and PCL/nHA formulations, in both BME and AME forms, demonstrated the full retention of the characteristic vibrational signatures of both constituents. The carbonyl stretching of PCL was consistently observed around 1720 cm^{-1}, together with the ether/ester backbone absorptions at 1160, 1240, and 1293 cm^{-1} [308], indicating that

neither BME nor AME specimens induced structural perturbation. The nanocomposite samples in both forms of BME and AME exhibit the characteristic peaks of nHA, including the symmetric P-O stretching vibration, ν_1, arising around 960 cm^{-1}, the asymmetric stretching vibrations of P-O bonds, ν_3, at 1020, and 1086 cm^{-1} as well as the peak emerging around 630 cm^{-1} representing the bending vibration of hydroxyl groups, ν_4, in the nHA crystal lattice [309]. Besides, no additional bonds or frequency shifts are detected across the processing routes, confirming that nHA preserved its crystalline vibrational identity after blending and fiber formation, while the polymer backbone remained chemically intact. However, this observation contrasts with the previous study by Xue et al. [310] who observed a shift of approximately 80 cm^{-1} for the phosphate ν_3 mode of hydroxyapatite when they mixed the particles with PCL. They believed that this shift could be due to the electronical interaction between PCL and nHA.

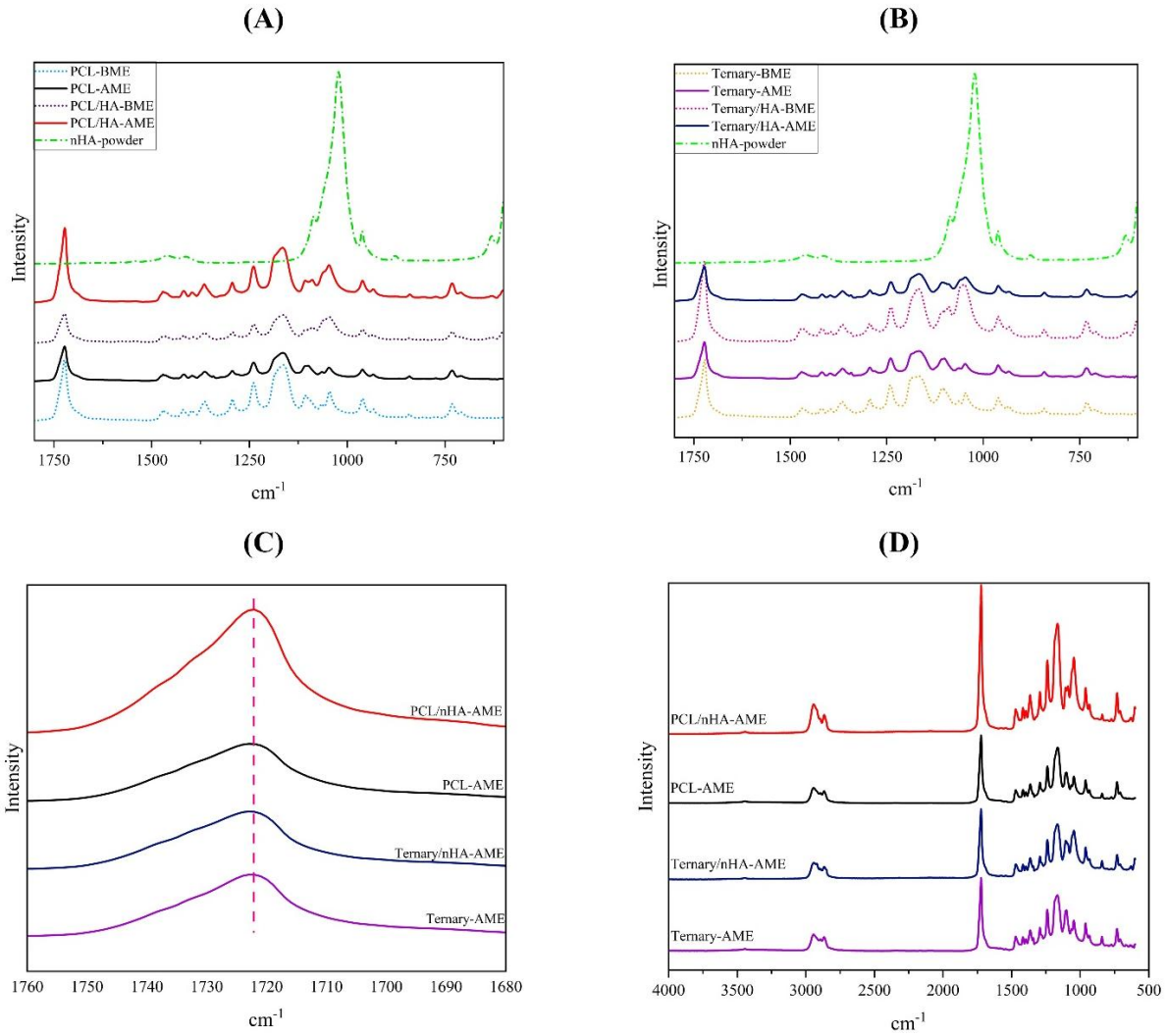

Figure 5.3 FTIR spectra comparing hydroxyapatite (nHA) loading and processing routes. (A) PCL-based formulations (pristine PCL and PCL/nHA) presented as melt-blended samples (BME) and electrospun fibers (AME). (B) Ternary-based formulations (PCL/PEG/PEO blend and its nHA-loaded counterpart) presented as melt-blended samples (BME) and melt electrospun fibers (AME). Key diagnostic absorptions-including ether linkages (C-O-C, ≈1293/1240/1160 cm^{-1}), carbonyl stretching (C=O, ≈1720 cm^{-1}) and phosphate groups (ν_1 ≈630 cm^{-1}; ν_3 ≈1030–1100 cm^{-1})-are displayed, with nHA powder (green trace) overlaid as reference. (C) Magnified carbonyl region shows no detectable peak shifting (vertical dashed line at 1720 cm^{-1}). (D) Full-range spectra (4000–600 cm^{-1}) for AME samples, confirming overall spectral consistency across formulations.

Figure 5.3B presents the FTIR spectra of BME and AME ternary blend and its nHA counterpart, with characteristic PCL and phosphate bands clearly identified. Figure 5.3B confirms the effective incorporation of nHA into the ternary blend systems, as the FTIR spectra of the three constituent

polymers (PCL/PEO/PEG) and the characteristic absorption of nanoparticles can be clearly detected. Particularly, the existence of phosphate vibration ν_1, ν_3, together with the hydroxyl vibration at approximately 630 cm^{-1}, in the mineral-loaded formulations, validates the successful incorporation of nHA. Most of the characteristic peaks of PEO/PEG overlapped with the PCL band vibrations; yet their contribution is consistent with the ternary blend formulation and explains part of the broad character of this spectral region. However, the most important conclusion of this part is that even the presence of PEO/PEG in the system did not cause hydrogen bonding between PEO/PEG and nHA. Additionally, the absence of a shift in the 630 cm^{-1} peak indicates that dehydroxylation of nHA did not occur at the processing temperature, which is consistent with the observations previously reported by Rapacz-Kmita et al.[309]. They did not observe dehydroxylation even at much higher temperatures for hydroxyapatite (above 1000 ˚C). Moreover, the sharper peaks in bulk melt-blended samples than in melt electrospun fibers are consistent with differences in film thickness and structural uniformity.

Figure 5.3C focuses on the carbonyl region (≈1720 cm^{-1}), suggesting that there are no peak shifts between the neat and nHA-loaded formulations. It implies that no hydrogen bonding, even in the presence of PEO/PEG, is detectable. Figure 5.3D shows the full-range spectra (4000-600 cm^{-1}) for the melt electrospun fibers, which confirms that there is no significant change or shift in the full range of the FTIR spectra of the AME samples.

5.3.3 Differential Scanning Calorimetry (DSC)

Figure 5.4 shows the thermal transitions of the melt electrospun fibers during the first heating cycle (Figure 5.4A) and cooling scan (Figure 5.4B) as DSC curves. The DSC runs of the samples before the melt electrospinning process (BME), including first heating scan, and cooling cycles, are presented in the Supporting Information (Figure S. 5.3).

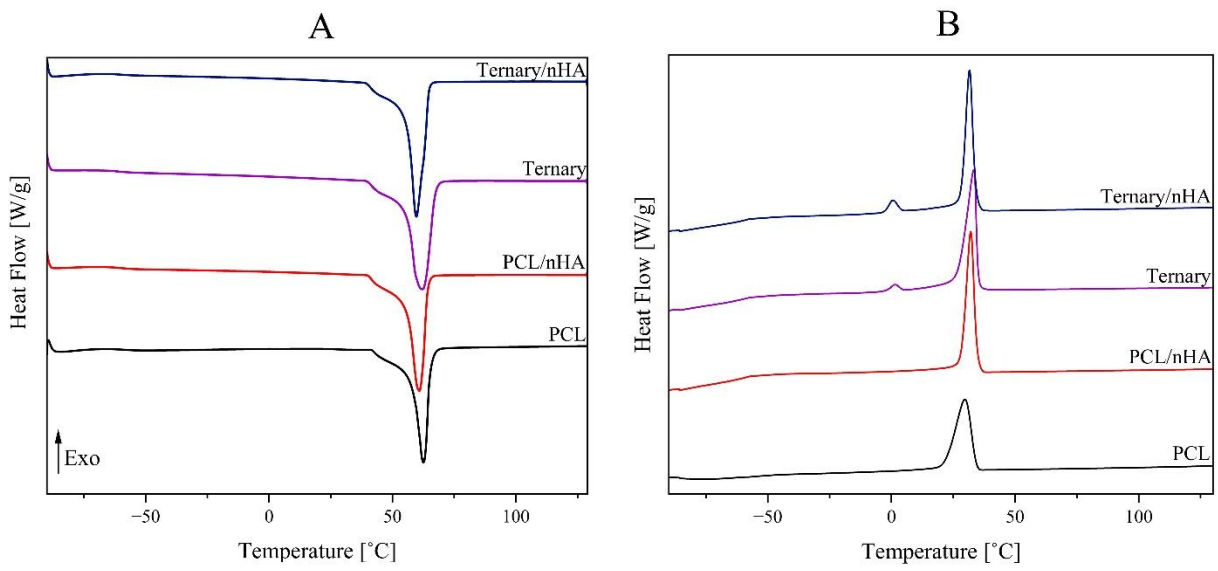

Figure 5.4 DSC of melt electrospun fibers (A) first heating endotherms. (B) Cooling exotherms. Heat flow is normalized per sample mass ($W.g^{-1}$) and exothermic direction is upward.

The important thermal characteristic data from both the first heating, and cooling scans are summarized in Table 5.3. Full details of the DSC results for the first heating cycle of the AME and BME samples, including T_g, T_m, ΔH_m, T_c, and ΔH_c values, are provided in Table S. 5.2 in the Supporting Information.

Table 5.3 Key thermal metrics obtained from the first heating cycle for melt electrospun fibers at a scan rate of 10 ˚C.min^{-1}

Sample	T_g[˚C]	T_m[˚C]	X_C [%]	T_C[˚C]
PCL	-50.5 ± 1.1	62.5 ± 0.8	37.7 ± 0.2	29.7 ± 0.1
PCL/nHA	-52.9 ± 0.3	60.9 ± 0.6	42.2 ± 0.1	32.1 ± 0.2
Ternary blend	-53.2 ± 0.8	62.0 ± 0.7	49.8 ± 0.3	33.3 ± 0.1, 1.5 ± 0.0
Ternary blend/nHA	-54.4 ± 0.5	59.7 ± 0.1	46.8 ± 0.2	31.6 ± 0.3, 0.5 ± 0.1

[1] Crystallinity percentage X_C is calculated using Equation 5.1.

In the ternary blend samples, only one melting point is observed during the first heating for both plain and nanocomposite ternary blends (Table 5.3). Consistent results were obtained from the DMA analysis, showing a single glass transition temperature (T_g) for Ternary blend/nHA (Figure S. 5.4). This implies that the components are miscible under the processing procedure employed in this paper. The results of the first heating cycle for the samples after melt blending, AME, (Table

S. 5.2 and Figure S. 5.3), and BME (before melt electrospinning), indicate that miscibility occurs during the melt blending step. In other words, since only one melting point is recorded for both plain and nanocomposite BME ternary blends in the first heating cycle, it can be concluded that the melt blending conditions are effective enough to make a miscible blend of PCL, PEO, and PEG. This observation can be considered as the result of the synergy of several factors, including the efficient mixing in the twin-screw microcompounder, which, due to its miniature design, creates high shear force and uniform thermal distribution, resulting in the breakdown of phase clusters and a more uniform distribution of components and nanoparticles throughout the system. In addition, the relatively high cooling rate after the melt exits the extruder reduces the opportunity for independent crystallization of each component and suppresses phase separation. Another factor could be the sequence of component addition; in this study, nHA was first dispersed in the PCL matrix, followed by the addition of PEO and PEG. Such a sequence probably facilitates the initial distribution of nanoparticles and increased compatibility among components, helping maintain a uniform structure during cooling and leading to the observation of a single melting point. The effect of different orders of component addition on the phase behavior of the system is the subject of a separate investigation and will be reported elsewhere. According to previous reports, the miscibility/immiscibility of PCL/PEO and PCL/PEG systems depends on several factors, including the mixing ratio, component molecular weight, cooling rate, processing conditions and evaluation temperature [278, 279, 286-288, 304]. Most studies show that these binary mixtures exhibit immiscible behavior at room temperature. However, for many of these systems, a phase diagram with an upper critical solution temperature (UCST) has been reported, suggesting the possibility of miscibility at higher temperatures [278, 279, 286-288, 311]. It is worth noting that most of these studies were conducted on film samples.

In contrast, the results of Kupka et al. [304] on PCL/PEO fibers produced by solution electrospinning show that specific process conditions and the fibers' limited radial dimensions significantly limit the formation of distinct phase domains. Although microdomains of each phase may form, macroscopic phase separation is not observed in the as-spun samples, and the system appears to exhibit miscible behavior [304]. Besides, they observed a single melting point during the first heating and two during the second heating cycle in the DSC test [304]. These findings are consistent with those of the present study and indicate that process conditions and dimensional scale can play a decisive role in the phase behavior of these mixtures.

Figure 5.4B introduces a crystallization peak, in addition to the PCL crystallization peak, occurring at approximately 1 ˚C, which is significantly lower than the crystallization temperatures of pure PEO and PEG, approximately 43 ˚C. The same observation was reported previously for PCL/PEG systems [287] where in the molten state, PEG chains were dispersed in the PCL phase. Then, during the cooling step, these PEG chains form microcrystalline structures. Since these crystalline structures are too small, their crystallization occurs at a low temperature, around 0 ˚C. In the current study, the emergence of the crystalline peak at approximately 1 ˚C can be attributed to the formation of microcrystalline structures of PEO/PEG chains within the matrix.

Table 5.3 shows that the addition of nanoparticles to PCL led to an increase in the percentage of crystallinity. SEM images (Figures 5.2A and B) also demonstrated that the nanoparticles were not uniformly dispersed and were present in the matrix as agglomerations. In a related study, Xue et al. [310] reported that when the hydroxyapatite content in PCL exceeds 7%, the aggregation of nanoparticles is enhanced, allowing for easier growth of PCL spherulites. Considering these results and the comparison with previous findings, it can be concluded that the aggregation of nanoparticles in the present system likely created similar conditions, which is what caused the small increase in the percentage of crystallinity in the PCL/nHA sample.

Table 5.3 shows that, unlike the PCL/nHA system, adding 10% nanoparticles to the ternary blend resulted in a decrease in melting temperature and crystallinity percentage. This is also consistent with the SEM images, where the nanoparticles were more uniformly distributed in the matrix in the ternary blend samples. Therefore, it can be concluded that in this system, physical interactions between the hydroxyapatite nanoparticles and the polymers in the environment played an important role in reducing crystallization. A similar observation was previously reported by Wang et al. [312] in the PEG/nHA system. They also attributed this behavior to physical interactions between nanoparticles and PEG chains, which, although causing thermal changes, did not show any effect on the FTIR spectra. This consistency of results suggests that physical interactions, even in the absence of noticeable chemical changes in the structure, can be a key factor in altering the thermal behavior and reducing the crystallization of nanocomposite polymeric systems.

5.3.4 Thermal stability

Figure 5.5 displays the thermogravimetric analysis (TGA) and derivative thermogravimetric analysis (DTG) curves for plain and nanocomposite PCL and ternary blend melt electrospun fibers

prior to and following water immersion, along with the results for hydroxyapatite nanoparticles. In addition, the extracted thermal parameters and gravimetric residual values are summarized in Table 5.4.

In Figures 5.5A and B, the thermogravimetric analysis (TGA) curves for plain PCL (Figure 5.5A) and PCL/nHA (Figure 5.5B) nanocomposite melt electrospun fibers before and after immersion in water for one week are seen. As shown, the thermal behavior of both systems before and after immersion is identical, and no significant change in the decomposition onset temperature or the weight residue is observed. This result indicates that although hydroxyapatite nanoparticles are inherently hydrophilic, after compounding in the PCL matrix, they are firmly entrapped within the polymer structure and are not leached or washed out during water immersion. The DTG diagrams of PCL/nHA in both conditions of as-spun (BW) and after water (AW) immersion are presented in Figure S. 5.5, Supplementary Information. Figure 5.5C shows a single degradation peak in the ternary blend system comprising PCL, PEO, and PEG, indicating the miscibility of the constituent components. This is consistent with the DSC results (Table 5.3, indicating the presence of only one melting peak in the first heating run), as well as the FTIR results (Figure 5.3, showing no chemical changes), and suggests the miscibility of the components on a macroscale. In contrast, in the ternary blend system containing nHA before water immersion, two distinct peaks were observed in the DTG diagram, Figure 5.5E. This phenomenon can be tied to the presence of localized hydrophilic PEO/PEG chains at the interface with the nHA surface, which degrade at lower temperatures, while other parts of the chains along with the PCL matrix decompose at higher temperatures. Following water immersion, the rapid decomposition peak disappeared, suggesting that the surface hydrophilic constituents had been either washed away or reorganized, and the system had returned to a more uniform thermal behavior (Figure 5.5D). Table 5.4 shows that the leaching percentage of nHAs in the ternary-nHA system (4.5%) was slightly higher than that of the PCL/nHA sample (0.2%). This dissimilarity can be attributed to the presence of a portion of nanoparticles in the PEO/PEG chains or the boundary areas between them, which were separated from the polymer matrix and transferred to the aqueous environment during immersion in water due to the partial dissolution of these hydrophilic chains. This behavior suggests that some of the nanoparticles embedded in these interphase areas or in the PEO/PEG chains were removed from the system due to the washing out of these phases, resulting in a slight increase in the leaching amount in the ternary sample.

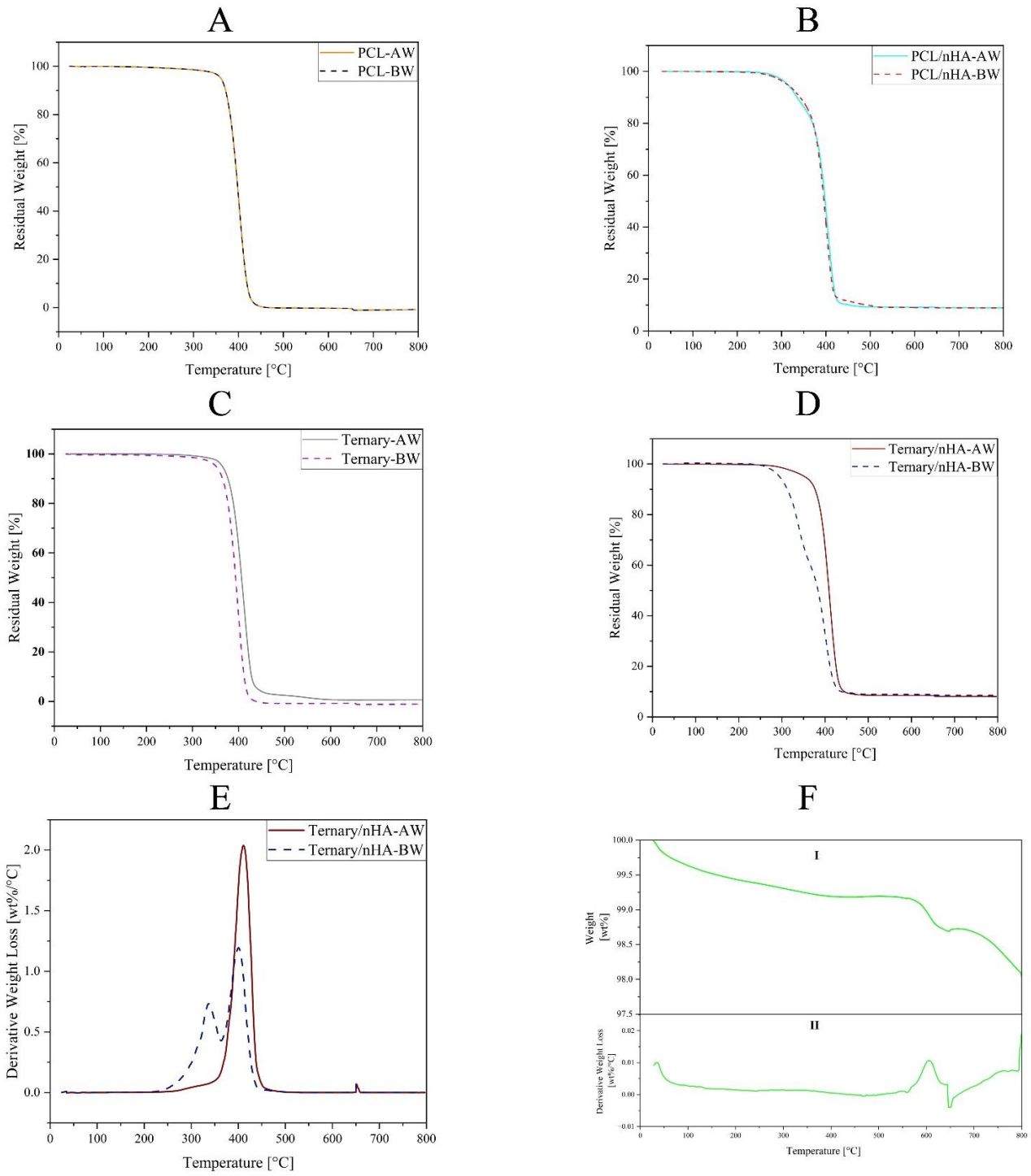

Figure 5.5 Comparing TGA curves of (A) PCL, (B) PCL/nHA, (C) Ternary blend, (D) Ternary blend/nHA melt electrospun fibers before (BW) and after (AW) immersion in water (E) Derived thermogravimetric (DTG) curves for the melt electrospun ternary blend/nHA fibers before (BW) and after (AW) immersion in water, and (F) the thermogravimetric (TGA) curve and its derivative (DTG) for hydroxyapatite nanoparticles in the powder form.

The TGA curves of nHA, Figure 5.5F, indicate that, under the test conditions, approximately 2% of the initial mass is lost. In all composite samples, approximately 8% (Figures 5.5B, D, E, and Table 5.4) of the total mass remains after the TGA test, whereas the initial amount of added nanoparticles was 10%. Given a 2% mass loss of nHA under the TGA procedure (Figure 5.5F) and considering the fact that the nanoparticles were dried prior to use, it can be concluded that the total nHA content in the samples is maintained, and almost no nHA leaching occurs during water immersion. These results show that, despite the presence of hydrophilic components such as PEO and PEG, hydroxyapatite nanoparticles did not form a separate hydrophilic phase with these components; instead, all components of the system are well mixed during the blending process, creating a uniform polymer phase in which the nanoparticles are embedded. Additionally, although the hydrophilic polymers (PEO and PEG) did not form a separate phase, their blending with PCL introduces hydrophilic chains into the system, which can help distribute nHA more evenly (Figures 5.2C and D).

Table 5.4 indicates that the incorporation of nHA into both PCL and ternary blend systems led to a reduction in the degradation onset temperatures (T_{onset}), 5% weight loss temperature (T_5), and 50% weight loss temperature (T_{50}). This decrease could be attributed to the surface catalytic effect of the active groups of nHA on ester bonds, as well as the presence of moisture adsorbed on the surface of the nanoparticles, which facilitates the chain scission process and causes degradation to start at a lower temperature [313]. Additionally, the relative decrease in crystallinity and increase in chain mobility in the presence of PEO/PEG and nHA may contribute to the decrease in thermal stability. However, after water immersion, especially in ternary blend/nHA, the T_5 and T_{50} values increased significantly. This indicates that the removal of extractable components and the reduction of surface moisture have weakened the rapid degradation pathways, leading to a relative improvement in thermal stability.

The inorganic residue (*Residue*) obtained from the TGA test, both before and after water immersion, was investigated as an indicator of the stability of nHAs within the melt electrospun fibers, Table 5.4. The difference between these two values (*ΔResidue*, Equation 5.2) was used to calculate the percentage of nanoparticles extracted from the environment (*nHA leached*) and the percentage of nanoparticles remaining in the sample (*nHA retention*) based on the relationships defined in Equation 5.3 and Equation 5.4. It should be noted that pure hydroxyapatite powder shows about 2% intrinsic mass loss in the TGA test, however, since the same heating conditions

were applied for both tests before and after immersion, this systematic weight loss in the *ΔResidue* difference is eliminated and does not affect the final values.

In the PCL/nHA system, the *ΔResidue* value was only about 0.02%, which, considering the initial proportion of 10% by weight of nHA in the sample, indicates about 0.2% release of nanoparticles from the structure. In contrast, in the ternary blend system containing nHA, the *ΔResidue* value was 0.45%, equivalent to 4.5% release of nanoparticles. This slight difference suggests that although in both systems, the mineral phase exhibits high stability in the aqueous environment, the presence of hydrophilic chains, PEO and PEG in the ternary blend structure, compared to the PCL/nHA system, created a higher permeability to the aqueous environment and led to a slightly lower nanoparticles retention.

Table 5.4 Results of thermogravimetric analysis (TGA) and calculated thermal parameters and residual weight of melt electrospun fibers before (BW) and after (AW) immersion in water[I]

Sample	PCL		PCL/nHA		Ternary blend		Ternary blend /nHA	
Condition	BW	AW	BW	AW	BW	AW	BW	AW
T_{Onset} [˚C] [II]	312.0	312.0	249.9	250.4	270.3	286.0	255.9	288.2
T_5 [˚C] [III]	361.1	361.1	312.5	313.8	351.3	364.8	294.5	353.0
T_{50} [˚C][III]	398.2	398.2	395.7	398.3	393.6	406.6	383.6	409.0
Residue @ 800 ˚C [%] [IV]	0	0	8.89	8.87	0	0	8.55	8.1
ΔResidue [%][IV]	-		0.02		-		0.45	
HA leached [%] [IV]	-		0.2		-		4.5	
HA retention [%] [IV]	-		99.8		-		95.5	

[I] The standard deviation (± SD) for all values is 0.0, so it is not included in the table.
[II] T_{onset} is determined by the tangential method.
[III] T_5 and T_{50} are the temperatures corresponding to 5% and 50% weight loss, respectively.
[IV] The residual value at 800 ˚C is detected, and the residual difference (*ΔResidue*), the percentage of nHA leached, and the percentage of nHA retained are calculated using Equation 5.2-5.4.

5.3.5 Mechanical properties

Figure 5.6 shows the schematic view of the uniaxial tensile test (Figure 5.6A) and the results of elastic modulus (Figure 5.6B), yield strain (Figure 5.6C), and yield stress (Figure 5.6D) after one

week of immersion of the samples in water for PCL, PCL/nHA, Ternary blend, and Ternary blend/nHA melt electrospun fibers.

Figure 5.6B shows that the modulus of the ternary blend/nHA melt electrospun fiber is lower than that of PCL/nHA. This decrease can be attributed to two factors: first, the smaller fiber diameter of the ternary blend/nHA sample, and second, the tendency of the PEO/PEG chains to aggregate around the nHA. This accumulation during exposure of the sample to an aqueous environment causes some of these chains to be washed away, which ultimately leads to disruption of fiber cohesion and weakening of mechanical modulus. In line with this observation, TGA test results also showed that the water immersion has a more significant effect on ternary blend/nHA than on neat ternary blend, which confirms the role of separation and leaching of hydrophilic chains around nanoparticles in reducing mechanical modulus. In other words, although considering the DSC results, PCL, PEO, and PEG are miscible under processing conditions, the presence of hydrophilic chains around the nanoparticles may cause some minor defects and reduce the structural perfection of the samples after immersion in water.

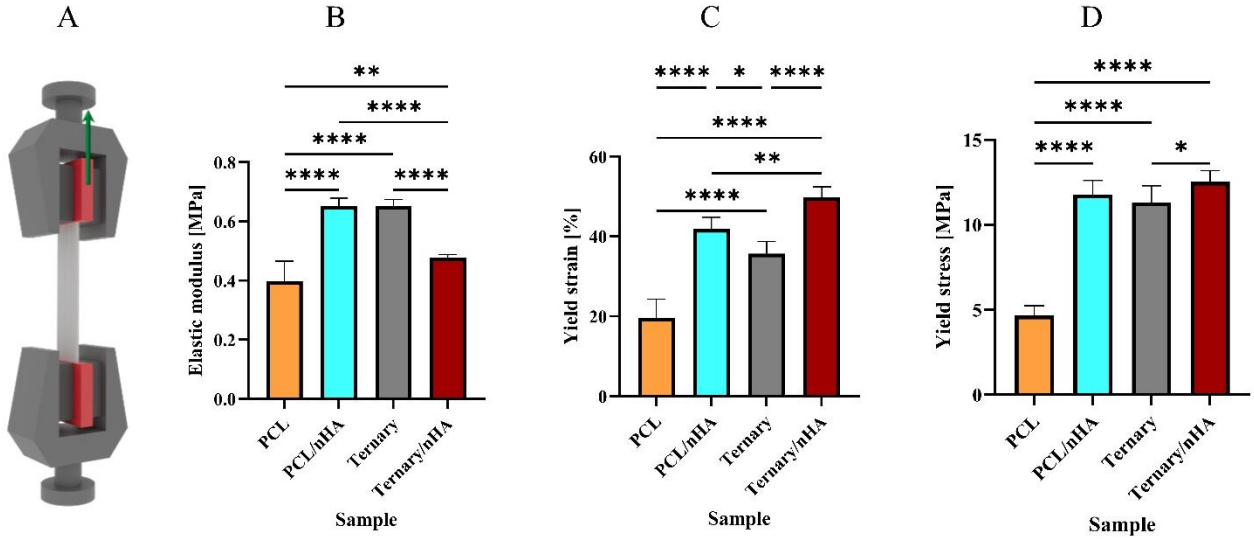

Figure 5.6 (A) Schematic view of uniaxial tensile testing on melt electrospun fibers after one week of water immersion, to evaluate mechanical properties. (B) Elastic modulus, (C) strain at the yield point, and (D) yield stress for PCL, PCL/nHA, ternary blend, and ternary blend/nHA samples. The results show a significant improvement in mechanical parameters with the addition of nHA as well as in ternary blend systems compared to neat PCL. Data are reported as mean ± standard deviation, and statistical differences were determined based on one-way ANOVA test with Tukey's post-test (*p < 0.05, **p < 0.01, ****p < 0.0001).

As shown in Figure 5.6C, the incorporation of nHAs led to an increase in yield strain in both melt electrospun PCL/nHA and Ternary blend/nHA fibers. In general, yield strain in polymer nanocomposites is governed by multiple factors, including the degree of crystallinity, the interactions between the nanoparticles and the polymer, and the dispersion state of the nanoparticles within the matrix. In PCL/nHA fibers, the particle-reinforcing effect of nHA is responsible for the rise in yield strain, although the crystallinity is higher than that of neat PCL fibers. The presence of nHA in the fibers promotes more efficient stress transfer within the PCL/nHA sample, thereby increasing the material's capacity for progressive deformation up to the yield point. The same observation has been documented in previous studies on PCL/nHA nanocomposites [313, 314]. In addition to the particle-reinforcing contribution, the Ternary/nHA system exhibits a distinct structural effect. As indicated by the DSC results (Table 5.3), the incorporation of nHA into the ternary blend reduces crystallinity. A decrease in crystallinity is typically associated with increased chain mobility. It can facilitate more plastic deformation before yielding.

Figure 5.6D demonstrates that the yield stress in the nanocomposite samples is higher than that in the samples without nanoparticles. This behavior results from the absorption of applied force by nHA, which enhances the tolerance threshold of the nanocomposites. In addition, it was observed that the yield stress in the ternary blend/nHA is higher than that in the PCL/nHA. This difference can be attributed to the more uniform dispersion of nanoparticles in the ternary blend structure, which enables better stress distribution and an improved yield stress compared to PCL/nHA.

5.3.6 Hydrolytic degradation behavior

The mass change graph of the samples during 28 weeks of immersion in PBS solution (Figure 5.7) indicates that PCL and PCL/nHA samples showed a negligible mass change (about 0.3 and 3%, respectively), while PCL/PEO/PEG and PCL/PEO/PEG/nHA ternary systems experienced a significant mass loss (about 21 and 25%, respectively). This difference indicates the simultaneous effect of the hydrophilic components (PEO and PEG) as well as HA nanoparticles on the permeability, swelling, and ultimately the hydrolytic degradation behavior of the system.

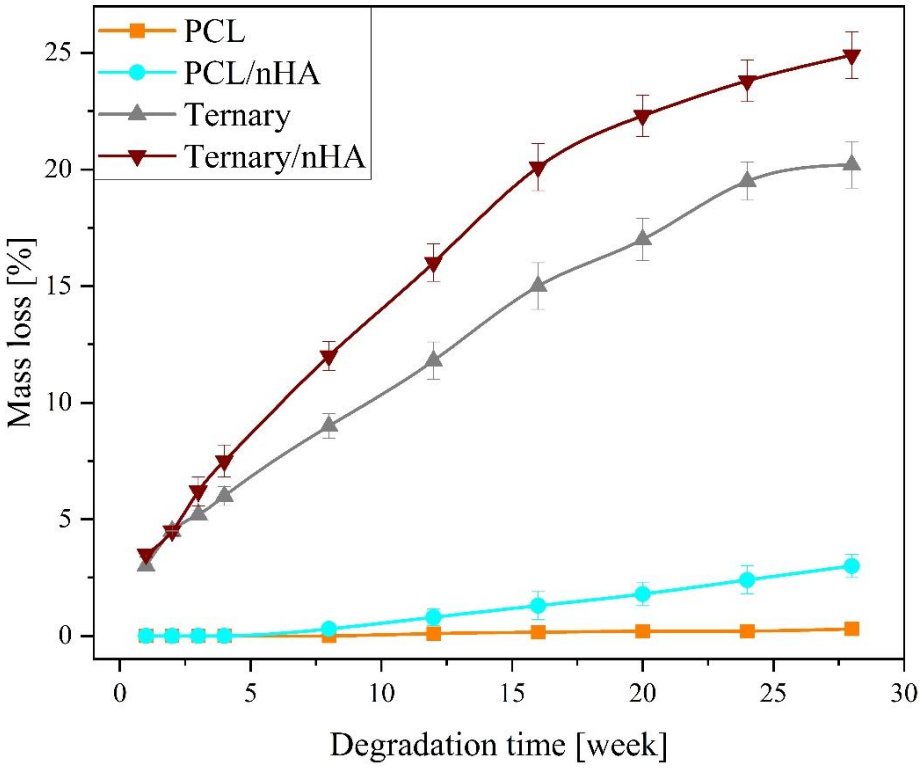

Figure 5.7 Changes in the percentage of mass loss of PCL, PCL/nHA, ternary blend, and ternary blend/nHA samples during 28 weeks in an aqueous environment. The ternary blend and ternary blend/nHA samples showed significant mass loss, while the PCL and PCL/nHA samples had high stability.

In the ternary sample without nanoparticles, although the total hydrophilic components constitute only 10% of the total composition, the mass loss exceeds their weight value. This phenomenon can be explained by the high water permeability and washing out of short and amorphous PCL chains, which occurs due to the presence of PEO and PEG. DSC and SEM studies revealed that, although these two hydrophilic components are mixed in the PCL matrix, the structure is not entirely homogeneous, with microcrystalline regions rich in PEO/PEG present within it (Figure 5.4B). Such regions, due to their high polarity, accelerate the penetration of water at the surface and the interface between the phases. As a result, in the first weeks of contact with the aqueous environment, water quickly penetrates the sample and, in addition to partially dissolving the PEG and PEO chains, leads to the separation of shorter and lighter PCL chains from the amorphous regions. Therefore, part of the weight loss is due to the washing out of minor components and amorphous PCL segments, rather than simply the loss of hydrophilic components. Additionally,

the presence of hydrophilic PEO/PEG chains in PCL can cause swelling in the system, which may accelerate the hydrolytic degradation of the sample.

Similar observations have been reported for other polymeric blend systems. For example, Visan et al. [315] observed in PCL/PEG (3/1) coatings that with only about 25% PEG, the mass loss in a simulated physiological environment increased from about 17% (after 2 weeks) to nearly 82% (after 16 weeks), and attributed this behavior to a combination of swelling, water infiltration, and the gradual withdrawal of short chains. Silva et al. [316] also reported that in PHB/PEG/VMT nanocomposites with only 5% PEG, the final mass loss was significantly higher than the nominal percentage of PEG, attributing this to the facilitation of water infiltration and the involvement of the main matrix in the degradation process. These results from independent studies demonstrate that the presence of even limited amounts of the hydrophilic phase may lead to a significant increase in mass reduction in polymer blends through morphological changes and the creation of diffusion pathways.

In the presence of nHAs, the PEO/PEG-rich microcrystalline domains identified by DSC (Figure 5.4B) may have a greater tendency to aggregate around the surface of the hydrophilic nanoparticles. This phenomenon could lead to increased local heterogeneity in the structure and, consequently, to the creation of more imperfections in the polymer matrix. Since the nanoparticles are uniformly dispersed throughout the system, these imperfections on a microscopic scale could create more cavities in the sample structure. Such subtle changes in the microstructure may account for the slight difference in mass loss observed between the two ternary systems with and without nanoparticles (25% for ternary-nHA vs. 21% for ternary).

For the kinetic analysis of this behavior, the experimental data are fitted based on an exponential model ($M_t=M_0.\ exp^{-kt}$) where M_t is the sample's mass at time point t, M_0 is the initial mass of the sample and k is the degradation rate constant. The results are summarized in Table 5.5. As can be seen, the degradation rate constant (k) in the PCL and PCL/nHA systems is in the range of 10^{-4} to 10^{-5} $week^{-1}$, and they do not reach a mass reduction of 10% during the test period, which indicates the high stability of these systems in the aqueous environment. In contrast, the k values in the ternary blend and ternary blend/nHA samples are significantly higher (about 10^{-2} $week^{-1}$), such that the time to reach 10% mass reduction in these two samples is about 8 and 11 weeks, and the time to reach 20% mass reduction is about 18 and 24 weeks, respectively. The high R^2 values (more than 0.9) also demonstrate a good fit of the model to the experimental data.

Table 5.5 Combining the results of exponential model fitting and experimental data to evaluate the degradation behavior of samples

Sample	mass loss @ 28 weeks[I] [%]	t_{10}[I] [week]	t_{20}[I] [week]	k[II] [week^{-1}]	R^{2} [II]
PCL	0.3 ± 0.0	(NR) 28 ≤	NR	9.4×10^{-5}	0.91
PCL /nHA	3.0 ± 0.5	(NR) 28 ≤	NR	9.4×10^{-4}	0.93
Ternary blend	20.9 ± 1.0	11≤	24 ≤	9.3×10^{-3}	0.90
Ternary blend/nHA	24.9 ± 1.0	8≤	18 ≤	1.2×10^{-2}	0.90

[I] The t_{10}, t_{20}, and percent mass loss at week 28 were obtained based on experimental data.
[II] The k and R^2 values are calculated from fitting the data with an exponential model ($M_t=M_0.\ e^{-kt}$).

Taken together, these results indicate that the presence of hydrophilic components (PEO and PEG) in the ternary blend system, as well as the synergistic effect of nHA, both play a decisive role in accelerating the hydrolytic degradation process. This feature could be of great importance in the design of biodegradable scaffolds with a controlled time course for bone tissue engineering.

5.4 Conclusion

This study illustrates that the fabrication of a ternary blend of PCL/PEO/PEG reinforced with nHA via the melt electrospinning technique constitutes a potential and effective method for creating nanocomposite fibers. The FTIR spectra suggest that the processing conditions, particularly the temperature, are safe enough to ensure that no dehydroxylation of nHA occurs in the system. In addition, despite the presence of multiple constituents in the blend, no detectable change in the system was observed. Morphological studies confirmed that the presence of hydrophilic polymers improved the dispersion of nanoparticles and causes the formation of channel-like surface patterns following water immersion. FTIR and DSC results showed that, although no significant chemical changes were made to the structure, physical interactions between the nanoparticles and the multicomponent matrix played a crucial role in reducing crystallinity and modifying the thermal behavior of the material. TGA results confirmed the high stability of nHA within the polymer matrix, showing only a negligible release after one week of immersion in water. Mechanical investigation demonstrated that the use of nanoparticles enhanced the yield stress and strain of the melt electrospun fibers. However, a decrease in modulus was inevitable in the ternary blend/nHA system due to the leaching of hydrophilic chains. Hydrolytic degradation studies also revealed that

ternary blend systems have a significantly higher degradation rate than PCL, which could be of critical importance in designing fibers with controlled degradation and simultaneous tissue regeneration. Overall, the findings of this study indicate that the use of ternary blend in melt electrospinning as an innovative strategy can provide a new pathway for the development of bioactive and biodegradable scaffolds in future bone tissue engineering applications.

5.5 Supporting Information Description

The supporting information file contains supplementary data and results that support the findings presented in the main text of the paper. In this file, microscopic images and elemental analyses of hydroxyapatite nanoparticles and fibers produced by melt electrospinning are presented, showing the nanoparticle size distribution, the uniformity of calcium and phosphorus elements on the fiber surface, and surface changes in the samples before and after exposure to an aqueous environment. Also, quantitative results from EDX analysis, including the percentage of calcium surface coverage, weight percentage of elements, and the Ca/P atomic ratio for different samples, are reported.

In addition, DSC test curves and tables are presented to investigate the thermal behavior and crystallization of the samples before and after the melt electrospinning process, providing detailed information on the glass transition temperature, melting temperature, enthalpy of fusion, and crystallization. Furthermore, dynamic mechanical analysis (DMA) results for the Ternary/nHA sample are provided to complement the DSC findings, offering enhanced sensitivity in detecting the α-relaxation and thereby supporting the assessment of glass transition behavior. In addition, the results of thermal decomposition tests are also presented to compare the degradation behavior of the PCL/nHA samples before and after water immersion. This set of supporting information enables a more detailed analysis of the microstructure, thermal stability, and mineral phase distribution in the scaffolds. It fully supports the interpretations presented in the manuscript.

Acknowledgments

The authors sincerely thank Mohsen Hasani Zadeh for his valuable scientific contributions. Special thanks are extended to Matthieu Gauthier and Claire Cerclé for their technical assistance. Financial support from the Natural Sciences and Engineering Research Council of Canada (NSERC); and the Fonds de recherche du Québec – Nature et Technologies (FRQNT) is gratefully acknowledged.

Data Availability Statement

The data supporting the findings of this study are openly available in Mendeley data at 10.17632/k42mmvwrb2.1.

5.6 Supplementary materials

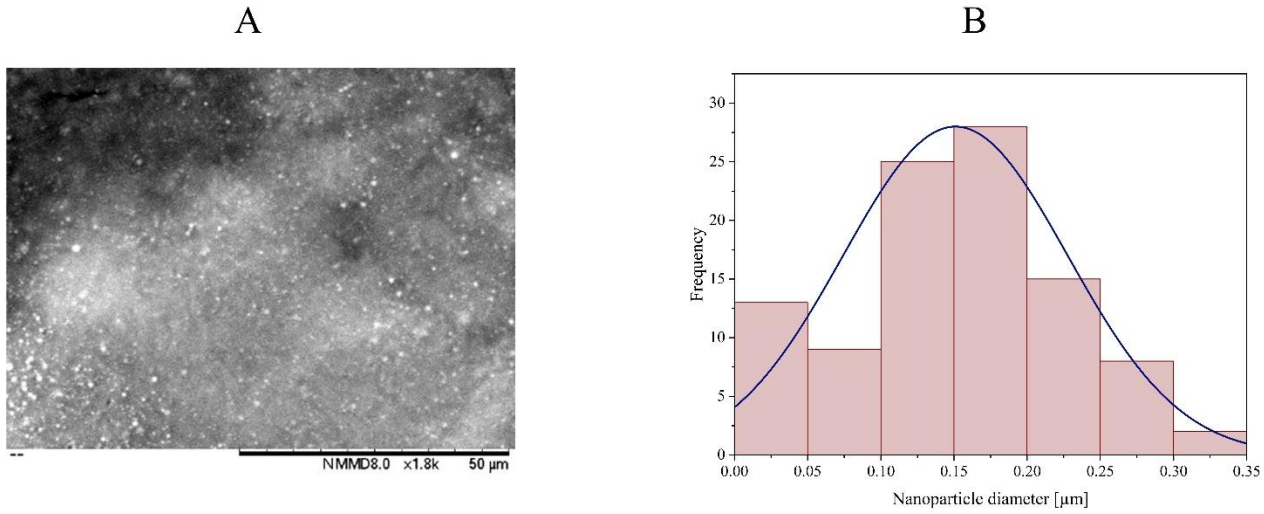

Figure S. 5.1 SEM image of hydroxyapatite nanoparticles in the initial state (A) as received from the supplier and histogram (B) of the size distribution of these nanoparticles. The scale bar in the SEM image is 50 µm.

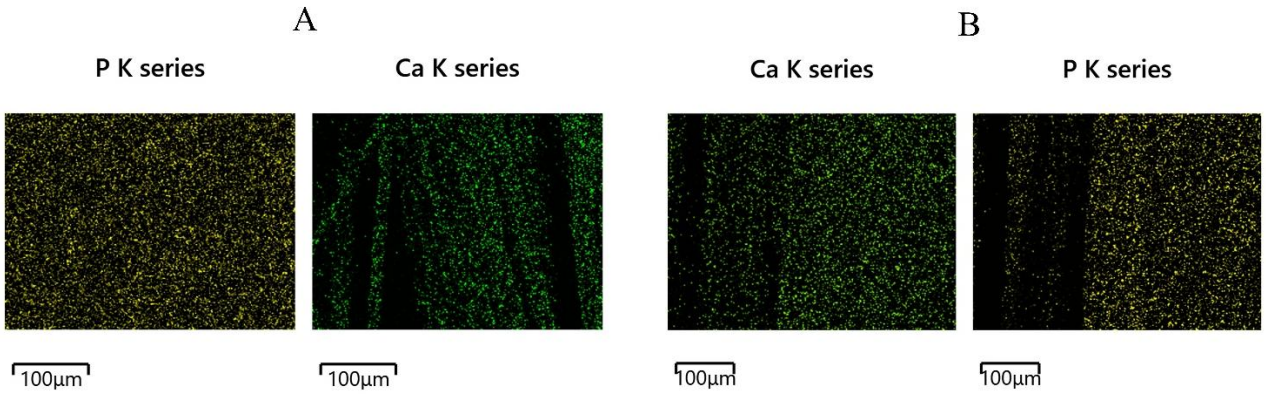

Figure S. 5.2 EDX mapping of the distribution of phosphorus (P) and calcium (Ca) elements on the surface of melt electrospun fibers before immersion in an aqueous medium. (A) PCL/nHA, and (B) ternary/nHA.

Table S. 5.1 Results of EDX analysis for PCL/nHA and Ternary/nHA melt electrospun fibers after one week of water immersion. The values indicate the percentage of surface area covered with calcium, the weight percentage of calcium and phosphorus elements, and the Ca/P atomic ratio in the samples.

Sample	Ca- map area [%]	Ca [wt %]	P [wt %]	Ca/P [atom %]
PCL/nHA- AW	92.0	7	2	2.7
Ternary/nHA- AW	92.7	11	4	2.1

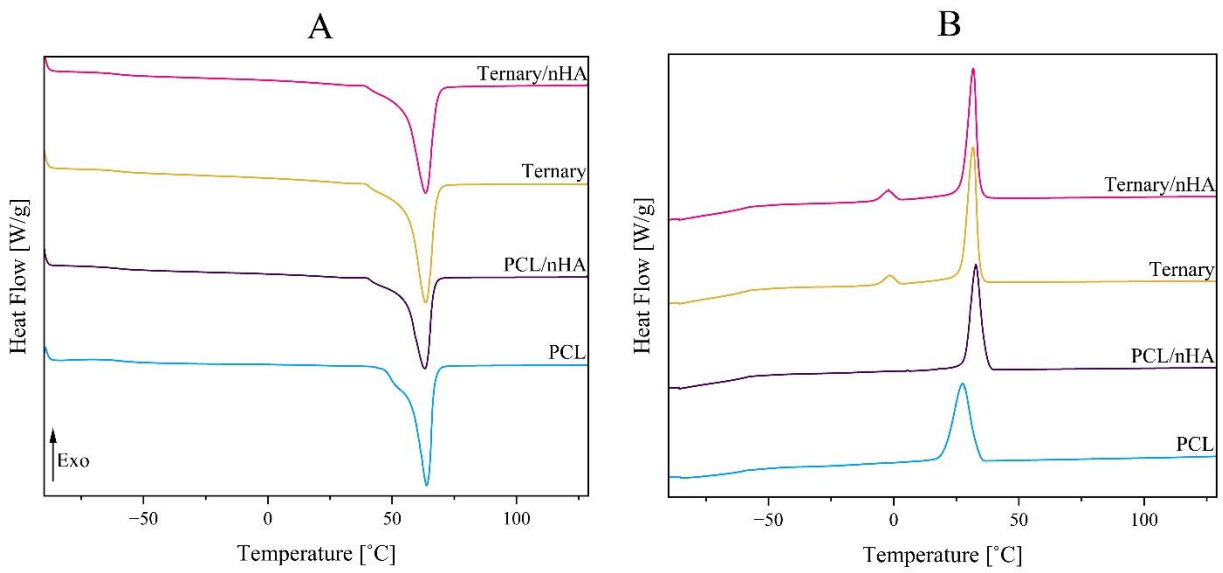

Figure S. 5.3 DSC curves for investigating the thermal behavior of samples before the melt electrospinning process (BME) in (A) first heating cycle and (B) cooling cycle. Exothermic direction is upward.

Table S. 5.2 DSC test results (first heating cycle) for PCL, PCL/nHA, ternary, and ternary/nHA samples. Data include glass transition temperature (T_g), melting temperature (T_m), melting enthalpy (ΔH_m), crystallization temperature (T_c), and crystallization enthalpy (ΔH_c). BME represents samples before the melt electrospinning process, and AME represents samples after the melt electrospinning process.

Sample			PCL	PCL/nHA	Ternary	Ternary/nHA
BME	T_g [˚C]		-51.4 ± 0.7	-53.5 ± 0.4	-53.1 ± 0.5	-53.6 ± 0.7
	Melting	T_m [˚C]	63.9 ± 1.0	63.2 ± 0.7	63.5 ± 0.9	63.5 ± 0.5
		ΔH_m [J/g]	60.8 ± 0.0	53.9 ± 0.2	67.8 ± 0.0	65.5 ± 0.2
	Crystallinity	$T_{C\text{-}PCL}$ [˚C]	27.5 ± 0.3	32.8 ± 0.1	31.7 ± 0.3	31.7 ± 0.2
		$T_{C\text{-}Dispersed}$ [˚C]	-	-	-1.8 ± 0.0	-2.0 ± 0.0
		$\Delta H_{C\text{-}PCL}$ [J/g]	45.2 ± 0.3	41.6 ± 0.5	47.2 ± 0.4	45.7 ± 0.3
		$\Delta H_{C\text{-}Dispersed}$ [J/g]	-	-	3.3 ± 0.0	3.8 ± 0.2
AME	T_g [˚C]		-50.5 ± 1.1	-52.9 ± 0.3	-53.2 ± 0.8	-54.4 ± 0.5
	Melting	T_m [˚C]	62.5 ± 0.8	60.9 ± 0.6	62.0 ± 0.7	59.7 ± 0.1
		ΔH_m [J/g]	52.3 ± 0.4	57.6 ± 0.2	72.6 ± 0.3	68.2 ± 0.3
	Crystallinity	$T_{C\text{-}PCL}$ [˚C]	29.7 ± 0.1	32.1 ± 0.2	33.3 ± 0.1	31.6 ± 0.3
		$T_{C\text{-}Dispersed}$ [˚C]	-	-	1.5 ± 0.0	0.5 ± 0.1
		$\Delta H_{C\text{-}PCL}$ [J/g]	40.6 ± 0.2	47.4 ± 0.2	50.3 ± 0.2	45.2 ± 0.3
		$\Delta H_{C\text{-}Dispersed}$ [J/g]	-	-	1.6 ± 0.0	3.6 ± 0.1

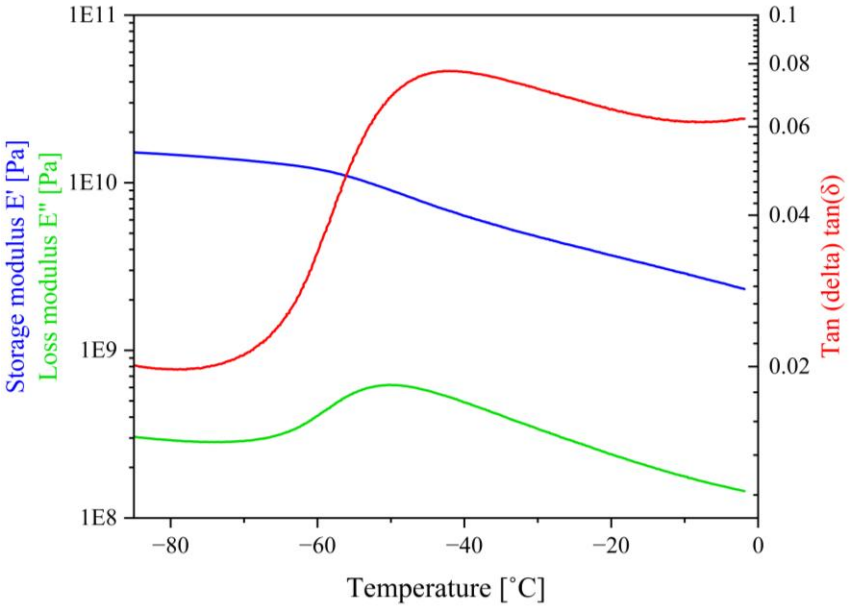

Figure S. 5.4 Temperature dependence of storage modulus (E′), loss modulus (E″), and damping factor (tan δ) for the Ternary/nHA system obtained by dynamic mechanical analysis (DMA). Measurements were performed in dual cantilever mode at a frequency of 1 Hz, a strain within the linear viscoelastic region (0.16%), and a heating rate of 3 ˚C min^{-1} over the temperature range of -85 to 0 ˚C.

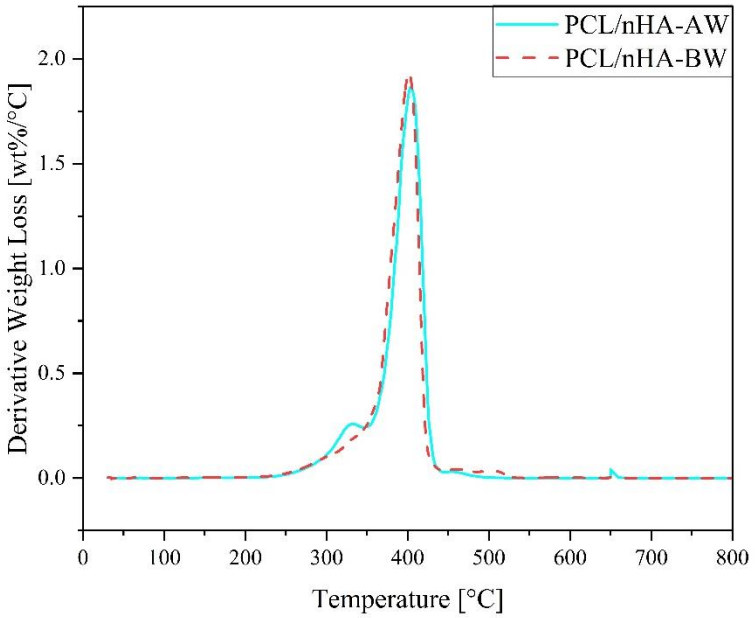

Figure S. 5.5 DTG curves of PCL/nHA samples before water immersion (BW) and after water immersion (AW). The results show that the thermal degradation behavior of the fibers was similar in both cases, and immersion in water or non-immersion does not significantly alter the thermal degradation profile.

CHAPTER 6 ARTICLE 3: BIOACTIVE NANOCOMPOSITE SCAFFOLDS BY MELT ELECTROSPINNING OF POLY-ε-CAPROLACTONE/POLYETHYLENE OXIDE/POLYETHYLENE GLYCOL-HYDROXYAPATITE BLENDS FOR BONE TISSUE ENGINEERING

Elham Karimi[a], Mansoureh Mohseni Garakani[b], Marie-Claude Heuzey[a], Frej Mighri[c], Derek H. Rosenzweig[b,d], Abdellah Ajji[a,*]

[a] Department of Chemical Engineering, Polytechnique Montréal, Montreal, Québec, Canada

[b] Department of Surgery, Division of Orthopaedic Surgery, McGill University, Montreal, Québec, Canada

[c] Department of Chemical Engineering, Laval University, Québec, Québec, Canada

[d] Department of Orthopedic Surgery, University of Connecticut School of Medicine, Farmington, Connecticut, 06032, USA

*Corresponding Author: abdellah.ajji@polymtl.ca

Submitted to ACS Applied Bio Materials, January 15, 2026

Authorship contribution statement of Elham Karimi: Conceptualization; Data curation; Formal analysis; Investigation; Methodology; Validation; Visualization; Writing – original draft; Writing – review and editing.

Abstract

Bone defects that are beyond the body's natural repair capacity remain a significant challenge in bone tissue engineering. In recent years, various synthetic materials have been introduced as potential alternatives for repairing these defects, but most of them have limitations. In particular, calcium phosphate cements (CPCs) possess desirable bioactivity but poor mechanical strength. Polymethyl methacrylate (PMMA) exhibits high structural stability, but lacks adequate degradability and bioactivity. These obstacles highlight the need to develop materials that balance structural integrity with biological function. In this study, poly-ε-caprolactone/polyethylene oxide/polyethylene glycol (PCL/PEO/PEG) nanocomposite scaffolds containing hydroxyapatite nanoparticles (nHA) were fabricated using solvent-free melt electrospinning and assessed for their physical, chemical, and biological properties. Three masterbatch systems (nHA@PCL,

nHA@PEO, and nHA@PEG) and varying percentages of nanoparticles (1%, 5%, 10%, and 20%) were investigated. The results showed that the nHA@PCL system resulted in better stability of nanoparticles after immersion, and ternary blend (PCL/PEO/PEG) scaffolds, especially Ternary-nHA10@PCL (PCL/PEO/PEG-nHA10@PCL), provided the highest hydrophilicity, cell adhesion, cellular metabolic activity, cell proliferation by DNA counting, and calcification deposition. Overall, blending nHA with PCL as the main component, along with the presence of hydrophilic polymers such as PEO and PEG, is an effective strategy for simultaneously promoting human osteoblast and vascular endothelial cell growth and activity, and Ternary-nHA10@PCL is introduced as the optimal option.

Keywords: Melt electrospinning, Polymeric blends, Hydroxyapatite, Nanocomposite scaffolds, Bioactive scaffolds, Bone tissue engineering

6.1 Introduction

Bone tissue regeneration is one of the fundamental challenges in regenerative medicine [10]. Bone defects resulting from trauma, degenerative diseases, or tissue resection surgeries often exceed the body's natural repair capacity and require the use of alternative scaffolds [59]. Autografts and allografts are still recognized as clinical standards [49, 317]. However, limitations such as resource scarcity, complications at harvest sites, and the risk of immune rejection underscore the need to develop novel techniques to manage these challenges [4]. Tissue engineering is a promising methodology combining scaffolds, cells and biologics to rebuild damaged tissues [318]. In the case of bone, scaffolds are often designed to resemble the structure and function of the extracellular matrix to facilitate the adhesion, proliferation, and differentiation of osteogenic cells [40, 319]. In this regard, key scaffold features, including biocompatibility, controlled biodegradability, porous microstructure, and desirable surface properties, are of particular importance [320]. In particular, surface hydrophilicity and the presence of bioactive agents play a decisive role in cellular interactions and the mineralization process [321].

One of the most popular synthetic polymers in this field is poly-ε-caprolactone (PCL), which has attracted wide attention due to its biocompatibility, biodegradability, and processability [94]. However, its hydrophobic nature and slow degradation rate can limit its biological performance [97]. To address these limitations, we turn to the melt blending process. Melt-blending protects the sample from the presence of residual solvent, allowing PCL mixing with biocompatible

hydrophilic polymers such as polyethylene oxide (PEO) and polyethylene glycol (PEG). The goal is to enhance the hydrophilicity and, consequently, the biocompatibility of the fabricated scaffold. For example, Remya et al. [113] reported that adding PEO to PCL scaffolds improved wettability, initial osteoblast cell adhesion, viability, and proliferation. Cao et al. [322] also showed improved mineral deposition and alkaline phosphatase (ALP) activity in the presence of PEG. Although PEO and PEG are chemically identical, their distinction is mainly based on a naming convention related to molecular weight range; PEG is usually used for lower molecular weights (below 20,000 g/mol) and PEO for higher molecular weights (above 20,000 g/mol) [323]. Nonetheless, this difference in molecular weight leads to significant differences in rheological behavior, the degree of chain entanglement, and, consequently, in their performance during processing [115, 324]. In particular, PEG, due to its lower molecular weight, primarily acts as a plasticizer, increasing chain mobility and reducing the system's viscosity [125]. In contrast, PEO, with a high molecular weight, acts as an elastic component, increasing extensional elasticity by increasing chain entanglement, which is essential for jet stability during electrospinning [115]. Recent studies have shown that combining these two polymers to create a broader molecular weight distribution (MWD) is more effective at improving electrospinning than simply increasing molecular weight [115]. It has also been reported that although each of these polymers has limited performance in electrospinning alone, their combination significantly improves process stability and fiber uniformity [115]. This approach has also been used in the present work to simultaneously utilize the plasticizer and elastic effects. On the other hand, the use of hydroxyapatite nanoparticles (nHA) as a bioactive phase, in addition to mimicking the mineral phase of the bone, may enhance the osteogenic properties of the scaffold and provide a promising environment for bone cell adhesion and differentiation [325-327]. However, most existing studies in this area have focused on solution electrospinning. In contrast, the development of multicomponent systems via melt electrospinning, especially for tissue engineering applications, has remained mostly untouched.

Among the various scaffold fabrication methods, melt electrospinning has attracted increasing attention as a solvent-free technology, as it reduces the need for post-processing steps and improves biosafety by eliminating organic solvents [14, 328, 329]. This method enables the production of continuous fiber networks with controllable diameters and a microstructure closely resembling that of the natural extracellular matrix, a desirable feature for bone tissue engineering [14]. From a manufacturing and production perspective, melt electrospinning has the potential for

scalability and reduced operating costs due to the continuous nature of the process and the lack of the need for solvents [14, 330]. In contrast, technologies such as melt electrowriting and extrusion-based printing, although they offer higher precision in controlling predefined geometries and layer-by-layer structures, the more discrete nature of their process can impose limitations on the production rate. In other words, the relative simplicity of the melt electrospinning process and the lack of need for complex pre-production designs can help reduce costs and facilitate large-scale development [14, 331, 332].

The present study aims to develop and investigate nanocomposite scaffolds based on the ternary composition of PCL/PEO/PEG along with hydroxyapatite nanoparticles. In this research, an attempt has been made to overcome the limitations of conventional PCL scaffolds by combining hydrophilic polymers and a mineral bioactive agent, and providing a suitable platform for simultaneous improvement of primary human osteoblast and vascular endothelial cell growth and activity.

6.2 Materials and Methods

6.2.1 Materials

Poly-ε-caprolactone (PCL; Capa™ 6500, Mn ≈ 50,000 $g.mol^{-1}$, granules) was obtained from Perstorp (Canada). Polyethylene glycol (PEG; Mn ≈ 20,000 $g.mol^{-1}$, flakes) and polyethylene oxide (PEO; Mv ≈ 600,000 $g.mol^{-1}$, powder) were bought from Sigma-Aldrich (USA). Hydroxyapatite nanoparticles (nHA; particle size < 200 nm, purity ≥ 97%) were purchased from Sigma-Aldrich (USA) and used as the bioactive component in the preparation of nanocomposites. All materials were used without any additional purification.

6.2.2 Scaffolds fabrication

6.2.2.1 Preparation of masterbatches and nanocomposites

All polymer formulations were prepared using a micro twin-screw compounder (DSM Xplore, Micro 5 cc, Netherlands) with a total batch mass of 3 g. Three different masterbatch routes were considered for the preparation of nanocomposites: (A) dispersion of hydroxyapatite nanoparticles in poly-ε-caprolactone (nHA@PCL), (B) dispersion of nanoparticles in polyethylene oxide (nHA@PEO), and (C) dispersion of nanoparticles in polyethylene glycol (nHA@PEG). The three different routes for preparing the masterbatches are schematically shown in Figure 6.1. In the first

step, the masterbatch was prepared for 7 min at 70 ˚C and 50 rpm, and in the second step, these masterbatches were mixed with the remaining components for 8 min under the same conditions. In total, the mixing time for each formulation was 15 min.

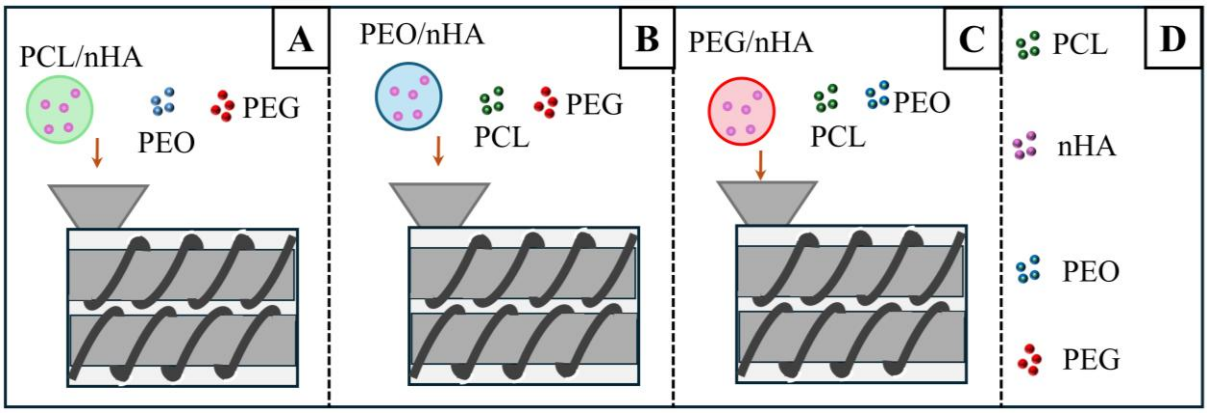

Figure 6.1 Schematic representation of three different routes for preparing polymer masterbatches, including: (A) dispersion of nanoparticles in PCL, (B) dispersion in PEO, (C) dispersion in PEG, and (D) base compounds.

To evaluate the content effect of nanoparticles on the final properties, formulations were prepared with different percentages of nHA (1, 5, 10, and 20 wt%). Control samples, including neat PCL, PCL/nHA nanocomposite, and PCL/PEO/PEG ternary blend (90/5/5 wt%) without nanoparticles, were also prepared. Table 6.1 presents the components and blends used in this study, along with their corresponding weight values. This study employs the naming scheme Ternary blend-nHAx@Host, where x represents the weight percentage of hydroxyapatite nanoparticles in the PCL/PEO/PEG ternary blend, and @Host denotes the polymer phase of the initial masterbatch (PCL, PEO or PEG).

In preliminary studies, various compositions of PEO and PEG, ranging from 5% to 25% wt% each (up to 50% wt% in total), were evaluated. The results showed that an increase of more than 5% of each component accelerates the degradation process in an aqueous environment and reduces the physical stability of the scaffolds. Accordingly, the current composition was selected as a system with a good balance between processability, structural stability, and desirable biological properties.

Table 6.1 Formulation composition of the samples used in this study

Sample code	Initial masterbatch	PCL [wt%/g]	PEO [wt%/g]	PEG [wt%/g]	nHA [wt%/g]
PCL	-	100/3.00	-	-	-
PCL-nHA10	nHA@ PCL	90/2.70	-	-	10/0.30
Ternary	-	90/2.70	5/0.15	5/0.15	-
Ternary-nHA1@PEO	nHA@ PEO	89/2.67	5/0.15	5/0.15	1/0.03
Ternary-nHA1@PEG	nHA@ PEG	89/2.67	5/0.15	5/0.15	1/0.03
Ternary-nHA1@PCL	nHA@ PCL	89/2.67	5/0.15	5/0.15	1/0.03
Ternary-nHA 5@PCL	nHA@ PCL	85/2.55	5/0.15	5/0.15	5/0.15
Ternary-nHA 10@PCL	nHA@ PCL	80/2.40	5/0.15	5/0.15	10/0.30
Ternary-nHA 20@PCL	nHA@ PCL	70/2.10	5/0.15	5/0.15	20/0.60

6.2.2.2 Melt electrospinning process

The melt-blended specimens were cut into small pieces using scissors, loaded into a 9-mL stainless steel syringe, and placed in the cylindrical heating chamber, which maintained a temperature of 130 ˚C throughout the process. The syringe was equipped with a steel needle (20G) that acted as a spinneret and had an electrical ground connection, while the rotating drum collector was set at a positive potential. The schematic of the apparatus used is shown in Figure 6.2.

To achieve uniform and aligned scaffolds, the process conditions were carefully controlled. The collector rotation speed was set to 21 rpm, the applied voltage was 7.5 kV, the needle tip-collector distance was 7.5 cm, and the feed rate was set to 1000 $\mu L.h^{-1}$. Under these conditions, all formulations, including the ternary blend (PCL/PEO/PEG), PCL/PEO/PEG/nHA nanocomposites with different percentages of nanoparticles, neat PCL, and PCL-nHA, were converted into continuous and aligned fibers with uniform morphology, which allowed for direct and reproducible comparisons between samples.

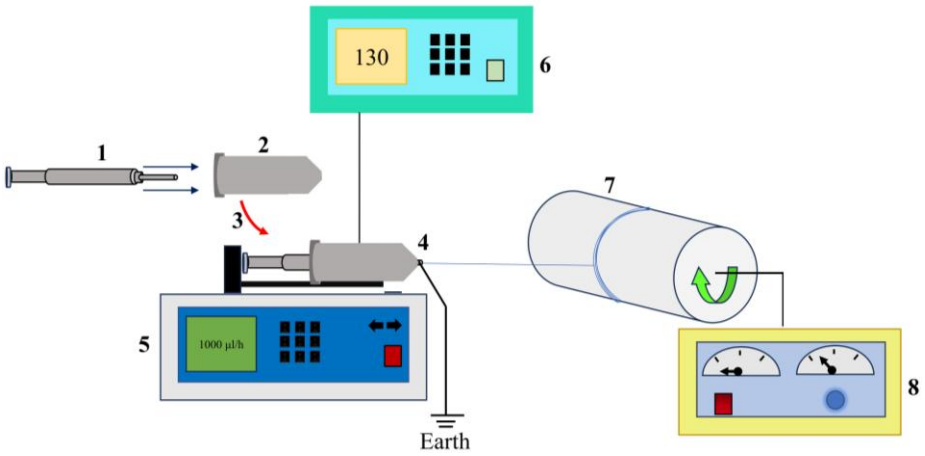

Figure 6.2 A schematic view of the melt electrospinning apparatus: (1) stainless steel syringe, (2) stainless steel heater, (3) to supply the molten mixture at a steady flow, the temperature-controlled syringe (in-line heater) was strapped onto the syringe pump, (4) needle, (5) pump, (6) temperature controller, (7) drum collector and (8) high voltage supplier.

6.2.3 Scaffold characterization

6.2.3.1 Morphology and nanoparticle retention

The morphology of melt electrospun scaffolds was examined via a scanning electron microscope (SEM; TM3030Plus, Hitachi, Japan) with the accelerating voltage set at 15 kV.

To identify and reveal the hydrophilic polymer phases (PEO and PEG) and evaluate the potential release of hydroxyapatite nanoparticles in contact with aqueous environment, the samples were immersed in deionized water for one week. After this step, the samples were dried under vacuum for 48 h to obliterate any residual moisture.

6.2.3.2 Contact angle measurement

To evaluate the cell adhesion potential, the hydrophilicity of the samples was investigated by measuring the static contact angle. For this purpose, an FDS tensiometer (model TBU 90E, Data Physics, Germany) was used at ambient temperature. The scaffolds were fixed to glass slides, and then five µL drops of deionized water (MilliQ) were applied to the sample surface using a microsyringe [333]. For each scaffold, the experiment was performed at least in six different positions. The data were analyzed using the device's dedicated software (SCA20-U), and the mean and standard deviation of the contact angle were reported.

6.2.4 Scaffolds biocompatibility

6.2.4.1 Cell culture conditions

6.2.4.1.1 Osteoblasts

Human osteoblast cells were isolated from the lumbar spine cortical bone (samples obtained from four donors. This study protocol was approved by the Research Institute of McGill University Health Center, Research Ethics Board (REB #2020-5647). Informed consent was obtained from the patients' families, and all procedures were conducted in collaboration with Transplant Québec. Detailed demographic information of the tissue donors is provided in Table 6.2. The osteoblast cell isolation was performed according to the protocol reported by Fairag et al. [334]. In this procedure, the cortical bone was clipped with sterile rangeurs into tiny chips (sized between 3-5 mm). Samples were soaked 5min, and washed three times with gentle shaking in sterile phosphate buffer saline (PBS) pH 7.4 (1X) (Gibco, Thermofisher, Canada) supplemented with Primocin (InvivoGen, San Diego, CA, USA) and Fungizone (Sigma-Aldrich, Oakville, ON, Canada). The bone chips were then incubated in high-glucose Dulbecco's modified Eagle medium (DMEM) with 25 mM HEPES, 1 mM sodium pyruvate and supplemented with 1% Pen-Strep (PS), and 10% fetal bovine serum (FBS) (all from Gibco, Thermofisher, Canada), containing 1.5 mg/mL collagenase II (Invitrogen), overnight (for 14-16 hours) at 37 ˚C on a rocker for complete removal of soft tissue. After three rounds of washing with sterile PBS 2X (with antibiotics), the cleaned bone chips were transferred to a T75 flask (Sarstedt, TC Flask T75, Stand, Vent. Cap, Germany) with complete growth media (DMEM plus 10% FBS and 1% PS) for a week to allow osteoblasts outgrowth from the bone chips. Following their outgrowth from the bone fragments, osteoblast cells at 80% confluence were passaged and utilized for the experiments between passage 1 and 4.

For seeding on the scaffolds, cells at passage 1 were cultured in DMEM supplemented with 10% FBS and 1% PS at 37 ˚C and 5% CO_2. At 90% confluence, cells were passaged with 0.25% trypsin-EDTA (1X) (Gibco, Thermo Fisher, Canada). Next, fresh DMEM containing 10% FBS and 1% PS was added. To separate the suspended cells in the media, the cell suspension was centrifuged for 5 min at 1500 rpm and then the pellet of the separated cells at the bottom of the vial were resuspended in fresh media, counted using a hemocytometer, and adjusted to 2.5×10^5 cells/mL.

Table 6.2 Demographic characteristics of vertebral tissue donors

Name	Age	Sex[1]	Cause of Death
Qth 328	27	F	Massive hemorrhage secondary to multiple road trauma (MVA)
Qth 305	73	F	CVA/Stroke
Qth 310	47	M	Anoxia, Cardiac Arrest
Qth 309	31	M	Head trauma

[1] Sex/gender is defined based on the received data from Transplant Québec.

6.2.4.1.2 Human umbilical vein endothelial cells (HUVECs)

HUVECs (Lonza, USA) were cultured at passage 4. The general culture conditions, including temperature, CO_2 level, and passage steps, were similar to those described for osteoblasts. The difference was that EGM®-2 complete culture medium (Lonza, USA) was used for HUVECs. This medium was prepared by combining 500 mL of EBM-2 Basal Medium with the contents of the EGM-2 SingleQuots supplement kit (CC-4176), including 0.5 mL hEGF, 0.5 mL hydrocortisone, 2.0 mL hFGF-b, 0.5 mL VEGF, 0.5 mL R3-IGF-1, 0.5 mL ascorbic acid, 0.5 mL heparin, 10.0 mL FBS, and 0.5 mL GA. After the cells reached approximately 90% confluency, they were washed with sterile PBS and detached with 0.25% trypsin-EDTA solution (1X), and the subsequent steps were similar to the osteoblast protocol.

6.2.4.2 Seeding of melt electrospun scaffolds

Aligned melt electrospun scaffolds (≈95 mm²) were sterilized by UV irradiation (5 min per side), preconditioned in DMEM supplemented with 1% PS for 10 min, and subsequently transferred to 48-well non-adherent plates (Sarstedt AG & Co., Germany)[273]. A cell suspension (200 µL, 5×10^4 cells) was seeded onto each scaffold, followed by overnight incubation at 37 ˚C in a humidified atmosphere with 5% CO_2. To ensure the accuracy of the measurement, the day after (24 hours after cell seeding), the scaffolds were transferred to new wells containing fresh medium. This procedure eliminated any interference from non-adherent cells, allowing only the signal from metabolically active cells attached to the scaffold to be recorded. From that time on, 500 µL of fresh medium was added to each sample.

Complete DMEM medium was used for osteoblasts, and complete EGM®-2 medium was used for HUVECs. The culture medium for osteoblast scaffolds was changed every three days, and the culture medium for HUVEC scaffolds was changed every other day. The samples were cultured for 28 days.

6.2.4.3 Cell adhesion, viability, and proliferation assays

6.2.4.3.1 Alamar Blue assay

The Alamar Blue assay (resazurin-based; Invitrogen, USA) was used to assess the cellular metabolic activity. At predetermined times, the culture medium was replaced with fresh assay solution containing 10% (v/v) Alamar Blue reagent in 90% supplemented high-glucose DMEM medium (Gibco, USA). For each scaffold, 200 µL of assay solution was added to 48-well plates, and the scaffolds were incubated for two hours at 37 ˚C in a humidified atmosphere containing 5% CO_2.

After incubation, 100 µL of the liquid from each well was transferred to 96-well plates (black half-area; Corning), and the fluorescence intensity was measured at an excitation wavelength of 540 nm and an emission wavelength of 585 nm using a Tecan Infinite M200 Pro microplate reader (Tecan Trading, AG). To eliminate background fluorescence, two types of controls were considered: (i) scaffolds without cells and (ii) test solution (DMEM containing 10% Alamar Blue) without contact with scaffolds or cells. The values obtained from these controls were subtracted from the signal of all samples. All tests were performed in at least three independent replicates ($n \geq 3$) for each condition and each time point, and the results were reported as mean ± standard deviation.

6.2.4.3.2 DNA quantification

DNA numbers were measured with Hoechst dye assay (Hoechst 33258, Thermo fisher scientific, Canada) according to the manufacturer's instructions. At predetermined times on days 1 and 28, each scaffold was incubated in 100 µL of 4 M guanidine hydrochloride (GuHCl) buffer (Sigma-Aldrich, USA) pH = 5.8 containing a complete protease inhibitor cocktail (Roche, USA) to ensure efficient cell lysis and nucleic acid stability. To minimize buffer interference, all GuHCl extracts were diluted 1:10 prior to analysis. Calf thymus DNA in 0.4 M GuHCl was used to prepare a standard curve.

Fluorescence measurements to determine DNA levels were performed via a Tecan Infinite M200 Pro microplate reader (Tecan Trading, AG) in black 96-well plates (Corning, half-area, clear bottom). Measurements were obtained at an excitation/emission wavelength of 352/ 461 nm. All experiments were performed at least triplicate, and DNA levels were normalized to cell number (assuming seven pg DNA per cell).

Data from the first day were considered as an index of cell adhesion, while measurements taken on the 28th day were used to assess the final state of the culture.

6.2.4.4 Calcification assay

Alizarin Red staining was used to determine the extracellular matrix calcification according to the protocol reported by Fairag et al. [335]. After 28 days of culture, the scaffolds containing osteoblasts were fixed with 4% paraformaldehyde (PFA, methanol-free, Thermo fisher scientific, USA) diluted in deionized water for 20 minutes at room temperature. The samples were then washed three times with PBS and stained with 1% Alizarin Red S (ARS, Sigma-Aldrich, USA) for 10 minutes. Surplus dye was eliminated through successive rinsing in distilled water to ensure that the negative control samples were free of background dye. For qualitative evaluation, the stained samples were imaged.

For quantitative analysis, the bound dye was extracted and transferred to 96-well plates (black half-area; Corning). The absorbance at 405 nm was measured employing a Tecan Infinite M200 Pro (Tecan Trading, AG) with standard settings (bandwidth, 9 nm; 25 flashes; linear and circular shaking). The results obtained were corrected by subtracting from those of control samples, i.e., samples without cells. In this regard, a standard curve was drawn using reference solutions, and the absorbance values of the samples were calculated based on this curve and reported as a quantitative indicator of calcium deposition.

6.2.5 Statistical analysis

Statistical analyses were performed using GraphPad Prism (version 10). Data distribution and variance consistency were assessed prior to analysis to confirm compliance with ANOVA assumptions. A one-way or two-way ANOVA with Tukey's post hoc test was used to compare the groups. Data were presented as mean ± standard deviation (Mean ± SD), and $p < 0.05$ was considered as the level of statistical significance difference between the studied groups.

6.3 Results and discussions

6.3.1 Optimization of Fabrication Strategy and Nanoparticle Loading

6.3.1.1 Effect of Masterbatch Strategy on Nanoparticle Dispersion

Figure 6.3 shows SEM images of PCL/PEO/PEG ternary blend fibers containing 1 wt% nHA prepared from three different masterbatch systems.

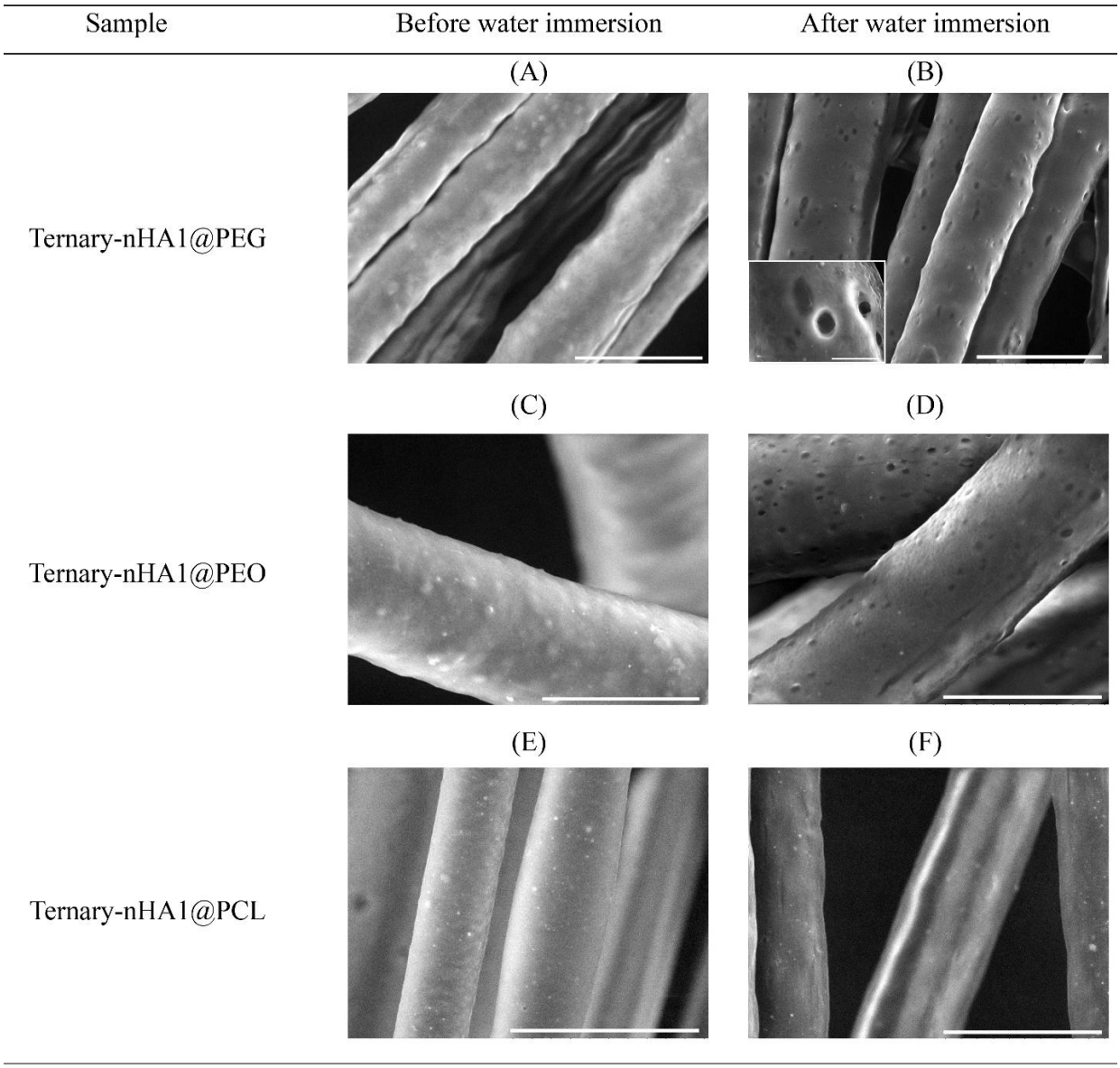

Figure 6.3 SEM images of PCL/PEO/PEG ternary blend fibers with 1% nHA prepared from three masterbatch routes. (A) Ternary-nHA1@PEG, before water immersion; (B) the same sample after one week of immersion. A magnified image is provided to more clearly show the created pores (scale bar: 10 μm). (C) Ternary-nHA1@PEO, before immersion; (D) the same sample after immersion. (E) Ternary-nHA1@PCL, before immersion; (F) the same sample after immersion. The scale bar of all images is 50 μm.

In Figures 6.3A, and B of the Ternary-nHA1@PEG sample, it can be seen that before water immersion (Figure 6.3A), the surface of the fibers, although devoid of open pores, has irregularities and protrusions in the form of nHA-rich domains. After one week of immersion (Figure 6.3B), these domains have transformed into numerous surface pores.

A similar behavior is observed in the Ternary-nHA1@PEO sample (Figures 6.3C, D). The surface of the fibers before immersion (Figure 6.3C) has a relatively rough texture, which is due to the presence of nanoparticles in the PEO phase. However, after immersion (Figure 6.3D), these areas have transformed into numerous pores. These results confirm that the initial distribution of nanoparticles in the hydrophilic phases (PEG or PEO) leads to an increase in heterogeneity and the creation of soluble domains in the aqueous medium, rather than improving the compatibility with PCL. This phenomenon is likely due to the strong interaction of hydroxyapatite nanoparticles with the hydrophilic chains of PEG and PEO, which causes local particle segregation in the PEO/PEG domains. It is noteworthy that, in the PEG and PEO-based systems, due to the hydrophilic nature of both polymers, it is not possible to directly separate the exact contribution of each nanoparticle-rich phase after water immersion; therefore, the observation of surface pores after immersion can be attributed to the dissolution of the hydrophilic nanoparticle-rich phases, without being able to determine with certainty their exact origin (PEO- or PEG-rich).

In contrast, the PCL-based masterbatch route (Figures 6.3E and F) exhibits entirely different behavior. In this case, the Ternary blend-nHA1@PCL fibers did not exhibit a noticeable change in surface morphology before and after immersion, with only slight surface patterns appearing, shallow and short channels. This indicates that the nanoparticles in this route were stably embedded in the PCL matrix, and even after partial removal of the hydrophilic phases, the surface properties associated with the presence of nHA were still maintained.

Overall, these results suggest that the choice of masterbatch route significantly influences the microstructure and stability of the fibers. Masterbatch preparation via PEG or PEO results in an increase in inhomogeneity of nHA distribution and the formation of pores after contact with water, due to the tendency of the particles to interact with hydrophilic phases. In contrast, the PCL-based route provides higher morphological stability and creates more suitable conditions for maintaining surface properties and performing subsequent biological tests. These observations are consistent with the Energy-Dispersive X-Ray (EDX) results, which show that after water immersion, no significant signals from calcium or phosphorus were observed in the Ternary-nHA1@PEO and Ternary-nHA1@PEG samples, (Supporting information, Figure S. 6.1). Furthermore, in our previous work [324], a comprehensive study of the persistence behavior of nHA after water immersion quantitatively confirmed the high stability of these nanoparticles in Ternary-nHAX@PCL samples, which, together with the present data, integrally imply the effective

retention of nHA in this system. In addition, the dispersion of nanoparticles appears more uniform, with no significant evidence of agglomeration or segregation. Previous studies have also shown that the order and method of adding nanoparticles during the preparation process of nanocomposites could significantly impact the morphology and compatibility of the polymer components [336-338].

6.3.1.2 Influence of Nanoparticle Content on Scaffold Performance

Figure 6.4 illustrates the process of selecting the optimal percentage of nHA in a Ternary blend-nHA@PCL scaffold, including the experimental design and decision-making path (Figure 6.4A), results of metabolic activity for day one (Figure 6.4B), and cell number measurements at different loadings (Figure 6.4C), and a time comparison of biological response (Figure 6.4D) to determine the appropriate percentage.

The reasoning behind choosing the ideal proportion of nHA in the Ternary blend-nHA@PCL scaffolds is shown in Figure 6.4A. In this design, the Alamar Blue assay was used on day 1 as an initial indicator of metabolic activity and an early screening parameter. DNA assay results were then used on day 28 to ensure continued proliferation and no reduction in cell numbers in the specimens. Based on these two complementary endpoints, the best options for time-course evaluations were selected, Ternary blend-nHA5@PCL and Ternary blend-nHA10@PCL. This approach aligns with strategies documented in clinical research that aim to minimize prolonged culture durations of cell seeding on scaffolds, thereby decreasing the interval between material preparation and implantation in the body, ideally in situ during surgery [339, 340]. In such approaches, the initial cell response is defined as a rapid screening indicator and then supported by confirmatory endpoints [341].

Figure 6.4B shows the results of osteoblast metabolic activity on samples with different amounts of nHA. As can be seen, increasing the nHA loading from 1 to 10 wt% results in a significant increase in the metabolic activity, while a noticeable decrease is observed at 20 wt%. This pattern suggests that there is an optimal amount for nHA loading in the early stages of cell adhesion or cell anchoring. The present finding is consistent with previous reports that show that gradually increasing nHA up to a certain threshold has beneficial effects, but excessive loading can lead to attenuation of the initial response due to changes in surface chemistry and energy, the creation of undesirable nanoscale roughness, or particle aggregation and agglomeration [342, 343].

Figure 6.4C shows the results of DNA quantification at day 28. The highest mean cell number is observed in the Ternary blend-nHA10@PCL group, although the difference with the Ternary blend-nHA5@PCL group is limited. Accordingly, the performance of the Ternary blend-nHA10@PCL in this test is interpreted as non-inferior to the other groups. This result indicates that the 10% loading not only produced a favorable response in the early stages (Figure 6.4B) but also remained at least on par with the other formulations in long-term cell proliferation (Figure 6.4C). These results are also consistent with the previous report that states the addition of nHA primarily affects the early stages of osteoblast behavior, such as cell adhesion, while its role in later stages, such as proliferation, is less pronounced [342]. Figure 6.4D shows the changes in metabolic activity of osteoblasts on scaffolds containing 5 and 10 wt% nHA at different time intervals. The Ternary blend-nHA10@PCL system presents higher values of metabolic activity than the Ternary-nHA5@PCL at most time points. Two-way ANOVA analysis also confirms that the observed difference, especially at day 1, was not merely transient but persisted over time. These results indicate that, despite the slight difference in the number of viable cells between the Ternary-nHA10 and Ternary-nHA5@PCL, the level of metabolic activity was almost higher in the Ternary-nHA10@PCL scaffolds. It implies that 10% nHA loading produced a more favorable biological response.

Overall, the data from metabolic activity and cell proliferation assays showed that 10 wt% nHA loading provides the best balance between initial cellular responses and long-term proliferation stability. This result complements the findings of the previous section, where the optimal formulation method based on PCL/nHA masterbatch was introduced. Accordingly, all subsequent tests and evaluations in this study were performed on samples prepared with this formulation method and with 10% loading as the optimal percentage composition.

To understand the phase behavior of the Ternary blend-nHA10@PCL system, the optimum formulation in the current study, the dynamic mechanical analysis (DMA) was performed. The results of the DMA test (Supporting information, Figure S. 6.2) indicate a single glass transition temperature for both the ternary and the Ternary blend-nHA10@PCL systems, suggesting miscibility of PCL, PEO, and PEG. However, the results of our previous study showed that this system is not completely ideal or homogeneous, and the limited tiny heterogeneous regions within the structure were observed [324].

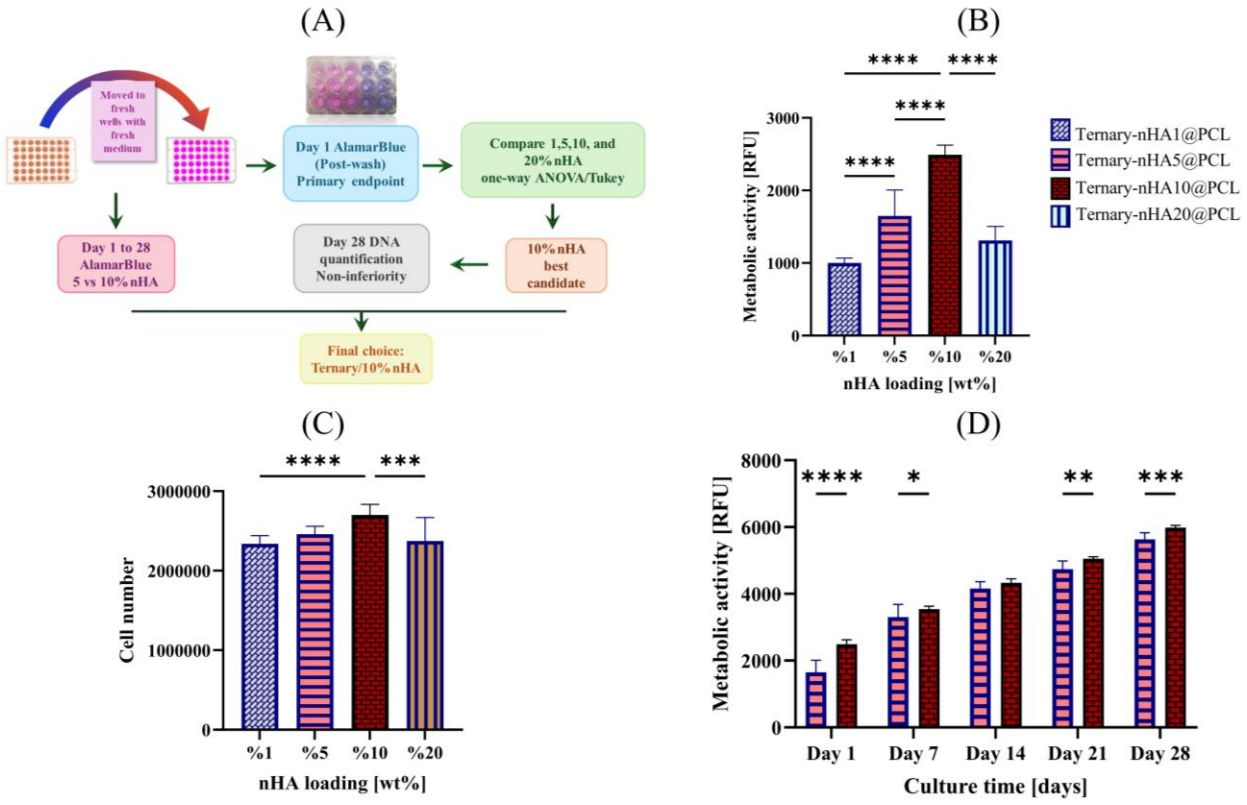

Figure 6.4 Assessment of the optimal quantity of nHA in the ternary blend formulated from the chosen PCL/nHA masterbatch. (A) Schematic design of the experiment and decision path. (B) Alamar Blue assay on day 1 for 1, 5, 10, and 20 wt% nHA loadings. (C) DNA-based cell count assay on day 28. (D) Time course of Alamar Blue for 10 wt% (optimal option) compared to 5 wt%. Error bars: SD., n = 3, *p < 0.05, **p < 0.01, ****p < 0.0001.

6.3.2 Evaluation of Optimized Scaffolds

6.3.2.1 Surface Wettability and Hydrophilicity of the Scaffolds

Figure 6.5 exhibits the results of the water contact angle test for different scaffolds. As can be seen, the neat PCL scaffold had the highest contact angle (125˚) and therefore presented the lowest surface hydrophilicity. The addition of nHA to PCL caused a significant decrease in the contact angle (from about 125˚ in the neat PCL sample to about 93˚), indicating an improvement in surface wettability. The chemical structure of hydroxyapatite is $Ca_5(PO_4)_3(OH)$, and the presence of hydroxyl (OH) groups potentially enhances the hydrophilicity of the sample [319, 344].

However, the most significant decrease in the contact angle was observed for the ternary scaffolds, particularly for the ternary sample containing nanoparticles with the contact angle of 79˚, indicating a notable increase in hydrophilicity in these systems (decrease of 46˚).

The increased hydrophilicity of the Ternary-nHA10@PCL surface can be owing to the introduction of OH groups of hydrophilic polymers (PEO and PEG) to the system as well as the effect of surface charge and roughness induced by nHA. This combination of factors, by creating a stable layer of water molecules on the surface, could prevent nonspecific adsorption of proteins and their structural changes, and consequently, could prevent the activation of primary immune pathways and the accumulation of inflammatory macrophages [345, 346].

The results of a study indicate that materials with modulated hydrophilic surfaces and functional groups such as -OH and -COOH can shift macrophage polarization from the inflammatory (M1) to the reparative (M2) phenotype, thereby accelerating the release of anti-inflammatory factors and the healing of damaged tissue [347]. In the Ternary-nHA10@PCL system, the combination of hydrophilic polymers, PEO and PEG, and inorganic nanoparticles, nHA, likely provides suitable conditions that could enable the scaffold surface to adsorb more serum proteins, thereby facilitating the initial establishment and adhesion of cells in the early stages of repair.

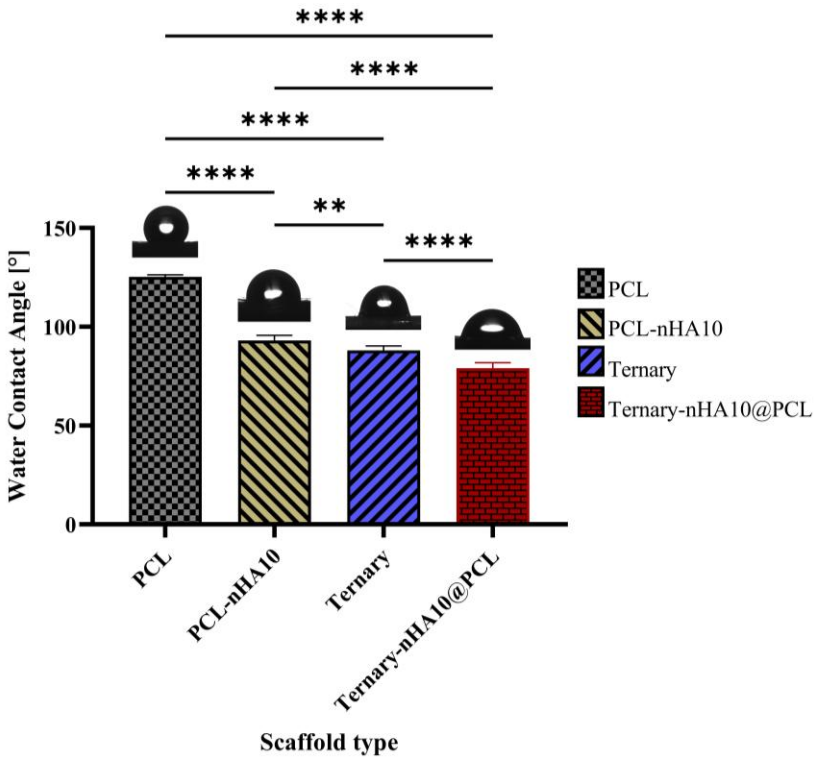

Figure 6.5 Evaluation of water contact angle on the surface of different scaffolds to investigate the wettability and hydrophilicity properties of the surface. Error bars: SD., n = 3, *p < 0.05, **p < 0.01, ****p < 0.0001.

In addition, controlled increases in hydrophilicity and appropriate changes in surface topography can regulate the type of cell-surface interaction, preventing the formation of tense, stable adhesions in fibroblasts and thus preventing the activation of mechanical pathways that lead to their differentiation into α-SMA-expressing myofibroblasts [348]. Capuani et al. [349] showed that this cellular reaction, triggered by reduced mechanical stresses in the attachment area and maintaining a softer adhesion, plays a crucial role in blocking excessive collagen accumulation, hampering fibrotic tissue formation, and, subsequently, limiting the foreign body response. Hence, the Ternary-nHA10@PCL melt electrospun scaffold is expected to significantly reduce the likelihood of unwanted responses, such as fibrosis, chronic inflammation, and the foreign body effect, which are commonly observed with PCL implants. Statistical analysis using ANOVA also confirmed that the contact angle reduction in the ternary and Ternary-nHA10@PCL scaffolds was significantly greater than that of the plain PCL and PCL-nHA10 scaffolds. These results clearly highlight the role of combining hydrophilic polymers with nanoparticles in enhancing the surface properties of PCL-based scaffolds for bone tissue engineering applications.

6.3.2.2 In Vitro Biological Evaluation

6.3.2.2.1 Cell adhesion and proliferation

Figure 6.6 shows the results of the biological evaluations of the scaffolds. In this study, two key primary human cell types were investigated: osteoblasts, as the cells responsible for bone formation, and HUVECs, as the cells involved in angiogenesis. This selection aimed to evaluate the ability of the scaffolds to support adhesion, viability growth and biochemical activity of these specific cells, which would be essential aspects for clinical translation in future work. Furthermore, the use of donor healthy osteoblasts could evaluate the potential of real-world use for these scaffolds under variability.

Figures 6.6A and B show the evaluation of cell adhesion on day 1. The results indicate that the addition of nHA not only increases osteoblast cell adhesion but also significantly increases HUVEC adhesion in the composite samples compared to the plain samples. This observation is consistent with the findings of Pezzatini et al. [350], who also pointed out the high biocompatibility of hydroxyapatite-containing scaffolds for endothelial cells. The addition of nHA to scaffolds provides a suitable substrate for the initial establishment of cells, which can be attributed to improvements in surface properties, such as increased roughness and changes in surface charge.

In other words, the presence of nHA can induce chemoattractant behavior by selectively adsorbing proteins and inducing the formation or stimulation of filopodia in cells [342, 351].

Figures 6.6C and D show the results of metabolic activity measurements over a 28-day culture period. Both cell lines exhibited a gradual and continuous increase in metabolic activity on the scaffolds; however, this trend was more pronounced in the Ternary-nHA10@PCL scaffold. In fact, the presence of hydroxyl groups from PEO and PEG chains, along with the addition of nHA to samples, creates conditions that promote cell establishment and proliferation. Figure 6.6C shows that the neat and nanocomposite ternary scaffolds provide a better substrate for the activity of HUVEC than the PCL scaffold. In the ternary blend samples, it appears that the presence of hydrophilic PEO and PEG chains in the system has led to microscale changes in the surface morphology (Figure 6.3F). In particular, when these chains come into contact with an aqueous environment, parts of them may dissolve in water, resulting in the formation of rough and fine-textured surfaces on the fibers. These surface changes could play a crucial role in enhancing the adhesion and activity of endothelial cells. This result suggests that the effect of the textured surface (Figure 6.3F), as well as its high hydrophilicity, is more significant than the direct presence of bioactive nanoparticles in enhancing the performance of HUVEC. In other words, although the addition of nHA can help improve the activity of HUVEC, the sensitivity of these cells to the hydrophilic surface is greater than the direct effect of the presence of nanoparticles. In contrast, the activity of osteoblasts is more sensitive to the presence of nHA, and they are more active on the nanocomposite samples.

Figures 6.6E and F show the DNA quantification results at day 28, which reinforce previous findings and indicate that the highest number of cells, both osteoblast and HUVEC, were observed on the Ternary-nHA10@PCL scaffold. Additionally, a comparison of the behavior of both cell lines on neat and nanocomposite scaffolds shows that for both cell lines, the addition of nHA improves cell activity. This effect could be due to the release of calcium ions from nHA into the culture medium [351]. Ca^{2+} is integral to the mineral matrix of bone and functions as a crucial intracellular messenger, regulating gene expression, osteoblast differentiation, and cell proliferation [352]. Liu et al. [353] explained that calcium signals could stimulate osteoblast function via calmodulin, triggering extracellular-signal-regulated kinase 1/2 (ERK1/2) and the intracellular signaling pathways, which are essential for controlling PI3K/Akt pathways [353].

Additionally, Amiryaghoubi et al. [320] revealed that partial degradation of PCL during cell culture processes could result in the release of small amounts of acidic by-products, which can lower the media pH and thus weaken cell activity. However, they showed that incorporating nHA into PCL might mitigate this issue by reducing the media's acidity and creating a more suitable environment for cell growth and proliferation [320].

Accordingly, it can be concluded that calcium ions released from nHA not only directly enhance bioactivity by increasing the adhesion and proliferation of osteoblasts and HUVEC cells, but also could accelerate tissue regeneration and enhance the biointegrability of the scaffold by activating Ca^{2+}-dependent signaling pathways. The results of an in vivo study have also clearly shown that the controlled release of Ca^{2+} ions from nHA-containing coatings can enhance bone formation in areas of bone defects and accelerate the rate of osteointegration in metallic implants [354].

Therefore, one of the main reasons for the superior performance of nHA-containing scaffolds compared to their counterparts without it seems to be the ability of these nanoparticles to provide a stable and bioactive source of calcium ions, a source that both creates a more favorable chemical environment and boosts cellular activity by stimulating key biological pathways.

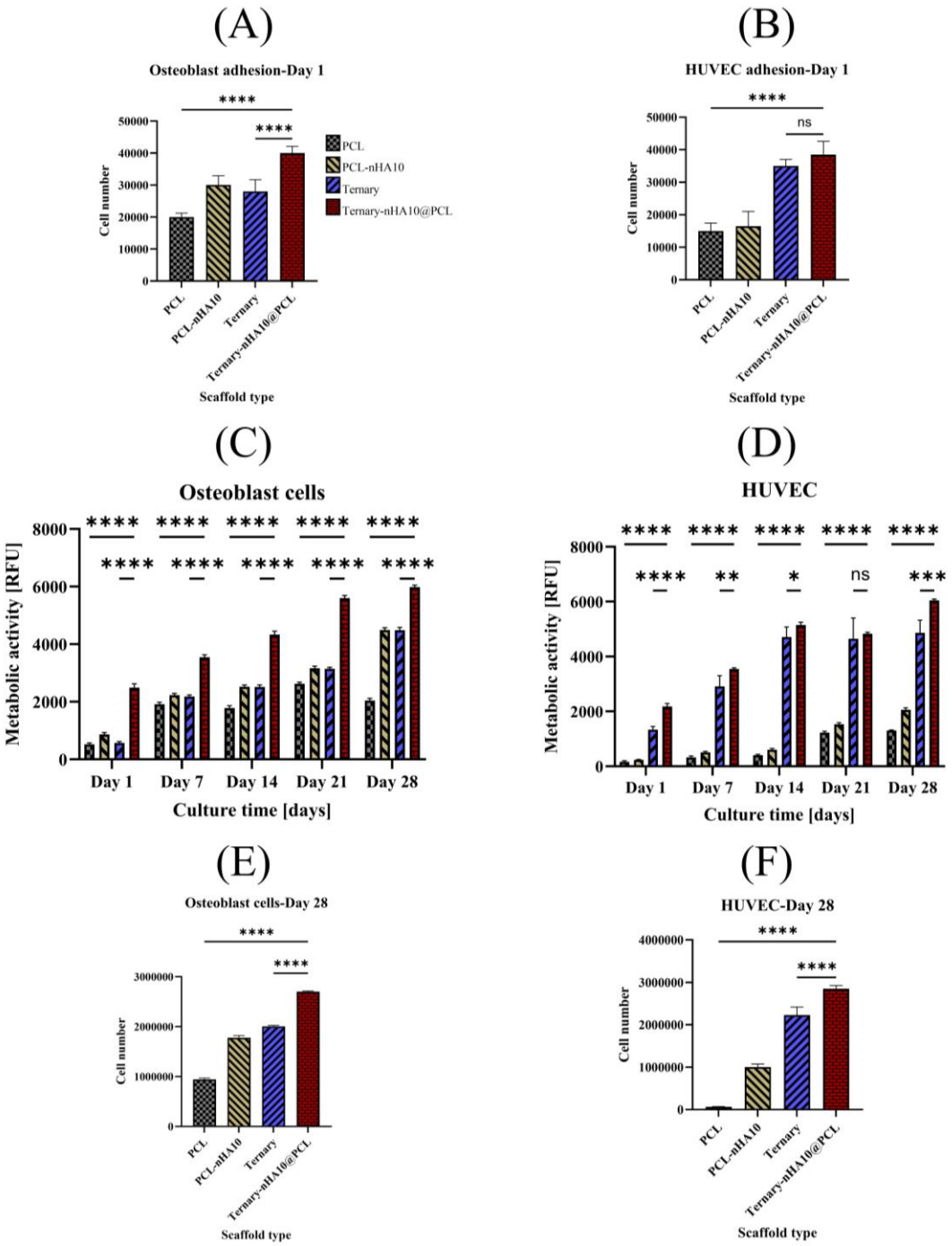

Figure 6.6 Results of cellular evaluation on different scaffolds. (A) Osteoblast cell adhesion at day 1; (B) HUVEC cell adhesion at day 1; (C) Metabolic activity of osteoblast cells during the culture period from day 1 to day 28 , the relative metabolic activity with respect to the PCL is reported in the Supporting Information (Figure S. 6.5); (D) Metabolic activity of HUVEC cells during the culture period from day 1 to day 28; (E) DNA quantification for osteoblast cells at day 28; (F) DNA quantification for HUVEC cells at day 28. To avoid cluttering the graphs, only the main comparisons between the Ternary-nHA10@PCL vs. the neat ternary, and the Tternary-nHA10@PCL vs. the neat PCL scaffolds are shown, while other comparisons are provided in the Supporting Information (Tables S. 6.1-4).

The average fiber diameter in the optimized sample (Ternary-nHA10@PCL) was measured in the range of tens of micrometers (about 27 μm) (Supporting information, Figure S. 6.3). These dimensions are in line with the typical sizes of target cells; osteoblasts are generally reported to be 15–25 μm [355, 356], and endothelial cells (HUVECs) are 10–20 μm [357, 358]. Such a length-scale adaptation facilitates effective cell–fiber contact and provides an appropriate substrate for cell adhesion, proliferation, and metabolic activity. Furthermore, the interfiber spaces in the specimens' structure could provide the required open pathways for nutrient exchange and cellular diffusion, which could explain the high biological responses.

Overall, the results in Figure 6.6 indicate that designing ternary scaffolds containing nHA is a potential strategy to enhance the biological performance of scaffolds. Such scaffolds can support bone cell (osteoblast) and vascular endothelial cell adhesion, growth and activity, and thus are considered promising options for bone tissue regeneration and advanced bone graft alternatives. Given their application in bone tissue engineering, the mechanical behavior of these scaffolds plays a decisive role in structural stability and performance under dynamic loading conditions. Our previous work showed that adding nHA and designing multicomponent PCL/PEO/PEG systems can improve yield stress, strain, and overall mechanical response [324]. At the same time, the blending of PEO and PEG with PCL improves the viscoelastic behavior and energy dissipation under cyclic loading (Supporting information, Figure S. 6.4). These properties are particularly important for mimicking natural bone behavior and enduring repetitive loads. Although in vivo testing is necessary for final evaluation, ex vivo/in vitro studies can serve as a practical intermediate step toward a more accurate assessment of tissue behavior. The present results provide promising evidence of the potential of the designed scaffolds for bone tissue regeneration.

6.3.2.2.2 Cellular calcification

Figure 6.7 shows the results of the evaluation of cellular calcification by the Alizarin Red assay. Quantitative data (Figure 6.7A) indicate that mineral deposition in scaffolds containing nHA was significantly higher than in samples without nanoparticles. Among the different groups, the Ternary-nHA10@PCL scaffold shows the highest mineralization, and these differences are reported to be significant based on the ANOVA statistical test. These findings confirm the reinforcing role of nHA in inducing osteogenic processes. As previously reported by Pansani et al.

[319], nHA acts as a focal point for mineral deposition by cells, promoting the mineralization of the extracellular matrix produced by osteoblasts [319].

Staining images (Figure 6.7B) also qualitatively confirm these results, clearly showing higher color intensity in ternary scaffolds containing nanoparticles compared to other groups. This suggests that the combination of PCL with PEO and PEG as hydrophilic polymers, along with the presence of nHA, provides more favorable conditions for osteoblast calcium deposition.

In studies that have investigated the performance of polymer scaffolds in inducing calcification, the reported values have generally been in a limited range. For example, in melt electrowritten scaffolds with different fiber arrangements, the calcification value after 21 days of human mesenchymal stem cell culture was approximately 0.3 Mm [359]. In a PCL/HA 3D printed system, the presence of 40 wt% hydroxyapatite resulted in a value of approximately 1.5 mM after 21 days of human mesenchymal stem cell culture [360]. Also, in melt electrowritten scaffolds in which hydroxyapatite was added intrafibrously or as a surface coating, the reported calcification values have mainly been between 0.01 and 0.15 mM [361].

In comparison, the amount of calcification observed in the Ternary–nHA10@PCL scaffold in this study, at 8–9 mM after 28 days of culture, indicates much higher calcification in this system. Given the difference in culture duration and the semiquantitative nature of the Alizarin Red assay, this comparison demonstrates the functional position of the Ternary–nHA10@PCL scaffold against the ranges reported in the literature. It suggests that the composition and microstructure of this scaffold provide conditions that support calcification with higher efficiency.

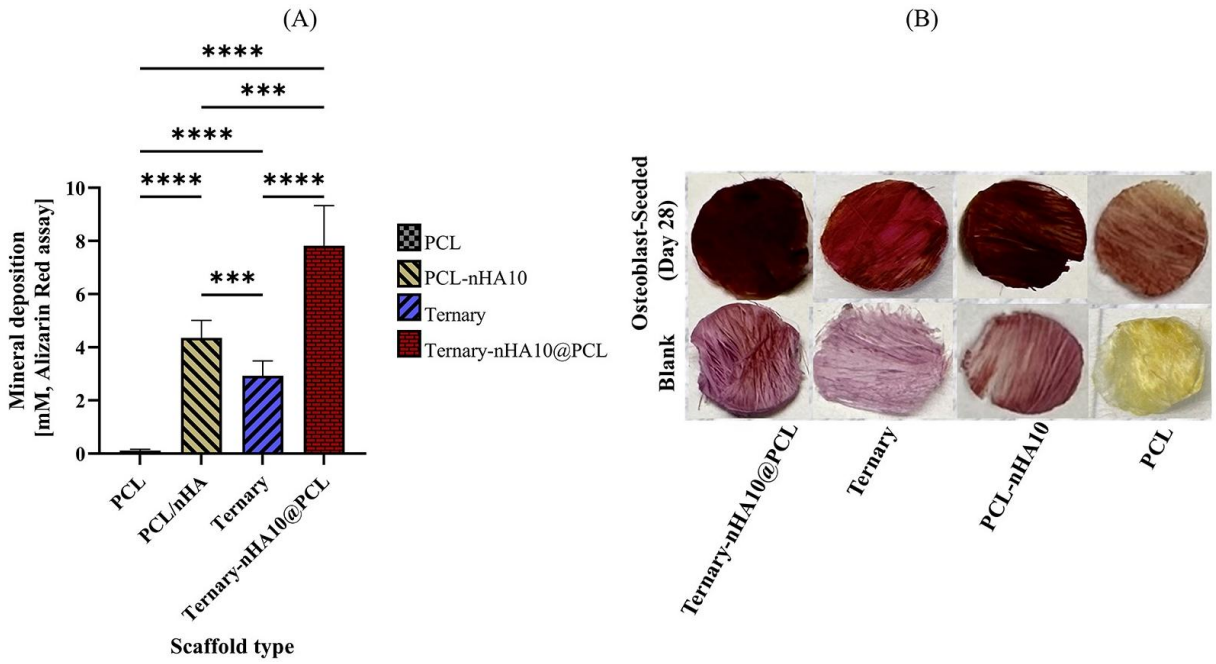

Figure 6.7 Evaluation of cellular mineralization using the Alizarin Red assay. (A) Quantitative comparison of mineral deposition by osteoblast cells after 28 days of culture. Error bars: SD., n = 3, *p < 0.05, **p < 0.01, ****p < 0.0001. The relative mineralization response with respect to neat PCL is presented in Supporting Information (Figure S. 6.6) (B) Representative images of Alizarin Red-stained samples for the indicated scaffolds, along with cell-free controls (Blank).

6.4 Conclusion

This study demonstrated that the choice of masterbatch route and nHA content plays a decisive role in the microstructure, hydrophilicity, and biofunctionality of melt electrospun scaffolds. The nHA@PCL route ensured surface stability and retention of nanoparticles after aqueous contact, and in combination with PEO/PEG, and increased surface hydrophilicity, factors that enhanced initial adhesion, sustained metabolic activity, cell proliferation, and calcification. The Ternary-nHA10@PCL formulation showed an optimal balance between initial response and long-term stability and was identified as a superior option for supporting increased cell adhesions, metabolic activity (growth) and calcified matrix deposition by primary osteoblasts as well as increased adhesion and metabolic activity of HUVEC cells – both suggesting high potential for translational osseointegration. Given the solvent-free nature of melt electrospun and favorable bioreadability, these systems hold promising prospects for the development of advanced bone graft alternatives. Ex vivo and in vivo evaluations, along with optimization of scaffold architecture are suggested avenues for further work.

6.5 Supporting Information Description

Supplementary Information: This file contains supporting data and results related to the structural, mechanical, and biological evaluations of the scaffolds. Specifically, EDX elemental mapping after water immersion, dynamic mechanical analysis (DMA) results, SEM images with fiber diameter distribution, and fatigue test results are presented. Also, the tables include full pairwise comparisons between all groups for DNA quantification tests in osteoblasts and HUVEC cells at days 1 and 28, and for the metabolic activity test (Alamar Blue) at different time points, based on one-way and two-way ANOVA analyses with Tukey's test. In addition, supplementary graphs are provided on osteoblast metabolic activity and calcium deposition at day 28 (Alizarin Red test), which support the results reported in the main text.

Acknowledgments

The authors sincerely thank Mohsen Hasani Zadeh and Avesta Gheysari for their valuable scientific contributions. Special thanks are extended to Matthieu Gauthier and Claire Cerclé for their technical assistance. Financial support from the Natural Sciences and Engineering Research Council of Canada (NSERC, Grant No. RGPIN-2021-03902) and the Fonds de recherche du Quebec—Nature et Technologies (FRQNT, Grant No. 2021-PR-285621) is sincerely acknowledged.

6.6 Supplementary materials

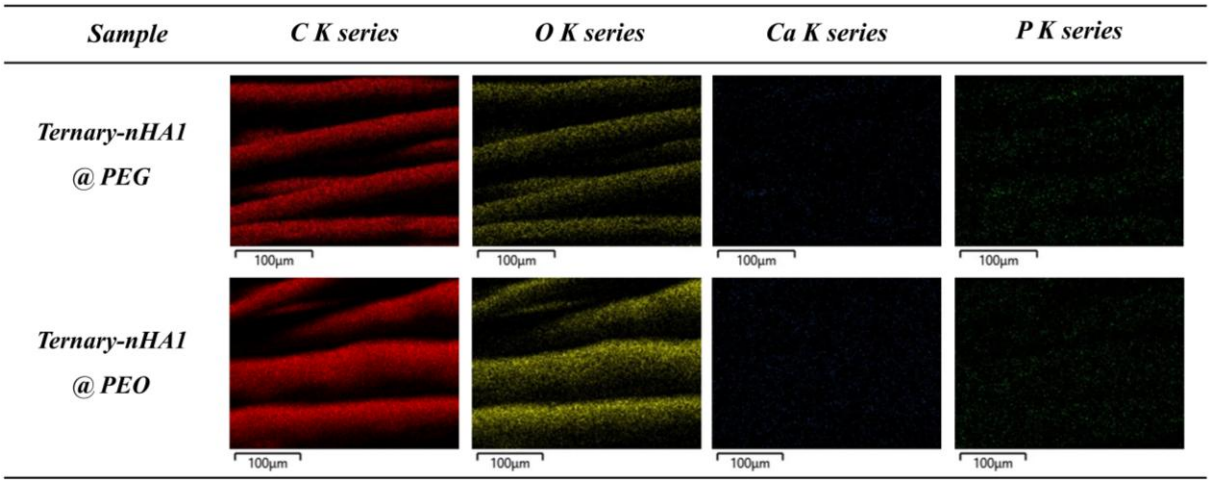

Figure S. 6.1 Energy-dispersive X-ray (EDX) elemental mapping of melt electrospun nanocomposite fibers after water immersion. Representative elemental maps of C, O, Ca, and P are shown for the ternary-nHA1@PEG and ternary-nHA1@PEO samples. In both systems, the Ca and P signals are weak and sparse after immersion, indicating a very limited detectable presence of hydroxyapatite nanoparticles (nHA) under these conditions. These observations support the reduced persistence of nHA in the PEG- and PEO-based systems following aqueous extraction.

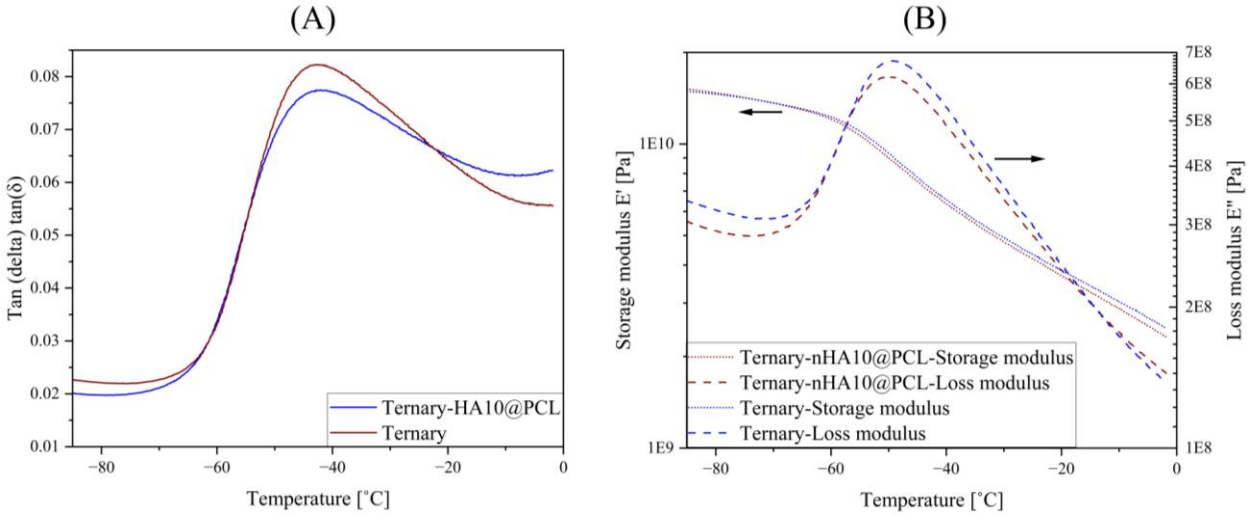

Figure S. 6.2 Temperature dependence of (A) damping factor (tan δ), (B) storage modulus (E′), and loss modulus (E″) for the Ternary and Ternary-nHA10@PCL systems obtained by dynamic mechanical analysis (DMA). Measurements were conducted in dual cantilever mode at a frequency of 1 Hz, a strain within the linear viscoelastic region (0.16%), and a heating rate of 3 ˚C min^{-1} over the temperature range of -85 to 0 ˚C.

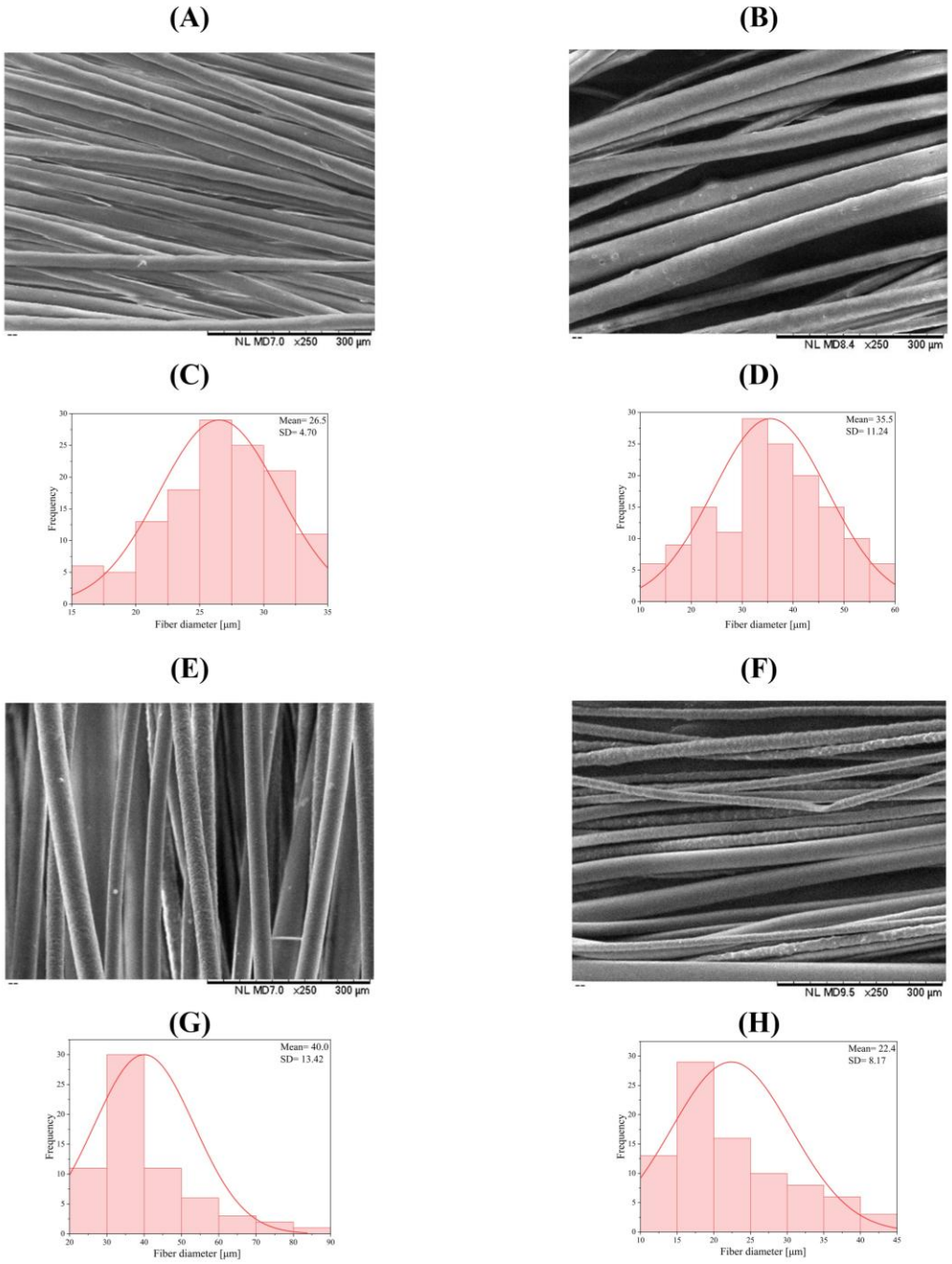

Figure S. 6.3 Scanning electron microscopy (SEM) images and corresponding fiber diameter distributions of electrospun scaffolds with different compositions. (A, B) SEM micrographs of ternary systems containing nHA at 10 wt% (ternary-nHA10@PCL) and 5 wt% (ternary-nHA5@PCL), respectively. (C, D) Fiber diameter histograms with Gaussian fitting obtained from ImageJ analysis for ternary-nHA10@PCL and ternary-nHA5@PCL, respectively. (E, F) SEM micrographs of PCL-based systems containing nHA at 10 wt% (PCL-nHA10) and 5 wt% (PCL-nHA5), respectively. (G, H) Corresponding fiber diameter distributions for PCL-nHA10 and PCL-nHA5. Fiber diameters were quantified from SEM images and reported as mean ± standard deviation.

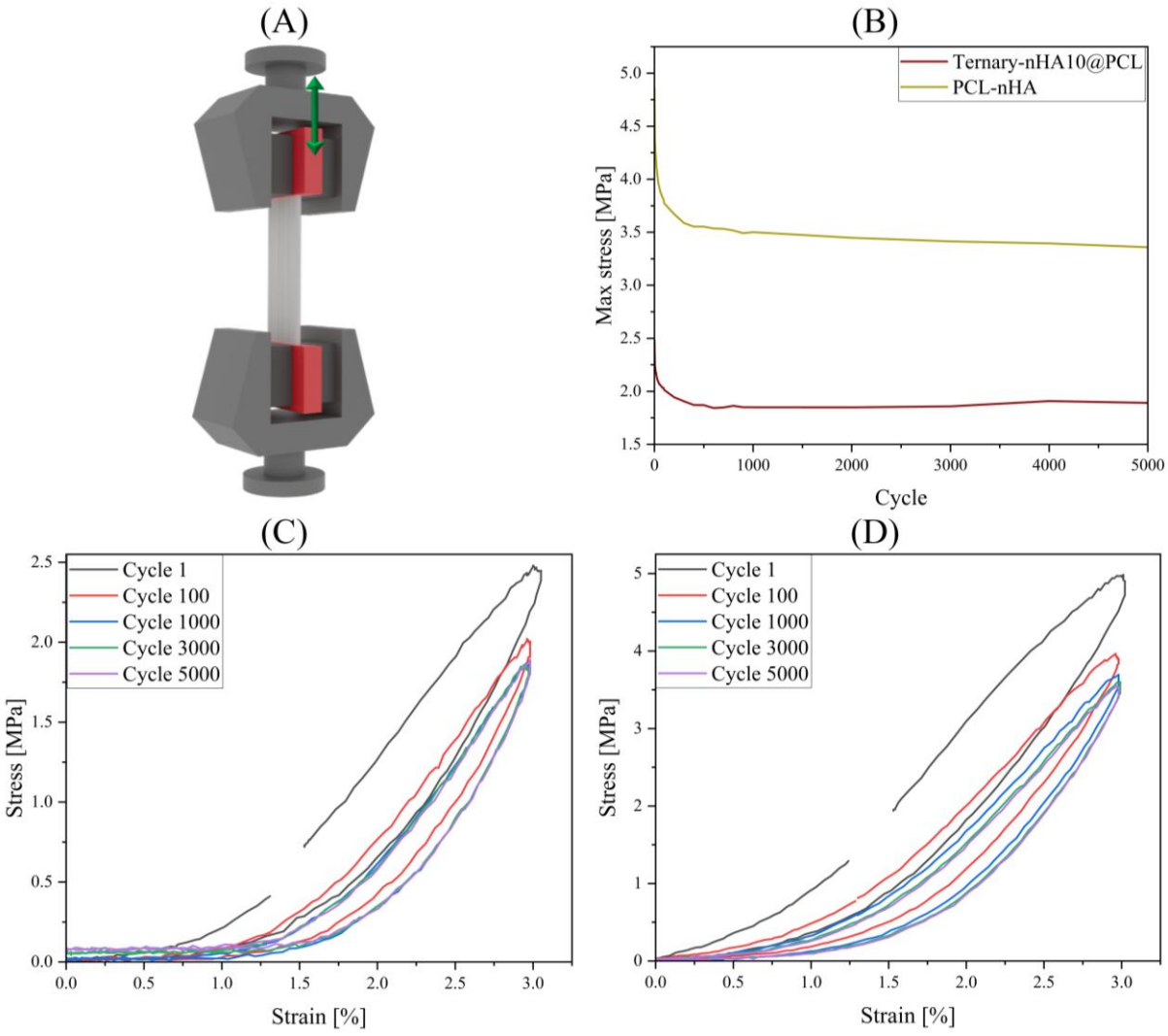

Figure S. 6.4 (A) Schematic illustration of the cyclic tensile (fatigue) test setup under uniaxial cyclic tensile loading along the fiber alignment direction. Rectangular specimens measuring approximately 10 mm × 5 mm and 350 µm thick were used. As shown, each specimen was mounted in a paper frame and gripped using sandpaper-covered tabs to minimize slippage during cyclic loading. Fatigue tests were conducted in strain-controlled tension–tension mode between 0 and 3% strain (strain amplitude of 1.5% and mean strain of 1.5%) at a frequency of 0.5 Hz for a total of 5000 cycles under ambient conditions. At least five specimens per group were tested. (B) Evolution of maximum stress as a function of loading cycle for PCL–nHA and Ternary–nHA10@PCL scaffolds, highlighting the mechanical stability and stress retention behavior over 5000 cycles. (C–D) Representative stress–strain hysteresis loops at selected cycles (1, 100, 1000, 3000, and 5000) for (C) Ternary–nHA10@PCL and (D) PCL–nHA samples, demonstrating cyclic softening, energy dissipation, and structural evolution during fatigue loading.

Table S. 6.1 pairwise comparisons between all groups in the DNA quantification test on day 1, for osteoblasts and HUVEC cells (Figures 6.6A and B in the main manuscript) based on one-way ANOVA statistical analysis[I]

Contrast	Osteoblast-Day 1	HUVEC-Day 1
PCL vs. PCL-nHA10	****↑	ns
PCL vs. Ternary	****↑	****↑
PCL vs. Ternary-nHA10	****↑	****↑
PCL-nHA10 vs. Ternary	ns	****↑
PCL-nHA10 vs. Ternary-nHA10	****↑	****↑
Ternary vs. Ternary-nHA10	****↑	ns

[I]One-way ANOVA was performed for analysis the data, followed by Tukey's multiple comparisons test (adjusted p values). All comparisons are reported in this table; in the main text, only key comparisons were marked with an asterisk. Significance thresholds are denoted as: ns = not significant; *p < 0.05; **p < 0.01; ***p < 0.001; ***p < 0.0001. Downward (↓) and upward (↑) arrows indicate the direction of the difference, with the arrow pointing toward the group showing the higher mean response. In other words, the upward arrow indicates that the parameter value in the second group is larger than in the first group.

Table S. 6.2 The pairwise comparisons between all groups in the osteoblast metabolic activity test (Alamar Blue test) at different time intervals (days 1, 7, 14, 21, and 28) (Figure 6.6C in the main manuscript), based on two-way ANOVA statistical analysis[I]

Contrast	Day 1	Day 7	Day 14	Day 21	Day 28
PCL vs. PCL-nHA10	****↑	****↑	****↑	****↑	****↑
PCL vs. Ternary	ns	****↑	****↑	****↑	****↑
PCL vs. Ternary-nHA10	****↑	****↑	****↑	****↑	****↑
PCL-nHA10 vs. Ternary	****↓	ns	ns	ns	ns
PCL-nHA10 vs. Ternary-nHA10	****↑	****↑	****↑	****↑	****↑
Ternary vs. Ternary-nHA10	****↑	****↑	****↑	****↑	****↑

[I]Two-way ANOVA was performed for analysis the data, followed by Tukey's multiple comparisons test (adjusted p values). All comparisons are reported in this table; in the main text, only key comparisons were marked with an asterisk. Significance thresholds are denoted as: ns = not significant; *p < 0.05; **p < 0.01; ***p < 0.001; ***p < 0.0001. Downward (↓) and upward (↑) arrows indicate the direction of the difference, with the arrow pointing toward the group showing the higher mean response. In other words, the upward arrow indicates that the parameter value in the second group is larger than in the first group.

Table S. 6.3 The pairwise comparisons between all groups in the HUVEC metabolic activity test (Alamar Blue test) at different time intervals (days 1, 7, 14, 21, and 28) (Figure 6.6D in the main manuscript), based on two-way ANOVA statistical analysis[I]

Contrast	Day 1	Day 7	Day 14	Day 21	Day 28
PCL vs. PCL-nHA10	**↑	****↑	****↑	****↑	****↑
PCL vs. Ternary	****↑	****↑	****↑	****↑	****↑
PCL vs. Ternary-nHA10	****↑	****↑	****↑	****↑	****↑
PCL-nHA10 vs. Ternary	****↑	****↑	****↑	****↑	****↑
PCL-nHA10 vs. Ternary-nHA10	****↑	****↑	****↑	****↑	****↑
Ternary vs. Ternary-nHA10	****↑	**↑	*↑	ns	***↑

[I]Two-way ANOVA was performed for analysis the data, followed by Tukey's multiple comparisons test (adjusted p values). All comparisons are reported in this table; in the main text, only key comparisons were marked with an asterisk. Significance thresholds are denoted as: ns = not significant; *p < 0.05; **p < 0.01; ***p < 0.001; ***p < 0.0001. Downward (↓) and upward (↑) arrows indicate the direction of the difference, with the arrow pointing toward the group showing the higher mean response. In other words, the upward arrow indicates that the parameter value in the second group is larger than in the first group.

Table S. 6.4 pairwise comparisons between all groups in the DNA quantification test on day 28, for osteoblasts and HUVEC cells (Figures 6.6E and F in the main manuscript) based on one-way ANOVA statistical analysis[I]

Contrast	Osteoblast-Day 28	HUVEC-Day 28
PCL vs. PCL-nHA10	****↑	****↑
PCL vs. Ternary	****↑	****↑
PCL vs. Ternary-nHA10	****↑	****↑
PCL-nHA10 vs. Ternary	****↑	****↑
PCL-nHA10 vs. Ternary-nHA10	****↑	****↑
Ternary vs. Ternary-nHA10	****↑	****↑

[I]One-way ANOVA was performed for analysis the data, followed by Tukey's multiple comparisons test (adjusted p values). All comparisons are reported in this table; in the main text, only key comparisons were marked with an asterisk. Significance thresholds are denoted as: ns = not significant; *p < 0.05; **p < 0.01; ***p < 0.001; ***p < 0.0001. Downward (↓) and upward (↑) arrows indicate the direction of the difference, with the arrow pointing toward the group showing the higher mean response. In other words, the upward arrow indicates that the parameter value in the second group is larger than in the first group.

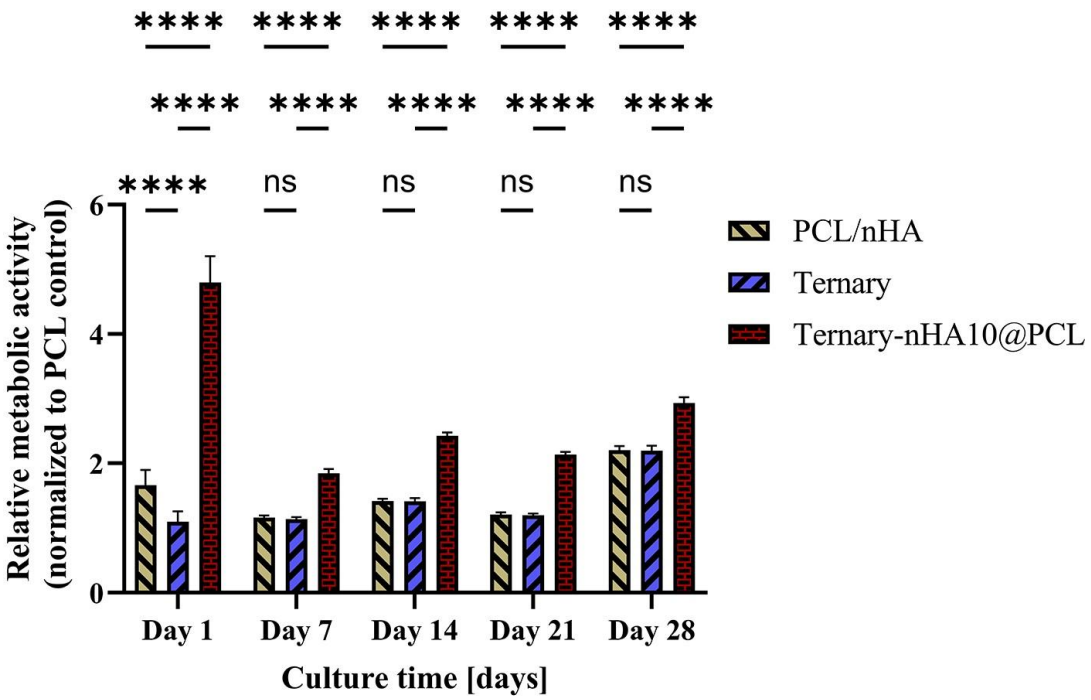

Figure S. 6.5 Relative metabolic activity of osteoblast cells on different scaffolds at different culture time points, obtained by Alamar Blue assay. All values are normalized to the PCL group as the control. Two-way ANOVA performed statistical comparisons; **** indicates highly significant ($p < 0.0001$) and ns indicates no significant difference.

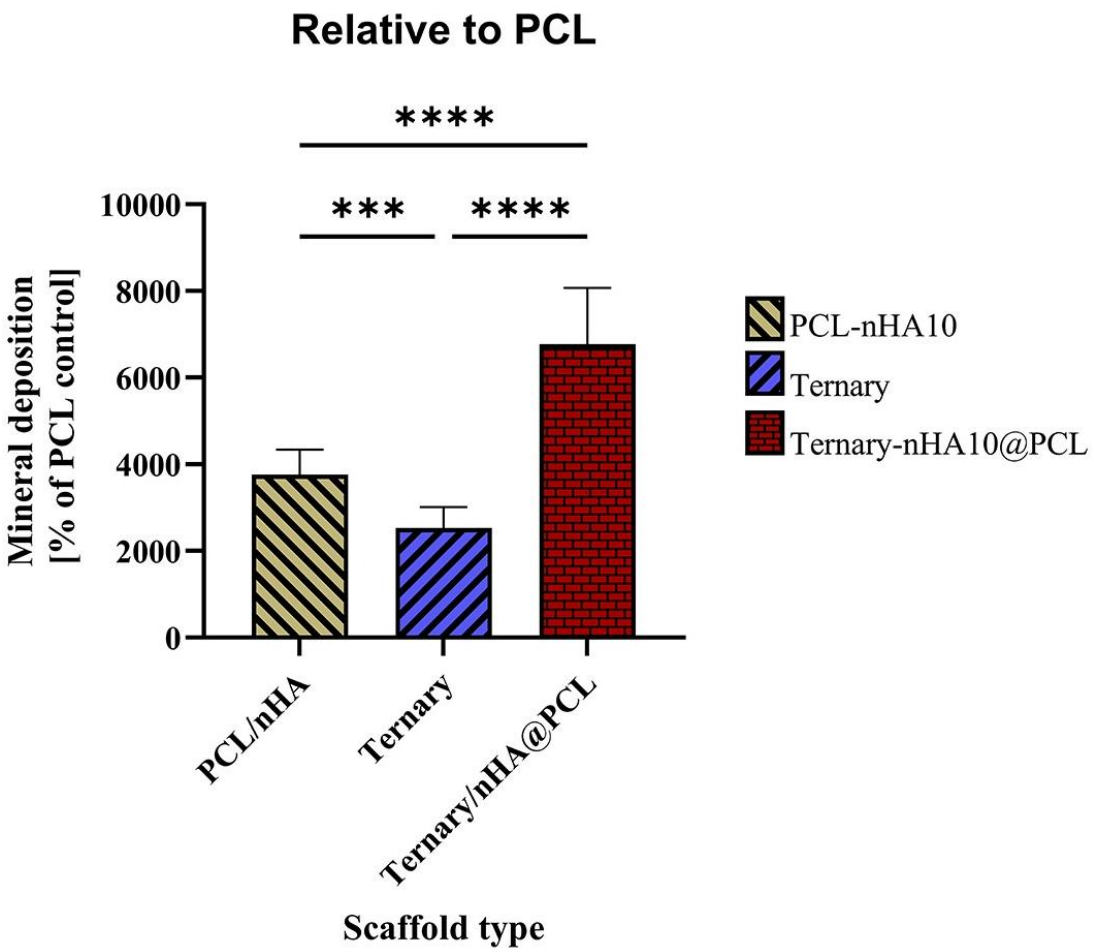

Figure S. 6.6 Calcium deposition of osteoblast cells on different scaffolds at day 28, assessed by Alizarin Red assay. All values are normalized to the PCL group as the control. Statistical comparisons are performed by one-way ANOVA; *** and **** indicate different levels of statistical significance ($p < 0.001$ and $p < 0.0001$, respectively).

CHAPTER 7 GENERAL DISCUSSION

One of the most fundamental questions in bone tissue engineering is, how can we design a structure that most closely resembles the complex and multidimensional properties of natural bone?

Bone requires a set of simultaneous properties to function properly: a porous and permeable structure for material exchange and cell infiltration, a bioactive surface for interaction with proteins and cells, adequate strength and modulus to withstand mechanical loads, and finally a degradation rate that can be coordinated with the rate of new matrix formation [2]. Achieving a set of these properties in a single material is usually not possible, and this is the essence of the present research: designing a multicomponent scaffold that can elicit desirable morphological, mechanical, and biological responses by leveraging the complementary behaviors of polymers and nanoparticles.

The first challenge in achieving such a scaffold is choosing the fabrication method. Since the presence of any organic solvent in the final structure can be harmful to the body, solution-based methods do not seem suitable [14]. In addition, achieving complete control over morphology, fiber orientation, and the formation of regular three-dimensional structures is difficult in solvent-based methods [362]. Therefore, melt electrospinning was chosen as the main approach in this research as a safe, scalable, solvent-free method with high geometric control [2].

Nevertheless, even choosing the proper process is not enough. A single polymer, such as PCL, although biocompatible, processable, and suitable for fiber production, cannot meet all biological and structural needs alone. Hydrophobicity, very slow degradation rate, and limitations in creating very fine microstructures are among the disadvantages of PCL [2]. In contrast, hydrophilic polymers such as PEG and PEO can wet the scaffold surface, create permeable channels, and even lead to interconnected pores upon controlled dissolution in an aqueous environment. Therefore, the design of a PCL/PEO/PEG ternary system was a suitable solution to meet the simultaneous biological and mechanical requirements.

This choice is not only scientifically logical but also addresses an important research gap, given the significant lack of research in the field of melt electrospinning of ternary systems. The rheological challenges, control of phase separation, thermal compatibility, and morphology evolution in such systems have not yet been comprehensively investigated, which further enhances the importance and novelty of the present work.

One of the fundamental challenges of this research, to achieve the first objective of the thesis, was the optimization of the parameters affecting the fiber fabricating process, especially those related to the melt electrospinning method. During the experiments, it was observed that if these parameters were improperly adjusted, solidification along the melt flight path was incomplete. As a result, the fibers, upon landing on the collector, melted together, forming fused structures.

Another important challenge of this project was to determine appropriate processing parameters for binary and ternary blends, taking their compositions into account, and to investigate the effect of each component on the system's melt electrospinning capability. For example, increasing the polyethylene oxide content in the blend would lead to very rapid solidification, causing jet instability and fiber breakage along the path. Therefore, simultaneous and precise adjustment of process parameters was necessary. For example, reducing the nozzle-to-collector distance could improve fiber cohesion, but other parameters must also be adjusted to prevent excessive fiber diameter growth.

One of the key findings of this study is the determining role of the molecular weight of the dispersed phase polymers in the stability of the jet and ultimately the formation of uniform fibers. The addition of PEG, a low-molecular-weight polymer, reduces the melt viscosity, increases the mobility of the PCL chains, and, as a plasticizer, improves the stretchability of the jet and reduces fiber diameter. In contrast, PEO with a high molecular weight and very high viscosity, due to the high density of chain entanglements, exhibits significant elastic behavior, making rheological measurements impossible. PEO plays an important role in creating porosity after water immersion by forming distinct, relatively large domains within the structure of melt electrospun fibers.

At the same time, microscopic studies showed that by carefully adjusting the ratio of these two hydrophilic polymers, the final morphology can be directed towards the creation of interconnected pores and a structure similar to natural bone tissue. This feature is key for cell penetration and the transport of vital substances. It is considered one of the main advantages of the three-component system over the single- and two-component systems.

One of the key questions in this research was whether porous scaffolds could be produced, in addition to aligned fibers, via the melt electrospinning apparatus. To answer this question, a stationary plate was used as the collector instead of a rotating drum. However, except for polycaprolactone, which enabled the production of porous scaffolds, the other binary and ternary samples yielded bamboo-hat-shaped structures, with the area near the edge quite thin and the

thickness gradually decreasing from the center to the edge, very similar to the shape of a bamboo hat.

In the next step, instead of aluminum foil, a perforated refractory sheet was used as a collector, with the assumption that the fibers would form on specific paths of the sheet and ultimately a porous scaffold would be obtained, because the initial structure of this sheet was inherently similar to a porous scaffold. However, this solution did not lead to the desired results either.

Another method investigated was to change the syringe's position at 1-minute intervals and move it back and forth over a set distance. Although this method showed better results than previous solutions, it was not considered an efficient or effective method for producing porous scaffolds.

Finally, due to the aforementioned limitations, further research focused on the production and investigation of scaffolds based on aligned fibers.

The addition of nanohydroxyapatite (nHA) is one of the most effective methods for enhancing bioactivity and inducing osteogenic behavior in bone tissue-engineered scaffolds [14, 363]; however, this approach poses a fundamental challenge.

In this design, controlling the migration, agglomeration, and stability mechanisms of nanoparticles among the three phases played an important role in the final quality. The addition of hydroxyapatite nanoparticles (nHA) to the polymeric blend system was a significant challenge in achieving the second objective of this research. In this regard, several approaches were experimentally investigated. In the first phase, the nanoparticles were added directly to the Brabender and mixed simultaneously with the other components; however, significant nanoparticle agglomeration was observed.

Next, another approach was adopted in which nHAs were separately dispersed into PEG, PEO, or PCL, and the resulting masterbatch (PEG-nHA, PEO-nHA, and PCL-nHA) was subsequently mixed with the other components using the Brabender. Although this method reduced particle agglomeration to some extent, the latter persisted in the final samples.

In the next stage, it was decided to prepare solutions of PEO/nHA or PEG/nHA in water. The choice of water as the solvent was important because there were no concerns about solvent residues or biocompatibility issues in the final melt electrospun scaffold. These solutions were then subjected to intense ultrasonic processing. However, this step presented several challenges. It was observed that samples containing PEO at concentrations higher than about 7 wt% rapidly gelled

rather than forming a uniform solution. Furthermore, even for the PEO/nHA solutions, ultrasonication led to rapid nanoparticle precipitation.

While this approach was somewhat successful for the PEG/nHA system, PEO-based systems faced serious problems; even varying ultrasonic temperature and time conditions could not prevent this instability. Finally, mechanical agitation proved more effective and stable for dispersing nanoparticles in PEO/nHA solutions than ultrasonication.

After preparing the solutions, the water was removed under vacuum at a moderate temperature. At this stage, drying of the PEO/nHA solution proceeded without problems, and the dried material was easily separated from the container. However, with PEG, the dried material completely adhered to the bottom of the container, making separation impossible. This step was repeated using containers of different materials, and finally, the best performance was achieved when the solution was poured into a flexible metal container. However, a severe color change in the container was observed, and the TGA results showed that about 50% of the nanoparticles adhered to the bottom of the container and were practically absent in the final sample.

Overall, the results showed that this approach was unable to eliminate nanoparticle agglomeration. Finally, it was decided to mix the components using a microcompounder, which was ultimately chosen as an effective and reliable approach for distributing nanoparticles throughout the polymeric blend system.

Since the addition of nHA directly to the blending system caused the formation of big agglomerations of nHAs in the system, it was decided to prepare a masterbatch of nHA with the blending components to see how the addition of nHA to different hosts, PCL, PEO, or PEG, can affect the final morphology of the ternary blend nanocomposite scaffolds. The results revealed that when nHA is derived from a masterbatch of PEO-nHA or PEG-nHA, it leads to nHA agglomeration in the hydrophilic region. After immersion of the fibers in an aqueous environment, they leached into the water. However, the addition of nHA to the system via a PCL-nHA masterbatch resulted in a uniform distribution of nanoparticles throughout the fibers. After water immersion, they remained in the fibers, with only about 5% of the initial amount of nHA leaching, and the resulting morphology improved mechanical and biological responses. A measured release of approximately 5% of the initially incorporated nHA corresponds to only a very small fraction of the total inorganic content and, in practical terms, suggests that the vast majority of nanoparticles remain retained within the scaffold during aqueous exposure. In the present system, where nHA was incorporated

at 10 wt%, this corresponds to the release of only a minor fraction of the mineral phase, indicating that nanoparticle retention within the matrix is generally high.

From a clinical perspective, such a low level of release would not be expected to raise major safety concerns, particularly because hydroxyapatite is not a foreign or cytotoxic inorganic additive, but a bioactive calcium phosphate chemically close to the mineral phase of native bone [38]. In fact, hydroxyapatite dissolution products are primarily calcium and phosphate ions, which are naturally present in physiological environments and are generally well tolerated within normal local concentration ranges [352]. At limited levels, such release is more likely to contribute to local ionic exchange and bioactivity than to induce toxicity [364].

The main concern would not be the absolute quantity released, but rather the form in which it is released. If the released fraction is present primarily as dissolved ionic species or very fine dispersed particles, it is unlikely to cause adverse effects and may even support mineral signaling [365]. In contrast, release in the form of large agglomerates could theoretically be less desirable because it may contribute to local particle accumulation or inflammatory recognition [365]. However, given the very low total released fraction and the improved dispersion observed in the optimized system, this risk is expected to be limited.

That said, from a translational standpoint, even small levels of nanoparticle release should not be interpreted only in terms of quantity, but also in terms of biological response [366]. A complete clinical assessment would still require dedicated evaluation of local inflammatory response, macrophage activation, and long-term particle fate under in vivo conditions. Therefore, based on the magnitude of release alone, 5% does not appear clinically alarming, but its biological significance should ultimately be interpreted in the context of particle form, local dose, and in vivo host response. The results of this stage showed that the initial phase, during which nHA was mixed, and the order of addition of the mixing component played important roles in the final morphology of the system and the localization of nHA.

Although the addition of nHA to PCL weakened the mechanical properties of the final scaffold due to the agglomeration, the incorporation of nHA into the optimum ternary blend system, fabricated from a masterbatch of PCL-nHA, improved the mechanical properties of the scaffold by creating synergy between the polymer phases and nHA. From a tissue engineering perspective, this finding is important because bone mass in the early stages of regeneration requires a modulus that is neither too high to cause shielding stress nor too low to cause structural collapse. The present

system strikes a good balance. Comparison of the mechanical properties of the developed scaffolds with those reported for natural bone shows that the scaffolds produced in this study approach the range required for trabecular (cancellous) bone applications. The tensile strength of trabecular bone is usually reported to be in the range of about 2 to 12 MPa, depending on the density and anatomical location [367-369]. In comparison, the ternary/nHA scaffold in this study showed yield stress values of about 11-13 MPa. These results indicate that the developed scaffold achieved the mechanical range required for trabecular bone and, in some cases, even approached the upper range reported for this type of bone. Furthermore, the relatively high strain retention, along with adequate strength, indicates that the scaffold not only has high strength but also can withstand deformation without sudden failure.

Accordingly, it can be concluded that the ternary/nHA scaffold developed in this study is mechanically suitable for applications related to low-load trabecular bone, like cranial bone regeneration.

Based on the degradation profile shown in Figure 5.16, the hydrolytic degradation of the developed systems occurs on a timescale that is broadly compatible with the biological timeline of bone healing, but the rate strongly depends on scaffold composition.

For bone repair, the relevant biological timescale is typically on the order of weeks to months [370]. Initial inflammatory and early reparative events occur within the first few days, early matrix deposition and vascularized tissue formation generally develop over the first 4–8 weeks, and more advanced mineralized tissue formation and remodeling usually extend over several months [370]. In most bone tissue engineering applications, a scaffold is expected to maintain sufficient structural integrity during the early healing period, particularly within the first 6–12 weeks, and then gradually degrade as new tissue assumes the load-bearing role [36, 370, 371].

In this context, the degradation behavior of the PCL-rich systems can be considered slow. Both PCL and PCL/nHA show minimal mass loss over the 28-week period (below approximately 3%), indicating high hydrolytic stability. This suggests that these systems retain structural integrity well beyond the early healing phase, which is beneficial for long-term mechanical support but may be too slow if rapid scaffold replacement by new tissue is desired.

By contrast, the ternary systems exhibit substantially faster degradation. The ternary scaffold shows approximately 20% mass loss after 28 weeks, while the ternary/nHA system reaches nearly 25% mass loss over the same period. This indicates a moderate and progressive degradation

profile, with measurable mass loss beginning early enough to support gradual pore generation and tissue infiltration, while still preserving the majority of the scaffold mass throughout the early and intermediate healing phases.

From a bone regeneration perspective, this degradation behavior is better aligned with the expected timeline of repair. It is not excessively fast, because the scaffold does not lose structural integrity during the critical early weeks of healing, but it is also not excessively slow, because degradation begins early enough to progressively create space for tissue ingrowth and remodeling. Therefore, relative to bone healing timescales, the degradation of the ternary systems can be considered intermediate and more biologically appropriate, whereas the degradation of neat PCL-based systems is comparatively slow and more suited to applications requiring prolonged structural support.

Biological evaluations showed that the hydrophilic surface and the presence of PEO/PEG domains provided favorable conditions for cell adhesion and initial metabolism. Osteoblast cells showed favorable metabolic activity, and patterns of increased DNA replication and mineralization indicated induction of osteogenic behavior. In addition, the contact angle results confirmed the improvement in surface hydrophilicity following the incorporation of nHA and the hydrophilic components PEO and PEG. To ensure consistency and comparability across all samples, all sessile drop contact angle measurements were performed under identical conditions, and the contact angle values were recorded at a fixed time point of 5 s after deposition of the water droplet on the surface. Although sessile drop measurements provide only a static assessment of wettability, maintaining a constant acquisition time for all samples ensured a consistent basis for comparative evaluation of relative surface hydrophilicity.

One of the main problems in implementing the third objective of this project was conducting experiments on humid days. In the summer, scaffolds seeded with cells were easily contaminated, and mold grew in the culture media. This problem was observed despite several steps of sample sterilization and disrupted the results of the biological experiments. Finally, by increasing the duration of ultraviolet (UV) exposure during sample preparation on humid days, this problem was resolved to an acceptable extent.

Another challenge in this part of the research was the growth conditions of human endothelial cells (HUVEC), which inherently have a relatively low growth rate. According to standard protocols, culture media are usually replaced every 3 days; however, during the experiments, it was observed

that with this time interval, HUVEC cells did not grow optimally, and their characteristic elongated morphology was poorly formed, so that most cells showed near-spherical morphology.

To overcome this issue, various approaches were investigated, and it was ultimately found that changing the culture media every other day could significantly improve proliferation and maintain the normal elongated morphology of HUVEC cells. This change in the culture protocol led to more uniform and stable cell growth during the experiments.

On the other hand, the scaffold's ability to support HUVEC behavior is critical, as bone regeneration is not possible without a successful angiogenic network [2]. The structure's conductivity and the permeability resulting from the presence of water-soluble phases provided conditions that enhanced the HUVEC proliferation. This phenomenon is a prerequisite for the survival of bone cells and the integrity of the new tissue from a clinical perspective [2].

Overall, the results of this study showed that the use of a three-component system consisting of a PCL base polymer, two hydrophilic components, PEO and PEG, and nanohydroxyapatite can simultaneously confer a harmonious set of process, structural, and biological properties in the scaffold. The presence of PEG, by reducing viscosity, improved jet stability and processability in the melt electrospinning method, enabling the production of thinner, more uniform fibers. On the other hand, the combination of PEO's unique physical structure led to the formation of pores and microstructures that play an important role in the permeability and material exchange within the scaffold. Together, these two hydrophilic polymers improved the surface behavior of the melt electrospun scaffold and provided suitable conditions for protein adsorption and initial cell adhesion. The addition of nHA also enhanced the scaffold's biological interactions by creating surface-active sites, thereby increasing cell activity. The properties of multicomponent melt electrospun scaffolds indicated that they offer a more balanced performance than single-component scaffolds, which is crucial for effective bone tissue regeneration.

Apart from the experiments discussed previously, additional attempts were conducted to further improve the functionality of the developed scaffolds through the incorporation of bioactive drugs for bone regeneration applications. One of the first challenges associated with drug incorporation into the melt electrospinning process is determining the appropriate stage and method for introducing the drug into the system [167, 372]. In general, drugs may be incorporated prior to electrospinning during blend preparation, introduced in-situ during processing through combined fabrication approaches, or deposited onto the fabricated scaffolds afterward using techniques such

as electrospraying or solution electrospinning [167]. For example, simultaneous use of melt electrospinning and solution electrospinning systems could potentially allow the incorporation of drugs within a biocompatible carrier polymer such as PEG [167]. Alternatively, the drug may be electrosprayed or electrospun onto the fabricated fibers after the melt electrospinning process [372]. However, since the primary objective of the present work was to eliminate the use of solvents and focus exclusively on melt blending and melt electrospinning, it was decided to incorporate the drug directly during the blend preparation stage prior to processing.

Another important challenge was the selection of suitable drugs capable of retaining their functionality and stability under the elevated temperatures involved in melt electrospinning, while also being beneficial for bone regeneration applications. In this regard, two drugs were identified as potential candidates: dexamethasone, which is widely recognized for promoting mesenchymal stem cell differentiation toward the osteogenic lineage [373, 374], and icariin, which is known for its positive effects on vascularization and bone regeneration [375, 376]. Both drugs were considered promising because of their relatively high degradation temperatures (above 200 ˚C) [377], making them more suitable for thermal processing conditions. Among these candidates, the experimental work was initiated with dexamethasone. Nevertheless, incorporation of drugs into scaffolds using only melt blending remains highly challenging because the required drug concentration is typically very low, requiring multiple dilution steps to achieve homogeneous distribution within the polymer matrix. In this regard, a masterbatch of PEG or PEO containing dexamethasone was first prepared and subsequently diluted several times through melt blending using the microcompounder in order to achieve the desired drug concentration. However, repeated thermal processing during the melt blending steps potentially increased the risk of drug degradation. Consequently, the preliminary trials did not lead to satisfactory results. Despite these limitations, incorporation of bioactive molecules into melt electrospun scaffolds remains a promising research direction for future studies.

In general, simultaneous examination of fiber morphology and chemical structure, along with biological outcomes, confirmed that melt electrospun PCL/PEO/PEG-nHA nanocomposite-aligned fibers can form a stable, environmentally friendly structure while supporting bone-related cell activity and angiogenesis. Taken together, these findings suggest that fine-tuning the component ratios and controlling the evolution of the microstructure could pave the way for the production of a new generation of multicomponent scaffolds that more closely mimic the complex

properties of natural bone in terms of surface, structural, and functional properties and are in line with today's clinical needs.

CHAPTER 8 CONCLUSION, ORIGINAL CONTRIBUTIONS, AND RECOMMENDATIONS

8.1 Conclusion

The present study aimed to develop and evaluate an innovative platform for bone tissue engineering, and included three complementary studies, each covering a part of the design, optimization, and validation of a melt-electrospun scaffold based on a ternary PCL/PEO/PEG system in the presence of hydroxyapatite (nHA) nanoparticles. The results of this study demonstrate that a careful combination of material engineering, microstructure control, and comprehensive biological evaluation can lead to a platform that simultaneously supports osteogenesis and angiogenesis and promotes key responses in bone regeneration.

In a first step, the findings showed that the presence of two hydrophilic components, PEO and PEG, alongside the PCL base polymer can effectively compensate for PCL's inherent limitations—including its high hydrophobicity and limited cell adhesion. The fabrication of fibers with controlled diameter and interconnected porosity provided a basis for producing structures that are more architecturally similar to bone ECM. The results showed that PEO and PEG as sacrificial components can form interconnected pores and aligned fibrils, respectively, leading to significant improvements in hydrophilicity through increasing surface roughness, protein adsorption, and initial cell adhesion. This formed the biological backbone of the study and highlighted the importance of choosing the ternary composition.

In the second step, a nanocomposite system based on a ternary PCL/PEO/PEG blend containing hydroxyapatite nanoparticles was developed through melt electrospinning. The results showed that adding hydrophilic polymers PEO and PEG to the PCL matrix improved the distribution of hydroxyapatite nanoparticles within the fibers and resulted in a more uniform microstructure than in the PCL/nHA system. In contrast, FTIR and DSC analyses showed that, without causing chemical changes in the structure, physical interactions between the system's components can affect its thermal behavior and crystallinity. TGA studies confirmed the high stability of the nanoparticles in the polymer matrix and their very low migration rate in aqueous media. At the same time, the mechanical tests showed that the presence of nanoparticles increased the stress and yield strain of the fibers. Furthermore, the presence of hydrophilic chains in the ternary system increased water permeability, thereby accelerating hydrolytic degradation compared to neat PCL.

Overall, the results of this study indicate that the design of a multicomponent polymeric blend with a bioactive mineral phase can provide an effective approach for producing biodegradable fibrous scaffolds with tunable properties for bone tissue engineering applications.

Finally, the third paper served as the point of consolidation of the results and, by comprehensively investigating the effect of the masterbatch preparation route (nHA@PCL, nHA@PEO, nHA@PEG) and selecting the optimal percentage of nanoparticles, completed the final framework for the scaffold design. The results clearly showed that only the PCL-based masterbatch route stabilizes the nanoparticles without forming unstable phases or destructive holes within the matrix. This ensured that the fibers did not undergo unwanted surface degradation or nanoparticle release upon contact with an aqueous environment, a critical feature in implant applications. Biological data also confirmed that the ternary-nHA10@PCL sample provided the best balance among initial cell adhesion, sustained metabolic activity, long-term proliferation, and mineralization induction. The proliferation of two cell lines (Osteoblast and HUVEC) also demonstrated that this system has a unique ability to support osteogenesis and angiogenesis—two processes that are essential for successful regeneration and functional integrity of bone tissue.

From a comparison of the three papers, it can be concluded that the structural and biological synergy in this project was not due to a single factor, but rather the result of a careful alignment of three principal factors:

- ✍ Engineering of the polymer composition to control solubility, hydrophilicity, and microstructure;
- ✍ Nanoparticle–polymer engineering to achieve stable dispersion and provide bioactive pathways;
- ✍ Bioengineering and performance evaluation to determine the structure that has the greatest potential in real-world regeneration conditions.

The final results show that the PCL/PEO/PEG–nHA10@PCL system is an up-and-coming platform for the development of next-generation scaffolds for the treatment of bone defects. This scaffold provides an efficient substrate for the formation of new bone tissue by significantly increasing hydrophilicity, improving cell behavior, and promoting mineralization. Furthermore, the process characteristics of melt electrospinning—in particular, the absence of a solvent, the ability to produce fibrous scaffold with controlled architecture, and scalability—enhance the potential to transfer the results of this project to industrial and clinical settings.

Overall, this thesis demonstrated that the classical limitations of PCL-based polymer scaffolds can be overcome by designing a controlled, multi-component system, resulting in a scaffold that is competitive with existing advanced options for bone regeneration across process, structural, biological, and functional perspectives. In vivo and ex vivo evaluations, long-term mechanical stability studies, and optimization of the biomimetic architecture could be the following steps to prepare this scaffold for clinical applications.

8.2 Original contributions

This work presents several important scientific contributions, explained below.

✍ **In the first part of this research study:**

The role of the molecular weight of hydrophilic polymers polyethylene oxide (PEO) and polyethylene glycol (PEG) in determining the morphology, phase distribution, and crystallization behavior of the poly(ε-caprolactone)/polyethylene oxide/polyethylene glycol (PCL/PEO/PEG) system during melt electrospinning was systematically investigated. The results showed that the molecular weight difference between PEO and PEG, despite their similar chemical structures, fundamentally influences the fibers' final morphology by controlling domain size and crystallization pattern, leading PEO to form coarse, highly crystalline phases. However, PEG mainly creates fine, amorphous phases.

In addition, it was shown that the melt electrospinning process could cause extensive phase rearrangements and alter the morphology and thermal behavior of the system when an electric field, a very high cooling rate, and shear stress are applied, without chemical change or structural degradation.

Finally, this study experimentally demonstrated that removing the hydrophilic phases PEO and PEG after water immersion led to the formation of a continuous, open three-dimensional network within the fibers and significantly increased the initial metabolic activity of cells compared to neat PCL. These results introduce the use of PEO and PEG as sacrificial phases to produce solvent-free scaffolds suitable for tissue engineering as a novel and practical approach.

✍ **In the second part of this research study:**

A ternary PCL/PEO/PEG system reinforced with hydroxyapatite nanoparticles (nHA) was successfully developed and demonstrated stable processability under melt electrospinning

conditions without the use of organic solvents, resulting in the formation of aligned fibers with relatively uniform diameter and morphology. This outcome addresses an existing gap in the scientific literature concerning the use of multicomponent systems in melt electrospinning. To incorporate nanoparticles into the polymer matrix, the components were initially compounded using a Brabender internal mixer. However, this approach resulted in pronounced nanoparticle agglomeration, indicating insufficient dispersion within the polymeric system. To overcome this limitation, the compounding strategy was subsequently shifted to a microcompounder. This modification markedly improved nanoparticle dispersion and enabled a more homogeneous distribution of nHA throughout the blend. Nevertheless, the increased shear and altered processing history associated with microcompounding also affected the phase morphology of the system. While the results of the first objective showed that blending of the three polymeric components under the initial processing conditions led to a phase-separated morphology, compounding through the microcompounder resulted in a more homogeneous structure with a single-phase morphology.SEM, EDX, and image analysis results showed that the presence of hydrophilic PEO and PEG phases leads to a more uniform distribution of hydroxyapatite nanoparticles on the surface and cross-section of the fibers compared to the PCL/nHA system. Also, after water immersion, shallow channel-like surface patterns form, suggesting the possibility of simultaneously controlling nanoparticle distribution and surface microstructure through ternary composition design.

Furthermore, it was shown that the effect of nHA on the thermal and crystallization behavior is strongly dependent on the system's composition. While the addition of nHA to neat PCL leads to a slight increase in crystallinity, the presence of the same amount of nHA in the ternary system causes a decrease in crystallinity and melting temperature, which is attributed to physical interactions between the nanoparticles and the hydrophilic chains. These results provide a clear picture of the composition-process relationship in melt electrospun ternary blend nanocomposites. At the same time, FTIR and TGA tests confirm the preservation of nHA's chemical structure.

Finally, by combining long-term hydrolytic degradation tests (up to 28 weeks) with TGA, it was shown that nHAs in both single-component and ternary systems remain mainly in the matrix, while the simultaneous presence of PEO/PEG and nHA significantly increases the ternary system's degradation rate compared to neat PCL. These results indicate that by adjusting the proportion of

hydrophilic phases and the amount of nHA, the hydrolytic degradation rate and mechanical stability of the fibers can be purposefully designed for different tissue engineering applications.

✍ **In the third part of this research study:**

A novel process strategy for stabilizing and uniformly distributing nHA in the solvent-free ternary blend fibers was presented. This strategy was based on the production of a PCL/nHA masterbatch and its stepwise mixing with other components. This approach effectively addressed nanoparticle instability in the aqueous environment and the formation of heterogeneous structures. The results showed that the nanoparticles in this system remained stably within the matrix and did not separate from the fiber structure after exposure to the aqueous environment.

In addition, an optimal nanoparticle loading ratio (10 wt%) was identified that simultaneously improved initial cell adhesion and maintained stable cell proliferation over long periods. Determining this optimal point allows selection of the nHA content based on biophysical principles and reduces the need for trial-and-error approaches.

In the final nanocomposite ternary blend melt electrospun fibers, the hydrophilic phases increase hydrophilicity and improve surface organization. PCL is responsible for maintaining structural stability, while nHA provides calcium-ion-based biological signals. The synergistic performance of the components explains why this scaffold exhibits superior biological performance compared to single-component systems.

Finally, this system achieved a quantitative mineral deposition (calcification) rate that is significantly higher than the values reported in the scientific literature for the peer scaffolds. This result indicates that the designed scaffold is not only biocompatible but also serves as an active substrate to enhance bone matrix formation, and it has high scientific value from an applied and translational perspective.

8.3 Recommendations

The following recommendations for future work are suggested based on the findings of this dissertation:

- Investigating the impact of scaffold architecture:

Fabricating random nonwoven scaffolds based on the ternary system and comparing their performance with that of existing aligned scaffolds can shed more light on the role of fiber arrangement in the mechanical behavior, porosity, and biological response of scaffolds.

- Advanced study of rheological behavior:

Although rheological tests on ternary and binary blends were conducted (see Appendix A and Chapter 4), comprehensive rheological investigations of PCL/PEO/PEG–nHA nanocomposites under varying temperature and shear rate conditions are still recommended to better understand their flow behavior and predict their processability.

.

- Comparison of different polymer blend preparation methods:

Evaluating the biological performance of fibers obtained from samples prepared with a Brabender compared to those produced by a microcompounder can determine the effects of mixing uniformity and process scale on cellular behavior.

- Investigating different methods of adding nanoparticles:

Creating scaffolds with pre-added hydroxyapatite nanoparticles and post-modification surface coating, and comparing the performance of these two groups, can clarify the roles of nanoparticle location and distribution.

- Enzymatic degradation assessment:

Studying the enzymatic degradation behavior of scaffolds under conditions similar to in vivo conditions is essential for predicting their durability and actual degradation rates in a physiological environment.

- Cell co-culture study:

Observing the co-culture behavior of osteoblasts and HUVEC cells on scaffolds can provide valuable evidence of the scaffold's ability to induce osteogenesis and vascularization simultaneously.

- Study of mesenchymal stem cell differentiation:

Investigating the rate and quality of mesenchymal stem cell differentiation into the osteoblastic lineage on the scaffold can evaluate the system's capacity to support early and advanced stages of bone formation.

- Investigation of alternative nanoparticles such as bioactive glass:

Given the prominent role of bioactive nanoparticles in bone tissue engineering, it is suggested that the effect of adding bioactive glass as an alternative or supplement to Hydroxyapatite nanoparticles on the mechanical, morphological, and biological behavior of the scaffold should be investigated.

- Loading of drugs and biological factors:

Adding bioactive compounds, such as Icariin or VEGF, to enhance angiogenesis, and evaluating the drug-release profile under different loading methods are important avenues for the development of this system.

- Evaluation of angiogenic behavior through advanced tests:

Performing the Ex-Ovo CAM test to examine vascular tube formation and the rate of angiogenesis in the presence of the scaffold can provide important functional evidence for evaluating biological effects.

- In Vivo / ex vivo Studies

Finally, it is suggested that in vivo and ex vivo tests be performed on the optimized scaffolds to assess their actual efficacy in repairing bone defects and the potential for translation into clinical applications.

REFERENCES

[1] X. Yuan *et al.*, "Recent advances in 3D printing of smart scaffolds for bone tissue engineering and regeneration," *Advanced Materials,* vol. 36, no. 34, p. 2403641, 2024.

[2] L. V. Bauso, V. La Fauci, C. Longo, and G. Calabrese, "Bone tissue engineering and nanotechnology: a promising combination for bone regeneration," *Biology,* vol. 13, no. 4, p. 237, 2024.

[3] M. U. Aslam Khan, M. A. Aslam, M. F. Bin Abdullah, and G. M. Stojanović, "Current perspectives of protein in bone tissue engineering: bone structure, ideal scaffolds, fabrication techniques, applications, scopes, and future advances," *ACS Applied Bio Materials,* vol. 7, no. 8, pp. 5082-5106, 2024.

[4] A. H. Hoveidaei *et al.*, "Clinical challenges in bone tissue engineering-A narrative review," *Bone,* vol. 192, p. 117363, 2025.

[5] B. G. Keselowsky, D. M. Collard, and A. J. García, "Surface chemistry modulates fibronectin conformation and directs integrin binding and specificity to control cell adhesion," *Journal of Biomedical Materials Research Part A: An Official Journal of The Society for Biomaterials, The Japanese Society for Biomaterials, and The Australian Society for Biomaterials and the Korean Society for Biomaterials,* vol. 66, no. 2, pp. 247-259, 2003.

[6] D. O. Golubchikov, A. K. Petrov, V. A. Popkov, P. V. Evdokimov, and V. I. Putlayev, "Advances in the Fabrication of Polycaprolactone-Based Composite Scaffolds for Bone Tissue Engineering: From Chemical Composition to Scaffold Architecture," *ACS Biomaterials Science & Engineering,* vol. 11, no. 6, pp. 3201-3227, 2025.

[7] A. Chandrakar *et al.*, "Melt electrowriting of hydrophilic/hydrophobic multiblock copolymers for bone tissue regeneration," *Biomaterials Advances,* vol. 169, p. 214167, 2025.

[8] C. I. Idumah, "Poly (α-caprolactone)(PCL) biopolymeric bionanoarchitectures for tissue engineering applications," *International Journal of Polymeric Materials and Polymeric Biomaterials,* vol. 74, no. 8, pp. 733-762, 2025.

[9] T. Kawai, "Preclinical evaluation and advancements in vascularized bone tissue engineering," *Biomimetics,* vol. 10, no. 7, p. 412, 2025.

[10] H. Gharacheh *et al.*, "Comparative evaluation of melt-vs. solution-printed poly (ε-caprolactone)/hydroxyapatite scaffolds for bone tissue engineering applications," *Soft Matter,* vol. 21, no. 5, pp. 844-854, 2025.

[11] S. R. Shah, C. D. Modi, S. Singh, D. D. Mori, M. M. Soniwala, and B. G. Prajapati, "Recent advances in additive manufacturing of polycaprolactone-based scaffolds for tissue engineering applications: a comprehensive review," *Regenerative Engineering and Translational Medicine,* vol. 11, no. 1, pp. 112-131, 2025.

[12] N. Siddiqui, S. Asawa, B. Birru, R. Baadhe, and S. Rao, "PCL-based composite scaffold matrices for tissue engineering applications," *Molecular biotechnology,* vol. 60, no. 7, pp. 506-532, 2018.

[13] T. D. Brown, P. D. Dalton, and D. W. Hutmacher, "Melt electrospinning today: An opportune time for an emerging polymer process," *Progress in Polymer Science,* vol. 56, pp. 116-166, 2016.

[14] A. Bachs-Herrera, O. Yousefzade, L. J. del Valle, and J. Puiggali, "Melt electrospinning of polymers: blends, nanocomposites, additives and applications," *Applied Sciences,* vol. 11, no. 4, p. 1808, 2021.

[15] A. Shi *et al.*, "Advancements in 3D gel culture systems for enhanced angiogenesis in bone tissue engineering," *Journal of Materials Chemistry B,* vol. 13, no. 11, pp. 3516-3527, 2025.

[16] X. Zhang *et al.*, "Nanoscale materials-based platforms for the treatment of bone-related diseases," *Matter,* vol. 4, no. 9, pp. 2727-2764, 2021.

[17] B. M. Manzini, L. M. R. Machado, P. Y. Noritomi, and J. V. L. Da Silva, "Advances in Bone tissue engineering: A fundamental review: BM Manzini et al," *Journal of biosciences,* vol. 46, no. 1, p. 17, 2021.

[18] M. Ansari, "Bone tissue regeneration: biology, strategies and interface studies," *Progress in biomaterials,* vol. 8, no. 4, pp. 223-237, 2019.

[19] J. P. Schmitz and J. O. Hollinger, "The critical size defect as an experimental model for craniomandibulofacial nonunions," *Clinical Orthopaedics and Related Research (1976-2007),* vol. 205, pp. 299-308, 1986.

[20] S.-T. J. Tsang, N. Ferreira, and A. H. R. Simpson, "The reconstruction of critical bone loss: the holy grail of orthopaedics," *Bone & Joint Research,* vol. 11, no. 6, pp. 409-412, 2022.

[21] A. Adamczyk, B. Meulenkamp, G. Wilken, and S. Papp, "Managing bone loss in open fractures," *OTA International,* vol. 3, no. 1, p. e059, 2020.

[22] E. Roddy, M. R. DeBaun, A. Daoud-Gray, Y. P. Yang, and M. J. Gardner, "Treatment of critical-sized bone defects: clinical and tissue engineering perspectives," *European Journal of Orthopaedic Surgery & Traumatology,* vol. 28, no. 3, pp. 351-362, 2018.

[23] E. H. Schemitsch, "Size matters: defining critical in bone defect size!," *Journal of orthopaedic trauma,* vol. 31, pp. S20-S22, 2017.

[24] M. I. Santos and R. L. Reis, "Vascularization in bone tissue engineering: physiology, current strategies, major hurdles and future challenges," *Macromolecular bioscience,* vol. 10, no. 1, pp. 12-27, 2010.

[25] J. R. García and A. J. García, "Biomaterial-mediated strategies targeting vascularization for bone repair," *Drug delivery and translational research,* vol. 6, no. 2, pp. 77-95, 2016.

[26] C. R. Black, V. Goriainov, D. Gibbs, J. Kanczler, R. S. Tare, and R. O. Oreffo, "Bone tissue engineering," *Current molecular biology reports,* vol. 1, no. 3, pp. 132-140, 2015.

[27] G. L. Koons, M. Diba, and A. G. Mikos, "Materials design for bone-tissue engineering," *Nature Reviews Materials,* vol. 5, no. 8, pp. 584-603, 2020.

[28] L. Bessette *et al.*, "Direct medical costs attributable to peripheral fractures in Canadian post-menopausal women," *Osteoporosis international,* vol. 23, no. 6, pp. 1757-1768, 2012.

[29] A. De Mori, M. Peña Fernández, G. Blunn, G. Tozzi, and M. Roldo, "3D printing and electrospinning of composite hydrogels for cartilage and bone tissue engineering," *Polymers,* vol. 10, no. 3, p. 285, 2018.

[30] R. Hopkins *et al.*, "The current economic burden of illness of osteoporosis in Canada," *Osteoporosis International,* vol. 27, no. 10, pp. 3023-3032, 2016.

[31] A. Vanasse *et al.*, "Secular trends of hip fractures in Québec, Canada," *Osteoporosis International,* vol. 23, no. 6, pp. 1665-1672, 2012.

[32] R. Modarres, T. B. Ouarda, A. Vanasse, M. G. Orzanco, and P. Gosselin, "Modeling seasonal variation of hip fracture in Montreal, Canada," *Bone,* vol. 50, no. 4, pp. 909-916, 2012.

[33] A. Oryan, S. Alidadi, A. Moshiri, and N. Maffulli, "Bone regenerative medicine: classic options, novel strategies, and future directions," *Journal of orthopaedic surgery and research,* vol. 9, no. 1, p. 18, 2014.

[34] A. R. Amini, C. T. Laurencin, and S. P. Nukavarapu, "Bone tissue engineering: recent advances and challenges," *Critical Reviews™ in Biomedical Engineering,* vol. 40, no. 5, 2012.

[35] A. G. Abdelaziz *et al.*, "A review of 3D polymeric scaffolds for bone tissue engineering: principles, fabrication techniques, immunomodulatory roles, and challenges," *Bioengineering,* vol. 10, no. 2, p. 204, 2023.

[36] S. Bose, M. Roy, and A. Bandyopadhyay, "Recent advances in bone tissue engineering scaffolds," *Trends in biotechnology,* vol. 30, no. 10, pp. 546-554, 2012.

[37] C. Shi, Z. Yuan, F. Han, C. Zhu, and B. Li, "Polymeric biomaterials for bone regeneration," *Annals of Joint,* vol. 1, no. 9, 2016.

[38] S. V. Dorozhkin, "Calcium orthophosphates in nature, biology and medicine," *Materials,* vol. 2, no. 2, pp. 399-498, 2009.

[39] W. Wang and K. W. Yeung, "Bone grafts and biomaterials substitutes for bone defect repair: A review," *Bioactive materials,* vol. 2, no. 4, pp. 224-247, 2017.

[40] N. Rezania, M. Asadi-Eydivand, N. Abolfathi, S. Bonakdar, M. Mehrjoo, and M. Solati-Hashjin, "Three-dimensional printing of polycaprolactone/hydroxyapatite bone tissue engineering scaffolds mechanical properties and biological behavior," *Journal of Materials Science: Materials in Medicine,* vol. 33, no. 3, p. 31, 2022.

[41] N. Goonoo, A. Bhaw-Luximon, G. L. Bowlin, and D. Jhurry, "An assessment of biopolymer-and synthetic polymer-based scaffolds for bone and vascular tissue engineering," *Polymer International,* vol. 62, no. 4, pp. 523-533, 2013.

[42] S. Anjum *et al.*, "Electrospun biomimetic nanofibrous scaffolds: a promising prospect for bone tissue engineering and regenerative medicine," *International Journal of Molecular Sciences,* vol. 23, no. 16, p. 9206, 2022.

[43] J. Xue, J. Xie, W. Liu, and Y. Xia, "Electrospun nanofibers: new concepts, materials, and applications," *Accounts of chemical research,* vol. 50, no. 8, pp. 1976-1987, 2017.

[44] K. N. Robles, F. t. Zahra, R. Mu, and T. Giorgio, "Advances in electrospun poly (ε-caprolactone)-based nanofibrous scaffolds for tissue engineering," *Polymers,* vol. 16, no. 20, p. 2853, 2024.

[45] N. Bhattarai, D. Edmondson, O. Veiseh, F. A. Matsen, and M. Zhang, "Electrospun chitosan-based nanofibers and their cellular compatibility," *Biomaterials,* vol. 26, no. 31, pp. 6176-6184, 2005.

[46] A. Hrynevich *et al.*, "Dimension-based design of melt electrowritten scaffolds," *Small,* vol. 14, no. 22, p. 1800232, 2018.

[47] M. L. Muerza-Cascante, D. Haylock, D. W. Hutmacher, and P. D. Dalton, "Melt electrospinning and its technologization in tissue engineering," *Tissue Engineering Part B: Reviews,* vol. 21, no. 2, pp. 187-202, 2015.

[48] N. Detta *et al.*, "Melt electrospinning of polycaprolactone and its blends with poly (ethylene glycol)," *Polymer international,* vol. 59, no. 11, pp. 1558-1562, 2010.

[49] R. De Pace, S. Molinari, E. Mazzoni, and G. Perale, "Bone regeneration: A review of current treatment strategies," *Journal of Clinical Medicine,* vol. 14, no. 6, p. 1838, 2025.

[50] R. Dimitriou, E. Jones, D. McGonagle, and P. V. Giannoudis, "Bone regeneration: current concepts and future directions," *BMC medicine,* vol. 9, no. 1, p. 66, 2011.

[51] Y. Qin *et al.*, "A metamaterial scaffold beyond modulus limits: enhanced osteogenesis and angiogenesis of critical bone defects," *Nature communications,* vol. 16, no. 1, p. 2180, 2025.

[52] M. Rościszewska and A. Zieliński, "Titanium Scaffolds–Hopes and Limitations," *American Journal of Biomedical Science & Research,* vol. 4, pp. 390-391, 2019.

[53] J. R. Mauney, C. Jaquiéry, V. Volloch, M. Heberer, I. Martin, and D. L. Kaplan, "In vitro and in vivo evaluation of differentially demineralized cancellous bone scaffolds combined with human bone marrow stromal cells for tissue engineering," *Biomaterials,* vol. 26, no. 16, pp. 3173-3185, 2005.

[54] Z. Amini and R. Lari, "A systematic review of decellularized allograft and xenograft–derived scaffolds in bone tissue regeneration," *Tissue and Cell,* vol. 69, p. 101494, 2021.

[55] M. Čandrlić *et al.*, "Comparison of injectable biphasic calcium phosphate and a bovine xenograft in socket preservation: qualitative and quantitative histologic study in humans," *International journal of molecular sciences,* vol. 23, no. 5, p. 2539, 2022.

[56] E. Zampara *et al.*, "A histologic and histomorphometric evaluation of an allograft, xenograft, and alloplast graft for alveolar ridge preservation in humans: a randomized controlled clinical trial," *Journal of Oral Implantology,* vol. 48, no. 6, pp. 541-549, 2022.

[57] S. Farjaminejad *et al.*, "Advances and challenges in polymer-based scaffolds for bone tissue engineering: A path towards personalized regenerative medicine," *Polymers,* vol. 16, no. 23, p. 3303, 2024.

[58] Á. E. Mercado-Pagán, A. M. Stahl, Y. Shanjani, and Y. Yang, "Vascularization in bone tissue engineering constructs," *Annals of biomedical engineering,* vol. 43, no. 3, pp. 718-729, 2015.

[59] S. Chahal, A. Kumar, and F. S. J. Hussian, "Development of biomimetic electrospun polymeric biomaterials for bone tissue engineering. A review," *Journal of biomaterials science, polymer edition,* vol. 30, no. 14, pp. 1308-1355, 2019.

[60] M. Filippi, G. Born, M. Chaaban, and A. Scherberich, "Natural polymeric scaffolds in bone regeneration," *Frontiers in bioengineering and biotechnology,* vol. 8, p. 474, 2020.

[61] A. Prasad, "State of art review on bioabsorbable polymeric scaffolds for bone tissue engineering," *Materials Today: Proceedings,* vol. 44, pp. 1391-1400, 2021.

[62] P. Feng, J. Jia, M. Liu, S. Peng, Z. Zhao, and C. Shuai, "Degradation mechanisms and acceleration strategies of poly (lactic acid) scaffold for bone regeneration," *Materials & Design,* vol. 210, p. 110066, 2021.

[63] J. L. Brash, T. A. Horbett, R. A. Latour, and P. Tengvall, "The blood compatibility challenge. Part 2: Protein adsorption phenomena governing blood reactivity," *Acta biomaterialia,* vol. 94, pp. 11-24, 2019.

[64] S. G. Pedrero, P. Llamas-Sillero, and J. Serrano-López, "A multidisciplinary journey towards bone tissue engineering," *Materials,* vol. 14, no. 17, p. 4896, 2021.

[65] H. Noh and E. A. Vogler, "Volumetric interpretation of protein adsorption: competition from mixtures and the Vroman effect," *Biomaterials,* vol. 28, no. 3, pp. 405-422, 2007.

[66] M. Rabe, D. Verdes, and S. Seeger, "Understanding protein adsorption phenomena at solid surfaces," *Advances in colloid and interface science,* vol. 162, no. 1-2, pp. 87-106, 2011.

[67] L.-C. Xu, J. W. Bauer, and C. A. Siedlecki, "Proteins, platelets, and blood coagulation at biomaterial interfaces," *Colloids and Surfaces B: Biointerfaces,* vol. 124, pp. 49-68, 2014.

[68] K. Nakanishi, T. Sakiyama, and K. Imamura, "On the adsorption of proteins on solid surfaces, a common but very complicated phenomenon," *Journal of bioscience and bioengineering,* vol. 91, no. 3, pp. 233-244, 2001.

[69] P. Roach, D. Farrar, and C. C. Perry, "Interpretation of protein adsorption: surface-induced conformational changes," *Journal of the American Chemical Society,* vol. 127, no. 22, pp. 8168-8173, 2005.

[70] B. Sivaraman and R. A. Latour, "The relationship between platelet adhesion on surfaces and the structure versus the amount of adsorbed fibrinogen," *Biomaterials,* vol. 31, no. 5, pp. 832-839, 2010.

[71] L. Zhang *et al.*, "The influence of surface chemistry on adsorbed fibrinogen conformation, orientation, fiber formation and platelet adhesion," *Acta biomaterialia,* vol. 54, pp. 164-174, 2017.

[72] J. N. Lindon, G. McManama, L. Kushner, E. W. Merrill, and E. W. Salzman, "Does the conformation of adsorbed fibrinogen dictate platelet interactions with artificial surfaces?," 1986.

[73] S. Sun, Y. Yue, X. Huang, and D. Meng, "Protein adsorption on blood-contact membranes," *Journal of membrane science,* vol. 222, no. 1-2, pp. 3-18, 2003.

[74] J. Anderson, T. Bonfield, and N. Ziats, "Protein adsorption and cellular adhesion and activation on biomedical polymers," *The International journal of artificial organs,* vol. 13, no. 6, pp. 375-382, 1990.

[75] M. Weber *et al.*, "Blood-contacting biomaterials: in vitro evaluation of the hemocompatibility," *Frontiers in bioengineering and biotechnology,* vol. 6, p. 99, 2018.

[76] E. Ellermann, N. Meyer, R. E. Cameron, and S. M. Best, "In vitro angiogenesis in response to biomaterial properties for bone tissue engineering: a review of the state of the art," *Regenerative Biomaterials,* vol. 10, p. rbad027, 2023.

[77] M. N. Collins, G. Ren, K. Young, S. Pina, R. L. Reis, and J. M. Oliveira, "Scaffold fabrication technologies and structure/function properties in bone tissue engineering," *Advanced functional materials,* vol. 31, no. 21, p. 2010609, 2021.

[78] C. Micheletti and F. A. Shah, "Bone hierarchical organization through the lens of materials science: present opportunities and future challenges," *Bone Reports,* vol. 22, p. 101783, 2024.

[79] K. S. Ogueri, T. Jafari, J. L. Escobar Ivirico, and C. T. Laurencin, "Polymeric biomaterials for scaffold-based bone regenerative engineering," *Regenerative engineering and translational medicine,* vol. 5, no. 2, pp. 128-154, 2019.

[80] L. Polo-Corrales, M. Latorre-Esteves, and J. E. Ramirez-Vick, "Scaffold design for bone regeneration," *Journal of nanoscience and nanotechnology,* vol. 14, no. 1, pp. 15-56, 2014.

[81] S. A. Naghavi *et al.*, "Mechanical characterisation and numerical modelling of TPMS-based gyroid and diamond Ti6Al4V scaffolds for bone implants: an integrated approach for translational consideration," *Bioengineering,* vol. 9, no. 10, p. 504, 2022.

[82] F. J. O'brien, "Biomaterials & scaffolds for tissue engineering," *Materials today,* vol. 14, no. 3, pp. 88-95, 2011.

[83] J. Henkel *et al.*, "Bone regeneration based on tissue engineering conceptions—a 21st century perspective," *Bone research,* vol. 1, no. 1, pp. 216-248, 2013.

[84] M. A. Woodruff *et al.*, "Bone tissue engineering: from bench to bedside," *Materials Today,* vol. 15, no. 10, pp. 430-435, 2012.

[85] S. Tajvar, A. Hadjizadeh, and S. S. Samandari, "Scaffold degradation in bone tissue engineering: an overview," *International Biodeterioration & Biodegradation,* vol. 180, p. 105599, 2023.

[86] F. Donnaloja, E. Jacchetti, M. Soncini, and M. T. Raimondi, "Natural and synthetic polymers for bone scaffolds optimization," *Polymers,* vol. 12, no. 4, p. 905, 2020.

[87] D. P. Bhattarai, L. E. Aguilar, C. H. Park, and C. S. Kim, "A review on properties of natural and synthetic based electrospun fibrous materials for bone tissue engineering," *Membranes,* vol. 8, no. 3, p. 62, 2018.

[88] A. M. Ferreira, P. Gentile, V. Chiono, and G. Ciardelli, "Collagen for bone tissue regeneration," *Acta biomaterialia,* vol. 8, no. 9, pp. 3191-3200, 2012.

[89] W.-H. Lee, C.-Y. Loo, and R. Rohanizadeh, "A review of chemical surface modification of bioceramics: effects on protein adsorption and cellular response," *Colloids and Surfaces B: Biointerfaces,* vol. 122, pp. 823-834, 2014.

[90] U. Hersel, C. Dahmen, and H. Kessler, "RGD modified polymers: biomaterials for stimulated cell adhesion and beyond," *Biomaterials,* vol. 24, no. 24, pp. 4385-4415, 2003.

[91] X. Liu, L. A. Smith, J. Hu, and P. X. Ma, "Biomimetic nanofibrous gelatin/apatite composite scaffolds for bone tissue engineering," *Biomaterials,* vol. 30, no. 12, pp. 2252-2258, 2009.

[92] M. A. Woodruff and D. W. Hutmacher, "The return of a forgotten polymer—Polycaprolactone in the 21st century," *Progress in polymer science,* vol. 35, no. 10, pp. 1217-1256, 2010.

[93] J. C. Middleton and A. J. Tipton, "Synthetic biodegradable polymers as orthopedic devices," *Biomaterials,* vol. 21, no. 23, pp. 2335-2346, 2000.

[94] M. Gharibshahian *et al.*, "Recent advances on 3D-printed PCL-based composite scaffolds for bone tissue engineering," *Frontiers in bioengineering and biotechnology,* vol. 11, p. 1168504, 2023.

[95] S. Farah, D. G. Anderson, and R. Langer, "Physical and mechanical properties of PLA, and their functions in widespread applications—A comprehensive review," *Advanced drug delivery reviews,* vol. 107, pp. 367-392, 2016.

[96] P. Gentile, V. Chiono, I. Carmagnola, and P. V. Hatton, "An overview of poly (lactic-co-glycolic) acid (PLGA)-based biomaterials for bone tissue engineering," *International journal of molecular sciences,* vol. 15, no. 3, pp. 3640-3659, 2014.

[97] H.-Y. Liang *et al.*, "Polycaprolactone in bone tissue engineering: a comprehensive review of innovations in scaffold fabrication and surface modifications," *Journal of functional biomaterials,* vol. 15, no. 9, p. 243, 2024.

[98] Z. Sheikh, S. Najeeb, Z. Khurshid, V. Verma, H. Rashid, and M. Glogauer, "Biodegradable materials for bone repair and tissue engineering applications," *Materials,* vol. 8, no. 9, pp. 5744-5794, 2015.

[99] D. Gupta, V. Dogra, D. Verma, A. K. Chaudhary, and M. Tewari, "PCL-based composites and their utilizations in the medical sector," *Bioresorbable polymers and their composites,* pp. 63-83, 2024.

[100] J. Baldwin *et al.*, "Periosteum tissue engineering in an orthotopic in vivo platform," *Biomaterials,* vol. 121, pp. 193-204, 2017.

[101] S. Sánchez-González, N. Diban, and A. Urtiaga, "Hydrolytic degradation and mechanical stability of poly (ε-Caprolactone)/reduced graphene oxide membranes as scaffolds for in vitro neural tissue regeneration," *Membranes,* vol. 8, no. 1, p. 12, 2018.

[102] N. Geoghegan *et al.*, "Controlled degradation of polycaprolactone-based micropillar arrays," *Biomaterials Science,* vol. 11, no. 9, pp. 3077-3091, 2023.

[103] G. R. da Silva, A. da Silva-Cunha Jr, F. Behar-Cohen, E. Ayres, and R. L. Oréfice, "Biodegradation of polyurethanes and nanocomposites to non-cytotoxic degradation products," *Polymer degradation and stability,* vol. 95, no. 4, pp. 491-499, 2010.

[104] A. Fuchs *et al.*, "A new multilayered membrane for tissue engineering of oral hard-and soft tissue by means of melt electrospinning writing and film casting–An in vitro study," *Journal of Cranio-Maxillofacial Surgery,* vol. 47, no. 4, pp. 695-703, 2019.

[105] M. L. Muerza-Cascante *et al.*, "Endosteal-like extracellular matrix expression on melt electrospun written scaffolds," *Acta biomaterialia,* vol. 52, pp. 145-158, 2017.

[106] T. D. Brown *et al.*, "Design and fabrication of tubular scaffolds via direct writing in a melt electrospinning mode," *Biointerphases,* vol. 7, no. 1, p. 13, 2012.

[107] S. Zaiss, T. D. Brown, J. C. Reichert, and A. Berner, "Poly (ε-caprolactone) scaffolds fabricated by melt electrospinning for bone tissue engineering," *Materials,* vol. 9, no. 4, p. 232, 2016.

[108] C. Vaquette, S. Saifzadeh, A. Farag, D. Hutmacher, and S. Ivanovski, "Periodontal tissue engineering with a multiphasic construct and cell sheets," *Journal of dental research,* vol. 98, no. 6, pp. 673-681, 2019.

[109] P. F. Costa, C. Vaquette, Q. Zhang, R. L. Reis, S. Ivanovski, and D. W. Hutmacher, "Advanced tissue engineering scaffold design for regeneration of the complex hierarchical periodontal structure," *Journal of clinical periodontology,* vol. 41, no. 3, pp. 283-294, 2014.

[110] J. M. Ameer, A. K. Pr, and N. Kasoju, "Strategies to tune electrospun scaffold porosity for effective cell response in tissue engineering," *Journal of functional biomaterials,* vol. 10, no. 3, p. 30, 2019.

[111] C. Wang and Y. Zhou, "Sacrificial biomaterials in 3D fabrication of scaffolds for tissue engineering applications," *Journal of Biomedical Materials Research Part B: Applied Biomaterials,* vol. 112, no. 1, p. e35312, 2024.

[112] M. S. B. Reddy, D. Ponnamma, R. Choudhary, and K. K. Sadasivuni, "A comparative review of natural and synthetic biopolymer composite scaffolds," *Polymers,* vol. 13, no. 7, p. 1105, 2021.

[113] K. Remya, S. Chandran, S. Mani, A. John, and P. Ramesh, "Hybrid polycaprolactone/polyethylene oxide scaffolds with tunable fiber surface morphology,

improved hydrophilicity and biodegradability for bone tissue engineering applications," *Journal of Biomaterials science, Polymer edition,* vol. 29, no. 12, pp. 1444-1462, 2018.

[114] A. Koski, K. Yim, and S. Shivkumar, "Effect of molecular weight on fibrous PVA produced by electrospinning," *Materials letters,* vol. 58, no. 3-4, pp. 493-497, 2004.

[115] É. J. Beaudoin, R. J. Zednik, and N. R. Demarquette, "Tuning polymer solution elasticity for electrospinning: effects of molecular weight distribution and elastic doping," *Rheologica Acta,* pp. 1-13, 2026.

[116] P. D. Dalton, J. Lleixà Calvet, A. Mourran, D. Klee, and M. Möller, "Melt electrospinning of poly-(ethylene glycol-block-ϵ-caprolactone)," *Biotechnology Journal: Healthcare Nutrition Technology,* vol. 1, no. 9, pp. 998-1006, 2006.

[117] C. D. Mansfied, T. Chen, M. Q. Ansari, and D. G. Baird, "The rheology of ultra-high molecular weight poly (ethylene oxide) dispersed in a low molecular weight carrier," *Physics of Fluids,* vol. 34, no. 2, 2022.

[118] A.-A. A. Abdel-Azim, W. Y. Boutros, and E.-S. M. Abdel-Bary, "Estimation of the compatibility of poly (ethylene glycol)/poly (ethylene oxide) blends from dilute solution viscosity measurements," *Polymer,* vol. 39, no. 12, pp. 2543-2549, 1998.

[119] F. Ramírez-Ruiz, I. Núñez-Tapia, M. C. Piña-Barba, M. A. Alvarez-Pérez, V. Guarino, and J. Serrano-Bello, "Polycaprolactone for hard tissue regeneration: scaffold design and in vivo implications," *Bioengineering,* vol. 12, no. 1, p. 46, 2025.

[120] T. K. Dash and V. B. Konkimalla, "Poly-ϵ-caprolactone based formulations for drug delivery and tissue engineering: A review," *Journal of Controlled Release,* vol. 158, no. 1, pp. 15-33, 2012.

[121] R. M. Allaf, "The effect of PEO/NaCl dual porogens in the fabrication of porous PCL membranes via a solid-state blending approach," *Scientific Reports,* vol. 15, no. 1, p. 454, 2025.

[122] V. Guarino, A. Guaccio, and L. Ambrosio, "Manipulating co-continuous polymer blends to create PCL scaffolds with fully interconnected and anisotropic pore architecture," *Journal of Applied Biomaterials and Biomechanics,* vol. 9, no. 1, pp. 34-39, 2011.

[123] A. Rezaei Kolahchi, A. Ajji, and P. J. Carreau, "Surface morphology and properties of ternary polymer blends: Effect of the migration of minor components," *The Journal of Physical Chemistry B,* vol. 118, no. 23, pp. 6316-6323, 2014.

[124] S. Sharma, P. Sudhakara, J. Singh, R. Ilyas, M. Asyraf, and M. Razman, "Critical review of biodegradable and bioactive polymer composites for bone tissue engineering and drug delivery applications," *Polymers,* vol. 13, no. 16, p. 2623, 2021.

[125] T. Nazari and H. Garmabi, "Thermo-rheological and interfacial properties of polylactic acid/polyethylene glycol blends toward the melt electrospinning ability," *Journal of Applied Polymer Science,* vol. 133, no. 44, 2016.

[126] S. Srouji, D. Ben-David, R. Lotan, E. Livne, R. Avrahami, and E. Zussman, "Slow-release human recombinant bone morphogenetic protein-2 embedded within electrospun scaffolds for regeneration of bone defect: in vitro and in vivo evaluation," *Tissue Engineering Part A,* vol. 17, no. 3-4, pp. 269-277, 2011.

[127] J. H. Lee *et al.*, "Biointerface control of electrospun fiber scaffolds for bone regeneration: engineered protein link to mineralized surface," *Acta biomaterialia,* vol. 10, no. 6, pp. 2750-2761, 2014.

[128] J. Hodge and C. Quint, "The improvement of cell infiltration in an electrospun scaffold with multiple synthetic biodegradable polymers using sacrificial PEO microparticles," *Journal of Biomedical Materials Research Part A,* vol. 107, no. 9, pp. 1954-1964, 2019.

[129] W. Lin, M. Chen, T. Qu, J. Li, and Y. Man, "Three-dimensional electrospun nanofibrous scaffolds for bone tissue engineering," *Journal of Biomedical Materials Research Part B: Applied Biomaterials,* vol. 108, no. 4, pp. 1311-1321, 2020.

[130] D. P. Simunec, J. Jacob, A. E. Kandjani, A. Trinchi, and A. Sola, "Facilitating the additive manufacture of high-performance polymers through polymer blending: A review," *European Polymer Journal,* vol. 201, p. 112553, 2023.

[131] C. Prem Kumar, N. Sivanagaraju, D. Loknath, G. N. Mallikarjun Rao, and M. Vakkalagadda, "Shape memory polymers, blends, and composites: processing, properties, and applications," *Polymer-Plastics Technology and Materials,* vol. 64, no. 9, pp. 1253-1281, 2025.

[132] G. Toskas *et al.*, "Chitosan (PEO)/silica hybrid nanofibers as a potential biomaterial for bone regeneration," *Carbohydrate Polymers,* vol. 94, no. 2, pp. 713-722, 2013.

[133] X. Hou *et al.*, "Entropically toughened robust biodegradable polymer blends and composites for bone tissue engineering," *ACS Applied Materials & Interfaces,* vol. 16, no. 2, pp. 2912-2920, 2024.

[134] G. K. Arbade, J. Srivastava, V. Tripathi, N. Lenka, and T. U. Patro, "Enhancement of hydrophilicity, biocompatibility and biodegradability of poly (ε-caprolactone) electrospun nanofiber scaffolds using poly (ethylene glycol) and poly (L-lactide-co-ε-caprolactone-co-glycolide) as additives for soft tissue engineering," *Journal of Biomaterials Science, Polymer Edition,* vol. 31, no. 13, pp. 1648-1670, 2020.

[135] H. R. Munj, M. T. Nelson, P. S. Karandikar, J. J. Lannutti, and D. L. Tomasko, "Biocompatible electrospun polymer blends for biomedical applications," *Journal of Biomedical Materials Research Part B: Applied Biomaterials,* vol. 102, no. 7, pp. 1517-1527, 2014.

[136] E. Behtouei *et al.*, "Bead-free and tough electrospun PCL/gelatin/PGS ternary nanofibrous scaffolds for tissue engineering application," *Journal of Applied Polymer Science,* vol. 139, no. 2, p. 51471, 2022.

[137] G. Costabeber *et al.*, "Additive manufacturing of polylactic acid scaffolds dip-coated with polycaprolactone for bone tissue engineering," *Materials Today Communications,* vol. 40, p. 109646, 2024.

[138] N. Tuancharoensri, G. M. Ross, S. Mahasaranon, P. D. Topham, and S. Ross, "Ternary blend nanofibres of poly (lactic acid), polycaprolactone and cellulose acetate butyrate for skin tissue scaffolds: influence of blend ratio and polycaprolactone molecular mass on miscibility, morphology, crystallinity and thermal properties," *Polymer International,* vol. 66, no. 11, pp. 1463-1472, 2017.

[139] R. Grande, L. A. Pessan, and A. J. Carvalho, "Thermoplastic blends of chitosan: A method for the preparation of high thermally stable blends with polyesters," *Carbohydrate polymers,* vol. 191, pp. 44-52, 2018.

[140] I. Luzinov, C. Pagnoulle, and R. Jérôme, "Ternary polymer blend with core–shell dispersed phases: effect of the core-forming polymer on phase morphology and mechanical properties," *Polymer,* vol. 41, no. 19, pp. 7099-7109, 2000.

[141] B. D. Favis and J.-P. Chalifoux, "The effect of viscosity ratio on the morphology of polypropylene/polycarbonate blends during processing," *Polymer Engineering & Science,* vol. 27, no. 21, pp. 1591-1600, 1987.

[142] S. Shokoohi and A. Arefazar, "A review on ternary immiscible polymer blends: morphology and effective parameters," *Polymers for Advanced Technologies,* vol. 20, no. 5, pp. 433-447, 2009.

[143] M. Hemmati, H. Nazokdast, and H. Shariat Panahi, "Study on morphology of ternary polymer blends. I. Effects of melt viscosity and interfacial interaction," *Journal of applied polymer science,* vol. 82, no. 5, pp. 1129-1137, 2001.

[144] S. Wu, "Phase structure and adhesion in polymer blends: a criterion for rubber toughening," *Polymer,* vol. 26, no. 12, pp. 1855-1863, 1985.

[145] L. A. Utracki, *Commercial polymer blends*. Springer Science & Business Media, 2013.

[146] L. A. Utracki and C. A. Wilkie, *Polymer blends handbook*. Kluwer academic publishers Dordrecht, 2002.

[147] R. Willemse, A. P. De Boer, J. Van Dam, and A. Gotsis, "Co-continuous morphologies in polymer blends: the influence of the interfacial tension," *Polymer,* vol. 40, no. 4, pp. 827-834, 1999.

[148] P. Pötschke and D. Paul, "Formation of co-continuous structures in melt-mixed immiscible polymer blends," *Journal of Macromolecular Science, Part C: Polymer Reviews,* vol. 43, no. 1, pp. 87-141, 2003.

[149] M. Sumita, K. Sakata, S. Asai, K. Miyasaka, and H. Nakagawa, "Dispersion of fillers and the electrical conductivity of polymer blends filled with carbon black," *Polymer bulletin,* vol. 25, no. 2, pp. 265-271, 1991.

[150] C. Harrats and N. Mekhilef, "Cocontinuous phase morphologies: predictions, generation, and practical applications," in *Micro-and Nanostructured Multiphase Polymer Blend Systems*: CRC Press, 2005, pp. 91-132.

[151] U. Sundararaj, C. Macosko, and C. K. Shih, "Evidence for inversion of phase continuity during morphology development in polymer blending," *Polymer Engineering & Science,* vol. 36, no. 13, pp. 1769-1781, 1996.

[152] K. Olonisakin, A. K. Mohanty, M. Thimmanagari, and M. Misra, "Recent advances in biodegradable polymer blends and their biocomposites: a comprehensive review," *Green Chemistry,* vol. 27, no. 38, pp. 11656-11704, 2025.

[153] S. Nagam Hanumantharao and S. Rao, "Multi-functional electrospun nanofibers from polymer blends for scaffold tissue engineering," *Fibers,* vol. 7, no. 7, p. 66, 2019.

[154] M. Nofar, D. Sacligil, P. J. Carreau, M. R. Kamal, and M.-C. Heuzey, "Poly (lactic acid) blends: Processing, properties and applications," *International journal of biological macromolecules,* vol. 125, pp. 307-360, 2019.

[155] N. Mekhilef and H. Verhoogt, "Phase inversion and dual-phase continuity in polymer blends: theoretical predictions and experimental results," *Polymer,* vol. 37, no. 18, pp. 4069-4077, 1996.

[156] C. M. Hansen, *Hansen solubility parameters: a user's handbook*. CRC press, 2007.

[157] M. Chastrette, M. Rajzmann, M. Chanon, and K. F. Purcell, "Approach to a general classification of solvents using a multivariate statistical treatment of quantitative solvent parameters," *Journal of the American Chemical Society,* vol. 107, no. 1, pp. 1-11, 1985.

[158] I. H. T. Guideline, "Impurities: Guideline for residual solvents Q3C (R5)," *Current Step,* vol. 4, pp. 1-25, 2005.

[159] A. Ojha and S. Bhargava, "International council for harmonisation (ICH) guidelines," in *Regulatory affairs in the pharmaceutical industry*: Elsevier, 2022, pp. 47-74.

[160] A. Hijano, I. Loscertales, S. Ibáñez, and F. Higuera, "Periodic emission of droplets from an oscillating electrified meniscus of a low-viscosity, highly conductive liquid," *Physical Review E,* vol. 91, no. 1, p. 013011, 2015.

[161] M. B. Dehaghi, M. Shams, F. Sohani, and P. Naderi, "Experimental study of the stable region of electrospray of ethanol-water mixtures with different concentrations by high-speed imaging," *Case Studies in Chemical and Environmental Engineering,* vol. 8, p. 100541, 2023.

[162] K. Garg and G. L. Bowlin, "Electrospinning jets and nanofibrous structures," *Biomicrofluidics,* vol. 5, no. 1, 2011.

[163] H. Yuan *et al.*, "Stable jet electrospinning for easy fabrication of aligned ultrafine fibers," *Journal of Materials Chemistry,* vol. 22, no. 37, pp. 19634-19638, 2012.

[164] E. Castillo-Orozco, A. Kar, and R. Kumar, "Non-dimensional groups for electrospray modes of highly conductive and viscous nanoparticle suspensions," *Scientific reports,* vol. 10, no. 1, p. 4405, 2020.

[165] D. R. Flores-Hernandez, B. Cardenas-Benitez, S. O. Martinez-Chapa, and J. Bonilla-Rios, "Tailoring the Diameters of Electro-Mechanically Spun Fibers by Controlling Their Deborah Numbers," *Polymers,* vol. 12, no. 6, p. 1358, 2020.

[166] D. Shou, L. Ye, and J. Fan, "Gas transport properties of electrospun polymer nanofibers," *Polymer,* vol. 55, no. 14, pp. 3149-3155, 2014.

[167] J. Xue, T. Wu, Y. Dai, and Y. Xia, "Electrospinning and electrospun nanofibers: methods, materials, and applications," *Chemical reviews,* vol. 119, no. 8, pp. 5298-5415, 2019.

[168] S. Ramakrishna, *An introduction to electrospinning and nanofibers*. World scientific, 2005.

[169] D. H. Reneker and A. L. Yarin, "Electrospinning jets and polymer nanofibers," *Polymer,* vol. 49, no. 10, pp. 2387-2425, 2008.

[170] M. M. Hohman, M. Shin, G. Rutledge, and M. P. Brenner, "Electrospinning and electrically forced jets. I. Stability theory," *Physics of fluids,* vol. 13, no. 8, pp. 2201-2220, 2001.

[171] N. Ardila, Z. Ajji, M.-C. Heuzey, and A. Ajji, "Chitosan electrospraying: Mapping of process stability and micro and nanoparticle formation," *Journal of Aerosol Science,* vol. 126, pp. 85-98, 2018.

[172] A. Greiner and J. H. Wendorff, "Electrospinning: a fascinating method for the preparation of ultrathin fibers," *Angewandte Chemie International Edition,* vol. 46, no. 30, pp. 5670-5703, 2007.

[173] D. Nurwaha, W. Han, and X. Wang, "Effects of processing parameters on electrospun fiber morphology," *Journal of the Textile Institute,* vol. 104, no. 4, pp. 419-425, 2013.

[174] J.-F. Agassant, P. Avenas, P. J. Carreau, B. Vergnes, and M. Vincent, *Polymer processing: principles and modeling*. Carl Hanser Verlag GmbH Co KG, 2017.

[175] N. Mayadeo, K. Morikawa, M. Naraghi, and M. J. Green, "Modeling of downstream heating in melt electrospinning of polymers," *Journal of Polymer Science Part B: Polymer Physics,* vol. 55, no. 18, pp. 1393-1405, 2017.

[176] E. Zhmayev, H. Zhou, and Y. L. Joo, "Modeling of non-isothermal polymer jets in melt electrospinning," *Journal of Non-Newtonian Fluid Mechanics,* vol. 153, no. 2-3, pp. 95-108, 2008.

[177] K. Morikawa, A. Vashisth, C. J. Grimme, M. J. Green, and M. Naraghi, "Wire melt electrospinning of thin polymeric fibers via strong electrostatic field gradients," *Macromolecular Materials and Engineering,* vol. 304, no. 1, p. 1800417, 2019.

[178] D. W. Hutmacher and P. D. Dalton, "Melt electrospinning," *Chemistry–An Asian Journal,* vol. 6, no. 1, pp. 44-56, 2011.

[179] T. Nazari and H. Garmabi, "The effects of processing parameters on the morphology of PLA/PEG melt electrospun fibers," *Polymer International,* vol. 67, no. 2, pp. 178-188, 2018.

[180] T. Nazari and H. Garmabi, "Polylactic acid/polyethylene glycol blend fibres prepared via melt electrospinning: effect of polyethylene glycol content," *Micro & Nano Letters,* vol. 9, no. 10, pp. 686-690, 2014.

[181] L. Cao *et al.*, "Morphologies and crystal structures of styrene–acrylonitrile/isotactic polypropylene ultrafine fibers fabricated by melt electrospinning," *Polymer Engineering & Science,* vol. 53, no. 12, pp. 2674-2682, 2013.

[182] M. Shahverdi, S. Seifi, A. Akbari, K. Mohammadi, A. Shamloo, and M. R. Movahhedy, "Melt electrowriting of PLA, PCL, and composite PLA/PCL scaffolds for tissue engineering application," *Scientific reports,* vol. 12, no. 1, p. 19935, 2022.

[183] M. Zakaria and K. Nakane, "Fabrication of polypropylene nanofibers from polypropylene/polyvinyl butyral blend films using laser-assisted melt-electrospinning," *Polymer Engineering & Science,* vol. 60, no. 2, pp. 362-370, 2020.

[184] Z. Wei, "Research process of polymer nanofibers prepared by melt spinning," in *IOP Conference Series: Materials Science and Engineering*, 2018, vol. 452, no. 2: IOP Publishing, p. 022002.

[185] L.-H. Zhang *et al.*, "Recent advances in melt electrospinning," *RSC advances,* vol. 6, no. 58, pp. 53400-53414, 2016.

[186] R. Banerjee and S. S. Ray, "Role of rheology in morphology development and advanced processing of thermoplastic polymer materials: A review," *ACS omega,* vol. 8, no. 31, pp. 27969-28001, 2023.

[187] O. Sadiku-Agboola, E. R. Sadiku, A. T. Adegbola, and O. F. Biotidara, "Rheological properties of polymers: structure and morphology of molten polymer blends," *Mater. Sci. Appl,* vol. 2, no. 01, pp. 30-41, 2011.

[188] S. Rastogi *et al.*, "Emerging Technologies in Bone Tissue Engineering: A Review," *Journal of Bionic Engineering,* vol. 22, no. 5, pp. 2261-2285, 2025.

[189] S. Hosseinpour, M. Ghazizadeh Ahsaie, M. Rezai Rad, M. T. Baghani, S. R. Motamedian, and A. Khojasteh, "Application of selected scaffolds for bone tissue engineering: a systematic review," *Oral and maxillofacial surgery,* vol. 21, no. 2, pp. 109-129, 2017.

[190] S. D. McCullen *et al.*, "Characterization of electrospun nanocomposite scaffolds and biocompatibility with adipose-derived human mesenchymal stem cells," *International journal of nanomedicine,* vol. 2, no. 2, pp. 253-263, 2007.

[191] H. Zhang, "Electrospun poly (lactic-co-glycolic acid)/multiwalled carbon nanotubes composite scaffolds for guided bone tissue regeneration," *Journal of Bioactive and Compatible Polymers,* vol. 26, no. 4, pp. 347-362, 2011.

[192] S. Nomura and T. Takano-Yamamoto, "Molecular events caused by mechanical stress in bone," *Matrix Biology,* vol. 19, no. 2, pp. 91-96, 2000.

[193] Y. Wu *et al.*, "A novel calcium phosphate ceramic–magnetic nanoparticle composite as a potential bone substitute," *Biomedical Materials,* vol. 5, no. 1, p. 015001, 2010.

[194] J. Meng *et al.*, "Paramagnetic nanofibrous composite films enhance the osteogenic responses of pre-osteoblast cells," *Nanoscale,* vol. 2, no. 12, pp. 2565-2569, 2010.

[195] H. Kotani *et al.*, "Strong static magnetic field stimulates bone formation to a definite orientation in vitro and in vivo," *Journal of Bone and Mineral Research,* vol. 17, no. 10, pp. 1814-1821, 2002.

[196] R. Leesungbok, S.-J. Ahn, S.-W. Lee, G.-H. Park, J.-S. Kang, and J.-J. Choi, "The effects of a static magnetic field on bone formation around a sandblasted, large-grit, acid-etched–treated titanium implant," *Journal of Oral Implantology,* vol. 39, no. S1, pp. 248-255, 2013.

[197] R. K. Singh *et al.*, "Potential of magnetic nanofiber scaffolds with mechanical and biological properties applicable for bone regeneration," *PloS one,* vol. 9, no. 4, p. e91584, 2014.

[198] M. Rizwan, M. Hamdi, and W. J. Basirun, "Bioglass® 45S5-based composites for bone tissue engineering and functional applications," *Journal of biomedical materials research Part A,* vol. 105, no. 11, pp. 3197-3223, 2017.

[199] S. Verrier, J. J. Blaker, V. Maquet, L. L. Hench, and A. R. Boccaccini, "PDLLA/Bioglass® composites for soft-tissue and hard-tissue engineering: an in vitro cell biology assessment," *Biomaterials,* vol. 25, no. 15, pp. 3013-3021, 2004.

[200] W. Helen, C. L. Merry, J. J. Blaker, and J. E. Gough, "Three-dimensional culture of annulus fibrosus cells within PDLLA/Bioglass® composite foam scaffolds: Assessment of cell attachment, proliferation and extracellular matrix production," *Biomaterials,* vol. 28, no. 11, pp. 2010-2020, 2007.

[201] X. B. Yang *et al.*, "Evaluation of human bone marrow stromal cell growth on biodegradable polymer/Bioglass® composites," *Biochemical and biophysical research communications,* vol. 342, no. 4, pp. 1098-1107, 2006.

[202] M. Amaral *et al.*, "Nanocrystalline diamond: In vitro biocompatibility assessment by MG63 and human bone marrow cells cultures," *Journal of Biomedical Materials Research Part A: An Official Journal of The Society for Biomaterials, The Japanese Society for Biomaterials, and The Australian Society for Biomaterials and the Korean Society for Biomaterials,* vol. 87, no. 1, pp. 91-99, 2008.

[203] L. Grausova *et al.*, "Enhanced growth and osteogenic differentiation of human osteoblast-like cells on boron-doped nanocrystalline diamond thin films," *PLoS One,* vol. 6, no. 6, p. e20943, 2011.

[204] A. M. Schrand, L. Dai, J. J. Schlager, S. M. Hussain, and E. Osawa, "Differential biocompatibility of carbon nanotubes and nanodiamonds," *Diamond and Related Materials,* vol. 16, no. 12, pp. 2118-2123, 2007.

[205] A. D. Salaam and D. Dean, "Electrospun polycaprolactone-nanodiamond composite scaffolds for bone tissue engineering," in *Global Congress on NanoEngineering for Medicine and Biology*, 2010, vol. 43925, pp. 367-370.

[206] A. Serafim, S. Cecoltan, A. Lungu, E. Vasile, H. Iovu, and I. Stancu, "Electrospun fish gelatin fibrous scaffolds with improved bio-interactions due to carboxylated nanodiamond loading," *RSC advances,* vol. 5, no. 116, pp. 95467-95477, 2015.

[207] K. Balagangadharan, R. Trivedi, M. Vairamani, and N. Selvamurugan, "Sinapic acid-loaded chitosan nanoparticles in polycaprolactone electrospun fibers for bone regeneration in vitro and in vivo," *Carbohydrate polymers,* vol. 216, pp. 1-16, 2019.

[208] A. Hivechi, S. H. Bahrami, and R. A. Siegel, "Investigation of morphological, mechanical and biological properties of cellulose nanocrystal reinforced electrospun gelatin nanofibers," *International journal of biological macromolecules,* vol. 124, pp. 411-417, 2019.

[209] C. Zhou *et al.*, "Electrospun bio-nanocomposite scaffolds for bone tissue engineering by cellulose nanocrystals reinforcing maleic anhydride grafted PLA," *ACS applied materials & interfaces,* vol. 5, no. 9, pp. 3847-3854, 2013.

[210] F. Fenouillot, P. Cassagnau, and J.-C. Majesté, "Uneven distribution of nanoparticles in immiscible fluids: Morphology development in polymer blends," *Polymer,* vol. 50, no. 6, pp. 1333-1350, 2009.

[211] M. J. Mochane, J. S. Sefadi, T. S. Motsoeneng, T. E. Mokoena, T. G. Mofokeng, and T. C. Mokhena, "The effect of filler localization on the properties of biopolymer blends, recent advances: A review," *Polymer Composites,* vol. 41, no. 7, pp. 2958-2979, 2020.

[212] A. Dasari, Z.-Z. Yu, and Y.-W. Mai, "Effect of blending sequence on microstructure of ternary nanocomposites," *Polymer,* vol. 46, no. 16, pp. 5986-5991, 2005.

[213] P. Pötschke, A. R. Bhattacharyya, and A. Janke, "Morphology and electrical resistivity of melt mixed blends of polyethylene and carbon nanotube filled polycarbonate," *Polymer,* vol. 44, no. 26, pp. 8061-8069, 2003.

[214] K. Y. Lee and L. A. Goettler, "Structure-property relationships in polymer blend nanocomposites," *Polymer Engineering & Science,* vol. 44, no. 6, pp. 1103-1111, 2004.

[215] R. Salehiyan and S. S. Ray, "Tuning the conductivity of nanocomposites through nanoparticle migration and interface crossing in immiscible polymer blends: A review on fundamental understanding," *Macromolecular Materials and Engineering,* vol. 304, no. 2, p. 1800431, 2019.

[216] G. Filippone, N. T. Dintcheva, F. La Mantia, and D. Acierno, "Using organoclay to promote morphology refinement and co-continuity in high-density polyethylene/polyamide 6 blends–Effect of filler content and polymer matrix composition," *Polymer,* vol. 51, no. 17, pp. 3956-3965, 2010.

[217] J. Plattier, L. Benyahia, M. Dorget, F. Niepceron, and J.-F. Tassin, "Viscosity-induced filler localisation in immiscible polymer blends," *Polymer,* vol. 59, pp. 260-269, 2015.

[218] A. Göldel, G. R. Kasaliwal, P. Pötschke, and G. Heinrich, "The kinetics of CNT transfer between immiscible blend phases during melt mixing," *Polymer,* vol. 53, no. 2, pp. 411-421, 2012.

[219] I. L. Tsiklin, A. V. Shabunin, A. V. Kolsanov, and L. T. Volova, "In vivo bone tissue engineering strategies: advances and prospects," *Polymers,* vol. 14, no. 15, p. 3222, 2022.

[220] S. R. Motamedian, P. Iranparvar, G. Nahvi, and A. Khojasteh, "Bone tissue engineering: a literature review," *Regeneration, Reconstruction & Restoration (Triple R),* vol. 1, no. 3, pp. 103-120, 2016.

[221] L. Roseti *et al.*, "Scaffolds for bone tissue engineering: state of the art and new perspectives," *Materials Science and Engineering: C,* vol. 78, pp. 1246-1262, 2017.

[222] E. A. Todd *et al.*, "Functional scaffolds for bone tissue regeneration: a comprehensive review of materials, methods, and future directions," *Journal of functional biomaterials,* vol. 15, no. 10, p. 280, 2024.

[223] W. Li, J. Zhou, and Y. Xu, "Study of the in vitro cytotoxicity testing of medical devices," *Biomedical reports,* vol. 3, no. 5, pp. 617-620, 2015.

[224] I. O. f. Standardization, "ISO 10993–5: 2009 Biological evaluation of mdeical devices, Part 5: Tests for in vitro cytotoxicity," 2009.

[225] S. K. Bhatia and A. B. Yetter, "Correlation of visual in vitro cytotoxicity ratings of biomaterials with quantitative in vitro cell viability measurements," *Cell biology and toxicology,* vol. 24, no. 4, pp. 315-319, 2008.

[226] X. Liu *et al.*, "A comparison of in vitro cytotoxicity assays in medical device regulatory studies," *Regulatory toxicology and pharmacology,* vol. 97, pp. 24-32, 2018.

[227] S. K. Jhamb, A. Goyal, A. Pandey, and A. Bhowmik, "A review of cytotoxicity testing methods and in vitro study of biodegradable Mg-1% Sn-2% HA composite by elution method," *Journal of Materials Science: Materials in Medicine,* vol. 36, no. 1, pp. 1-18, 2025.

[228] S. Gruber and A. Nickel, "Toxic or not toxic? The specifications of the standard ISO 10993-5 are not explicit enough to yield comparable results in the cytotoxicity assessment of an identical medical device," *Frontiers in medical technology,* vol. 5, p. 1195529, 2023.

[229] K. A. Kilian, B. Bugarija, B. T. Lahn, and M. Mrksich, "Geometric cues for directing the differentiation of mesenchymal stem cells," *Proceedings of the National Academy of Sciences,* vol. 107, no. 11, pp. 4872-4877, 2010.

[230] A. Buxboim, I. L. Ivanovska, and D. E. Discher, "Matrix elasticity, cytoskeletal forces and physics of the nucleus: how deeply do cells ‘feel’outside and in?," *Journal of cell science,* vol. 123, no. 3, pp. 297-308, 2010.

[231] M. V. Park, D. P. Lankveld, H. van Loveren, and W. H. de Jong, "The status of in vitro toxicity studies in the risk assessment of nanomaterials," *Nanomedicine,* vol. 4, no. 6, pp. 669-685, 2009.

[232] F. Fendi, B. Abdullah, S. Suryani, A. N. Usman, and D. Tahir, "Development and application of hydroxyapatite-based scaffolds for bone tissue regeneration: A systematic literature review," *Bone,* vol. 183, p. 117075, 2024.

[233] A.-M. Yousefi, P. F. James, R. Akbarzadeh, A. Subramanian, C. Flavin, and H. Oudadesse, "Prospect of stem cells in bone tissue engineering: a review," *Stem cells international,* vol. 2016, no. 1, p. 6180487, 2016.

[234] T. Livingston, P. Ducheyne, and J. Garino, "In vivo evaluation of a bioactive scaffold for bone tissue engineering," *Journal of Biomedical Materials Research: An Official Journal of The Society for Biomaterials, The Japanese Society for Biomaterials, and The Australian Society for Biomaterials and the Korean Society for Biomaterials,* vol. 62, no. 1, pp. 1-13, 2002.

[235] E. Cramer, K. Ito, and S. Hofmann, "Ex vivo bone models and their potential in preclinical evaluation," *Current Osteoporosis Reports,* vol. 19, no. 1, pp. 75-87, 2021.

[236] S. S. Piglionico, C. Pons, O. Romieu, F. Cuisinier, B. Levallois, and I. V. Panayotov, "In vitro, ex vivo, and in vivo models for dental pulp regeneration," *Journal of Materials Science: Materials in Medicine,* vol. 34, no. 4, p. 15, 2023.

[237] M. P. Stewart, A. Sharei, X. Ding, G. Sahay, R. Langer, and K. F. Jensen, "In vitro and ex vivo strategies for intracellular delivery," *Nature,* vol. 538, no. 7624, pp. 183-192, 2016.

[238] E. Tsiridis, N. Gurav, G. Bailey, R. Sambrook, and L. Di Silvio, "A novel ex vivo culture system for studying bone repair," *Injury,* vol. 37, no. 3, pp. S10-S17, 2006.

[239] A. Abubakar, M. Noordin, T. Azmi, U. Kaka, and M. Loqman, "The use of rats and mice as animal models in ex vivo bone growth and development studies," *Bone & joint research,* vol. 5, no. 12, pp. 610-618, 2016.

[240] M. Sakagami, "In vivo, in vitro and ex vivo models to assess pulmonary absorption and disposition of inhaled therapeutics for systemic delivery," *Advanced drug delivery reviews,* vol. 58, no. 9-10, pp. 1030-1060, 2006.

[241] K. Sharun, S. A. Banu, T. El Khassawna, and C. P. Pennisi, "Ex Vivo Models: Transforming Standards in Preclinical Bone Regeneration Research," *Discovery medicine,* vol. 38, no. 204, pp. 305-309, 2026.

[242] T. Bellido and J. Delgado Calle, "Ex vivo organ cultures as models to study bone biology," *Journal of Bone and Mineral Research Plus,* vol. 4, no. 3, p. e10345, 2020.

[243] F. Hamandi and T. Goswami, "Hierarchical structure and properties of the bone at nano level," *Bioengineering,* vol. 9, no. 11, p. 677, 2022.

[244] V. Karageorgiou and D. Kaplan, "Porosity of 3D biomaterial scaffolds and osteogenesis," *Biomaterials,* vol. 26, no. 27, pp. 5474-5491, 2005.

[245] M. N. Gómez-Cerezo, J. Peña, S. Ivanovski, D. Arcos, M. Vallet-Regí, and C. Vaquette, "Multiscale porosity in mesoporous bioglass 3D-printed scaffolds for bone regeneration," *Materials Science and Engineering: C,* vol. 120, p. 111706, 2021.

[246] S. Deville, E. Saiz, and A. P. Tomsia, "Freeze casting of hydroxyapatite scaffolds for bone tissue engineering," *Biomaterials,* vol. 27, no. 32, pp. 5480-5489, 2006.

[247] Aminatun *et al.*, "Biopolymer-based polycaprolactone-hydroxyapatite scaffolds for bone tissue engineering," *International Journal of Polymeric Materials and Polymeric Biomaterials,* vol. 72, no. 5, pp. 376-385, 2023.

[248] L. Bacakova, E. Filova, M. Parizek, T. Ruml, and V. Svorcik, "Modulation of cell adhesion, proliferation and differentiation on materials designed for body implants," *Biotechnology advances,* vol. 29, no. 6, pp. 739-767, 2011.

[249] F. N. Alaribe, S. L. Manoto, and S. C. Motaung, "Scaffolds from biomaterials: advantages and limitations in bone and tissue engineering," *Biologia,* vol. 71, no. 4, pp. 353-366, 2016.

[250] S. K. Wong, M. M. F. Yee, K.-Y. Chin, and S. Ima-Nirwana, "A review of the application of natural and synthetic scaffolds in bone regeneration," *Journal of functional biomaterials,* vol. 14, no. 5, p. 286, 2023.

[251] Y. Ma *et al.*, "Electrospinning-based bone tissue scaffold construction: Progress and trends," *Materials & Design,* vol. 252, p. 113792, 2025.

[252] S. A. S. Nasrollah *et al.*, "Polyurethane in Bone Tissue Engineering: Bioprinting Vs. Electrospinning," *Colloids and Surfaces B: Biointerfaces,* p. 115270, 2025.

[253] G. Kathiresan, K. Adaikalam, and H. S. Kim, "Advantages of electrospinning biomimetic scaffolds for the current trend of tissue engineering applications," *Journal of Applied Polymer Science,* vol. 142, no. 33, p. e57309, 2025.

[254] Y. Li, X. Li, Z. Liu, Y. Wang, and T. Jiao, "Recent progress in the strategies and applications of electrospinning electroactive tissue engineering scaffolds," *ACS Biomaterials Science & Engineering,* vol. 11, no. 6, pp. 3182-3200, 2025.

[255] N. T. Hiep and B.-T. Lee, "Electro-spinning of PLGA/PCL blends for tissue engineering and their biocompatibility," *Journal of Materials Science: Materials in Medicine,* vol. 21, no. 6, pp. 1969-1978, 2010.

[256] Z. Mohammadalizadeh, E. Bahremandi-Toloue, and S. Karbasi, "Synthetic-based blended electrospun scaffolds in tissue engineering applications," *Journal of Materials Science,* vol. 57, no. 6, pp. 4020-4079, 2022.

[257] A. P. Kishan and E. M. Cosgriff-Hernandez, "Recent advancements in electrospinning design for tissue engineering applications: A review," *Journal of Biomedical Materials Research Part A,* vol. 105, no. 10, pp. 2892-2905, 2017.

[258] R. Wang *et al.*, "Study on repair of periodontal bone defect in rats with PCL-PEG electrospun nanofibers combined with amniotic homogenate supernatant," *American Journal of Translational Research,* vol. 17, no. 12, p. 9478, 2025.

[259] H. B. Eitouni and N. P. Balsara, "Thermodynamics of polymer blends," in *Physical Properties of Polymers Handbook*: Springer, 2007, pp. 339-356.

[260] A. A. A. Abdel-Azim, A. M. Atta, M. S. Farahat, and W. Y. Boutros, "Miscibility of polystyrene with poly (ethylene oxide) and poly (ethylene glycol)," *Journal of applied polymer science,* vol. 69, no. 8, pp. 1471-1482, 1998.

[261] M. Tahir, S. Vicini, and A. Sionkowska, "Electrospun materials based on polymer and biopolymer blends—a review," *Polymers,* vol. 15, no. 7, p. 1654, 2023.

[262] M. Bognitzki *et al.*, "Preparation of fibers with nanoscaled morphologies: Electrospinning of polymer blends," *Polymer Engineering & Science,* vol. 41, no. 6, pp. 982-989, 2001.

[263] M. Hasanizadeh, A. Aroujalian, and A. Raisi, "Fabrication of PES/NaX nanocomposite nanofibrous adsorbent for the removal of Cu2+, Co2+ and Fe2+ from aqueous solutions," *Desalination and Water Treatment,* vol. 78, pp. 221-230, 2017.

[264] R. Scaffaro, F. Lopresti, L. Botta, S. Rigogliuso, and G. Ghersi, "Melt processed PCL/PEG scaffold with discrete pore size gradient for selective cellular infiltration," *Macromolecular Materials and Engineering,* vol. 301, no. 2, pp. 182-190, 2016.

[265] M. Bousmina, A. Ait-Kadi, and J. Faisant, "Determination of shear rate and viscosity from batch mixer data," *Journal of rheology,* vol. 43, no. 2, pp. 415-433, 1999.

[266] F. Shakeel, N. Haq, I. A. Alsarra, and S. Alshehri, "Solubility, Hansen solubility parameters and thermodynamic behavior of emtricitabine in various (polyethylene glycol-400+ water)

mixtures: Computational modeling and thermodynamics," *Molecules,* vol. 25, no. 7, p. 1559, 2020.

[267] M. Fernández-Berridi, T. Otero, G. Guzmán, and J. Elorza, "Determination of the solubility parameter of poly (ethylene oxide) at 25° C by gas-liquid chromatography," *Polymer,* vol. 23, no. 9, pp. 1361-1366, 1982.

[268] N. A. Peppas and E. W. Merrill, "Poly (vinyl alcohol) hydrogels: reinforcement of radiation-crosslinked networks by crystallization," *Journal of Polymer Science: Polymer Chemistry Edition,* vol. 14, no. 2, pp. 441-457, 1976.

[269] M. Salzano de Luna, A. Causa, and G. Filippone, "Interfacially-located nanoparticles anticipate the onset of co-continuity in immiscible polymer blends," *Polymers,* vol. 9, no. 9, p. 393, 2017.

[270] V. Izraylit, M. Heuchel, O. E. Gould, K. Kratz, and A. Lendlein, "Strain recovery and stress relaxation behaviour of multiblock copolymer blends physically cross-linked with PLA stereocomplexation," *Polymer,* vol. 209, p. 122984, 2020.

[271] E. Maccaferri, L. Mazzocchetti, T. Benelli, T. M. Brugo, A. Zucchelli, and L. Giorgini, "Rubbery nanofibers by co-electrospinning of almost immiscible NBR and PCL blends," *Materials & Design,* vol. 186, p. 108210, 2020.

[272] J. Krajenta, M. Polińska, G. Lapienis, and A. Pawlak, "The crystallization of poly (ethylene oxide) with limited density of macromolecular entanglements," *Polymer,* vol. 197, p. 122500, 2020.

[273] M. Mohseni Garakani, M. E. Cooke, M. R. Wertheimer, D. H. Rosenzweig, and A. Ajji, "A novel 3D in vitro tissue model for bone-metastasized breast cancer: A preclinical tool in drug discovery and testing," *Plasma Processes and Polymers,* vol. 19, no. 7, p. 2100206, 2022.

[274] P. K. Khan *et al.*, "Influence of single and binary doping of strontium and lithium on in vivo biological properties of bioactive glass scaffolds," *Scientific reports,* vol. 6, no. 1, p. 32964, 2016.

[275] S. Lu *et al.*, "Effect of PEO molecular weight on the miscibility and dynamics in epoxy/PEO blends," *The European Physical Journal E,* vol. 38, no. 11, p. 118, 2015.

[276] S. Su, R. Kopitzky, and C. Berrenrath, "Experimental determination of molecular weight-dependent miscibility of PBAT/PLA blends," *Polymers,* vol. 13, no. 21, p. 3686, 2021.

[277] R. Nayak, R. Padhye, I. L. Kyratzis, Y. B. Truong, and L. Arnold, "Effect of viscosity and electrical conductivity on the morphology and fiber diameter in melt electrospinning of polypropylene," *Textile Research Journal,* vol. 83, no. 6, pp. 606-617, 2013.

[278] P. Nguyen Tri and R. E. Prud'homme, "Crystallization and segregation behavior at the submicrometer scale of PCL/PEG blends," *Macromolecules,* vol. 51, no. 18, pp. 7266-7273, 2018.

[279] H. Huo, C. Guo, J. Zhou, and X. Zhao, "The combination of fluctuation-assisted crystallization and interface-assisted crystallization in a crystalline/crystalline blend of poly (ethylene oxide) and poly (ε-caprolactone)," *Colloid and Polymer Science,* vol. 292, no. 4, pp. 971-983, 2014.

[280] X. Y. D. Soo *et al.*, "Electrospun PEO/PEG fibers as potential flexible phase change materials for thermal energy regulation," in *Exploration*, 2024, vol. 4, no. 1: Wiley Online Library, p. 20230016.

[281] N. Tian, J. Chen, and Y. Liu, "Crystallization in blend of polycaprolactone and high molecular weight polyethylene oxide," *Nuclear Analysis,* vol. 2, no. 4, p. 100090, 2023.

[282] L. Gong *et al.*, "Discovery of β-form crystal structure in electrospun poly [(R)-3-hydroxybutyrate-co-(R)-3-hydroxyhexanoate](PHBHx) nanofibers: from fiber mats to single fibers," *Macromolecules,* vol. 48, no. 17, pp. 6197-6205, 2015.

[283] Y. Taşgin, M. E. Pekdemir, M. Yilmaz, M. S. Kanca, and M. Kök, "Physical and shielding properties of Er2O3 rare earth oxide compound content on PCL/PEG blend," *Polymer bulletin,* vol. 81, no. 4, pp. 2915-2931, 2024.

[284] M. H. Huang *et al.*, "Degradation and cell culture studies on block copolymers prepared by ring opening polymerization of ϵ-caprolactone in the presence of poly (ethylene glycol)," *Journal of Biomedical Materials Research Part A: An Official Journal of The Society for Biomaterials, The Japanese Society for Biomaterials, and The Australian Society for Biomaterials and the Korean Society for Biomaterials,* vol. 69, no. 3, pp. 417-427, 2004.

[285] L. Jovanska, C.-H. Chiu, Y.-C. Yeh, W.-D. Chiang, C.-C. Hsieh, and R. Wang, "Development of a PCL-PEO double network colorimetric pH sensor using electrospun fibers containing Hibiscus rosa sinensis extract and silver nanoparticles for food monitoring," *Food Chemistry,* vol. 368, p. 130813, 2022.

[286] W.-T. Chuang, U.-S. Jeng, H.-S. Sheu, and P.-D. Hong, "Competition between phase separation and crystallization in a PCL/PEG polymer blend captured by synchronized SAXS, WAXS, and DSC," *Macromolecular research,* vol. 14, no. 1, pp. 45-51, 2006.

[287] C. Luo, W. Chen, and Y. Gao, "Fractional crystallization behavior of PCL and PEG in blends," *Polymer Science Series A,* vol. 58, no. 2, pp. 196-205, 2016.

[288] W.-T. Chuang, K.-S. Shih, and P.-D. Hong, "Kinetics of phase separation in poly (ε-caprolactone)/poly (ethylene glycol) blends," *Journal of Polymer Research,* vol. 12, no. 3, pp. 197-204, 2005.

[289] D. Xia *et al.*, "Robust hierarchical porous Polycaprolactone/nano-Hydroxyapatite/Polyethylene glycol scaffolds with boosted in vitro osteogenic ability," *Colloids and Surfaces A: Physicochemical and Engineering Aspects,* vol. 681, p. 132740, 2024.

[290] A. R. Calore *et al.*, "Manufacturing of scaffolds with interconnected internal open porosity and surface roughness," *Acta Biomaterialia,* vol. 156, pp. 158-176, 2023.

[291] A. G. Giacaman, I. D. Styliari, V. Taresco, D. Pritchard, C. Alexander, and F. R. Rose, "Development of bioactive electrospun scaffolds suitable to support skin fibroblasts and release Lucilia sericata maggot excretion/secretion," *SN Applied Sciences,* vol. 4, no. 12, p. 331, 2022.

[292] J. Lee, D. Kim, C. H. Jang, and G. H. Kim, "Highly elastic 3D-printed gelatin/HA/placental-extract scaffolds for bone tissue engineering," *Theranostics,* vol. 12, no. 9, p. 4051, 2022.

[293] W. Liu, N. Cheong, Z. He, and T. Zhang, "Application of hydroxyapatite composites in bone tissue engineering: a review," *Journal of Functional Biomaterials,* vol. 16, no. 4, p. 127, 2025.

[294] S. Sebastiani, F. Buccino, Z. Qin, and L. M. Vergani, "Structural influences on bone tissue engineering: A review and perspective," *Matter,* vol. 8, no. 9, 2025.

[295] A. Garimella, S. B. Ghosh, and S. Bandyopadhyay-Ghosh, "Biomaterials for bone tissue engineering: achievements to date and future directions," *Biomedical Materials,* vol. 20, no. 1, p. 012001, 2025.

[296] S. S. Khobragade, M. Deshmukh, U. Vyas, and R. G. Ingle, "Innovative approaches in bone tissue engineering: Strategies for cancer treatment and recovery," *International Journal of Molecular Sciences,* vol. 26, no. 9, p. 3937, 2025.

[297] P. Chocholata, V. Kulda, and V. Babuska, "Fabrication of scaffolds for bone-tissue regeneration," *Materials,* vol. 12, no. 4, p. 568, 2019.

[298] T. Huang *et al.*, "Application and development of electrospun nanofiber scaffolds for bone tissue engineering," *ACS Biomaterials Science & Engineering,* vol. 10, no. 7, pp. 4114-4144, 2024.

[299] V. Cárdenas *et al.*, "Tuning the properties of polycaprolactone-based fibers by using polyethylene oxide/polycaprolactone block copolymers," *Journal of Polymer Research,* vol. 31, no. 2, p. 60, 2024.

[300] A. Cordoba *et al.*, "Electrospun bioactive fibers of PCL/Starch loaded with bioglass nanoparticles with potential application in bone tissue engineering: An in vitro and in vivo study," *Journal of Drug Delivery Science and Technology,* p. 107496, 2025.

[301] K. Virijević *et al.*, "AI-driven optimization of PCL/PEG electrospun scaffolds for enhanced in vivo wound healing," *ACS Applied Materials & Interfaces,* vol. 16, no. 18, pp. 22989-23002, 2024.

[302] J. Maitra and N. Bhardwaj, "Development of bio-based polymeric blends–a comprehensive review," *Journal of Biomaterials Science, Polymer Edition,* vol. 36, no. 1, pp. 102-136, 2025.

[303] D. Bani Mustafa, T. Sakai, O. Sato, M. Ikebe, and S.-F. Chou, "Electrospun ibuprofen-loaded blend PCL/PEO fibers for topical drug delivery applications," *Polymers,* vol. 16, no. 13, p. 1934, 2024.

[304] V. Kupka *et al.*, "Well-blended PCL/PEO electrospun nanofibers with functional properties enhanced by plasma processing," *Polymers,* vol. 12, no. 6, p. 1403, 2020.

[305] J. Li, W. Wang, D. Xu, X. Wang, and Y. Mao, "Preparation of sulfoaluminate cementitious material using harmful titanium gypsum: Material properties and heavy metal immobilization characteristics," *Waste Disposal & Sustainable Energy,* vol. 2, no. 2, pp. 127-137, 2020.

[306] E. Vey, C. Rodger, J. Booth, M. Claybourn, A. F. Miller, and A. Saiani, "Degradation kinetics of poly (lactic-co-glycolic) acid block copolymer cast films in phosphate buffer

solution as revealed by infrared and Raman spectroscopies," *Polymer degradation and stability,* vol. 96, no. 10, pp. 1882-1889, 2011.

[307] I. Cacciotti, M. Calderone, and A. Bianco, "Tailoring the properties of electrospun PHBV mats: Co-solution blending and selective removal of PEO," *European polymer journal,* vol. 49, no. 10, pp. 3210-3222, 2013.

[308] H.-W. Kim, J. C. Knowles, and H.-E. Kim, "Hydroxyapatite/poly (ε-caprolactone) composite coatings on hydroxyapatite porous bone scaffold for drug delivery," *Biomaterials,* vol. 25, no. 7-8, pp. 1279-1287, 2004.

[309] A. Rapacz-Kmita, C. Paluszkiewicz, A. Ślósarczyk, and Z. Paszkiewicz, "FTIR and XRD investigations on the thermal stability of hydroxyapatite during hot pressing and pressureless sintering processes," *Journal of Molecular Structure,* vol. 744, pp. 653-656, 2005.

[310] W. Xue, P. Chen, F. Wang, and L. Wang, "Melt spinning of nano-hydroxyapatite and polycaprolactone composite fibers for bone scaffold application," *Journal of Materials Science,* vol. 54, no. 11, pp. 8602-8612, 2019.

[311] J. Li, Y. Zhang, Y. Jiacuo, Y. Shang, H. Huo, and S. Jiang, "Miscibility and rheologically determined phase diagram of poly (ethylene oxide)/poly (ε-caprolactone) blends," *Polymer bulletin,* vol. 68, no. 5, pp. 1405-1423, 2012.

[312] Y. Wang, D. Liang, F. Liu, W. Zhang, X. Di, and C. Wang, "A polyethylene glycol/hydroxyapatite composite phase change material for thermal energy storage," *Applied Thermal Engineering,* vol. 113, pp. 1475-1482, 2017.

[313] M. P. Motloung, T. G. Mofokeng, and S. S. Ray, "Viscoelastic, thermal, and mechanical properties of melt-processed poly (ε-caprolactone)(PCL)/hydroxyapatite (HAP) composites," *Materials,* vol. 15, no. 1, p. 104, 2021.

[314] H. Li, C. Huang, X. Jin, and Q. Ke, "An electrospun poly (ε-caprolactone) nanocomposite fibrous mat with a high content of hydroxyapatite to promote cell infiltration," *RSC advances,* vol. 8, no. 44, pp. 25228-25235, 2018.

[315] A. Visan *et al.*, "Long-term evaluation of dip-coated PCL-blend-PEG coatings in simulated conditions, Polymers (Basel) 12 (2020) 717," ed.

[316] R. d. N. Silva, L. R. C. da Silva, A. C. L. de Morais, T. S. Alves, and R. Barbosa, "Study of the hydrolytic degradation of poly-3-hydroxybutyrate in the development of blends and

polymeric bionanocomposites," *Journal of Thermoplastic Composite Materials,* vol. 34, no. 7, pp. 884-901, 2021.

[317] N. Abedi, A. Sadeghian, M. Kouhi, H. J. Haugen, O. Savabi, and F. Nejatidanesh, "Immunomodulation in bone tissue engineering: recent advancements in scaffold design and biological modifications for enhanced regeneration," *ACS Biomaterials Science & Engineering,* vol. 11, no. 3, pp. 1269-1290, 2025.

[318] P. B. Kasi *et al.*, "Electroconductive gelatin/hyaluronic acid/hydroxyapatite scaffolds for enhanced cell proliferation and osteogenic differentiation in bone tissue engineering," *Biomaterials Advances,* vol. 173, p. 214286, 2025.

[319] T. N. Pansani, C. A. de Souza Costa, L. M. Cardoso, A. M. Claro, H. d. S. Barud, and F. G. Basso, "Synthesis, characterization, and osteogenic ability of fibrillar polycaprolactone scaffolds containing hydroxyapatite nanoparticles," *ACS Applied Materials & Interfaces,* vol. 17, no. 14, pp. 20647-20657, 2025.

[320] N. Amiryaghoubi and R. J. Esfahlan, "Applications of hydroxyapatite-based polymeric scaffolds in bone tissue engineering: an update," *Advanced Pharmaceutical Bulletin,* vol. 14, no. 4, p. 794, 2024.

[321] L. Dejob, B. Toury, S. Tadier, L. Gremillard, C. Gaillard, and V. Salles, "Electrospinning of in situ synthesized silica-based and calcium phosphate bioceramics for applications in bone tissue engineering: A review," *Acta Biomaterialia,* vol. 123, pp. 123-153, 2021.

[322] Z. Cao, H. Zhuo, W. Zhu, X. Peng, and J. Li, "Rational construction of PCL-PEG/CS/AST nanofiber for bone repair and regeneration," *Frontiers in Bioengineering and Biotechnology,* vol. 12, p. 1515043, 2025.

[323] A. Jahani and H. Nassira, "Polyethylene glycol-based materials: Transformative applications in biomedicine and the food industry," *Mater. Chem. Horiz,* vol. 3, p. 1074, 2024.

[324] E. Karimi, F. Mighri, M. C. Heuzey, and A. Ajji, "Melt Electrospinning of Poly (ε-Caprolactone)/Polyethylene Oxide/Polyethylene Glycol—Hydroxyapatite Nanocomposite Fibers: Morphology, Properties, and Hydrolytic Degradation," *Polymer Engineering & Science,* 2026.

[325] C. Feng *et al.*, "Co-inspired hydroxyapatite-based scaffolds for vascularized bone regeneration," *Acta biomaterialia,* vol. 119, pp. 419-431, 2021.

[326] M. L. Gatto *et al.*, "Combined effects of HA concentration and unit cell geometry on the biomechanical behavior of PCL/HA scaffold for tissue engineering applications produced by LPBF," *Materials,* vol. 16, no. 14, p. 4950, 2023.

[327] V. Chopra *et al.*, "Advancements in 3D-4D printing of hydroxyapatite composites for bone tissue engineering," *Ceramics International,* vol. 50, no. 20, pp. 38819-38840, 2024.

[328] Y. Yin *et al.*, "Melt electrowriting for biomimetic tissue engineering: advances in scaffold design, materials, and multifunctional applications," *Polymers for Advanced Technologies,* vol. 36, no. 1, p. e70067, 2025.

[329] J. Wang, L. Tang, K. He, H. Wang, W. Wang, and Y. Tang, "Preparation and optimization of PBAT-Based scaffolds via melt electrowriting for bone tissue engineering," *ACS Applied Polymer Materials,* vol. 7, no. 17, pp. 11581-11597, 2025.

[330] T. M. Robinson, D. W. Hutmacher, and P. D. Dalton, "The next frontier in melt electrospinning: taming the jet," *Advanced Functional Materials,* vol. 29, no. 44, p. 1904664, 2019.

[331] V. Sgarminato, C. Tonda-Turo, and G. Ciardelli, "Reviewing recently developed technologies to direct cell activity through the control of pore size: From the macro-to the nanoscale," *Journal of Biomedical Materials Research Part B: Applied Biomaterials,* vol. 108, no. 4, pp. 1176-1185, 2020.

[332] H. Ju, W. Mirihanage, W. Wang, and Z. M. Kilic, "Review on Melt Electrowriting Modelling and Applications," *Machines,* vol. 13, no. 9, p. 763, 2025.

[333] M. M. Garakani *et al.*, "A novel 3D co-culture platform for integrating tissue interfaces for tumor growth, migration and therapeutic sensitivity:“PP-3D-S”," *Biomaterials Advances,* vol. 134, p. 112566, 2022.

[334] R. Fairag, D. H. Rosenzweig, J. L. Ramirez-Garcialuna, M. H. Weber, and L. Haglund, "Three-dimensional printed polylactic acid scaffolds promote bone-like matrix deposition in vitro," *ACS applied materials & interfaces,* vol. 11, no. 17, pp. 15306-15315, 2019.

[335] R. Fairag *et al.*, "A composite lactide-mineral 3D-printed scaffold for bone repair and regeneration," *Frontiers in Cell and Developmental Biology,* vol. 9, p. 654518, 2021.

[336] A. Dorigato and G. Fredi, "Effect of nanofillers addition on the compatibilization of polymer blends," *Advanced Industrial and Engineering Polymer Research,* vol. 7, no. 4, pp. 405-427, 2024.

[337] M. Hassan and N. Sultana, "Characterization, drug loading and antibacterial activity of nanohydroxyapatite/polycaprolactone (nHA/PCL) electrospun membrane. 3 Biotech. 2017; 7 (4): 249," *Cited Here,* 2017.

[338] S. M. Hosseiny, S. H. Jafari, H. A. Khonakdar, F. Hemmati, and M. R. Kalaee, "A correlation between morphology and mechanical performance of injected-molded PE/EVA/clay nanocomposites: Insight into phase miscibility and interfacial phenomena," *Journal of Applied Polymer Science,* vol. 137, no. 45, p. 49401, 2020.

[339] A. R. Khan, A. D. Gholap, N. S. Grewal, Z. Jun, M. Khalid, and H.-J. Zhang, "Advances in smart hybrid scaffolds: A strategic approach for regenerative clinical applications," *Engineered Regeneration,* vol. 6, pp. 85-110, 2025.

[340] R. Banerjee, Y. Li, and S. S. Ray, "Nanoparticle-induced morphology evolution and property expression in immiscible polymer blend composites− A review of fundamental understanding on nanoparticle migration and interface crossing," *Polymer,* vol. 316, p. 127844, 2025.

[341] G. Fredi and A. Dorigato, "Compatibilization of biopolymer blends: A review," *Advanced Industrial and Engineering Polymer Research,* vol. 7, no. 4, pp. 373-404, 2024.

[342] M. Ngiam, S. Liao, A. J. Patil, Z. Cheng, C. K. Chan, and S. Ramakrishna, "The fabrication of nano-hydroxyapatite on PLGA and PLGA/collagen nanofibrous composite scaffolds and their effects in osteoblastic behavior for bone tissue engineering," *Bone,* vol. 45, no. 1, pp. 4-16, 2009.

[343] M. Mohammadi, M.-C. Heuzey, P. J. Carreau, and A. Taguet, "Morphological and rheological properties of PLA, PBAT, and PLA/PBAT blend nanocomposites containing CNCs," *Nanomaterials,* vol. 11, no. 4, p. 857, 2021.

[344] M. Bigerelle and K. Anselme, "A kinetic approach to osteoblast adhesion on biomaterial surface," *Journal of Biomedical Materials Research Part A: An Official Journal of The Society for Biomaterials, The Japanese Society for Biomaterials, and The Australian Society for Biomaterials and the Korean Society for Biomaterials,* vol. 75, no. 3, pp. 530-540, 2005.

[345] K. L. Prime and G. M. Whitesides, "Self-assembled organic monolayers: Model systems for studying adsorption of proteins at aurfaces," *Science,* vol. 252, no. 5009, pp. 1164-1167, 1991.

[346] M. D. Swartzlander, C. A. Barnes, A. K. Blakney, J. L. Kaar, T. R. Kyriakides, and S. J. Bryant, "Linking the foreign body response and protein adsorption to PEG-based hydrogels using proteomics," *Biomaterials,* vol. 41, pp. 26-36, 2015.

[347] E. A. Vogler, "Protein adsorption in three dimensions," *Biomaterials,* vol. 33, no. 5, pp. 1201-1237, 2012.

[348] G. Zhou, H. Loppnow, and T. Groth, "A macrophage/fibroblast co-culture system using a cell migration chamber to study inflammatory effects of biomaterials," *Acta biomaterialia,* vol. 26, pp. 54-63, 2015.

[349] S. Capuani, G. Malgir, C. Y. X. Chua, and A. Grattoni, "Advanced strategies to thwart foreign body response to implantable devices," *Bioengineering & Translational Medicine,* vol. 7, no. 3, p. e10300, 2022.

[350] S. Pezzatini *et al.*, "The effect of hydroxyapatite nanocrystals on microvascular endothelial cell viability and functions," *Journal of Biomedical Materials Research Part A: An Official Journal of The Society for Biomaterials, The Japanese Society for Biomaterials, and The Australian Society for Biomaterials and the Korean Society for Biomaterials,* vol. 76, no. 3, pp. 656-663, 2006.

[351] H. Yu, P. H. Wooley, and S.-Y. Yang, "Biocompatibility of Poly-ε-caprolactone-hydroxyapatite composite on mouse bone marrow-derived osteoblasts and endothelial cells," *Journal of Orthopaedic Surgery and Research,* vol. 4, no. 1, p. 5, 2009.

[352] U. Szałaj, A. Chodara, S. Gierlotka, J. Wojnarowicz, and W. Łojkowski, "Enhanced release of calcium ions from hydroxyapatite nanoparticles with an increase in their specific surface area," *Materials,* vol. 16, no. 19, p. 6397, 2023.

[353] D. Liu *et al.*, "Activation of extracellular-signal regulated kinase (ERK1/2) by fluid shear is Ca2+-and ATP-dependent in MC3T3-E1 osteoblasts," *Bone,* vol. 42, no. 4, pp. 644-652, 2008.

[354] J. K. Foskett, C. White, K.-H. Cheung, and D.-O. D. Mak, "Inositol trisphosphate receptor Ca2+ release channels," *Physiological reviews,* vol. 87, no. 2, pp. 593-658, 2007.

[355] S. Puckett, R. Pareta, and T. J. Webster, "Nano rough micron patterned titanium for directing osteoblast morphology and adhesion," *International journal of nanomedicine,* vol. 3, no. 2, pp. 229-241, 2008.

[356] M. Pilia, T. Guda, S. M. Shiels, and M. R. Appleford, "Influence of substrate curvature on osteoblast orientation and extracellular matrix deposition," *Journal of biological engineering,* vol. 7, no. 1, p. 23, 2013.

[357] B. Garipcan *et al.*, "Image analysis of endothelial microstructure and endothelial cell dimensions of human arteries–a preliminary study," *Advanced engineering materials,* vol. 13, no. 1-2, pp. B54-B57, 2011.

[358] N. Jiménez, V. J. Krouwer, and J. A. Post, "A new, rapid and reproducible method to obtain high quality endothelium in vitro," *Cytotechnology,* vol. 65, no. 1, pp. 1-14, 2013.

[359] K. F. Eichholz and D. A. Hoey, "Mediating human stem cell behaviour via defined fibrous architectures by melt electrospinning writing," *Acta biomaterialia,* vol. 75, pp. 140-151, 2018.

[360] S. Biscaia *et al.*, "3D printed poly (?-caprolactone)/hydroxyapatite scaffolds for bone tissue engineering: a comparative study on a composite preparation by melt blending or solvent casting techniques and the influence of bioceramic content on scaffold properties," *International journal of molecular sciences,* vol. 23, no. 4, p. 2318, 2022.

[361] K. F. Eichholz and D. A. Hoey, "Melt electrowritten scaffolds with bone-inspired fibrous and mineral architectures to enhance BMP2 delivery and human MSC osteogenesis," *bioRxiv,* p. 734855, 2019.

[362] M. A. Obeid, L. Akil, Y. M. Abul-Haija, and I. Khadra, "Formulation of polycaprolactone meshes by melt electrospinning for controlled release of daunorubicin in tumour therapy," *Colloids and Surfaces A: Physicochemical and Engineering Aspects,* vol. 699, p. 134873, 2024.

[363] H. Bilgili, M. Aydin, M. Sahin, S. Sahin, S. Cetinel, and G. Kiziltas, "3D-printed functionally graded PCL-HA scaffolds with multi-scale porosity, ACS Omega 10 (2025) 6502–6519," ed.

[364] M. Trzaskowska *et al.*, "Biocompatible nanocomposite hydroxyapatite-based granules with increased specific surface area and bioresorbability for bone regenerative medicine applications," *Scientific Reports,* vol. 14, no. 1, p. 28137, 2024.

[365] G. Mestres, M. Espanol, W. Xia, C. Persson, M.-P. Ginebra, and M. K. Ott, "Inflammatory response to nano-and microstructured hydroxyapatite," *PLoS One,* vol. 10, no. 4, p. e0120381, 2015.

[366] J. Wang *et al.*, "Nano-hydroxyapatite coating promotes porous calcium phosphate ceramic-induced osteogenesis via BMP/Smad signaling pathway," *International journal of nanomedicine,* pp. 7987-8000, 2019.

[367] E. Giesen, M. Ding, M. Dalstra, and T. Van Eijden, "Mechanical properties of cancellous bone in the human mandibular condyle are anisotropic," *Journal of biomechanics,* vol. 34, no. 6, pp. 799-803, 2001.

[368] A. Wubneh, E. K. Tsekoura, C. Ayranci, and H. Uludağ, "Current state of fabrication technologies and materials for bone tissue engineering," *Acta biomaterialia,* vol. 80, pp. 1-30, 2018.

[369] S. J. Kaplan, W. C. Hayes, J. L. Stone, and G. S. Beaupré, "Tensile strength of bovine trabecular bone," *Journal of biomechanics,* vol. 18, no. 9, pp. 723-727, 1985.

[370] J. R. Perez, D. Kouroupis, D. J. Li, T. M. Best, L. Kaplan, and D. Correa, "Tissue engineering and cell-based therapies for fractures and bone defects," *Frontiers in bioengineering and biotechnology,* vol. 6, p. 105, 2018.

[371] J. R. Sheen, A. Mabrouk, and V. V. Garla, "Fracture healing overview," in *StatPearls [Internet]*: StatPearls Publishing, 2023.

[372] C. T. Lim, "Nanofiber technology: current status and emerging developments," *Progress in polymer science,* vol. 70, pp. 1-17, 2017.

[373] M. Yuasa *et al.*, "Dexamethasone enhances osteogenic differentiation of bone marrow-and muscle-derived stromal cells and augments ectopic bone formation induced by bone morphogenetic protein-2," *PloS one,* vol. 10, no. 2, p. e0116462, 2015.

[374] M. B. Sordi *et al.*, "Effect of dexamethasone as osteogenic supplementation in in vitro osteogenic differentiation of stem cells from human exfoliated deciduous teeth," *Journal of Materials Science: Materials in Medicine,* vol. 32, no. 1, p. 1, 2021.

[375] J. Mi, Y. Yang, X. Zhu, S. Zheng, and J. Zhao, "Osteogenic action of the natural plant material icariin and its potential use in biomedical tissue engineering," *American journal of translational research,* vol. 17, no. 8, p. 5814, 2025.

[376] Z. Seyedi *et al.*, "Icariin: a promising natural product in biomedicine and tissue engineering," *Journal of Functional Biomaterials,* vol. 14, no. 1, p. 44, 2023.

[377] R. Svoboda, R. Vrbenský, J. Honzíček, and M. Chromčíková, "Thermal Stability of Dexamethasone—Evaluation with Regard to Modern Medicinal and Pharmaceutical 3D-Printing Applications," *Molecules,* vol. 30, no. 21, p. 4234, 2025.

APPENDIX A RHEOLOGICAL PROPERTIES

Objective

In this study, rheology was used as a key, reliable tool to investigate the behavior of polymer systems and better understand their structural and morphological properties. Since the rheological behavior of polymers is directly affected by the interaction between the different components of the system, the degree of miscibility, the distribution of phases, and the internal structure of the materials, rheological analysis can provide valuable information about the behavior of these systems during the process as well as their final structure [14,186]. For this reason, the study of rheological properties plays an important role in interpreting the behavior of polymer blends, as well as the relationships among the process, structure, and final properties.

The results of the isothermal rheological tests, presented in Chapter 4, showed that the selected process temperature for the studied systems did not lead to thermal degradation of the polymers and that appropriate process stability was maintained throughout the test time. This is of great importance in the melt electrospinning process because any thermal degradation can lead to changes in the flow behavior, process instability, and ultimately changes in the morphology of the produced fibers [186,187]. In addition, the results of the frequency sweep test provided more detailed information on the viscoelastic behavior of the systems, the degree of polymer chain entanglement, and the processability of the samples.

Methodology

Melt rheological properties of the neat PCL, binary and ternary blends were evaluated using an MCR-302 rotational rheometer (Anton Paar, Graz, Austria) under the nitrogen atmosphere to avoid oxidation. The experiments were conducted at 150˚C, the same temperature at which the blends were melt electrospun. The instrument's parallel-plate geometry had a 1 mm spacing and a 25 mm diameter. To avoid affecting the structure of the blends, an amplitude sweep test was conducted first to identify the linear viscoelastic region (LVE region), while the frequency was adjusted at ten 1/s, and the strain was varied from 0.01 to 100%. Accordingly, the frequency sweep test was performed when the strain was adjusted at 5% as a value within the LVE limit, and the frequency was varied in the range of 600 to 0. 011/s. To evaluate the stability of the components and to

estimate the morphological changes of the samples at the melt electrospinning temperature, the time-dependent test in the oscillation mode was done for the samples when the frequency was set at one 1/s. To verify whether the arising curves in the time-dependent test result from coarsening or degradation, the frequency test was done for the samples from high to low and low to high consecutively. To mitigate experimental errors, the tests were replicated three times, and the mean values were documented.

Results and discussion

The viscoelastic properties of the samples were investigated using small-amplitude oscillatory shear rheological experiments to evaluate the melt electrospinability of neat PCL and the different blend systems, as well as to gain further insight into their phase morphologies and structural behavior. The complex viscosity of the samples as a function of angular frequency at 150 °C is presented in Figure A.1.

The rheological results demonstrate that the viscoelastic behavior of the systems is strongly dependent on blend composition. Most samples, particularly those containing PEO, exhibited clear frequency-dependent complex viscosity, indicating pronounced shear-thinning behavior. In contrast, neat PCL and PEG-rich blends showed comparatively lower viscosity and a more Newtonian-like response over a broader low-frequency region.

The incorporation of PEG significantly reduced the complex viscosity of the PCL-based blends, especially in the binary PCL/PEG systems. This behavior can be attributed to the relatively low molecular weight of PEG and its plasticizing effect, which likely enhanced chain mobility and reduced the effective entanglement density of the polymer chains. As a result, PEG improved the flow behavior and processability of the blends by lowering the melt viscosity. In addition, PCL/PEG binary blends exhibited a more pronounced Newtonian plateau region at low frequencies followed by shear-thinning behavior at higher frequencies.

In contrast, the incorporation of PEO resulted in a considerable increase in complex viscosity together with stronger shear-thinning behavior. This behavior is mainly associated with the high molecular weight of PEO, which increases chain entanglement and restricts molecular mobility in the molten state. A clear example is the significantly higher viscosity of the PCL/PEO (50/50) blend compared with the PCL/PEG (50/50) system over the investigated frequency range.

For the ternary PCL/PEO/PEG blends, the rheological behavior indicates that the influence of PEO was dominant over the viscosity-reducing effect of PEG. Consequently, the ternary systems exhibited higher complex viscosity and more pronounced shear-thinning behavior compared with the PCL/PEG binary blends. Although the ternary blends contained equal amounts of PEO and PEG, the high molecular weight contribution of PEO played a more significant role in controlling the rheological response of the system. Overall, the viscosity of the ternary blends generally fell within the range of the PCL/PEO binary systems, further highlighting the dominant contribution of PEO to the melt behavior of the blends.

Among all investigated systems, the PEO/PEG (75/25) blend exhibited the highest complex viscosity over most of the studied frequency range. This behavior can mainly be attributed to the dominant contribution of high-molecular-weight PEO and the resulting higher degree of chain entanglement with PEG than PCL. PEG behaves like an utterly viscous polymer at such a high temperature. This is why PEG's curve is not shown in Figure A.1. On the other hand, PEO is a pure elastic polymer even at 150˚C, so its curve is not depicted in Figure A.1.

Overall, the Figure A.1 provided valuable evidence for understanding the processability, viscoelastic behavior, and morphological characteristics of the polymeric systems investigated in this study.

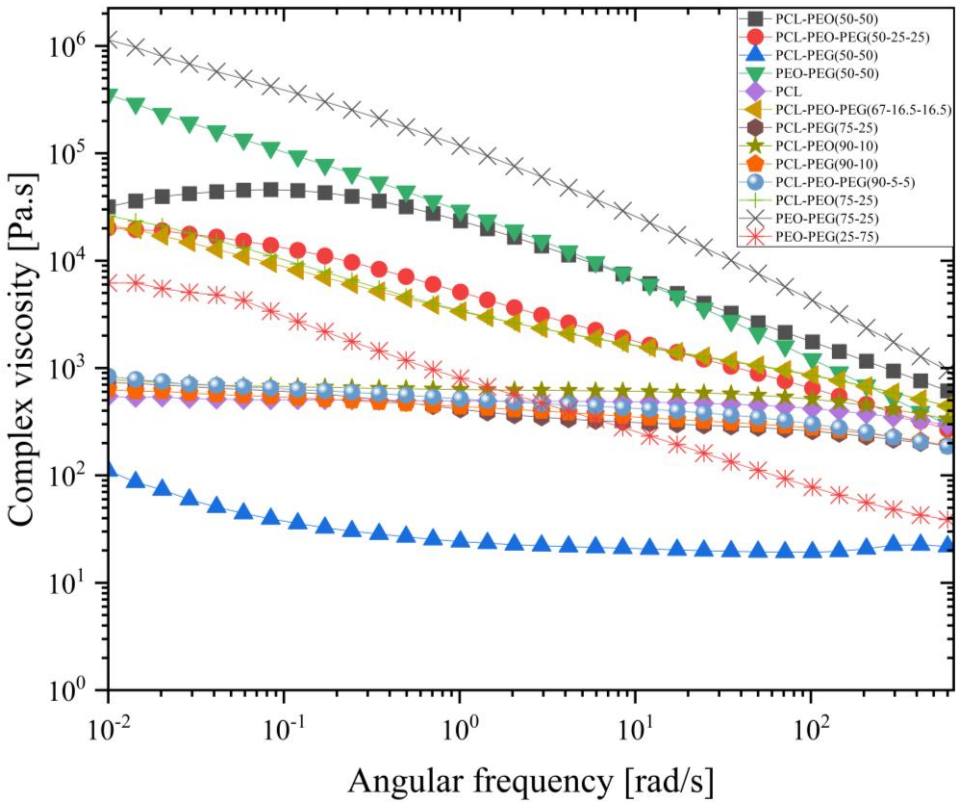

Figure A. 1 Complex viscosity of pure PCL and its binary and ternary blends with PEO and PEG at 150 ˚C as a function of frequency.

Figure A.2 presents the storage modulus (G') and loss modulus (G'') of the investigated polymeric systems as a function of angular frequency at 150 ˚C. The viscoelastic behavior of the blends was strongly influenced by blend composition, molecular weight of the components, and the interactions between the different phases. In general, all samples exhibited frequency-dependent viscoelastic behavior, although the magnitude of the response varied significantly depending on the system composition.

During the pumping process prior to melt electrospinning, samples PCL/PEO (50/50), PEO/PEG (50/50), PEO/PEG (75/25), and PEO/PEG (25/75) exhibited poor flowability and were considerably more difficult to process compared with the other systems. The rheological results are consistent with these observations. These samples showed more elastic-dominant viscoelastic behavior over a broad frequency range, characterized by higher storage modulus values and regions where $G' > G''(\tan\,\delta < 1)$. Such behavior indicates that the elastic contribution of the melt became dominant over the viscous contribution, resulting in increased resistance to flow and reduced melt processability. Although these systems were still in the molten state, their highly

elastic response can significantly limit chain mobility during pumping and melt electrospinning processes.

The PEO-containing systems exhibited significantly higher storage and loss modulus values compared with PEG-rich and neat PCL systems. This behavior is mainly related to the high molecular weight of PEO, which promotes chain entanglement and increases the elastic nature of the polymer melt. The increased entanglement density restricts molecular relaxation and enhances the viscoelastic response of the system, particularly at low frequencies where long-range chain motions become more important. As a result, the incorporation of PEO strongly increased both the elasticity and viscosity of the blends.

In addition, the presence of a relaxation shoulder in the G'curves of the PCL/PEO blends suggests the existence of phase heterogeneity and possible partial immiscibility between PCL and PEO. In multiphase polymer systems, such rheological features are often associated with interfacial relaxation phenomena originating from phase-separated morphologies. This observation is consistent with the morphological analyses presented in this study, which demonstrated the presence of separated phases in PEO-containing systems. Therefore, the rheological behavior further supports the existence of heterogeneous structures within these blends.

In contrast, increasing PEG concentration in the PCL/PEG binary blends resulted in a reduction in both storage and loss modulus values over the investigated frequency range. This behavior can be attributed to the relatively low molecular weight of PEG and its plasticizing effect on the polymeric system. PEG enhances chain mobility, reduces the effective entanglement density, and facilitates molecular motion in the melt state. Consequently, the blends exhibited more liquid-like viscoelastic behavior and improved flow characteristics compared with the PEO-containing systems. The reduction in dynamic moduli with increasing PEG concentration further confirms the role of PEG in improving melt processability and reducing the rigidity of the polymer network.

For the ternary PCL/PEO/PEG systems, the rheological behavior demonstrated that the influence of PEO remained dominant despite the presence of PEG. Although PEG contributed to reducing the rigidity of the system to some extent, the high molecular weight and strong entanglement effect of PEO governed the overall viscoelastic response of the ternary blends. Consequently, these systems exhibited higher modulus values and stronger elastic behavior compared with the PCL/PEG binary blends.

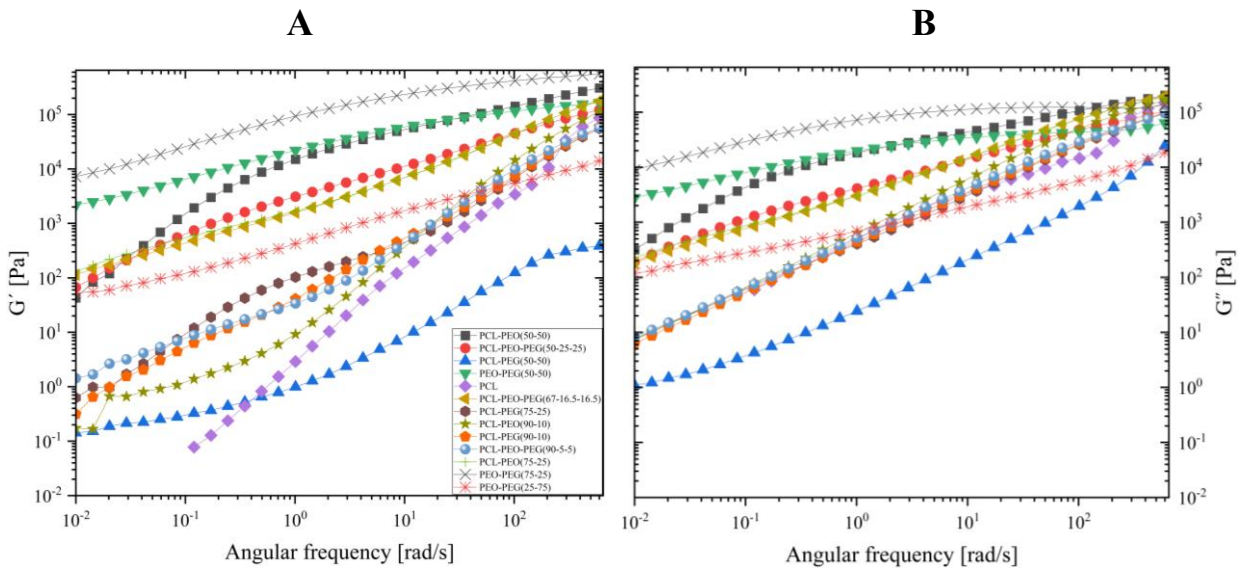

Figure A. 2 (A) Storage modulus (G′) and (B) loss modulus (G″) as a function of frequency.